THE UNIVERSITY OF CHICAGO

QUANTUM NETWORKING WITH SUPERCONDUCTING QUBITS

A DISSERTATION SUBMITTED TO
THE FACULTY OF THE PRITZKER SCHOOL OF MOLECULAR ENGINEERING
IN CANDIDACY FOR THE DEGREE OF
DOCTOR OF PHILOSOPHY

BY
HAOXIONG YAN

CHICAGO, ILLINOIS
AUGUST 2024

To my family

TABLE OF CONTENTS

LIST OF FIGURES

LIST OF TABLES

ACKNOWLEDGMENTS

I would like to first thank my advisor, Andrew Cleland, for his patience and support, as well as for the delicious roast turkey he made for Thanksgiving.

I also want to thank my thesis committee: Hannes Bernien, Alex High, and Liang Jiang.

The completion of this work would not have been possible without the support of my group members. Hung-Shen first introduced me to the lab and taught me all the basic techniques. Youpeng did outstanding work, and we continue to benefit from the setup he built. I learned a great deal about electronics from him. Ming-Han helped me catch up with the qubit fabrication process after the pandemic, and I still remember the nights we spent together in the cleanroom. Joel also worked on a long transmission line project, and without his help, I could not have completed the three-node project. I am also grateful to Joel for his comments on this thesis. These former group members built the lab and their hard work greatly inspired me. They also provided tremendous support during my job search. I wish them all the best with their future career.

Xuntao helped complete the router project, and I appreciate his assistance. I wish him the best as he continues his PhD journey. Hong, I hope you enjoy exploring the field of acoustics. Chris proposed the resistance measurement approach to identify defects in long transmission lines and has always been kind and patient in the lab. Yash and Jacob dedicated significant time to improving the fabrication process, and we hope to achieve qubits with longer coherence times soon. Gustav and Sasha, our postdocs, are incredibly knowledgeable, and I learned a lot from our idea exchanges. Shiheng, our young graduate student, and Jeffrey, our undergrad, are continuously building the new measurement workflow. I believe the lab will keep improving thanks to the efforts of these talented students and postdocs. Jian, our visiting professor, introduced me to the field of materials science.

This work would not have been possible without our theory collaborators: Allen Zang, Andrew Lingenfelter, and Qian Xu. I am fortunate to have incredible theorists like Liang

Jiang and Aash Clerk in UChicago, whom we can always turn to for help.

I also want to express my respect and gratitude to the pioneers in the field of superconducting qubits, particularly the group of John Martinis. I learned the fundamentals of transmons from Jimmy Chen's thesis and the physics of transmon readout from Daniel Sank's thesis. I hope my thesis can similarly serve as a valuable introductory resource for beginners in this field. Additionally, I would like to thank Xuegang Li and Prof. Luyan Sun, who provided me with the opportunity to learn about superconducting qubits during my undergraduate studies.

I want to thank my high school teachers, Shujuan He and Genglei Li, for encouraging me to explore the field of physics.

I am deeply grateful to my parents, Hongguang Yan and Rongmin Guan, for their unconditional love. I also appreciate my aunts, Yan Zhang and Xing Yan, for their help and warm welcome in the U.S. Finally, I want to thank my beloved wife, Jiaqi Li, for her unwavering support and companionship.

ABSTRACT

Superconducting qubits, created using Josephson-based superconducting circuits, offer a promising platform for quantum computing. These circuits have been successfully scaled to hundreds of qubits. However, further scaling of superconducting quantum processors faces challenges such as fabrication yield, frequency collisions, and chip-scale correlated errors induced by cosmic rays. One potential solution is to interconnect small superconducting quantum processors to form a quantum network, facilitating distributed quantum computing. Several experimental results on superconducting quantum networks with various topologies have been presented. These results pave the way for distributed quantum computing and offer testbeds for various quantum communication protocols.

CHAPTER 1

BUILDING BLOCKS OF SUPERCONDUCTING QUANTUM NETWORKS

1.1 Introduction

Quantum technologies, e.g. quantum key distribution [1], quantum computing [2, 3, 4, 5], quantum simulation [6] and quantum sensing [7], make use of quantum mechanics to achieve advantages in solving certain problems.

Quantum mechanics explains the behavior of nature at atomic and subatomic scales. The state of a quantum system $|\psi\rangle$ is represented as a vector in a complex Hilbert space, with its time evolution governed by the Schrödinger equation. This evolution can be described using a unitary operator applied to the quantum state, which is determined by the system's Hamiltonian. When the system is measured, the measured results will be an eigenstate of the measurement basis.

The simplest quantum system is a two-level system, which has two eigenstates, denoted as $|0\rangle$ and $|1\rangle$. The state of a two-level system can be written as a superposition of $|0\rangle$ and $|1\rangle$: $|\psi\rangle = \alpha|0\rangle + \beta|1\rangle$, where α and β are complex numbers that satisfy the normalization condition $|\alpha|^2 + |\beta|^2 = 1$. The two-level system serves as the basic unit of information in quantum computing, analogous to the binary bit in classical computing, and is known as a qubit (quantum bit). By engineering the system's Hamiltonian, various operations can be implemented, which are treated as quantum gates. When multiple qubits are combined, the Hilbert space of the entire system expands exponentially. By designing specific sequences of gates, we can develop algorithms that provide significant speedup for certain computational tasks [2, 3, 4, 5].

In practice, the system inevitably interacts with the environment, introducing noise and causing errors in quantum gates. To protect qubits from noise, quantum error correction is

employed, which encodes a logical qubit using multiple physical qubits [8]. To successfully run the quantum algorithms and achieve speedup in solving practical problems (practical quantum advantage), quantum error correction is essential.

Superconducting qubits made by Josephson-based superconducting circuits provide a promising platform for quantum computing. These circuits have been successfully scaled to hundreds of qubits [9, 10, 11, 12]. However, to realize a practical quantum advantage, millions of physical qubits are needed [13, 14]. To further scale up superconducting quantum processors, we arrive at challenges like fabrication yield, frequency collisions [15], chip-scale correlated errors induced by cosmic rays [16, 17, 18, 19]. One potential solution is to connect small superconducting quantum processors [20, 21, 22] to realize distributed quantum computing [23, 24, 25, 26, 27]. This forms a quantum network [28], which can also be used for multi-node quantum communication [29, 30], distributed quantum sensing [31], etc.

Since 2018, there have been many efforts to build superconducting quantum networks, including connecting transmon qubits [32, 33, 34, 35] or microwave cavities [36] with superconducting cables, mounting superconducting quantum processors together using the flip-chip technique [37, 38], and converting the microwave photons to optical photons [39]. Spatially separated cryogenic systems have been built for superconducting quantum networks [40, 41, 42]. In this thesis, we first introduce the foundational components of superconducting quantum networks and present various network topologies based on these components. These results pave the way for distributed quantum computing and provide testbeds for various quantum communication protocols.

In this chapter, we start with the quantization of a linear LC circuit and introduce the building blocks of superconducting quantum networks, i.e. quantum processing units – transmon qubits and quantum communication channels – transmission lines.

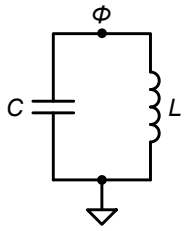

Figure 1.1: Circuit for an LC resonator.

1.2 LC circuit

1.2.1 Hamiltonian

Here we begin with the quantization of an LC resonator [43]. The circuit is shown in Fig. 1.1. Suppose the capacitor has charge Q, the total Lagrangian $\mathcal{L}$ is

$$\mathcal{L} = T - U = \frac{L\dot{Q}^2}{2} - \frac{Q^2}{2C}, \tag{1.1}$$

where $\dot{Q} = \mathrm{d}Q/\mathrm{d}t$. The conjugate coordinate to Q is

$$\Phi = \frac{\partial \mathcal{L}}{\partial \dot{Q}} = L\dot{Q}. \tag{1.2}$$

Using the canonical quantization, we have[1]

$$[Q, \Phi] = i\hbar. \tag{1.3}$$

By defining the creation and annihilation operators,

$$a = \frac{1}{\sqrt{2\hbar}}\left(\left(\frac{L}{C}\right)^{\frac{1}{4}} Q + i\left(\frac{C}{L}\right)^{\frac{1}{4}} \Phi\right), \tag{1.4}$$

$$a^\dagger = \frac{1}{\sqrt{2\hbar}}\left(\left(\frac{L}{C}\right)^{\frac{1}{4}} Q - i\left(\frac{C}{L}\right)^{\frac{1}{4}} \Phi\right). \tag{1.5}$$

1. We will omit all the hats ˆ on the quantum operators.

The operators a and $a^\dagger$ satisfy the commutation relation:

$$[a, a^\dagger] = 1. \tag{1.6}$$

The Hamiltonian can be written as

$$H = \Phi\dot{Q} - \mathcal{L} = \frac{\Phi^2}{2L} + \frac{Q^2}{2C} = \hbar\omega_0(a^\dagger a + \frac{1}{2}), \tag{1.7}$$

where $\omega_0 = 1/\sqrt{LC}$, which is the same as the Hamiltonian of a harmonic oscillator.

Alternatively, we can choose the integral of the voltage at node Φ in the circuit to be the free parameter, defined as

$$\Phi(t) = \int_{-\infty}^{t} \mathrm{d}\tau\ V(\tau), \tag{1.8}$$

which is also known as the node flux. The total Lagrangian $\mathcal{L}$ becomes

$$\mathcal{L} = T - U = \frac{C\dot{\Phi}^2}{2} - \frac{\Phi^2}{2L}. \tag{1.9}$$

The conjugate coordinate to Φ is

$$Q = \frac{\partial\mathcal{L}}{\partial\dot{\Phi}} = C\dot{\Phi}. \tag{1.10}$$

Following the same process of canonical quantization, we have

$$[\Phi, Q] = i\hbar, \tag{1.11}$$

$$a = \frac{1}{\sqrt{2\hbar}}\left(\left(\frac{C}{L}\right)^{\frac{1}{4}}\Phi + i\left(\frac{L}{C}\right)^{\frac{1}{4}}Q\right), \tag{1.12}$$

$$a^\dagger = \frac{1}{\sqrt{2\hbar}}\left(\left(\frac{C}{L}\right)^{\frac{1}{4}}\Phi - i\left(\frac{L}{C}\right)^{\frac{1}{4}}Q\right), \tag{1.13}$$

$$[a, a^\dagger] = 1, \tag{1.14}$$

$$H = Q\dot{\Phi} - \mathcal{L} = \frac{\Phi^2}{2L} + \frac{Q^2}{2C} = \hbar\omega_0(a^\dagger a + \frac{1}{2}). \tag{1.15}$$

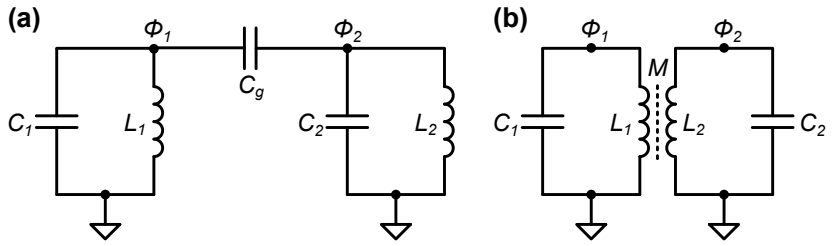

Figure 1.2: Circuits for coupled LC resonators: (a) capacitive and (b) inductive coupling.

From the above quantization process, we can see that the results of the quantization don't depend on the choice of the free parameter. For the following discussion, we will always choose the node flux Φ to be the free parameter to do the quantization, which is more convenient for Josephson junctions.

1.2.2 Coupling

Next, we consider two coupled LC resonators (see Fig. 1.2). We first consider capacitive coupling where two LC resonators are coupled with a capacitor C_g (see Fig. 1.2(a)). The total Lagrangian $\mathcal{L}$ is

$$\mathcal{L} = \frac{C_1\dot{\Phi}_1^2}{2} + \frac{C_2\dot{\Phi}_2^2}{2} + \frac{C_g}{2}(\dot{\Phi}_1 - \dot{\Phi}_2)^2 - \frac{\Phi_1^2}{2L_1} - \frac{\Phi_2^2}{2L_2}. \tag{1.16}$$

The conjugate coordinates to Φ_1 and Φ_2 are

$$\begin{bmatrix} Q_1 \\ Q_2 \end{bmatrix} = \begin{bmatrix} \frac{\partial\mathcal{L}}{\partial\dot{\Phi}_1} \\ \frac{\partial\mathcal{L}}{\partial\dot{\Phi}_2} \end{bmatrix} = \begin{bmatrix} C_1 + C_g & -C_g \\ -C_g & C_2 + C_g \end{bmatrix} \begin{bmatrix} \dot{\Phi}_1 \\ \dot{\Phi}_2 \end{bmatrix}. \tag{1.17}$$

The total Hamiltonian is

$$
\begin{aligned}
H = Q_1\dot{\Phi}_1 + Q_2\dot{\Phi}_2 - \mathcal{L} &= \frac{1}{2}(C_1 + C_g)\dot{\Phi}_1^2 + \frac{1}{2}(C_2 + C_g)\dot{\Phi}_2^2 - C_g\dot{\Phi}_1\dot{\Phi}_2 + \frac{\Phi_1^2}{2L_1} + \frac{\Phi_2^2}{2L_2} \\
&= \frac{1}{2}\begin{bmatrix} Q_1 & Q_2 \end{bmatrix}\begin{bmatrix} \dot{\Phi}_1 \\ \dot{\Phi}_2 \end{bmatrix} + \frac{\Phi_1^2}{2L_1} + \frac{\Phi_2^2}{2L_2} \\
&= \frac{1}{2}\begin{bmatrix} Q_1 & Q_2 \end{bmatrix}\begin{bmatrix} C_1 + C_g & -C_g \\ -C_g & C_2 + C_g \end{bmatrix}^{-1}\begin{bmatrix} Q_1 \\ Q_2 \end{bmatrix} + \frac{\Phi_1^2}{2L_1} + \frac{\Phi_2^2}{2L_2}. \qquad (1.18)
\end{aligned}
$$

After doing the math, we have the Hamiltonian,

$$
\begin{aligned}
H &= \frac{1}{2}\frac{Q_1^2}{C_1 + \frac{C_2C_g}{C_2+C_g}} + \frac{1}{2}\frac{Q_2^2}{C_2 + \frac{C_1C_g}{C_1+C_g}} + \frac{C_g}{C_1C_2 + C_1C_g + C_2C_g}Q_1Q_2 + \frac{\Phi_1^2}{2L_1} + \frac{\Phi_2^2}{2L_2} \\
&= \hbar\omega_1(a_1^\dagger a_1 + \frac{1}{2}) + \hbar\omega_2(a_2^\dagger a_2 + \frac{1}{2}) - \frac{\hbar}{2}\frac{C_g\sqrt{\omega_1\omega_2}}{\sqrt{(C_1 + C_g)(C_2 + C_g)}}(a_1 - a_1^\dagger)(a_2 - a_2^\dagger) \\
&= \hbar\omega_1(a_1^\dagger a_1 + \frac{1}{2}) + \hbar\omega_2(a_2^\dagger a_2 + \frac{1}{2}) - \hbar g(a_1 - a_1^\dagger)(a_2 - a_2^\dagger), \qquad (1.19)
\end{aligned}
$$

where the coupling strength g is

$$
g = \frac{1}{2}\frac{C_g\sqrt{\omega_1\omega_2}}{\sqrt{(C_1 + C_g)(C_2 + C_g)}}. \qquad (1.20)
$$

Next, we consider inductive coupling where two LC resonators are coupled with mutual inductance M (see Fig. 1.2(b)). The total Lagrangian $\mathcal{L}$ is

$$
\mathcal{L} = \frac{C_1\dot{\Phi}_1^2}{2} + \frac{C_2\dot{\Phi}_2^2}{2} - \frac{\Phi_1^2}{2L_1} - \frac{\Phi_2^2}{2L_2} - \frac{M}{L_1L_2}\Phi_1\Phi_2. \qquad (1.21)
$$

The conjugate coordinates to Φ_1 and Φ_2 are

$$\begin{bmatrix} Q_1 \\ Q_2 \end{bmatrix} = \begin{bmatrix} \frac{\partial \mathcal{L}}{\partial \dot{\Phi}_1} \\ \frac{\partial \mathcal{L}}{\partial \dot{\Phi}_2} \end{bmatrix} = \begin{bmatrix} C_1 \dot{\Phi}_1 \\ C_2 \dot{\Phi}_2 \end{bmatrix}. \tag{1.22}$$

The total Hamiltonian is

$$\begin{aligned} H &= Q_1\dot{\Phi}_1 + Q_2\dot{\Phi}_2 - \mathcal{L} = \frac{Q_1^2}{2C_1} + \frac{Q_2^2}{2C_2} + \frac{\Phi_1^2}{2L_1} + \frac{\Phi_2^2}{2L_2} + \frac{M}{L_1L_2}\Phi_1\Phi_2 \\ &= \hbar\omega_1(a_1^\dagger a_1 + \frac{1}{2}) + \hbar\omega_2(a_2^\dagger a_2 + \frac{1}{2}) + \frac{\hbar}{2}\frac{M\sqrt{\omega_1\omega_2}}{\sqrt{L_1L_2}}(a_1 + a_1^\dagger)(a_2 + a_2^\dagger) \\ &= \hbar\omega_1(a_1^\dagger a_1 + \frac{1}{2}) + \hbar\omega_2(a_2^\dagger a_2 + \frac{1}{2}) + \hbar g(a_1 + a_1^\dagger)(a_2 + a_2^\dagger), \end{aligned} \tag{1.23}$$

where the coupling strength g is

$$g = \frac{1}{2}\frac{M\sqrt{\omega_1\omega_2}}{\sqrt{L_1L_2}}. \tag{1.24}$$

The mutual inductive coupling will not shift the resonator frequencies like the capacitive coupling. If the two resonators are coupled by a shared inductor (see Figs. 1.27 and E.3), the frequency shift will be similar to the capacitive coupling.

The capacitive coupling $-g(a_1 - a_1^\dagger)(a_2 - a_2^\dagger)$ has a different form from the inductive coupling $g(a_1 + a_1^\dagger)(a_2 + a_2^\dagger)$. They will become the same under the rotation wave approximation (RWA), $g(a_1 a_2^\dagger + a_1^\dagger a_2)$, which assumes the resonator detuning $|\omega_1 - \omega_2|$ is much smaller than the resonator frequencies ω_1 and ω_2. Their non-RWA terms have different signs, i.e. $g(a_1 a_2 + a_1^\dagger a_2^\dagger)$ for the inductive coupling and $-g(a_1 a_2 + a_1^\dagger a_2^\dagger)$ for the capacitive coupling. When there are both types of couplings, we can engineer the non-RWA term to zero [44].

When there is only inductive coupling, by redefining the creation and annihilation operators as $b = ia$, $b^\dagger = -ia^\dagger$, the inductive coupling term comes back to the form of capacitive coupling, $-g(b_1 - b_1^\dagger)(b_2 - b_2^\dagger)$.

The coupling strengths g derived above are both positive because of the way we define

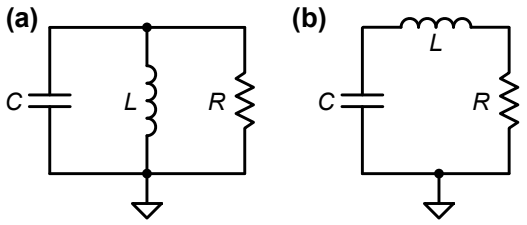

Figure 1.3: Circuits for lossy resonators: (a) parallel and (b) series RLC resonators.

the modes. When there are only two modes, the sign of g doesn't matter since we can always flip the sign of g by redefining the creation and annihilation operators of one mode as $b_1 = -a_1$, $b_1^\dagger = -a_1^\dagger$. When there are multiple modes or different types of couplings, we need to be careful with the signs of the couplings.

1.2.3 Lossy resonator

In reality, there are always different mechanisms causing the energy stored in the resonator to dissipate. Two major mechanisms are dielectric loss and conductive loss, among others. We can use the dissipation rate κ and the quality factor Q to quantify this effect. The phenomenological dissipation rate κ describes the rate of energy loss in the resonator and the quality factor Q is defined as

$$Q = \frac{\omega_0}{\kappa}, \tag{1.25}$$

where $\omega_0 = 1/\sqrt{LC}$ is the resonant frequency of the resonator. To model the lossy element in a classical resonant circuit, we can add a phenomenological resistor R in the circuit (see Fig. 1.3). Depending on how the resistor is connected, the quality factor Q and dissipation rate κ have different forms [45]. For a parallel resonator where the resistor is connected in parallel (see Fig. 1.3(a)), its quality factor Q and dissipation rate κ can be written as

$$Q = R\sqrt{\frac{C}{L}}, \tag{1.26}$$

$$\kappa = \frac{1}{RC}. \tag{1.27}$$

For a series resonator where the resistor is connected in series (see Fig. 1.3(b)), its quality factor Q and dissipation rate κ can be written as

$$Q = \frac{1}{R}\sqrt{\frac{L}{C}}, \tag{1.28}$$

$$\kappa = \frac{R}{L}. \tag{1.29}$$

In quantum mechanics, the existence of energy loss means that the system evolution is no longer unitary and the system is coupled to the environment. The Lindblad master equation can be used to model such processes when the noise is Markovian [46]. The time evolution of the system density matrix ρ is given by

$$\dot{\rho} = -\frac{i}{\hbar}[H, \rho] + \sum_i \gamma_i \Big(L_i \rho L_i^\dagger - \frac{1}{2}\big\{ L_i^\dagger L_i, \rho \big\} \Big), \tag{1.30}$$

where $\{A, B\} = AB + BA$ is the anticommutator, $\{L_i\}$ are a set of jump operators and $\{\gamma_i\}$ are their corresponding damping rates. If a lossy resonator is coupled to a zero-temperature bath, we have one jump operator $L_1 = a$ and its damping rate $\gamma_1 = \kappa$. We can write down the Heisenberg equation of motion for the annihilation operator a,

$$\dot{a} = -(i\omega_0 + \frac{\kappa}{2})a, \tag{1.31}$$

from which we can verify that the total energy $\langle H(t) \rangle \propto \langle a^\dagger(t) a(t) \rangle$ in the system decays exponentially, $e^{-\kappa t}$.

1.2.4 Linear network

The circuits in actual experiments are not as simple as LC resonators. However, for any resonance in a linear circuit, we can always model it as either a parallel or a series LC resonator near its resonant frequency. If there is resonance in the circuit, its input impedance

	parallel	series
R_{eff}	$1/\text{Re}[Y_{\text{in}}(\omega_0)]$	$\text{Re}[Z_{\text{in}}(\omega_0)]$
L_{eff}	$1/\omega_0^2 C_{\text{eff}}$	$\frac{1}{2}\frac{\text{d}}{\text{d}\omega}\text{Im}[Z_{\text{in}}(\omega)]\|_{\omega=\omega_0}$
C_{eff}	$\frac{1}{2}\frac{\text{d}}{\text{d}\omega}\text{Im}[Y_{\text{in}}(\omega)]\|_{\omega=\omega_0}$	$1/\omega_0^2 L_{\text{eff}}$
κ	$1/R_{\text{eff}}C_{\text{eff}}$	$R_{\text{eff}}/L_{\text{eff}}$

Table 1.1: Effective RLC for a linear circuit near its resonant frequency ω_0.

Z_{in} near that resonance can be written as

$$Z_{\text{in}}(\omega) = k_1 + jk_2\frac{\omega - \omega_0}{\omega_0}, \tag{1.32}$$

where j is the complex operator in AC circuits, k_1 and k_2 are all real numbers with units of resistance and ω_0 is the resonant frequency. Note that we assume there is always loss in the system, so the resonant frequency ω_0 is the zero in $\text{Im}[Z_{\text{in}}]$. Otherwise, there are also resonant modes at the poles in $\text{Im}[Z_{\text{in}}]$ (zeros in $\text{Im}[Y_{\text{in}}]$) if the system is lossless. For a parallel LC resonator, we can write down its input impedance Z_{in} near its resonant frequency ω_0,

$$Z_{\text{in}}(\omega) = \frac{1}{1/R + j\omega C + 1/j\omega L} = R - 2jR^2C(\omega - \omega_0). \tag{1.33}$$

For a series LC resonator, we can write down its input impedance Z_{in} near its resonant frequency ω_0,

$$Z_{\text{in}}(\omega) = R + j\omega L + \frac{1}{j\omega C} = R + 2jL(\omega - \omega_0). \tag{1.34}$$

Comparing Eq. 1.32 with the impedances for parallel and series resonators, we can find that when $k_2 < 0$, the resonant mode acts like a parallel resonator, and when $k_2 > 0$, the resonant mode acts like a series resonator. Furthermore, we can write down the effective capacitance C_{eff}, inductance L_{eff}, and resistance R_{eff} of the resonant mode. Note that for a parallel resonance, analyzing its input admittance Y_{in} is more convenient and we have $\text{Re}[Z_{\text{in}}(\omega_0)] = 1/\text{Re}[Y_{\text{in}}(\omega_0)]$. The results are summarized in Table 1.1. Note that for a lossless circuit, the imaginary part of its impedance always strictly monotonically increases

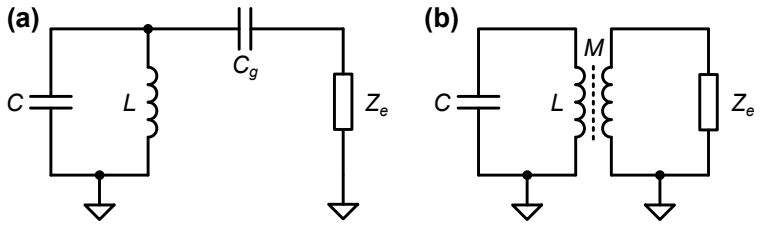

Figure 1.4: Circuits for (a) parallel and (b) series resonators coupled to external circuits.

(Foster's reactance theorem), which means there is always a parallel (series) resonance between two series (parallel) resonances. Depending on the boundary condition at the probe point, we can only see certain types of resonances.

We can use the above results to analyze the circuits where a lossless LC resonator is weakly coupled to an external lossy circuit (see Fig. 1.4). We assume there are no resonances in the external circuit or the resonances are far away from the bare resonant frequency of the LC resonator $\omega_0 = 1/\sqrt{LC}$, which is different from the discussion in Section 1.2.2.

For a parallel LC resonator coupled to an external circuit Z_e through some small capacitance $C_g \ll C$ (see Fig. 1.4(a)), we can find its effective resistance R_{eff} at the resonant frequency ω_0,

$$R_{\text{eff}} = 1/\text{Re}[Y_{\text{in}}(\omega_0)] = 1/\text{Re}\Big[\frac{j\omega_0 C_g/Z_e(\omega_0)}{j\omega_0 C_g + 1/Z_e(\omega_0)}\Big] = \frac{1}{\omega_0^2 C_g^2 \text{Re}[Z_e(\omega_0)]}, \tag{1.35}$$

with which we can get the dissipation rate κ for the damped parallel LC resonator,

$$\kappa = \frac{1}{R_{\text{eff}} C_{\text{eff}}} = \frac{\omega_0^2 C_g^2}{C} \text{Re}[Z_e(\omega_0)]. \tag{1.36}$$

Note that the bare resonant frequency of the full circuit will shift a little bit from ω_0 because of the capacitor C_g.

A similar analysis can be done for a series LC resonator coupled to an external circuit Z_e through some small mutual inductance $M \ll L$ (see Fig. 1.4). To calculate the effective resistance R_{eff} caused by the loading of the external circuit Z_e, we need to transform the

external impedance Z_e to an impedance Z_e' in series with the LC circuit. This can be calculated from Kirchhoff's circuit laws. Assume the current in the LC circuit is i_1, the current in the external circuit is i_2 and the voltage generated by the mutual inductance in the LC circuit is v, we have

$$-j\omega M i_2 = v, \tag{1.37}$$

$$Z_e i_2 - j\omega M i_1 = 0, \tag{1.38}$$

from which we can get the effective in-series impedance Z_e',

$$Z_e' = \frac{v}{i_1} = \frac{\omega^2 M^2}{Z_e}. \tag{1.39}$$

The effective resistance R_{eff} for this damped LC resonator is

$$R_{\text{eff}} = \text{Re}[Z_e'] = \text{Re}\Big[\frac{\omega_0^2 M^2}{Z_e}\Big] = \omega_0^2 M^2 \text{Re}[Y_e], \tag{1.40}$$

where $Y_e = 1/Z_e$ is the admittance of the external circuit. The dissipation rate κ of the damped resonator is

$$\kappa = \frac{R_{\text{eff}}}{L_{\text{eff}}} = \frac{\omega_0^2 M^2}{L} \text{Re}[Y_e]. \tag{1.41}$$

One example of the above circuits is two coupled resonators with large detuning (see Fig. 1.5). We can calculate how a lossy resonator damps another lossless resonator when their detuning is large. Assume the lossy resonator in the external circuit has resistance R_e, inductance L_e, capacitance C_e, resonant frequency $\omega_e = 1/\sqrt{L_e C_e}$, and dissipation rate κ_e.

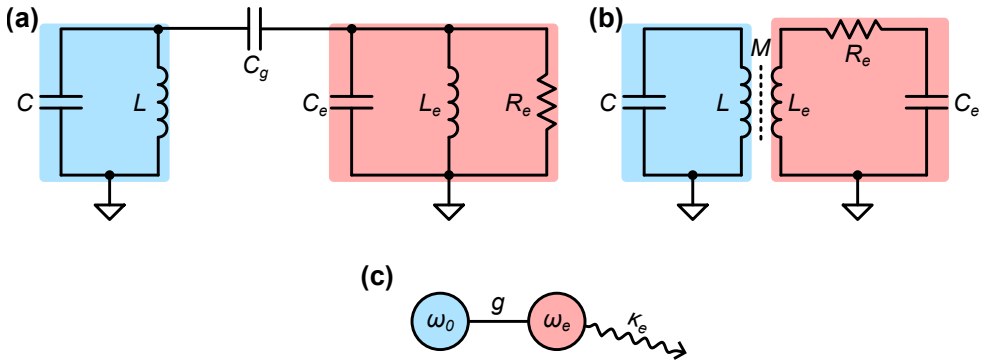

Figure 1.5: Circuits for a lossless resonator coupled to a lossy resonator with (a) capacitive coupling, (b) inductive coupling, and (c) their coupled-mode representation.

In the case of capacitively coupled parallel resonators (see Fig. 1.5(a)), we have

$$\begin{aligned}\kappa &= \frac{\omega_0^2 C_g^2}{C}\mathrm{Re}[Z_e(\omega_0)] = \frac{\omega_0^2 C_g^2}{C}\mathrm{Re}\Big[\frac{1}{j\omega_0 C_e + 1/j\omega_0 L_e + 1/R_e}\Big] \\ &= \frac{\omega_0^4}{(\omega_e^2-\omega_0^2)^2}\frac{C_g^2}{CC_e}\frac{1}{R_e C_e} = \frac{g^2}{\Delta^2}\kappa_e,\end{aligned} \tag{1.42}$$

where $\Delta = \omega_e - \omega_0$ is the detuning between two resonators and g is the coupling strength derived in Eq. 1.20 for capacitively coupled resonators. In the case of inductively coupled series resonators (see Fig. 1.5(b)), we have

$$\begin{aligned}\kappa &= \frac{\omega_0^2 M^2}{L}\mathrm{Re}[Y_e] = \frac{\omega_0^2 M^2}{L}\mathrm{Re}\Big[\frac{1}{1/j\omega C_e + j\omega L_e + R_e}\Big] \\ &= \frac{\omega_0^4}{(\omega_e^2-\omega_0^2)^2}\frac{M^2}{LL_e}\frac{R_e}{L_e} = \frac{g^2}{\Delta^2}\kappa_e,\end{aligned} \tag{1.43}$$

where g is the coupling strength derived in Eq. 1.24 for inductively coupled resonators. The dissipation rates in the two cases have the same form,

$$\kappa = \frac{g^2}{\Delta^2}\kappa_e, \tag{1.44}$$

which is called Purcell effect [47].

The above impedance analysis can solve most problems in linear circuit analysis. In experiments, we only drive and probe certain resonant modes in the circuit. The resonant modes found by the impedance are the eigenmodes of the system and might be the hybridization of the modes we care about. In a more general scheme, the system Hamiltonian H can be written as

$$H/\hbar = \sum_{j=1}^{N} \omega_j (a_j^\dagger a_j + \frac{1}{2}) + \sum_{\{j,k\}} c_{j,k}(a_j a_k^\dagger + a_j^\dagger a_k), \tag{1.45}$$

where $c_{j,k}$ is the coupling strength between the jth and kth modes, and the rotating wave approximation (RWA) has been applied. From the Lindblad master equation (Eq. 1.30), the equation of motion (EOM) for $\{a_j\}$ can be written as

$$\frac{\mathrm{d}}{\mathrm{d}t}\vec{A}(t) = \mathbf{M}\vec{A}(t), \tag{1.46}$$

$$\mathbf{M}_{jk} = -(i\omega_j + \frac{\kappa_j}{2})\delta_{jk} - ic_{j,k}, \tag{1.47}$$

where $\vec{A}(t) = [a_1(t), a_2(t), \cdots, a_N(t)]^T$, κ_j is the dissipation rate of the jth mode. To solve Eq. 1.46 is basically to diagonalize the $N \times N$ matrix $\mathbf{M}$. The real part of the jth eigenvalue of $\mathbf{M}$ gives the dissipation rate of the jth eigenmode in the system and the imaginary part gives its resonant frequency. Using this formalism, we can also analyze how a detuned lossy resonator damps a coupled lossless resonator (see Fig. 1.5(c)). In this case, the matrix $\mathbf{M}$ can be written as

$$\mathbf{M} = \begin{bmatrix} -i\omega_0 & -ig \\ -ig & -i\omega_e - \kappa_e/2 \end{bmatrix}, \tag{1.48}$$

from which we can find the dissipation rate for the first mode,

$$\kappa = \frac{\kappa_e}{2} - \mathrm{Re}\left[\sqrt{(\frac{\kappa_e}{2} + i\Delta)^2 - 4g^2}\right] = \frac{g^2}{\kappa_e^2/4 + \Delta^2}\kappa_e, \tag{1.49}$$

where $\Delta = \omega_e - \omega_0$ is the detuning between two resonators and we assume $\sqrt{\kappa_e^2 + \Delta^2} \gg g$.

When $|\Delta| \gg \kappa_e$, we have

$$\kappa = \frac{g^2}{\Delta^2}\kappa_e, \tag{1.50}$$

which is exactly the same as Eq. 1.44. When $\Delta = 0$, we have

$$\kappa = \frac{4g^2}{\kappa_e}, \tag{1.51}$$

which is the decay rate of the resonator when weakly coupled to a resonant lossy resonator (e.g. a bandpass filter [48]).

When a lossless resonator is coupled to a Markovian bath, we can also use the quantum linear response theory [46] (see Appendix A) to calculate its dissipation rate κ. Fermi's golden rule determines its dissipation rate κ:

$$\kappa = 2\pi g^2 \rho_b(\omega_0), \tag{1.52}$$

where $\rho_b(\omega_0)$ is the density of states seen by the lossless resonator at its frequency ω_0, and we assume the resonator is coupled to the operator b of the environment in the form of $g(a_0 b^\dagger + a_0^\dagger b)$. When coupled to a lossy resonator as we discussed above (see Fig. 1.5(c)), the operator b becomes the annihilation operator a_e of the lossy resonator and we can treat the lossy resonator as a Markovian bath when there is no coherent swapping between two resonators (i.e. $|\Delta| \gg g$ or $\kappa_e \gg g$). The density of states $\rho_{a_e}(\omega)$ can be calculated from the quantum linear response theory (see Appendix A),

$$\begin{aligned}\rho_{a_e}(\omega) &= \frac{1}{\pi}\mathrm{Re}\Big[\int_0^\infty \mathrm{d}t\, e^{i\omega t}\langle[a_e(t), a_e^\dagger(0)]\rangle\Big] = \frac{1}{\pi}\mathrm{Re}\Big[\int_0^\infty \mathrm{d}t\, e^{i\omega t} e^{-i\omega_e t - \frac{\kappa_e}{2}t}\Big] \\ &= \frac{1}{\pi}\mathrm{Re}\Big[\frac{1}{\kappa_e/2 - i(\omega - \omega_e)}\Big] = \frac{1}{\pi}\frac{\kappa_e/2}{\kappa_e^2/4 + (\omega - \omega_e)^2}.\end{aligned} \tag{1.53}$$

Inserting this into the expression for κ, we have

$$\kappa = \frac{g^2}{\kappa_e^2/4 + \Delta^2}\kappa_e, \tag{1.54}$$

which is same as Eq. 1.49. There is no surprise that the results are the same with the two methods as the Lindblad master equation can be derived from the quantum linear response theory combined with the Markov assumption. The density of states can be used to characterize the properties of a bath.

1.2.5 Scattering

To experimentally study a linear network, the most common way is to measure its scattering parameters. For a classical linear circuit, its scattering parameters can be directly calculated from its impedance [45]. Especially for a two-port network, its transmission coefficients S_{21}, S_{12} and its reflection coefficients S_{11}, S_{22} can be efficiently calculated from the $ABCD$ matrices [45].

When we are talking about scattering in a quantum system, it means that we are driving the system and we need to introduce the quantum input-output theory to solve the dynamics [49, 50] (see Appendix B). Suppose each mode in the system is only coupled to one external port, the Heisenberg equations of motion (Eq. 1.46) will become quantum Langevin equations,

$$\frac{\mathrm{d}}{\mathrm{d}t}\vec{A}(t) = \mathbf{M}\vec{A}(t) - \mathbf{K}\vec{A}_{\mathrm{in}}(t), \tag{1.55}$$

$$\mathbf{M}_{jk} = -(i\omega_j + \frac{\kappa_j}{2})\delta_{jk} - ic_{j,k}, \tag{1.56}$$

$$\mathbf{K}_{jk} = \delta_{jk}\sqrt{\kappa_j^{\mathrm{ext}}}, \tag{1.57}$$

where $\kappa_j = \kappa_j^{\mathrm{int}} + \kappa_j^{\mathrm{ext}}$ is the total dissipation rate for the jth mode, κ_j^{int} and κ_j^{ext} are the

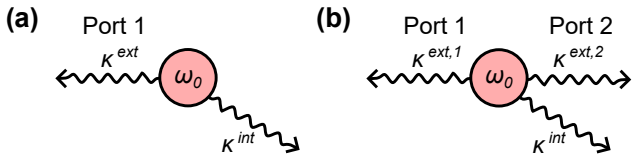

Figure 1.6: Scattering of a resonator with (a) one external port and (b) two external ports.

internal and external dissipation rates respectively, and $\vec{A}_{\rm in}(t) = [a_1^{\rm in}(t), a_2^{\rm in}(t), \cdots, a_N^{\rm in}(t)]^T$ is the vector of input fields. We have the input-output relation (see Appendix B),

$$\vec{A}_{\rm out}(t) = \mathbf{K}\vec{A}(t) + \vec{A}_{\rm in}(t), \tag{1.58}$$

where $\vec{A}_{\rm out}(t) = [a_1^{\rm out}(t), a_2^{\rm out}(t), \cdots, a_N^{\rm out}(t)]^T$ is the vector of output fields. Assume we drive the system with a signal of frequency ω, we can Fourier transform the above equations and get

$$-i\omega\vec{A}(\omega) = \mathbf{M}\vec{A}(\omega) - \mathbf{K}\vec{A}_{\rm in}(\omega), \tag{1.59}$$

$$\vec{A}_{\rm out}(\omega) = \mathbf{K}\vec{A}(\omega) + \vec{A}_{\rm in}(\omega). \tag{1.60}$$

The S-parameters S_{jk} can be calculated as

$$S_{jk}(\omega) = \frac{a_j^{\rm out}(\omega)}{a_k^{\rm in}(\omega)} = \sqrt{\kappa_j^{\rm ext}\kappa_k^{\rm ext}}[(i\omega\mathbf{I} + \mathbf{M})^{-1}]_{jk} + \delta_{jk}. \tag{1.61}$$

A simple example is the reflection of a resonator (see Fig. 1.6(a)). The reflection coefficient S_{11} is

$$S_{11}(\omega) = \frac{a^{\rm out}(\omega)}{a^{\rm in}(\omega)} = 1 + \frac{\kappa^{\rm ext}}{i(\omega - \omega_0) - \kappa/2}, \tag{1.62}$$

where ω_0 is the resonant frequency and the total dissipation rate $\kappa = \kappa^{\rm int} + \kappa^{\rm ext}$. Note that the S-parameters derived from $ABCD$ matrices have a different sign before i, which comes from the different definition of the complex operator j in AC circuits, $j = -i$. We can find

that when $\kappa^{\text{int}} = 0$, $|S_{11}(\omega)| = 1$, and when $\kappa^{\text{int}} = \kappa^{\text{ext}}$, $|S_{11}(\omega_0)| = 0$. If we define the loaded quality factor Q_l as $Q_l = \omega_0/\kappa$ and the coupling quality factor Q_c as $Q_c = \omega_0/\kappa^{\text{ext}}$, S_{11} can be rewritten as

$$S_{11}(\omega) = 1 - \frac{Q_l}{Q_c} \frac{2}{1 - 2iQ_l \frac{\omega - \omega_0}{\omega_0}}. \tag{1.63}$$

The above analysis can also be extended to one resonator with multiple ports. Here we give an example of a resonator coupled to two ports (see Fig. 1.6(b)). The quantum Langevin equation and input-output relations are

$$\dot{a}(t) = -(i\omega_0 + \frac{\kappa}{2})a(t) - \sqrt{\kappa^{\text{ext},1}}a^{\text{in},1}(t) - \sqrt{\kappa^{\text{ext},2}}a^{\text{in},2}(t), \tag{1.64}$$

$$a^{\text{out},1}(t) = \sqrt{\kappa^{\text{ext},1}}a(t) + a^{\text{in},1}(t), \tag{1.65}$$

$$a^{\text{out},2}(t) = \sqrt{\kappa^{\text{ext},2}}a(t) + a^{\text{in},2}(t). \tag{1.66}$$

The reflection coefficients S_{11} and S_{22} have the same form of Eq. 1.62 and the transmission coefficient can be calculated as

$$S_{21}(\omega) = \frac{a^{\text{out},2}(\omega)}{a^{\text{in},1}(\omega)} = \frac{\sqrt{\kappa^{\text{ext},1}\kappa^{\text{ext},2}}}{i(\omega - \omega_0) - \kappa/2}. \tag{1.67}$$

We can see that $|S_{21}(\omega)|$ reaches the maximum value at ω_0, which performs like a bandpass filter with a bandwidth of κ. When the two ports are equally coupled, $\kappa^{\text{ext},1} = \kappa^{\text{ext},2} = \kappa/2$, it acts like a bandpass filter with no insertion loss ($|S_{21}(\omega_0)| = 1$).

1.3 Transmission line

In this section, we discuss transmission lines, which are commonly used as quantum communication channels in superconducting quantum networks.

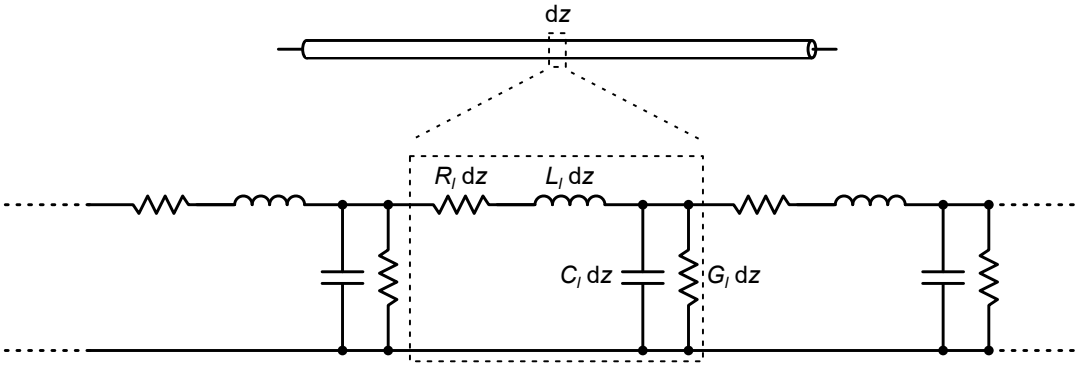

Figure 1.7: Lumped-element equivalent circuit for a transmission line.

1.3.1 Hamiltonian

The effective circuit for a transmission line is shown in Fig. 1.7, from which we can see that it cannot be modeled as some lumped-element circuits and contains infinite degrees of freedom. To quantize it, we start with its classical dynamics. For a transmission line, we have the telegrapher equations to describe its dynamics [45],

$$\frac{\partial v(z,t)}{\partial z} = -R_l i(z,t) - L_l \frac{\partial i(z,t)}{\partial t}, \tag{1.68}$$

$$\frac{\partial i(z,t)}{\partial z} = -G_l v(z,t) - C_l \frac{\partial v(z,t)}{\partial t}, \tag{1.69}$$

where $v(z,t)$ and $i(z,t)$ are the voltage and current at position z and time t, R_l is the distributed resistance, L_l is the distributed inductance, C_l is the capacitance per length and G_l is the conductance per length. Assuming there is no loss, we have $R_l = G_l = 0$. The telegrapher equations become

$$\frac{\partial v(z,t)}{\partial z} = -L_l \frac{\partial i(z,t)}{\partial t}, \tag{1.70}$$

$$\frac{\partial i(z,t)}{\partial z} = -C_l \frac{\partial v(z,t)}{\partial t}. \tag{1.71}$$

We can define the local node flux $\phi(z,t)$ as

$$\phi(z,t) = \int_{-\infty}^{t} \mathrm{d}\tau \; v(z,\tau), \tag{1.72}$$

which has the dynamical equation,

$$\frac{\partial^2 \phi}{\partial t^2} - \frac{1}{L_l C_l} \frac{\partial^2 \phi}{\partial z^2} = 0. \tag{1.73}$$

The Lagrangian density $\mathcal{L}_l$ can be written as

$$\mathcal{L}_l = \frac{C_l}{2}(\partial_t \phi)^2 - \frac{1}{2L_l}(\partial_z \phi)^2. \tag{1.74}$$

The conjugate to ϕ is

$$\pi = \frac{\partial \mathcal{L}_l}{\partial \dot{\phi}} = C_l \dot{\phi}. \tag{1.75}$$

With Fourier transformation, we can write ϕ and π in the form,

$$\phi(z,t) = \sqrt{\frac{\hbar}{C_l}} \int \frac{\mathrm{d}k}{\sqrt{2\pi}\sqrt{2\omega_k}} \Big(a_k e^{ikz - i\omega_k t} + a_k^* e^{-ikz + i\omega_k t} \Big), \tag{1.76}$$

$$\pi(z,t) = \sqrt{\hbar C_l} \int \frac{\mathrm{d}k}{\sqrt{2\pi}\sqrt{2\omega_k}} \Big(- i\omega_k a_k e^{ikz - i\omega_k t} + i\omega_k a_k^* e^{-ikz + i\omega_k t} \Big), \tag{1.77}$$

where we set a_k to be dimensionless and we have the dispersion relation,

$$\omega_k = \frac{1}{\sqrt{L_l C_l}} |k| = v_p |k|, \tag{1.78}$$

where $v_p = 1/\sqrt{L_l C_l}$ is the phase velocity in the transmission line. We can write $\phi(z,t)$ and $\pi(z,t)$ as quantum operators,

$$\phi(z,t) = \sqrt{\frac{\hbar}{C_l}} \int \frac{\mathrm{d}k}{\sqrt{2\pi}\sqrt{2\omega_k}} \Big(a_k e^{ikz - i\omega_k t} + a_k^\dagger e^{-ikz + i\omega_k t} \Big), \tag{1.79}$$

$$\pi(z,t) = \sqrt{\hbar C_l} \int \frac{\mathrm{d}k}{\sqrt{2\pi}\sqrt{2\omega_k}} \Big(-i\omega_k a_k e^{ikz - i\omega_k t} + i\omega_k a_k^\dagger e^{-ikz + i\omega_k t} \Big). \tag{1.80}$$

The operators a_k and $a_k^\dagger$ can be written in ϕ and π as

$$a_k = \frac{1}{2}\sqrt{2\omega_k} \int \mathrm{d}z \; e^{ikz} \left(\sqrt{\frac{C_l}{\hbar}} \phi(z,t) + i \sqrt{\frac{1}{\hbar C_l}} \pi(z,t) \right), \tag{1.81}$$

$$a_k^\dagger = \frac{1}{2}\sqrt{2\omega_k} \int \mathrm{d}z \; e^{-ikz} \left(\sqrt{\frac{C_l}{\hbar}} \phi(z,t) - i \sqrt{\frac{1}{\hbar C_l}} \pi(z,t) \right). \tag{1.82}$$

Following the process of canonical quantization, we have the commutation relationship,

$$[\phi(z,t), \pi(z',t)] = i\hbar\delta(z - z'), \tag{1.83}$$

from which we can get the commutation relation for a_k and $a_k^\dagger$,

$$[a_k, a_{k'}^\dagger] = \delta(k - k'). \tag{1.84}$$

We can rewrite the Hamiltonian density $\mathcal{H}_l$ as

$$\mathcal{H}_l = \pi\dot{\phi} - \mathcal{L}_l = \frac{C_l}{2}(\partial_t \phi)^2 + \frac{1}{2L_l}(\partial_z \phi)^2 = \frac{\pi^2}{2C_l} + \frac{(\partial_z \phi)^2}{2L_l}, \tag{1.85}$$

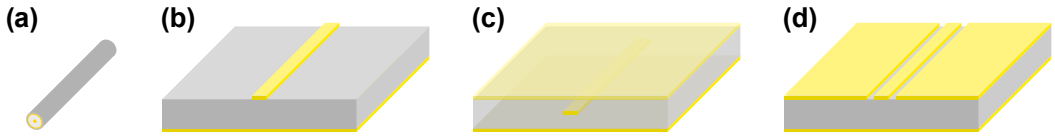

Figure 1.8: Different types of transmission lines: (a) coaxial cable, (b) microstrip, (c) stripline, and (d) coplanar waveguide (CPW).

from which we can get the total Hamiltonian H and write it in a_k and $a_k^\dagger$,

$$\begin{aligned} H &= \int \mathrm{d}z\, \mathcal{H}_l = \int \mathrm{d}z \left(\frac{\pi^2}{2C_l} + \frac{(\partial_z \phi)^2}{2L_l}\right) \\ &= \frac{\hbar}{2} \int \mathrm{d}z \int \frac{\mathrm{d}k_1}{\sqrt{2\pi}} \int \frac{\mathrm{d}k_2}{\sqrt{2\pi}} \Big(\frac{\omega_{k_1}\omega_{k_2}}{\sqrt{2\omega_{k1}}\sqrt{2\omega_{k_2}}} + \frac{k_1 k_2}{\sqrt{2\omega_{k1}}\sqrt{2\omega_{k_2}}} \frac{1}{L_l C_l} \Big) \\ &\quad \times \Big(- a_{k_1} e^{ik_1 z - i\omega_{k_1} t} + a_{k_1}^\dagger e^{-ik_1 z + i\omega_{k_1} t} \Big) \Big(a_{k_2} e^{ik_2 z - i\omega_{k_2} t} - a_{k_2}^\dagger e^{-ik_2 z + i\omega_{k_2} t} \Big) \\ &= \frac{\hbar}{2} \int \mathrm{d}k\ \omega_k (a_k a_k^\dagger + a_k^\dagger a_k) = \int \mathrm{d}k\ \hbar\omega_k (a_k^\dagger a_k + \frac{1}{2}), \end{aligned} \tag{1.86}$$

which is similar to the quantization of the Klein-Gordon field [51].

Common types of transmission lines are coaxial cable, microstrip, stripline, and coplanar waveguide (CPW) (see Fig. 1.8). There are other types of waveguides with different structures [52, 53, 54, 55, 56, 57, 58]. Their quantization results are the same as the transmission lines because of the translational symmetry but with different dispersion relations [59], which will give a different phase velocity v_p and group velocity v_g in the waveguide [45].

1.3.2 Transmission line resonator

From the discussion above, we can see that there are an infinite number of modes in the system. If we consider a transmission line with finite length, then we need to add some boundary conditions to the system. We will see from the following discussion that there are a countably infinite number of resonant modes with equal frequency spacing in the system for certain boundary conditions.

To find the resonances in the system, we can calculate the input impedance Z_{in} for a

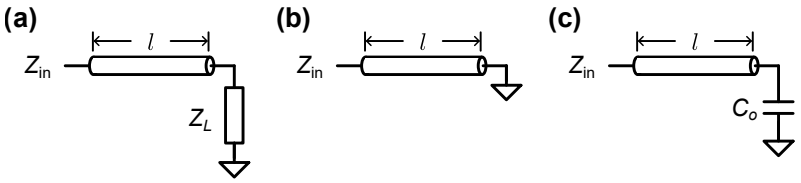

Figure 1.9: Circuits for a transmission line terminated with (a) load impedance Z_L, (b) a short end, and (c) an open end.

transmission line with length l terminated with load impedance Z_L (see Fig. 1.9(a)). The input impedance Z_{in} can be calculated as [45],

$$Z_{\text{in}}(\omega) = Z_0 \frac{Z_L + Z_0 \tanh \gamma l}{Z_0 + Z_L \tanh \gamma l}, \tag{1.87}$$

where $Z_0 = \sqrt{(R_l + j\omega L_l)/(G_l + j\omega C_l)}$ is the characteristic impedance and $\gamma = \alpha + j\beta = \sqrt{(R_l + j\omega L_l)(G_l + j\omega C_l)}$. The imaginary part β can also be written using the phase velocity $\beta = \omega/v_p$. When the transmission line is terminated with its characteristic impedance $Z_L = Z_0$, we have $Z_{\text{in}} = Z_0$. When the transmission line is low-loss and shorted at the end (see Fig. 1.9(b)), we have $\alpha l \ll 1$ and $Z_L = 0$, which gives

$$Z_{\text{in}}(\omega) = Z_0 \tanh \gamma l = Z_0 \frac{\alpha l + j \tan \beta l}{1 + j\alpha l \tan \beta l}. \tag{1.88}$$

When $\beta l = \omega l/v_p = n\pi$, we have series resonances and when $\beta l = \omega l/v_p = (n + \frac{1}{2})\pi$, we have parallel resonances. Their effective RLC can be calculated from Table 1.1. A similar analysis can also be done for open-end transmission lines (see Fig. 1.9(c)), where $Z_L = 1/j\omega C_o$, with $C_o \to 0$, which gives

$$Z_{\text{in}}(\omega) = Z_0 \frac{1}{\tanh \gamma l} = Z_0 \frac{1 + j\alpha l \tan \beta l}{\alpha l + j \tan \beta l}. \tag{1.89}$$

When $\beta l = \omega l/v_p = n\pi$, we have parallel resonances and when $\beta l = \omega l/v_p = (n + \frac{1}{2})\pi$, we have series resonances. The effective RLC, quality factors, and dissipation rates of these modes are listed in Table 1.2. We can see that all the modes have the same dissipation rate,

	Short-end		Open-end	
	series	parallel	parallel	series
ω_n	$n\pi v_p/l$	$(n+1/2)\pi v_p/l$	$n\pi v_p/l$	$(n+1/2)\pi v_p/l$
R_n	$Z_0\alpha l$	$Z_0/\alpha l$	$Z_0/\alpha l$	$Z_0\alpha l$
L_n	$n\pi Z_0/2\omega_n$	$4Z_0/(2n+1)\pi\omega_n$	$2Z_0/n\pi\omega_n$	$(2n+1)Z_0\pi/4\omega_n$
C_n	$2/n\pi Z_0\omega_n$	$(2n+1)\pi/4Z_0\omega_n$	$n\pi/2Z_0\omega_n$	$4/(2n+1)Z_0\pi\omega_n$
Q_n	$n\pi/2\alpha l$	$(2n+1)\pi/4\alpha l$	$n\pi/2\alpha l$	$(2n+1)\pi/4\alpha l$
κ_n	$2\alpha v_p$	$2\alpha v_p$	$2\alpha v_p$	$2\alpha v_p$

Table 1.2: Effective RLC for the resonant modes in l-long transmission lines with short and open ends.

which is also independent of the length of the transmission line.

For microwave signals, the wavelength is comparable to the dimension of the elements, which makes it hard to directly make LC resonators as discussed in Sec. 1.2 (but still possible with small footprints, see e.g. Refs. [57, 58, 60]). From the above discussion, we can use the transmission lines to make the resonators conveniently although there will be other resonances at higher frequencies. In experiments, we usually use the CPW type of transmission lines (see Fig. 1.8(d)) to make resonators in a planar structure [61].

Lossy transmission line resonator

In experiments, we need to drive the resonator with a drive line, which will damp the resonator. Here we give an example of how the drive line damps a $\lambda/4$ transmission line resonator. We couple the drive line to the transmission line resonator either inductively or capacitively as shown in Fig. 1.10.

When the drive line with resistance Z_e is coupled to the $\lambda/4$ transmission line resonator inductively (see Fig. 1.10(a)), the resonator dissipation rate κ (coupling to the external drive line) can be calculated using Eq. 1.41,

$$\kappa = \frac{\omega_0^2 M^2}{L_{\text{eff}}}\frac{1}{Z_e} = \frac{\omega_0^2 M^2}{Z_e}\frac{4\omega_0\cos^2\theta}{Z_0\pi} = \frac{4\omega_0^3 M^2}{Z_e Z_0\pi}\cos^2\theta \tag{1.90}$$

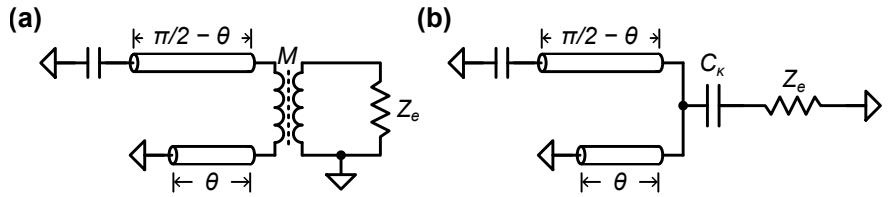

Figure 1.10: Circuit for driving a $\lambda/4$ resonator with (a) inductive coupling and (b) capacitive coupling.

where we label $\beta l = \theta$ and assume the transmission line impedance to be Z_0. Note that the effective inductance L_{eff} seen by the drive line calculated from Table 1.1 depends on the coupling position θ.

When the drive line is coupled to the $\lambda/4$ transmission line resonator capacitively (see Fig. 1.10(b)), the resonator dissipation rate κ (coupling to the external drive line) can be calculated using Eq. 1.36,

$$\kappa = \frac{\omega_0^2 C_\kappa^2}{C_{\text{eff}}} Z_e = \omega_0^2 C_\kappa^2 Z_e \frac{4\omega_0 Z_0 \sin^2\theta}{\pi} = \frac{4\omega_0^3 C_\kappa^2 Z_0 Z_e}{\pi} \sin^2\theta, \tag{1.91}$$

where the effective capacitance C_{eff} seen by the drive line calculated from Table 1.1 also depends on the coupling position θ.

Coupled transmission line resonators

We also need to deal with coupled transmission line resonators. Here we give an example of coupled $\lambda/4$ and $\lambda/2$ resonators. The coupled transmission lines will have both coupled mutual inductance M and capacitance C_c. Here we treat them separately as is shown in Fig. 1.11. We label $\beta l = \theta$ and assume they have the same impedance Z_0. To calculate the coupling strength using Eqs. 1.20 and 1.24, we need to calculate the effective RLC at the coupling point, which can be calculated using the results in Table 1.1 and is dependent on the position of the coupling point. For the inductive coupling (see Fig. 1.11(a)), the effective

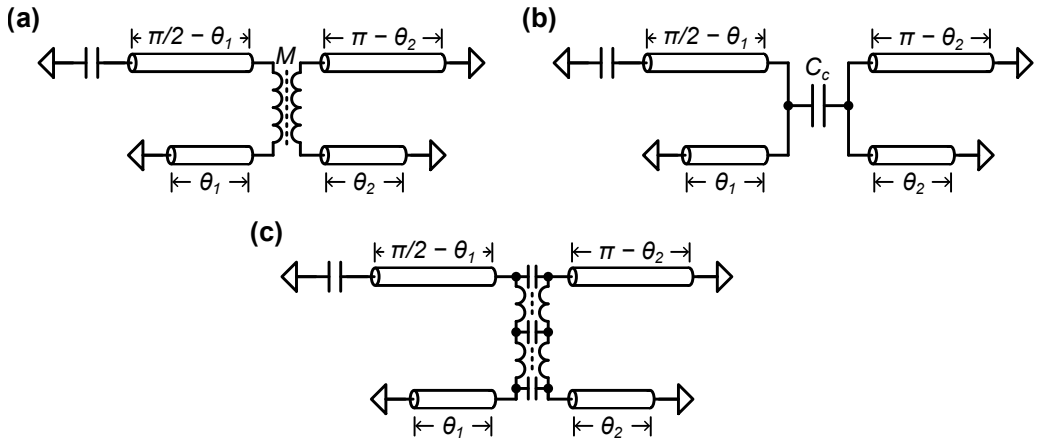

Figure 1.11: Circuits for coupled $\lambda/4$ (left) and $\lambda/2$ (right) resonators with (a) inductive coupling, (b) capacitive coupling and (c) combined coupling.

coupling strength g_i can be calculated as

$$\begin{aligned} g_i &= \frac{1}{2}\frac{M}{\sqrt{L_{1,\text{eff}}L_{2,\text{eff}}}}\sqrt{\omega_1\omega_2} = \frac{1}{2}M\sqrt{\frac{4\omega_1\cos^2\theta_1}{Z_0\pi}}\sqrt{\frac{2\omega_2\cos^2\theta_2}{Z_0\pi}}\sqrt{\omega_1\omega_2} \\ &= \frac{\sqrt{2}}{\pi}\frac{M}{Z_0}\omega_1\omega_2|\cos\theta_1\cos\theta_2|. \end{aligned} \tag{1.92}$$

For the capacitive coupling (see Fig. 1.11(b)), the effective coupling strength g_c can be calculated as

$$\begin{aligned} g_c &= \frac{1}{2}\frac{C_c}{\sqrt{C_{1,\text{eff}}C_{2,\text{eff}}}}\sqrt{\omega_1\omega_2} = \frac{1}{2}C_c\sqrt{\frac{4\omega_1 Z_0\sin^2\theta_1}{\pi}}\sqrt{\frac{2\omega_2 Z_0\sin^2\theta_2}{\pi}}\sqrt{\omega_1\omega_2} \\ &= \frac{\sqrt{2}}{\pi}C_c Z_0\omega_1\omega_2|\sin\theta_1\sin\theta_2|. \end{aligned} \tag{1.93}$$

The actual coupling strength will be the combination of these two types of coupling as shown in Fig. 1.11(c). The signs of different couplings matter here. We need to introduce the coupled line theory to solve such a circuit. More details can be found in Appendix D.

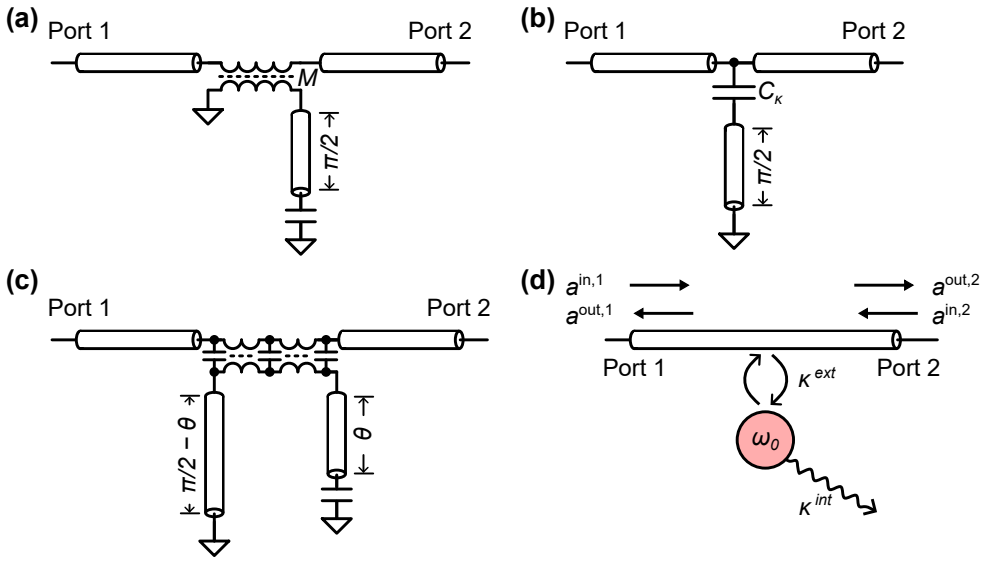

Figure 1.12: Circuits for a $\lambda/4$ resonator coupled to a transmission line with (a) inductive coupling, (b) capacitive coupling, (c) combined coupling, and (d) their coupled-mode representation.

1.3.3 Scattering of a hanger resonator

In Fig. 1.6, we give an example of the scattering of a resonator. By measuring the S-parameters, we can determine the coupling quality factor $Q_c = \omega_0/\kappa_{\text{ext}}$ and the internal quality factor $Q_i = \omega_0/\kappa_{\text{int}}$ of the resonator. However, this scheme requires one external port for each resonator, which is not efficient. Another common way is to couple many resonators to a transmission line in a hanger-type structure. By measuring the transmission S_{21} and reflection S_{11}, we can get the quality factors of all resonators. Here we give an example of a $\lambda/4$ resonator coupled to the transmission line inductively, capacitively, or with combined couplings in a hanger-type structure as shown in Fig. 1.12(a-c). The S-parameters in these circuits can be directly calculated from $ABCD$ matrices [45]. Readers can find detailed derivations in Refs. [62, 63, 64] and Appendix D.

Like what we did in Section 1.2.5, we can also use quantum input-output theory to analyze this scattering process. The representation is shown in Fig. 1.12(d) and we label all the input and output fields at each port. The quantum Langevin equation and input-output

relations are [65, 66]

$$\dot{a}(t) = -(i\omega_0 + \frac{\kappa}{2})a(t) - \sqrt{\frac{\kappa^{\text{ext}}}{2}}\, a^{\text{in},1}(t) - \sqrt{\frac{\kappa^{\text{ext}}}{2}}\, a^{\text{in},2}(t), \tag{1.94}$$

$$a^{\text{out},1}(t) = \sqrt{\frac{\kappa^{\text{ext}}}{2}}\, a(t) + a^{\text{in},2}(t), \tag{1.95}$$

$$a^{\text{out},2}(t) = \sqrt{\frac{\kappa^{\text{ext}}}{2}}\, a(t) + a^{\text{in},1}(t), \tag{1.96}$$

from which we can get the reflection coefficient S_{11} and transmission coefficient S_{21},

$$S_{11}(\omega) = \frac{a^{\text{out},1}(\omega)}{a^{\text{in},1}(\omega)} = -\frac{\kappa^{\text{ext}}/2}{\kappa/2 - i(\omega - \omega_0)} = -\frac{Q_l}{Q_c}\frac{1}{1 - 2iQ_l\frac{\omega-\omega_0}{\omega_0}}, \tag{1.97}$$

$$S_{21}(\omega) = \frac{a^{\text{out},2}(\omega)}{a^{\text{in},1}(\omega)} = 1 - \frac{\kappa^{\text{ext}}/2}{\kappa/2 - i(\omega - \omega_0)} = 1 - \frac{Q_l}{Q_c}\frac{1}{1 - 2iQ_l\frac{\omega-\omega_0}{\omega_0}}, \tag{1.98}$$

where $Q_l = \omega/\kappa$ is the loaded quality factor, and $\kappa = \kappa^{\text{ext}} + \kappa^{\text{int}}$ is the total dissipation rate. The readers can verify that for different coupling schemes, S_{21} and S_{11} can always be written in this form near the resonance. Note that the S-parameters derived from $ABCD$ matrices have a different sign before i, which comes from the different definition of the complex operator j in AC circuits, $j = -i$, as we mentioned before. Examples of the transmission S_{21} are shown in Fig. 1.13(a-b). For the inductively coupled $\lambda/4$ resonator (Fig. 1.12(a)), its κ^{ext} and Q_c can be calculated from Eq. 1.90 by setting $Z_e = 2Z_0$ and $\theta = 0$,

$$\kappa^{\text{ext}} = \frac{4\omega_0^3 M^2}{Z_e Z_0 \pi} = \frac{2\omega_0^3 M^2}{\pi Z_0^2}, \tag{1.99}$$

$$Q_c = \frac{\omega_0}{\kappa^{\text{ext}}} = \frac{\pi Z_0^2}{2\omega_0^2 M^2}, \tag{1.100}$$

where we assume the $\lambda/4$ resonator and the transmission line have the same characteristic impedance Z_0. For the capacitively coupled $\lambda/4$ resonator (Fig. 1.12(b)), its κ^{ext} and Q_c

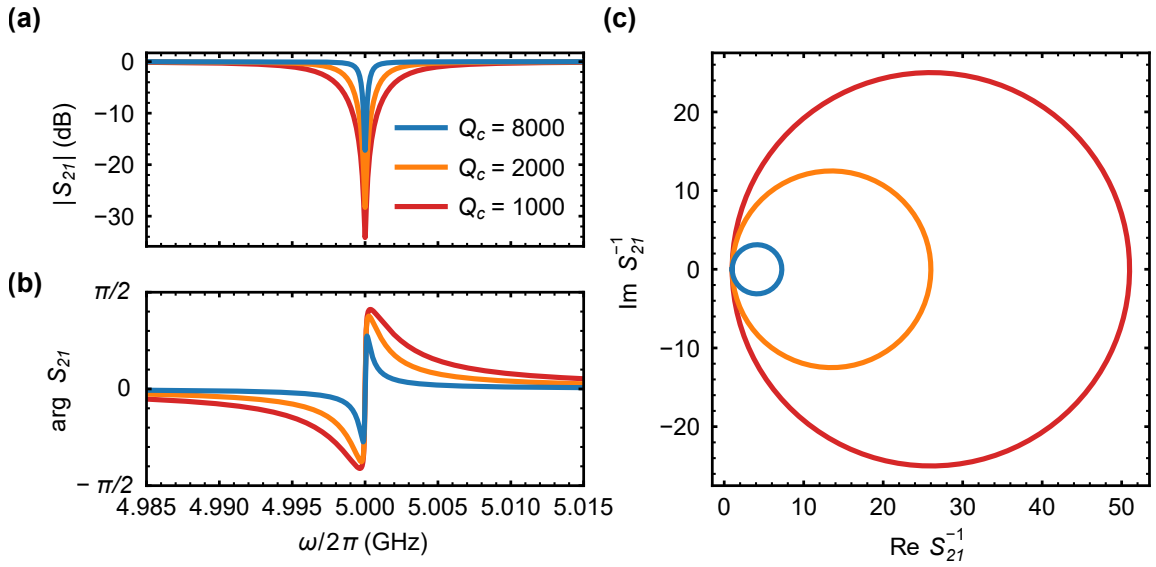

Figure 1.13: Transmission S_{21} (a) amplitude and (b) phase of hanger resonators with different Q_c. (c) $\mathrm{Re}\, S_{21}^{-1}$ and $\mathrm{Im}\, S_{21}^{-1}$ form a circle with radius $Q_i/2Q_c$. The related parameters are $\omega_0/2\pi = 5$ GHz and $Q_i = 5 \times 10^4$.

can be calculated from Eq. 1.91 by setting $Z_e = Z_0/2$ and $\theta = \pi/2$,

$$\kappa^{\mathrm{ext}} = \frac{4\omega_0^3 C_\kappa^2 Z_0 Z_e}{\pi} = \frac{2\omega_0^3 C_\kappa^2 Z_0^2}{\pi}, \tag{1.101}$$

$$Q_c = \frac{\omega_0}{\kappa^{\mathrm{ext}}} = \frac{\pi}{2\omega_0^2 Z_0^2 C_\kappa^2}. \tag{1.102}$$

When there exist both capacitive and inductive couplings (see Fig. 1.12(c)), we need to introduce the coupled line theory to solve such a circuit. More details can be found in Appendix D.

By placing resonators of different frequencies at different positions, we can measure their quality factors with two ports in total. In experiments, we prefer transmission measurements as the reflection measurements are limited by the isolation of the circulators used in the measurement setup. We note that S_{21} forms a circle in the complex plane, with a radius of

$Q_l/2Q_c$. We can also write down the inverse of S_{21}, which is

$$S_{21}^{-1}(\omega) = 1 + \frac{Q_i}{Q_c}\frac{1}{1 - 2iQ_i\frac{\omega-\omega_0}{\omega_0}}, \tag{1.103}$$

which also forms a circle in the complex plane but with a radius of $Q_i/2Q_c$ (see Fig. 1.13(c)), more sensitive to Q_i. By fitting the circle of S_{21}^{-1} in the complex plane, we can extract Q_i of high Q resonators from a transmission measurement [67]. Considering the background attenuation and noise, the actual measured transmission $\widetilde{S}_{21}$ will be [68],

$$\widetilde{S}_{21}(\omega) = Ae^{i\alpha}e^{-i\omega\tau}S_{21}(\omega), \tag{1.104}$$

where A, α, and τ are parameters determined by the background.

Transmission lines also enrich the physics of circuit quantum electrodynamics. For example, we can engineer the lifetime of an artificial atom by coupling it to multiple points on a transmission line [69, 70] or control the propagating direction of the emitted photon by coupling multiple artificial atoms to a transmission line [71, 72].

1.4 Transmon qubit

For linear circuits, their dynamics can be efficiently simulated. Introducing non-linearity can help us create qubits – the basic elements of quantum computing. In this section, we will introduce the most commonly used superconducting qubit – the transmon qubit.

1.4.1 Hamiltonian

The basic transmon structure contains a Josephson junction and a capacitor [73, 74] (see Fig. 1.14). The voltage $V(t)$ and current $I(t)$ across a Josephson junction satisfy the Joseph-

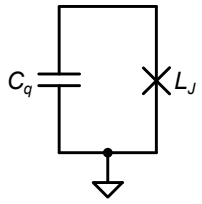

Figure 1.14: Circuit for a transmon with a Josephson junction replacing the inductor in the LC resonator.

son equations [75],

$$V(t) = \frac{\hbar}{2e}\frac{\partial \phi}{\partial t}, \tag{1.105}$$

$$I(t) = I_c \sin\phi, \tag{1.106}$$

where ϕ is the Josephson phase and I_c is the critical current of the junction. The phase ϕ is related to the node flux Φ as

$$\phi = \frac{2e}{\hbar}\Phi = 2\pi\frac{\Phi}{\Phi_0}, \tag{1.107}$$

where $\Phi_0 = 2\pi\hbar/2e$ is the flux quantum. The energy stored in the junction is

$$\begin{aligned} U &= \int_{-\infty}^{t} \mathrm{d}\tau\ V(\tau)I(\tau) = \frac{\hbar}{2e}\int_{-\infty}^{t} \mathrm{d}\tau\ I_c \sin\phi \frac{\partial\phi}{\partial\tau} \\ &= -\frac{\hbar}{2e} I_c \cos\phi = -\Big(\frac{\hbar}{2e}\Big)^2 \frac{1}{L_J}\cos\phi = -E_J\cos\phi \end{aligned} \tag{1.108}$$

where $L_J = \Phi_0/2\pi I_c$ is the Josephson inductance and $E_J = L_J I_c^2 = \Phi_0 I_c/2\pi$ is the Josephson energy. The total Lagrangian for a transmon is

$$\mathcal{L} = T - U = \frac{C_q}{2}\Big(\frac{\hbar}{2e}\Big)^2\dot{\phi}^2 + E_J\cos\phi. \tag{1.109}$$

The conjugate coordinate to ϕ is

$$n\hbar = \frac{\partial\mathcal{L}}{\partial\dot{\phi}} = C_q\Big(\frac{\hbar}{2e}\Big)^2\dot{\phi}, \tag{1.110}$$

and with canonical quantization we have

$$[\phi, n] = i. \tag{1.111}$$

n can also be written as $Q/2e$, which is the number of Cooper pairs. We can obtain the Hamiltonian

$$H = n\hbar\dot{\phi} - \mathcal{L} = 4E_C n^2 - E_J \cos\phi, \tag{1.112}$$

where $E_C = e^2/2C_q$. In the transmon limit, $E_J \gg E_C$. By Taylor expansion, we have

$$H = 4E_C n^2 - E_J + \frac{1}{2}E_J\phi^2 - \frac{1}{24}E_J\phi^4 + \cdots \tag{1.113}$$

By defining the creation and annihilation operators,

$$a = \frac{1}{\sqrt{2}}\left(\left(\frac{E_J}{8E_C}\right)^{\frac{1}{4}}\phi + i\left(\frac{8E_C}{E_J}\right)^{\frac{1}{4}}n\right), \tag{1.114}$$

$$a^\dagger = \frac{1}{\sqrt{2}}\left(\left(\frac{E_J}{8E_C}\right)^{\frac{1}{4}}\phi - i\left(\frac{8E_C}{8E_J}\right)^{\frac{1}{4}}n\right), \tag{1.115}$$

the operators n and ϕ can be written as

$$\phi = \frac{1}{\sqrt{2}}\left(\frac{8E_C}{E_J}\right)^{\frac{1}{4}}(a + a^\dagger), \tag{1.116}$$

$$n = -\frac{i}{\sqrt{2}}\left(\frac{E_J}{8E_C}\right)^{\frac{1}{4}}(a - a^\dagger), \tag{1.117}$$

and the Hamiltonian H can be written as

$$H = \sqrt{8E_C E_J}(a^\dagger a + \frac{1}{2}) - E_J - \frac{E_C}{12}(a + a^\dagger)^4 + \cdots \tag{1.118}$$

In leading order, the energies of the first n energy levels are

$$E_m = \sqrt{8E_C E_J}m - \frac{E_C}{2}(m^2 + m) + \text{const.} \tag{1.119}$$

In reality, Eq. 1.106 is not accurate and the eigenenergies will shift a little bit when considering the higher harmonics in the junction [76]. We will label the ground state as $|g\rangle$, the first excited state as $|e\rangle$, and the second excited state as $|f\rangle$. The frequency of a transmon qubit ω_q is defined as the energy gap between the $|g\rangle$ and $|e\rangle$ states,

$$\hbar\omega_q = \hbar\omega_{10} = E_1 - E_0 = \sqrt{8E_J E_C} - E_C. \tag{1.120}$$

The anharmonicity η is defined as

$$\eta = (E_{21} - E_{10})/\hbar = -E_C/\hbar, \tag{1.121}$$

which describes how atom-like the transmon is. A typical transmon Hamiltonian considering only three energy levels is like a Duffing oscillator,

$$H/\hbar = \omega_q a^\dagger a + \frac{\eta}{2} a^\dagger a^\dagger a a. \tag{1.122}$$

In experiment, we usually design the transmons to have frequency $\omega_q/2\pi \sim 5$ GHz and anharmonicity $\eta/2\pi \sim -200$ MHz, which correspond to $C_q \sim 90$ fF and $L_J \sim 8$ nH. Some commercial electromagnetic simulation software (e.g. Sonnet[2], Ansys HFSS[3], etc.) can be used to simulate the circuit layout. Examples using Sonnet for transmon design can be found in Ref. [77].

For an actual device, there is always some wiring inductance in series with the junc-

2. `https://www.sonnetsoftware.com`

3. `https://www.ansys.com/products/electronics/ansys-hfss`

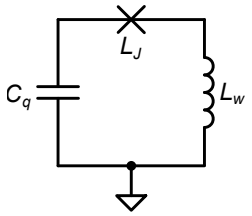

Figure 1.15: Circuit for a transmon with wiring inductance L_w.

tion, which will change the anharmonicity as more linear components are introduced (see Fig. 1.15). Assuming the wiring inductance is L_w and following the black-box superconducting circuit quantization [78], we can get the effective anharmonicity η (to first order),

$$\eta = -\Big(\frac{L_J}{L_J + L_w}\Big)^3 E_C/\hbar. \tag{1.123}$$

This wiring inductor L_w can be used to couple circuits inductively.

1.4.2 z control

To tune the frequency of a transmon, we use a superconducting quantum interference device (SQUID) to substitute the single Josephson junction (see Fig. 1.16). By applying the external flux $\Phi_{\text{ext}} = \Phi_0\phi_{\text{ext}}/2\pi$ to the SQUID, we can change the effective Josephson energy to tune the frequency of the transmon [73]. A SQUID consists of two Josephson junctions in parallel which form a loop. The total energy stored in a SQUID is

$$U = -E_{J_1}\cos\phi_1 - E_{J_2}\cos\phi_2, \tag{1.124}$$

The flux quantization leads to

$$\phi_1 - \phi_2 = 2m\pi + \phi_{\text{ext}}. \tag{1.125}$$

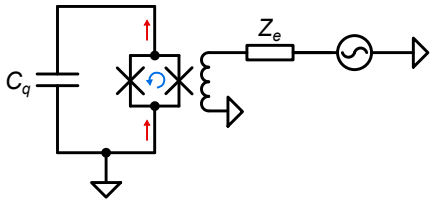

Figure 1.16: Circuit for transmon z control.

U can be rewritten as

$$U = -(E_{J_1} + E_{J_2}) \cos\left(\frac{\phi_{\text{ext}}}{2}\right) \sqrt{1 + d^2 \tan^2\left(\frac{\phi_{\text{ext}}}{2}\right)} \cos\left(\frac{\phi_1 + \phi_2}{2} - \phi_0\right), \tag{1.126}$$

where $d = (E_{J_2} - E_{J_1})/(E_{J_2} + E_{J_1})$ and $\phi_0 = \arctan(d \tan(\phi_{\text{ext}}/2))$. The parameter d describes how asymmetric the SQUID is. When $d = 0$, U becomes

$$U = -2E_J \cos\left(\frac{\phi_{\text{ext}}}{2}\right) \cos\left(\frac{\phi_1 + \phi_2}{2}\right). \tag{1.127}$$

By changing the external flux Φ_{ext}, we can tune the effective E_J of the SQUID loop. The effective Josephson inductance for a symmetric SQUID becomes $L_J/2|\cos(\phi_{\text{ext}}/2)|$, where L_J is the Josephson inductance of one junction.

The external flux across the SQUID loop Φ_{ext} is determined by the mutual inductance M_{squid} between the z-bias line and the loop (the induced current direction is shown blue in Fig. 1.16). Assuming the current on the z-bias line is I, the external flux across the SQUID loop is $\Phi_{\text{ext}} = M_{\text{squid}} I$. The typical value for M_{squid} in experiments is around 2 pH. The fluctuations in the current will shift the qubit frequency causing the dephasing. To get a long qubit pure dephasing time T_ϕ, we can place the qubit at its maximum frequency or minimum frequency for asymmetric SQUIDs.

When we design the z-bias line, we also need to minimize the mutual inductance M_{qubit} between the z-bias line and the qubit mode (the induced current direction is shown red in Fig. 1.16), which damps the qubit. The external loss introduced by the z-bias line can be

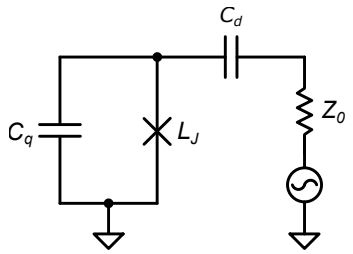

Figure 1.17: Circuit for transmon xy control.

calculated using Eq. 1.41,

$$\kappa_q = \frac{\omega_q^2 M_{\text{qubit}}^2}{L_{\text{eff}}} \frac{1}{Z_e} = \frac{\omega_q^4 C_q M_{\text{qubit}}^2}{Z_e}, \tag{1.128}$$

where Z_e is the impedance of the z-bias line. For $M_{\text{qubit}} = 0.5$ pH and $Z_e = 50\ \Omega$, qubit relaxation time $T_1 = \kappa_q^{-1}$ will be limited to around 2 ms. To further minimize the damping effect of the z-bias line, some extra filtering circuits (usually a low pass filter) can be added on the z-bias line to engineer the control line impedance $Z_e(\omega)$ at the qubit frequency ω_q [79, 80]. Note that this coupling M_{qubit} can be used to Rabi drive the qubit, but it will also modulate the qubit frequency at the same time. In the following section, we will introduce how to drive the qubit with a capacitively coupled control line.

1.4.3 xy control

To drive a transmon, we use a voltage source $V_d(t)$ coupled to the qubit by a capacitor C_d (see Fig. 1.17). The total Lagrangian is

$$\mathcal{L} = T - U = \frac{C_q}{2}\Big(\frac{\hbar}{2e}\Big)^2 \dot{\phi}^2 + \frac{C_d}{2}\Big(V_d - \frac{\hbar}{2e}\dot{\phi}\Big)^2 + E_J \cos\phi. \tag{1.129}$$

The conjugate coordinate to ϕ is

$$n\hbar = \frac{\partial \mathcal{L}}{\partial \dot{\phi}} = (C_q + C_d)\Big(\frac{\hbar}{2e}\Big)^2 \dot{\phi} - C_d V_d \frac{\hbar}{2e}, \tag{1.130}$$

and with canonical quantization we have

$$[\phi, n] = i. \tag{1.131}$$

We can obtain the Hamiltonian

$$H = n\hbar\dot{\phi} - \mathcal{L} = 4E_C n^2 - E_J \cos\phi + \frac{C_d}{C_q + C_d} 2neV_d - \frac{1}{2}\frac{C_q C_d}{C_q + C_d} V_d^2, \tag{1.132}$$

where $E_C = e^2/2(C_q + C_d)$. We can ignore the last term since it does not affect the dynamics of the qubit. Note that the above Hamiltonian can be rewritten as

$$H = 4E_C(n - n_g)^2 - E_J \cos\phi, \tag{1.133}$$

with $n_g = -C_d V_d/2e$. Fluctuations in n_g lead to a change in energy levels which will cause dephasing. In the transmon limit, $E_J \gg E_C$, the charge dispersion decreases exponentially with E_J/E_C, while the decrease in anharmonicity is described by a power law [73]. Thus transmons are insensitive to such charge fluctuations. Write the driving term H_d using creation and annihilation operators, we can get

$$H_d = \frac{C_d}{C_q + C_d} 2neV_d = i\sqrt{(\hbar\omega_q + E_C)E_C}\frac{C_d V_d}{e}(a^\dagger - a), \tag{1.134}$$

where ω_q is the qubit frequency, as defined in Eq. 1.120. Constraining it in two energy levels, we have

$$H_d = \sqrt{(\hbar\omega_q + E_C)E_C}\frac{C_d V_d}{e}\sigma_y. \tag{1.135}$$

When $V_d(t) = V_0 \cos\omega_q t$, we can Rabi drive the qubit, from which we can construct single qubit xy rotations. Considering the third level of transmon $|f\rangle$, this on-resonance drive pulse will excite qubit to the $|f\rangle$ state causing leakage errors. There are several ways to minimize

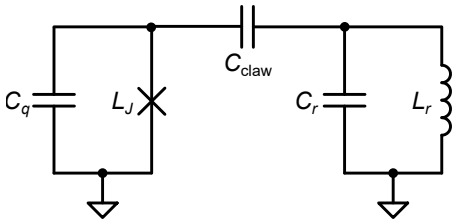

Figure 1.18: Circuit for transmon readout: a readout resonator is coupled to the transmon with a capacitor C_{claw}.

the leakage by shaping the pulse envelope [81, 82]. The state-of-the-art single-qubit gate fidelity is over 99.99%, mainly limited by qubit coherence times [83].

The external loss caused by the xy-drive line can be calculated using Eq. 1.36,

$$\kappa_q = \frac{\omega_q^2 C_d^2}{C_q} Z_0, \tag{1.136}$$

where $Z_0 = 50\ \Omega$ is the characteristic impedance of xy-drive line. Usually, we set C_d to be 30 aF, which gives a T_1 limit of 2 ms. Although we can make C_d smaller and drive harder, most of the driving signals will dissipate on the attenuators on the control line, causing potential heating. We cannot directly use linear circuits to filter the xy control line like the z line since the signals on xy lines are on resonance with the qubit unless using a subharmonic drive (e.g. $\omega_d = \omega_q/3$) [84, 85]. There exist some filtering protocols using the feature of Josephson junctions which saturate under high power [86].

1.4.4 Readout

Dispersive readout

A popular way to measure the state of transmon qubit is to probe the frequency shift of a dispersively coupled readout resonator [73, 87]. The readout circuit is shown in Fig. 1.18, where a transmon is capacitively coupled to the readout resonator like Fig. 1.2(a). We can also do inductive coupling like Fig. 1.2(b), but transmons usually have large capacitor pads

and short wiring length (small L_w), which is more convenient for capacitive coupling. If we constrain the qubit to two energy levels, we can write down the qubit-oscillator coupling Hamiltonian from Eq. 1.19 with the rotating wave approximation (RWA),

$$H/\hbar = \omega_r(a^\dagger a + \frac{1}{2}) - \frac{1}{2}\omega_q\sigma_z + c_{qr}(a^\dagger\sigma^- + a\sigma^+), \tag{1.137}$$

where c_{qr} is the qubit-resonator coupling strength. In the dispersive limit $|\Delta_{qr}| \gg |c_{qr}|$, where the detuning $\Delta_{qr} = \omega_q - \omega_r$, we can expand it in powers of c_{qr}/Δ_{qr} to second order by applying a unitary transformation $U = e^{\frac{c_{qr}}{\Delta_{qr}}(a^\dagger\sigma^- - a\sigma^+)}$ (see Appendix C),

$$\begin{aligned} H/\hbar &= \omega_r(a^\dagger a + \frac{1}{2}) - \frac{1}{2}\omega_q\sigma_z + \chi a^\dagger a\sigma_z + \mathcal{O}\Big(\frac{c_{qr}^3}{\Delta_{qr}^2}\Big) \\ &= \omega_r(a^\dagger a + \frac{1}{2}) - \frac{1}{2}(\omega_q - 2\chi a^\dagger a)\sigma_z \\ &= (\omega_r + \chi\sigma_z)a^\dagger a - \frac{1}{2}\omega_q\sigma_z + \omega_r(a^\dagger a + \frac{1}{2}), \end{aligned} \tag{1.138}$$

where $\chi = -c_{qr}^2/\Delta_{qr}$ is the "dispersive shift". Taking the third level $|f\rangle$ into account [73], we have

$$\chi = -\frac{c_{qr}^2}{\Delta_{qr}}\frac{\eta}{\Delta_{qr}+\eta} \simeq -\frac{c_{qr}^2}{\Delta_{qr}^2}\eta, \tag{1.139}$$

where η is the anharmonicity of the transmon, which is negative. From Eq. 1.138, we can see that the state of transmon will change the effective frequency of the readout resonator. When the qubit is in $|g\rangle$ ($|e\rangle$) state, the frequency of the readout resonator is $\omega_{r,|g\rangle} = \omega_r + \chi$ ($\omega_{r,|e\rangle} = \omega_r - \chi$). Measuring the state of the qubit is equivalent to measuring the frequency shift of the readout resonator, which can be done by a scattering measurement.

In Section 1.2.5, we discussed the scattering of a resonator, and in Section 1.3.3, we discussed the scattering of a hanger resonator. Both types of measurements can be used to probe the frequency shift by sending a probe signal with frequency ω_p and measuring its transmission $S_{21}(\omega_p)$ or reflection $S_{11}(\omega_p)$. To get a larger signal-to-noise ratio (SNR),

we want to maximize the difference of $S(\omega_p)$ between the $|g\rangle$ state and $|e\rangle$ state, $|\Delta S(\omega_p)|$, where S can be either S_{11} or S_{21}. From Eqs. 1.63, 1.67, 1.97, and 1.98, we can see that $|\Delta S(\omega_p)|$ have similar forms no matter what types of measurements we perform,

$$|\Delta S(\omega_p)| \propto \Big|\frac{1}{1+2jQ_l(\omega_p-\omega_{r,|g\rangle})/\omega_{r,|g\rangle}} - \frac{1}{1+2jQ_l(\omega_p-\omega_{r,|e\rangle})/\omega_{r,|e\rangle}}\Big| \tag{1.140}$$

$$\simeq \frac{2Q_l|\chi|}{\omega_r}\sqrt{\frac{1}{1+4Q_l^2(\omega_p-\omega_{r,|g\rangle})^2/\omega_r^2}\frac{1}{1+4Q_l^2(\omega_p-\omega_{r,|e\rangle})^2/\omega_r^2}}, \tag{1.141}$$

where $Q_l = \omega_r/\kappa_r$ is the loaded quality factor of the readout resonator. The difference $|\Delta S(\omega_p)|$ reaches maximum when $\omega_p = (\omega_{r,|g\rangle} + \omega_{r,|e\rangle})/2$. If we set the frequency of the probe tone ω_p to this value, the difference $|\Delta S(\omega_p)|$ will be

$$|\Delta S(\omega_p)| = |\Delta S(\omega_r)| \propto \frac{2Q_l|\chi|/\omega_r}{1+4Q_l^2\chi^2/\omega_r^2}, \tag{1.142}$$

which reaches the maximum when

$$2|\chi| = \frac{\omega_r}{Q_l} = \kappa_r. \tag{1.143}$$

We can get the maximum readout visibility when the readout resonator frequency shift between $|g\rangle$ and $|e\rangle$ states $2|\chi|$ equals the readout resonator dissipation rate κ_r. Ref. [88] presents several different ways to derive this maximum visibility condition.

For direct scattering of a resonator discussed in Section 1.2.5, we usually can only measure one qubit with one readout line (see e.g. Ref. [80]), while for the scattering of a hanger resonator discussed in Section 1.3.3, we can do multiplexed readout by placing multiple readout resonators with different frequencies at different positions on the readout line. However, for the scattering of a hanger resonator, half of the scattered signal will leak through the input port while the other half will leak through the output port, which means if we only measure S_{11} or S_{21}, we will lose half of the signal. This can be further improved by col-

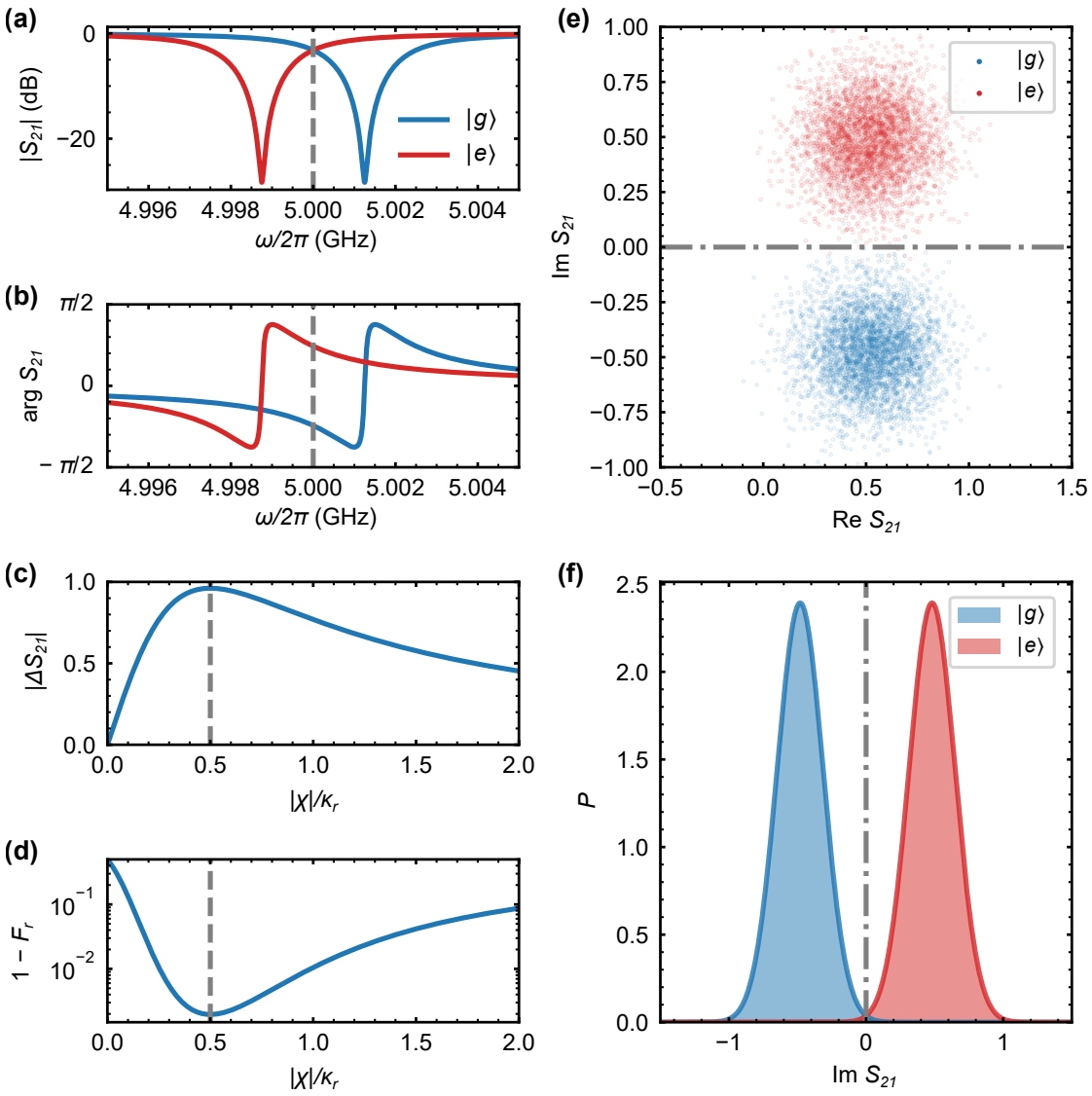

Figure 1.19: Dispersive readout of superconducting qubits using a hanger resonator. Transmission S_{21} (a) amplitude and (b) phase for qubit $|g\rangle$ and $|e\rangle$ states, where $\omega_r/2\pi = 5$ GHz, $\chi = 1.25$ MHz. (c) Transmission difference $|\Delta S_{21}|$ between $|g\rangle$ and $|e\rangle$ states when $\omega_p = \omega_r$, which reaches maximum when $2|\chi| = \kappa_r$. (d) Readout fidelity F_r changes as $|\chi|/\kappa_r$, with Gaussian noise $3\sigma = 0.5$. (e) Repeated measured S_{21} for $|g\rangle$ and $|e\rangle$ states with Gaussian noise $3\sigma = 0.5$, measured at $\omega_p = \omega_r$ and $2|\chi| = \kappa_r$. (f) Distribution of measured S_{21} projected to Im S_{21} axis. All calculations assume $Q_i = 5 \times 10^4$, $Q_c = 2 \times 10^3$.

lecting both signals and doing interference [89], engineering the readout resonator to have directional decay [90, 91], or inserting a Purcell filter with a weakly coupled input port and a strongly coupled output port [48], which we will discuss later in this section.

In Fig. 1.19, we give an example of dispersive readout by measuring the transmission $S_{21}(\omega_p)$ of a hanger readout resonator. Before the signal arrives at the detector, it will catch noises which can be typically described by two-dimensional Gaussian distribution. Repeatedly running the measurement, the measured results will look like Fig. 1.19(e). If we assume the noise level to be $3\sigma = 0.5$, we can extract the readout fidelity F_r (see Fig. 1.19(d)), which is defined as the average of the assigned probabilities $(F_g + F_e)/2$, where F_g (F_e) is defined as the measured probability of the $|g\rangle$ ($|e\rangle$) state when the qubit is prepared in the corresponding state. The fidelity F_e is usually below F_g in experiments because of qubit decay during the measurement.

The above discussion is about measuring the S-parameters, where we assume the readout time τ is much longer than the readout resonator lifetime κ_r^{-1}, $\kappa_r\tau \gg 1$. For fast readout, when τ is only several times of κ_r^{-1}, larger $|\chi|/\kappa_r$ helps improve the SNR [92].

Parametric amplifier

A direct way to increase SNR is to increase the power of the input readout signals. However, high power will drive the qubit to higher excited states [93, 94, 95, 96]. Another way is to amplify the output signal, right after the signal comes out of the sample before it catches any thermal noise. A common type of amplifier used for such applications is the Josephson parametric amplifier (JPA). A good introduction can be found in Ref. [97]. Normal JPAs are limited by gain-bandwidth constraints. By engineering the impedance, we can break this constraint and make JPAs broadband [98, 99, 100, 101]. Another common type of amplifier is the Josephson traveling-wave parametric amplifier (JTWPA) [102], which are transmission lines comprised of series-connected junctions. JTWPAs usually do not have a fundamental gain-bandwidth constraint but are noisier than JPAs.

Purcell filter

Like other control lines, the measurement circuit also damps the qubit. We have discussed its mechanism, the Purcell effect [47], in Section 1.2.4. The qubit lifetime $T_{1,\text{bare}}$ is limited by the Purcell effect as

$$T_{1,\text{bare}} = \kappa_q^{-1} = \frac{\Delta_{qr}^2}{c_{qr}^2}\frac{1}{\kappa_r}. \tag{1.144}$$

Similar to the other control lines, we can also use some filtering circuits to protect the qubit from the Purcell effect, and those filters are called Purcell filters [103]. Purcell filters engineer the electrical environment seen by the readout resonator, which suppresses the resonator decay at qubit frequency ω_q. With the Purcell filter, the qubit T_1 will be limited as [104]

$$T_1 = \frac{\Delta_{qr}^2}{c_{qr}^2}\frac{1}{\kappa_r(\omega_q)} = T_{1,\text{bare}}\frac{\kappa_r(\omega_r)}{\kappa_r(\omega_q)}, \tag{1.145}$$

where $\kappa_r(\omega)$ is the resonator decay rate at frequency ω.

As we discussed in Section 1.2.4, engineering $\kappa_r(\omega)$ of the readout resonator is equivalent to engineering the impedance $Z(\omega)$ / admittance $Y(\omega)$ of its coupled circuits. There are many Purcell filters based on different classical filters, e.g. low pass [105], high pass [106], bandpass [48], and bandstop [103, 107] filters.

Bandpass Purcell filters are commonly used because of their flexibility as we can put the readout resonators in the passband and put the qubits either above or below the passband. The simplest bandpass filter is a resonator inline [48, 108, 109] as is shown in Fig. 1.6(b) and Eq. 1.67. However, this kind of design has limited bandwidth or isolation (see Eq. 1.53), which limits the multiplexed readout capacity. For larger qubit numbers, one solution is to design an individual filter for each readout resonator [110], which requires the filter frequency to match well with the readout resonator frequency [111]. Another solution is to increase the number of stages of the bandpass filter to make its passband broader. Refs. [112, 113, 114] designed classical bandpass filters with small footprints. By connecting them on the readout

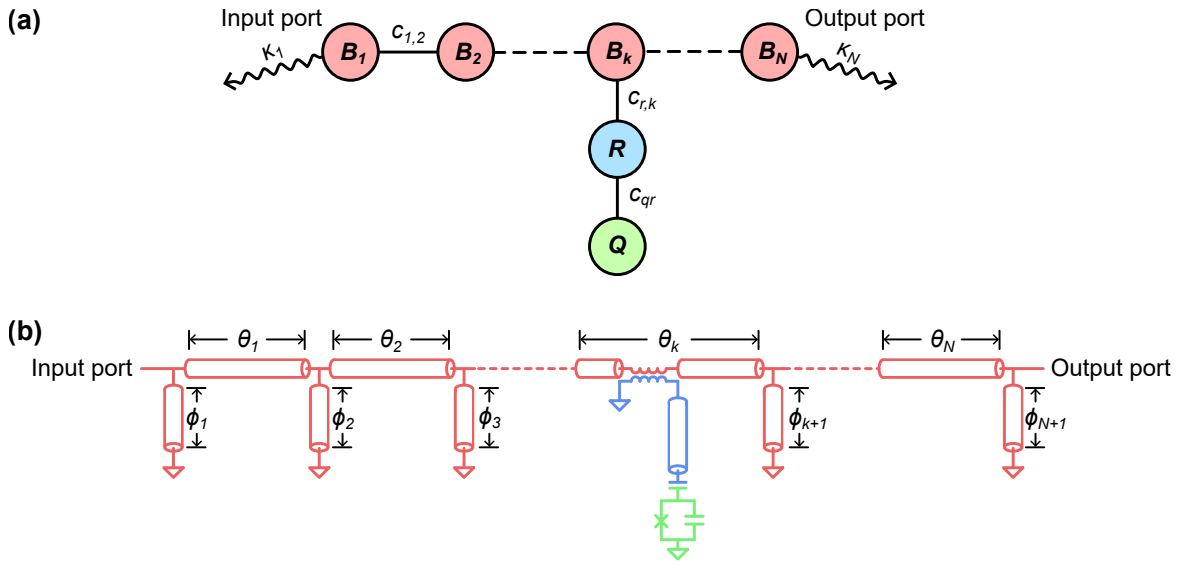

Figure 1.20: (a) Coupled-mode representation of dispersive readout with an Nth-order bandpass Purcell filter: the qubit Q is coupled to the readout resonator R with coupling c_{qr}, which is further coupled to the kth stage of the bandpass filter B_k with coupling $c_{r,k}$. κ_j represents the dissipation rate for the jth resonator B_j. $c_{j,j+1}$ represents coupling between resonators B_j and B_{j+1} in the filter. The values of κ_j and $c_{j,j+1}$ are listed in Appendix E. (b) Circuit realization using coupled $\lambda/2$ resonators as the bandpass filter and a $\lambda/4$ resonator as the readout resonator. The lengths of sections of the bandpass filter are listed in Appendix E.

line, we can get pretty good qubit protection. However, these external circuits will introduce more insertion loss, causing the loss of readout signals. Ref. [58] designed a broadband bandpass filter and put the readout resonator in the middle of the filter, but this filter has equally coupled input and output ports, which will lose half of the readout signal like scattering of a hanger resonator. In the following, we will discuss broadband bandpass Purcell filter design based on the synthesis of classical bandpass filters.

The design flow of bandpass filters is shown in Appendix E, from which we know that a multi-stage bandpass filter can be modeled as coupled resonators and a large insertion loss (asymmetric) filter corresponds to a filter with a weakly coupled input port and a strongly coupled output port ($\kappa_1 \ll \kappa_N$). To realize qubit readout, we need to couple the readout resonator to one stage of the filter as is shown in Fig. 1.20(a). Like what we have discussed in Section 1.2.4, we can use the density of states to characterize the property of the filter,

which serves as a Markovian bath to the readout resonator. Since we couple the readout resonator to only one stage of the filter, the density of states becomes the local density of states (LDOS) $\rho_k(\omega)$, which is defined as (see Appendix A)

$$\rho_k(\omega) = \frac{1}{\pi}\mathrm{Re}\Big[\int_0^\infty \mathrm{d}t\, e^{i\omega t}\langle[a_k(t), a_k^\dagger(0)]\rangle\Big], \tag{1.146}$$

where we assume the readout resonator is coupled to the kth stage of the filter and a_k ($a_k^\dagger$) is the annihilation (creation) operator of the resonator of the kth stage. The readout resonator decay rate κ_r is determined by the Fermi's golden rule as

$$\kappa_r(\omega) = 2\pi c_{r,k}^2 \rho_k(\omega), \tag{1.147}$$

where $c_{r,k}$ is the coupling strength between the readout resonator and the kth stage. The ratio $\kappa_r(\omega_r)/\kappa_r(\omega_q) = \rho_k(\omega_r)/\rho_k(\omega_q)$ quantifies the qubit protection. Depending on whether the readout resonator is capacitively or inductively coupled to the filter stage, the LDOS $\rho_k(\omega)$ is proportional to $\mathrm{Re}[Z_k(\omega)]$ or $\mathrm{Re}[Y_k(\omega)]$ where Z_k (Y_k) is the impedance (admittance) from the coupling point of the kth stage to ground.

The calculated LDOS of 4-stage filters with 0 dB and 20 dB insertion loss are shown in Fig. 1.21. We can see that for the conventional filter with equally coupled input and output ports (0 dB insertion loss), we can get better qubit protection when the readout resonator is coupled to the middle of the filter. For the asymmetric filter (20 dB insertion loss), $\rho_1(\omega)$ is flat in the passband and there are $k-1$ near-zero points in ρ_k. Similar features are found on filters with different stages [115]. When the readout resonator is coupled to the kth filter stage and its frequency is close to these near-zero points, it barely decays and cannot be used to do qubit readout. We will couple the readout resonator to the first (middle) stage of the filter with larger (zero) insertion loss.

In Fig. 1.22, we calculate the qubit T_1 limit using the classical coupled resonator model

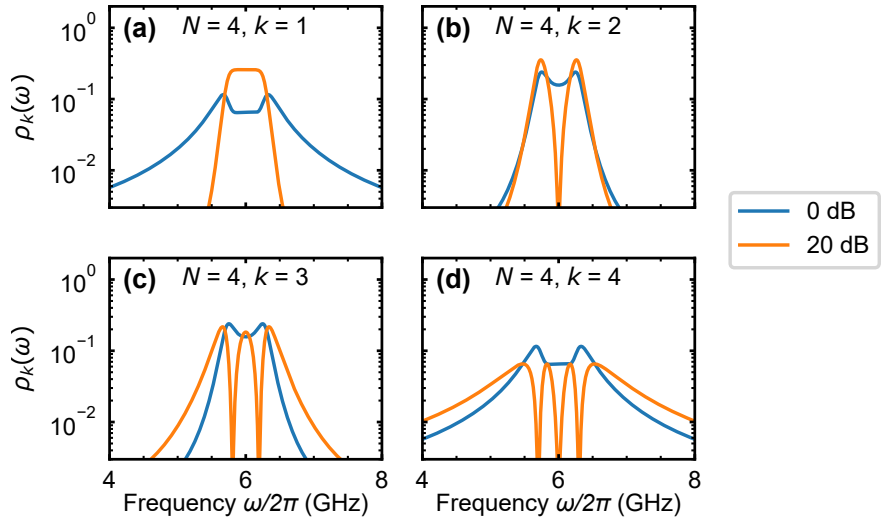

Figure 1.21: Local density of states (LDOS) $\rho_k(\omega)$ for the filter stages $k = 1$ to 4 for $N = 4$ order bandpass filters with 0 dB (blue) and 20 dB (orange) insertion loss. Bandpass filter center frequency $\omega_0/2\pi = 6$ GHz and bandwidth $\Delta\omega/2\pi = 600$ MHz.

by treating the qubit as a resonator (see Section 1.2.4). We find that adding more stages and using larger qubit-resonator detuning gives a longer qubit lifetime. Comparing a 0 dB with a 20 dB insertion loss filter, the higher insertion loss filter affords better protection. We find that for symmetric filters (0 dB insertion loss) with order $N = 2m$ or $N = 2m - 1$, the qubit lifetime T_1 scales as $T_1 \propto \Delta_{qr}^{2m+2}$. For asymmetric filters (large insertion loss) with order N, the qubit lifetime scales as $T_1 \propto \Delta_{qr}^{2N+2}$, consistent with the single-stage bandpass filter $T_1 \propto \Delta_{qr}^4$ [48]. We empirically find that these power law exponents are approximately two times the number of resonators the qubit decays through [115]. To get qubit T_1 over 1 ms, while maintaining large bandwidth ($\Delta\omega = 600$ MHz) and achieving fast readout ($\kappa_r/2\pi = 15$ MHz), we only need a 4-stage filter with large insertion loss (see Fig. 1.22). We present a circuit to realize the bandpass filter as is shown in Fig. 1.20(a). Inductively coupled $\lambda/2$ resonators act as the bandpass filter and the $\lambda/4$ resonator acts as the readout resonator. Note that we have discussed the coupling between a $\lambda/2$ and a $\lambda/4$ resonator in Eqs. 1.92 and 1.93. The related parameters of the circuit are listed in Appendix E and some alternative circuits can be found in Ref. [115]. We also experimentally demonstrate

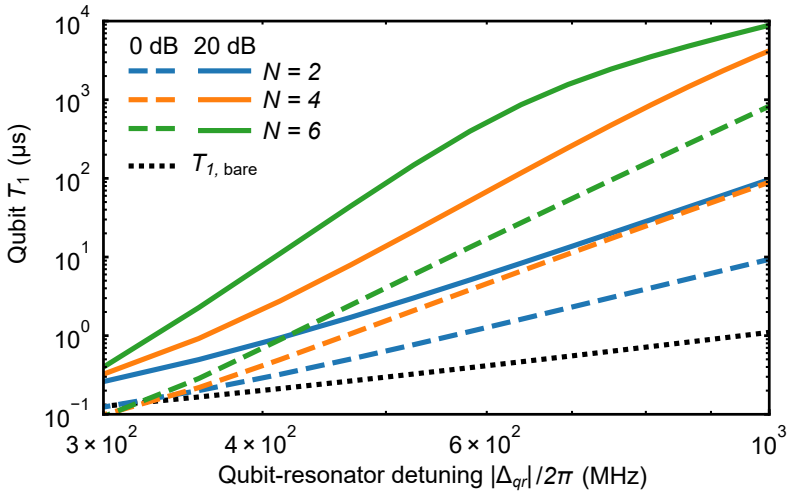

Figure 1.22: Qubit lifetime T_1 versus qubit-resonator detuning Δ_{qr} for bandpass filters with 0 dB (dashed lines) and 20 dB (solid lines) insertion loss. The filter center frequency $\omega_0/2\pi$ is 6 GHz, its bandwidth $\Delta\omega/2\pi$ is 600 MHz, the readout resonator frequency $\omega_r/2\pi$ is 6 GHz, the readout resonator dissipation rate $\kappa_r/2\pi$ is 15 MHz, and the qubit-resonator coupling $c_{qr}/2\pi$ is 100 MHz.

the functionality of these filters with the results shown in Refs. [115, 116].

Other than the filters we discussed above, there are also some novel filters. For example, Ref. [117] introduced an "intrinsic" Purcell filter where they used a $\lambda/4$ resonator as the readout resonator. By engineering the coupling point of the readout resonator, the emission of the qubit mode is suppressed. Ref. [118] introduced a nonlinear Purcell filter where Josephson junctions were added to the filter to dynamically tune the decay rate of the readout resonator κ_r during the measurement by Kerr non-linearity.

The dispersive readout scheme introduced above is commonly used. There also exist other protocols which promise faster readout. Refs. [92, 119] introduced "qubit cloaking", where several drive pulses are applied to the system to pump the readout resonator without disturbing the qubit before the measurement. Ref. [120] proposed to use longitudinal qubit-resonator coupling $\sigma_x(a^\dagger + a)$ to realize fast readout. Note that these novel Purcell filters and readout schemes can be combined with the bandpass filters discussed above to achieve better overall performance.

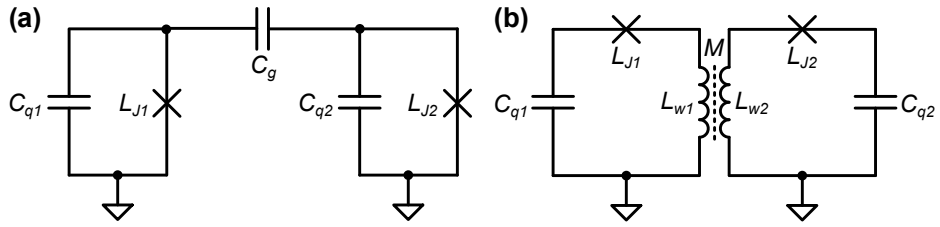

Figure 1.23: Circuits for coupled transmons with (a) capacitive coupling and (d) inductive coupling.

1.4.5 Fixed coupling

The above discussion mainly focuses on the control of single qubits. To realize practical quantum computing, two-qubit gates are necessary. To realize qubit-qubit interaction, we need to couple two transmons. Similar to the resonator-resonator coupling schemes discussed in Section 1.2.2, transmons can also be coupled capacitively or inductively (see Fig. 1.23). The most common way is capacitive coupling as transmons usually have large capacitor pads which make capacitive coupling more convenient [121]. An example of inductive coupling can be found in Ref. [122]. Modeling the Duffing oscillators as in Eq. 1.122, the coupled two-qubit Hamiltonian can be written as

$$H/\hbar = \sum_{j=1,2} \left(\omega_j a_j^\dagger a_j + \frac{\eta_j}{2} a_j^\dagger a_j^\dagger a_j a_j\right) - g(a_1 - a_1^\dagger)(a_2 - a_2^\dagger), \tag{1.148}$$

where $a_j^\dagger$ (a_j) is the creation (annihilation) operator for the jth qubit, ω_j and η_j are frequency and anharmonicity of the jth qubit, and g is their coupling strength. The expression of g can be found in Eqs. 1.20 and 1.24. These kinds of coupling are always on. Thus the nearest-neighbor qubits' frequencies need to be tuned away $|\Delta| = |\omega_1 - \omega_2| \gg g$ so that they will not "see" each other.

When two qubits Q_1 and Q_2 are on resonance, $\omega_1 = \omega_2$, two qubits will exchange their states as is shown in Fig. 1.24(a-b). With a duration of $\tau_{\text{iSWAP}} = \pi/2g$, we can realize an iSWAP gate, while with half of the duration, we can realize a $\sqrt{\text{iSWAP}}$ gate.

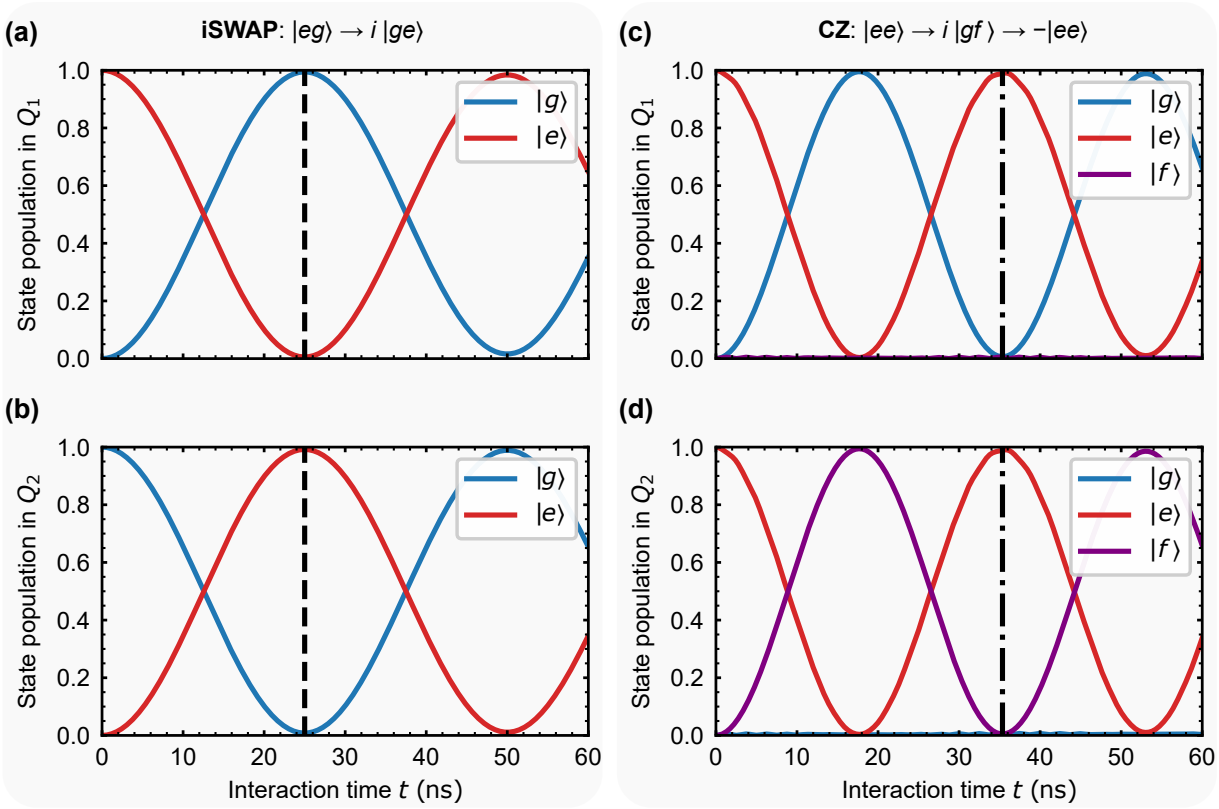

Figure 1.24: Evolution of state populations from numerical simulations for (a-b) iSWAP and (c-d) CZ gates. For the iSWAP gate, two qubits are on resonance, $\omega_1/2\pi = \omega_2/2\pi = 5$ GHz, and initialized in the $|eg\rangle$ state. The dashed line represents the duration of an iSWAP gate. For the CZ gate, $|ee\rangle$ is on resonance with $|gf\rangle$, $\omega_1/2\pi = \omega_2/2\pi + \eta_2/2\pi = 4.8$ GHz, and qubits are initialized in the $|ee\rangle$ state. The dash-dotted line represents the duration of a CZ gate. The qubit anharmonicities $\eta_1/2\pi = \eta_2/2\pi = -200$ MHz, the coupling strength $g/2\pi = 10$ MHz, the qubit lifetimes $T_1 = 10$ μs and dephasing times $T_2 = 2$ μs.

Furthermore, we can realize controlled-Z (CZ) gates with the $|f\rangle$ state. If we bring $|ee\rangle$ on resonance with $|gf\rangle$, the state $|ee\rangle$ will evolve as $|ee\rangle \rightarrow i|gf\rangle \rightarrow -|ee\rangle$, while the other states $|gg\rangle$, $|ge\rangle$ and $|eg\rangle$ will accumulate zero phase. Thus we can realize a CZ gate with a duration of $\tau_{\mathrm{CZ}} = \pi/\sqrt{2}g$. The evolution starting with the state $|ee\rangle$ is shown in Fig. 1.24(c-d). Note that by combining a CZ gate with two single qubit gates, we can construct a controlled-NOT (CNOT) gate.

CZ gates with fidelity over 99% can be achieved with fixed coupling [121]. The fidelity is limited not only by qubit coherence times, and leakage to higher excited states but also by

noisy flux pulses [123]. Although the two-qubit gate fidelity above the surface code threshold can be achieved [121, 13], there exists residual ZZ interaction with this fixed coupling scheme, which comes from the anharmonicity of qubits. The ZZ interaction H_{ZZ} can be written as,

$$H_{ZZ} = \zeta a_1^\dagger a_1 a_2^\dagger a_2. \tag{1.149}$$

With this interaction, the $|ee\rangle$ state will accumulate extra phases during qubit idling times. The ZZ coupling strength ζ can be obtained from the Schrieffer-Wolff transformation (see Appendix C) similar to what we did to get the Hamiltonian of dispersive readout. To the second order of $g/|\Delta|$, the ZZ interaction strength ζ can be written as [121, 124],

$$\zeta = 2g^2 \frac{\eta_1 + \eta_2}{(\Delta + \eta_1)(\Delta - \eta_2)}. \tag{1.150}$$

If $\eta_2 = 0$, we come back to the dispersive shift in Eq. 1.139, $\zeta = -2\chi$, where the factor of -2 comes from the difference between σ_z and $a^\dagger a$. For coupling strength $g/2\pi = 10$ MHz, anharmonicity $\eta/2\pi = -200$ MHz and detuning $\Delta/2\pi = 400$ MHz, the ZZ coupling strength $\zeta/2\pi$ will be around -0.7 MHz, which is not negligible compared with qubit dissipation rates. When two qubits are on resonance, $\Delta = 0$, the ZZ interaction strength $\zeta = -4g^2/\eta$ will be around 2 MHz, which will give unwanted phase accumulation for the iSWAP gate. H_{ZZ} can be further suppressed either by engineered fixed coupling schemes [124] or tunable couplers which we will discuss in Section 1.5.

1.4.6 Benchmarking

Given a device with multiple qubits, we need to characterize these qubits efficiently. In this section, we are going to introduce several methods to benchmark the quantum gates, e.g. quantum process tomography, randomized benchmarking, and cross-entropy benchmarking.

Gate fidelity

Here we start with the definition of gate fidelity. For an arbitrary ideal unitary operation U_i and an actual quantum process $\mathcal{E}(\cdot)$, the gate fidelity $\mathcal{F}_g$ is defined as [125]

$$\mathcal{F}_g = \int \mathrm{d}\psi \langle\psi|U_i^\dagger \mathcal{E}(\psi) U_i|\psi\rangle, \tag{1.151}$$

where the integral satisfies $\int \mathrm{d}\psi = 1$. When $\mathcal{E}(\cdot)$ is also a unitary operation U, i.e. $\mathcal{E}(\psi) = U|\psi\rangle\langle\psi|U^\dagger$, we have [126]

$$\mathcal{F}_g = \frac{1}{d(d+1)}\big(\mathrm{Tr}(MM^\dagger) + |\mathrm{Tr}(M)|^2\big), \tag{1.152}$$

where d is the dimension of the Hilbert space, and M is defined as $M = U_i^\dagger U$. In reality, gate fidelities are mainly limited by qubit relaxation times T_1 and pure dephasing times T_ϕ, where qubit dephasing times satisfy $1/T_2 = 1/2T_1 + 1/T_\phi$. When the quantum process $\mathcal{E}(\cdot)$ operates in the qubit computational space, e.g. single-qubit gates and iSWAP gates, the gate fidelity can be estimated as [127]

$$\mathcal{F}_g = 1 - \frac{d}{2(d+1)}\tau \sum_k \big(\frac{1}{T_{1,k}} + \frac{1}{T_{\phi,k}}\big), \tag{1.153}$$

where τ is the gate duration, d is the dimension of the Hilbert space, and $T_{1,k}$ ($T_{\phi,k}$) is the relaxation (pure dephasing) time of the kth qubit. The above result is up to the first order of τ/T_1 and τ/T_ϕ. For higher-order terms, the gate fidelity $\mathcal{F}_g$ will be gate-dependent. If the qubits leave the computational space during the quantum process $\mathcal{E}(\cdot)$, e.g. CZ gates, Ref. [128] gives an analytical expression of $\mathcal{F}_g$ using T_1, T_ϕ and τ, which is gate-dependent to the first order of τ/T_1 and τ/T_ϕ.

State fidelity

Given a target quantum state described by the density matrix ρ_i, and an actual state described by density matrix ρ, the state fidelity $\mathcal{F}$ of ρ is defined as [129]

$$\mathcal{F} = \left(\mathrm{Tr}\sqrt{\sqrt{\rho_i}\rho\sqrt{\rho_i}}\right)^2. \tag{1.154}$$

The ideal state ρ_i is usually a pure sate which can be written as $\rho_i = |\psi_i\rangle\langle\psi_i|$, the above expression can be simplified to

$$\mathcal{F} = \mathrm{Tr}(\rho_i\rho) = \langle\psi_i|\rho|\psi_i\rangle. \tag{1.155}$$

Quantum state tomography

In experiments, we need to do state tomography to extract the density matrix ρ [125]. For superconducting qubits, the measurement is along the z-axis in the Bloch's sphere. We need to apply a single qubit rotation, e.g. an $X/2$ or $Y/2$ gate before the measurement to rotate the state on the y-axis or x-axis to the z-axis. We apply gates from the set $\{I, X/2, Y/2\}$ to each qubit after state generation, and perform simultaneous readout of all qubits to get the probabilities on different axes. The density matrices directly calculated from these probabilities usually are not physical because of limited readout fidelity. We will use some convex optimization methods to reconstruct the density matrices to constrain them to be physical, i.e. Hermitian, have a unit trace, and positive semi-definite. Note that for an N-qubit system, we need to do $k3^N$ measurements to extract the full density matrix, where k is the repetitions to get each probability. The number of measurements grows exponentially with the number of qubits and does not apply to large systems.

Because of limited readout fidelity, the measured $|e\rangle$ state probability P_e^M for a single qubit ranges from $[1 - F_g, F_e]$, where F_g and F_e are assigned probability for $|g\rangle$ and $|e\rangle$

states described in Section 1.4.4. One trick is to stretch the range from $[1-F_g, F_e]$ to $[0,1]$, which is called the readout correction [126]. Assuming the measured state probabilities are $\widetilde{\mathbf{P}} = [\widetilde{P}_g, \widetilde{P}_e]^T = [1-\widetilde{P}_e, \widetilde{P}_e]^T$, the corrected state probabilities are $\mathbf{P} = [P_g, P_e] = \mathbf{F^{-1}}\widetilde{\mathbf{P}}$, where $\mathbf{F}$ is defined as

$$\mathbf{F} = \begin{bmatrix} F_g & 1-F_e \\ 1-F_g & F_e \end{bmatrix}. \tag{1.156}$$

For multiple qubits, we can just tensor their individual $\mathbf{F}$-matrix, or we can directly measure their total $\mathbf{F}$-matrix in case of interference of simultaneous readout between different qubits. Although this trick is widely used in the field of superconducting qubits, it assumes $\widetilde{\mathbf{P}} = \mathbf{FP}$, which is not strictly correct.

Quantum process tomography

Quantum process tomography, as its name implies, is the tomography of a quantum process, which can be qubit decay, quantum gates, etc. A general quantum process $\mathcal{E}(\cdot)$ can be described using Kraus decomposition [125], which is

$$\mathcal{E}(\rho) = \sum_i K_i \rho K_i^\dagger, \tag{1.157}$$

where $\{K_i\}$ are called Kraus operators, which satisfy

$$\sum_i K_i^\dagger K_i = I. \tag{1.158}$$

To describe an arbitrary quantum process, we usually choose a fixed set of operators $\{E_i\}$. Eq. 1.157 can be written as

$$\mathcal{E}(\rho) = \sum_{m,n=0}^{d^2-1} \chi_{mn} E_m \rho E_n^\dagger, \tag{1.159}$$

where d is the dimension of the system and χ is the quantum process matrix. The process matrix χ contains d^4-d^2 independent real parameters. For single qubit process tomography, $\{E_i\}$ can be chosen as $\{I, X, -iY, Z\}$. The process matrix χ can be expressed as

$$\chi = \Lambda \begin{bmatrix} \rho'_1 & \rho'_2 \\ \rho'_3 & \rho'_4 \end{bmatrix} \Lambda, \tag{1.160}$$

where $\Lambda = \frac{1}{2}\begin{bmatrix} I & X \\ X & -I \end{bmatrix}$, $\rho'_i = \mathcal{E}(\rho_i)$, with $\rho_1 = |0\rangle\langle 0|$, $\rho_2 = \rho_1 X$, $\rho_3 = X\rho_1$ and $\rho_4 = X\rho_1 X$. In experiments, we prepare different initial states $|\psi_{\text{ini}}\rangle$ by applying gates from the set $\{I, X, X/2, Y/2\}$, which gives the states $|0\rangle = |g\rangle$, $|1\rangle = |e\rangle$, $|+\rangle = (|g\rangle + |e\rangle)/\sqrt{2}$ and $|i\rangle = (|g\rangle + i|e\rangle)/\sqrt{2}$. Then we apply the quantum process $\mathcal{E}(\cdot)$ to these initial states and extract the final states $\mathcal{E}(|\psi_{\text{ini}}\rangle\langle\psi_{\text{ini}}|)$ with state tomography. From the measurement results, we can determine ρ'_i in the process matrix χ,

$$\rho'_1 = \mathcal{E}(|0\rangle\langle 0|), \tag{1.161}$$

$$\rho'_4 = \mathcal{E}(|1\rangle\langle 1|), \tag{1.162}$$

$$\rho'_2 = \mathcal{E}(|+\rangle\langle +|) + i\mathcal{E}(|i\rangle\langle i|) - (1+i)(\rho'_1 + \rho'_4)/2, \tag{1.163}$$

$$\rho'_3 = \mathcal{E}(|+\rangle\langle +|) - i\mathcal{E}(|i\rangle\langle i|) - (1-i)(\rho'_1 + \rho'_4)/2, \tag{1.164}$$

with which we can extract the process matrix χ for a single qubit operation. For two-qubit operations, we choose the $\{E_i\}$ as $\{I, X, -iY, Z\} \otimes \{I, X, -iY, Z\}$ and the process matrix χ can also be determined from the final states similar as the single qubit case. The process fidelity $\mathcal{F}_p$ is defined as

$$\mathcal{F}_p = \text{Tr}(\chi_{\text{ideal}}\chi), \tag{1.165}$$

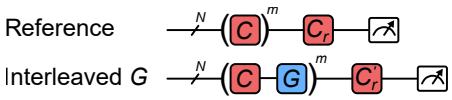

Figure 1.25: Quantum circuits for randomized benchmarking (RB) of N qubits. The reference circuit is shown on the top, with m random Clifford gates C and a recovery Clifford gate C_r which rotates all the qubits to the ground states. The bottom circuit is the circuit for the interleaved gate G, where G is inserted in each cycle. Their difference gives the fidelity of gate G.

where χ_{ideal} is the ideal process matrix. The process fidelity $\mathcal{F}_p$ is related to the gate fidelity $\mathcal{F}_g$ as [130],

$$\mathcal{F}_g = \frac{1 + d\mathcal{F}_p}{1 + d}, \tag{1.166}$$

where d is the dimension of the Hilbert space. Like quantum state tomography, the precision of quantum process tomography is limited by readout and state preparation errors. For an N-qubit operation, we need $k12^N$ measurements to get the full χ matrix, where k is the repetitions to get each probability.

Randomized benchmarking (RB)

Quantum process tomography gives all the information of a quantum operation. However, its performance is limited by readout and state preparation errors. For the state-of-the-art superconducting quantum processors, the gate errors (around 10^{-3} to 10^{-4}) are far below the readout and reset errors (around 10^{-2}). Thus we need to find some benchmarking protocols that are insensitive to readout errors. One example is randomized benchmarking (RB), which was first introduced in Ref. [131] and experimentally demonstrated in Ref. [132].

The quantum circuits for RB are shown in Fig. 1.25. We first prepare the qubits in the ground states, which can be done by leaving the qubits to decay. Then we apply random gates C chosen from the Clifford group for m cycles. Finally, we apply a recovery gate C_r to rotate all the qubit states back to ground states. Because the combination or inverse of any Clifford gates is still a Clifford gate, C_r will still be a Clifford gate. Ideally, if all the gates

are perfect, the probability of the qubit measured in ground states will not change as we increase the number of cycles m. However, because gate errors accumulate, the probability measured in ground states will decay as,

$$P_{\text{ref}}(m) = Ap_{\text{ref}}^m + B, \tag{1.167}$$

where p_{ref} is the sequence fidelity as well as the depolarization fidelity per cycle, and A and B are limited by readout fidelities. For perfect readout and reset, we have $A = 1 - 1/d$ and $B = 1/d$, where d is the dimension of the Hilbert space. Note that to get $P_{\text{ref}}(m)$, we need to choose different random gate sequences and average them out to depolarize the noise. The sequence fidelity p_{ref} gives an average error per Clifford gate e_{ref} as

$$e_{\text{ref}} = \frac{d-1}{d}(1 - p_{\text{ref}}). \tag{1.168}$$

To extract the gate fidelity of a specific Clifford gate G, we interleave the gate G in each cycle and apply a recovery pulse C_r' to rotate the qubits to ground states (see Fig. 1.25). The measured ground states probability decays faster as

$$P_{\text{gate}}(k) = Ap_{\text{gate}}^m + B, \tag{1.169}$$

from which we can get the gate error of G, $e_{\text{gate}} = 1 - \mathcal{F}_g$, as

$$e_{\text{gate}} = \frac{d-1}{d}\Big(1 - \frac{p_{\text{gate}}}{p_{\text{ref}}}\Big). \tag{1.170}$$

We only need the sequence decay rate p to extract the gate fidelity, thus RB is robust to readout errors. Ref. [133] compared quantum process tomography with RB and found that RB predicts the gate errors more precisely.

For a single qubit, there are 24 Clifford gates, and all of them can be constructed from

Figure 1.26: Quantum circuit for cross-entropy benchmarking (XEB) of N qubits, with m random gates R applied.

the set of single qubit rotations $\{I, X, Y, X/2, Y/2, -X/2, -Y/2\}$. For two qubits, there are 11520 Clifford gates and all of them can be constructed with the single qubit rotations and the two-qubit CZ gate [121].

Cross-entropy benchmarking (XEB)

RB is limited to Clifford gates only, while cross-entropy benchmarking (XEB) works for an arbitrary gate. XEB was first introduced to demonstrate the quantum supremacy [134, 135]. The quantum circuit for XEB is shown in Fig. 1.26. The qubits are initialized in ground states, then we apply m random gates. The result state ρ_m will be

$$\rho_m = p^m \rho_{\text{ideal},m} + \frac{1}{d}(1 - p^m) I, \tag{1.171}$$

where p is the depolarization fidelity per cycle, the same as the sequence fidelity per cycle in RB. Finally, we perform the measurements and get the probability $P_{\text{exp}}(x)$ of different bit strings x. Then the problem becomes estimating p^m from $P_{\text{exp}}(x)$. Note that we know what random gates we apply, so we can directly calculate $\rho_{\text{ideal},m}$ and get the probability measured in bit string x, $P_{\text{ideal}}(x)$, in the ideal case. Multiply the matrix $\text{diag}(P_{\text{ideal}}(0), P_{\text{ideal}}(1), \cdots, P_{\text{ideal}}(d-1))$ on both sides of the Eq. 1.171 and take the trace, we have

$$\sum_{x=0}^{d-1} P_{\text{ideal}}(x) P_{\text{exp}}(x) = p^m \sum_{x=0}^{d-1} P_{\text{ideal}}^2(x) + \frac{1}{d}(1 - p^m). \tag{1.172}$$

We can do a linear fit between $\left(\sum_x P_{\text{ideal}}(x) P_{\text{exp}}(x)\right) - 1/d$ and $\left(\sum_x P_{\text{ideal}}^2(x)\right) - 1/d$ with different m-cycle sequences to get an estimation of p^m, written as $p_{\text{est}}(m)$. Then for different cycles m, we can get p by fitting $p_{\text{est}}(m)$ and m. The average gate error e per cycle can be

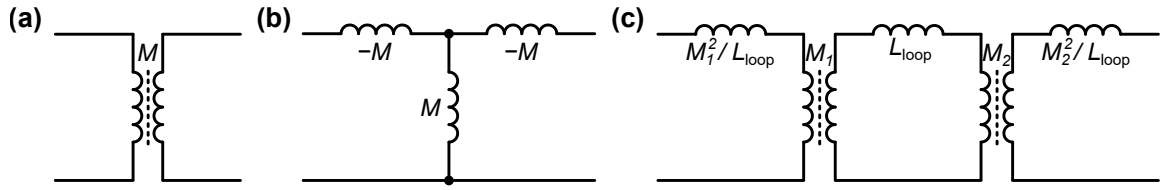

Figure 1.27: (a) Inductively coupled circuit, (b) the equivalent T-circuit with a shared inductor M, and (c) another equivalent circuit with an extra loop with $M = M_1 M_2 / L_{\text{loop}}$.

calculated the same as RB, $e = (1-p)(1-1/d)$. Similar to the interleaved RB, we can also do an interleaved XEB to get the gate error for an interleaved gate. Ref. [135] used both RB and XEB to benchmark their gates, and the results are consistent. Note that RB can be treated as a special case of XEB. With the recovery gate in RB, the ideal density matrix becomes $\rho_{\text{ideal},m} = |0\rangle\langle 0|$, then we have $P_{\text{ideal}}(0) = 1$ and Eq. 1.172 becomes Eq. 1.167.

1.5 Tunable coupler

With qubits (transmons) and quantum channels (transmission lines), we are ready to build a superconducting quantum network. However, the fixed coupling limits the functionality of the quantum network. In this section, we are going to introduce two types of couplers based on how they are coupled to the qubits, which can be used to realize tunable qubit-qubit or qubit-channel interactions.

1.5.1 Inductive coupler

A Josephson junction can be treated as a non-linear inductor, which is tunable by changing the flux through a loop (e.g. a SQUID loop) containing it. It is natural to start with a tunable mutual inductive coupling.

Before we start, it is better to introduce some equivalent inductively coupled circuits (see Fig. 1.27), which can help us simplify the circuits. For two circuits coupled with mutual inductance M shown in Fig. 1.27(a), it can be transformed to a T-circuit with a shared

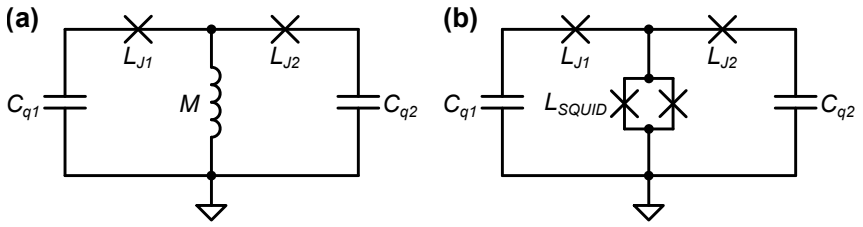

Figure 1.28: Circuits for inductively coupled transmons with a shared (a) inductor and (b) SQUID.

inductor M as is shown in Fig. 1.27(b), which can be verified by Kirchhoff's circuit laws, similar as what we did in Eq. 1.37. Furthermore, we can introduce an extra loop coupled to two circuits which can mediate inductive coupling between two circuits (see Fig. 1.27(c)). The effective mutual inductance M between the left and right circuits can be obtained from Kirchhoff's circuit laws,

$$M = \frac{M_1 M_2}{L_{\text{loop}}}. \tag{1.173}$$

Looking at the coupled transmons with inductive coupling in Fig. 1.23(b), we can directly transform it to a circuit in Fig. 1.28(a) using the transformation introduced in Fig. 1.27(b). A simple way to realize tunable coupling is to replace the shared inductor M in Fig. 1.28(a) with a SQUID as is shown in Fig. 1.28(b). The SQUID can be treated as a tunable inductor, with equivalent inductance $L_{\text{SQUID}} = L_J/2|\cos(\phi_{\text{ext}}/2)|$ when it is symmetric, where L_J is the Josephson inductance for one junction and $\phi_{\text{ext}} = 2\pi\Phi_{\text{ext}}/\Phi_0$, with Φ_{ext} the external flux across the SQUID loop. However, L_{SQUID} cannot be set to zero, which means that the coupling cannot be turned off. Examples using this kind of tunable coupler can be found in Refs. [80, 136]. This coupler also requires a galvanic connection to the shared tunable inductor (SQUID), limiting its application.

Fig. 1.27(c) introduced a loop, where we can put a Josephson junction in the loop as is shown in Fig. 1.29(a). This circuit can be further transformed by replacing the mutual inductors with shared inductors, which gives the circuit shown in Fig. 1.29(b). This kind of coupler was first introduced in Ref. [137], where they called it gmon. For the following

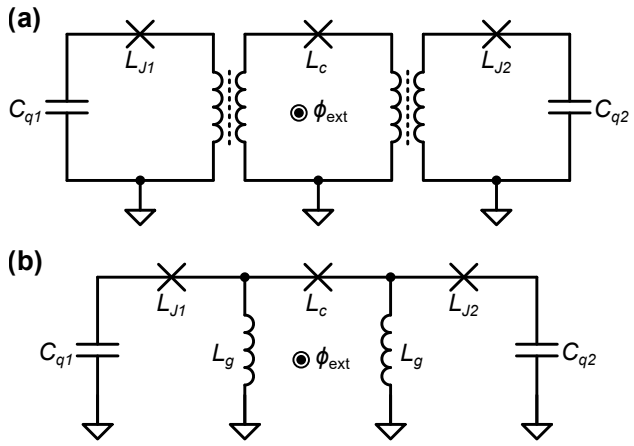

Figure 1.29: Circuits for transmons coupled with a gmon.

discussion, we will focus on the gmon circuit in Fig. 1.29(b).

In the gmon circuit, we can directly write down the effective mutual inductance M_{eff} between two transmons from Eq. 1.173,

$$M_{\text{eff}} = \frac{L_g^2}{2L_g + L_c/\cos\delta}, \tag{1.174}$$

where δ is the phase difference across the coupler junction, L_c is the Josephson inductance of the coupler junction, and L_g is the linear inductance to ground. If we consider some stray wiring inductance L_w in series with the coupler junction [77], the effective mutual inductance M_{eff} needs to be modified as

$$M_{\text{eff}} = \frac{L_g^2}{2L_g + L_w + L_c/\cos\delta}. \tag{1.175}$$

With the effective mutual inductance M_{eff}, we can directly write down the coupling strength g between two qubits using Eq. 1.24,

$$g = \frac{\sqrt{\omega_{q1}\omega_{q2}}}{2} \frac{M_{\text{eff}}}{\sqrt{(L_{J1} + L_g)(L_{J2} + L_g)}}. \tag{1.176}$$

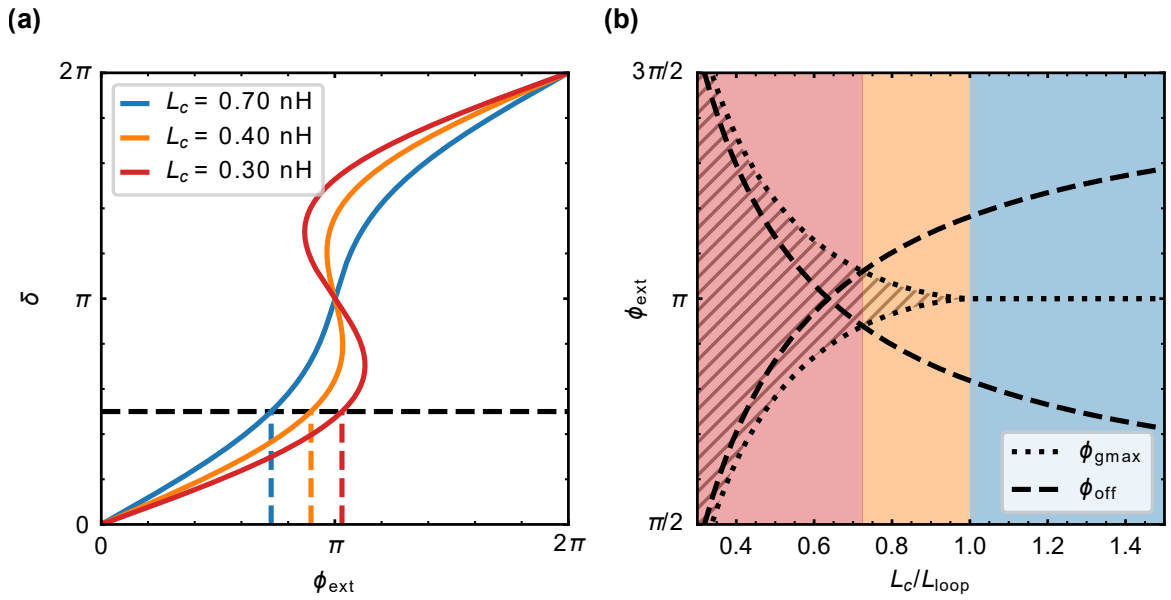

Figure 1.30: (a) Junction phase δ versus external phase ϕ_{ext}. Dashed lines show the coupling off points. (b) ϕ_{gmax} (dotted lines) and ϕ_{off} (dashed lines) versus L_c/L_{loop}, where L_{loop} is defined as $2L_g + L_w$. Here we already extract the regime with multiple solutions of δ. The red regime is where the coupler cannot be turned off, the orange regime is where the coupler can be turned off but exists a regime with multiple solutions of δ, and the blue regime is where the coupler can work at any ϕ_{ext}.

When the two qubits are identical, we have

$$g = \frac{\omega_q}{2} \frac{L_g}{L_J + L_g} \frac{L_g}{2L_g + L_w + L_c/\cos\delta}. \tag{1.177}$$

The external phase through the coupler loop $\phi_{\text{ext}} = 2\pi\Phi_{\text{ext}}/\Phi_0$ is related to junction phase difference δ as [138]

$$\delta + \frac{2L_g + L_w}{L_c} \sin\delta = \phi_{\text{ext}}. \tag{1.178}$$

The junction phase difference δ versus external phase ϕ_{ext} is shown in Fig. 1.30(a). For $L_c > 2L_g + L_w$, there is always a solution for δ for a given ϕ_{ext}. When $L_c < 2L_g + L_w$, there are some regimes where multiple δ exist for a given ϕ_{ext}, which comes from the neglect of the junction self-capacitance. For this kind of singularity, readers can refer to Refs. [139, 140] for more discussion. We will try to avoid such regimes in experiments. The zero coupling

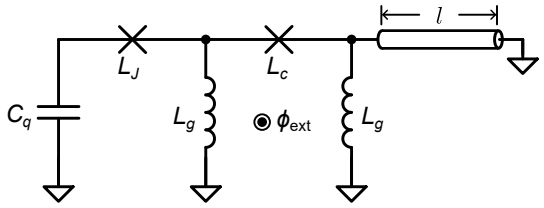

Figure 1.31: Circuit for a transmon coupled to a transmission line with a gmon.

point ϕ_{off} is at $M_{\text{eff}} = 0$, which satisfies

$$\phi_{\text{off}} \bmod 2\pi = \Big(\frac{\pi}{2} + \frac{2L_g + L_w}{L_c}, \frac{3\pi}{2} - \frac{2L_g + L_w}{L_c}\Big). \tag{1.179}$$

The maximum coupling point ϕ_{gmax} is at

$$\phi_{\text{gmax}} \bmod 2\pi = \pi. \tag{1.180}$$

When $L_c < 2L_g + L_w$, because of the existence of multiple solutions, we cannot reach the ϕ_{gmax} points. When $L_c < 0.725(2L_g + L_w)$, we cannot reach ϕ_{off}, which means we cannot turn the coupler off when the coupler junction L_c is too small. The fluxes ϕ_{off} and ϕ_{gmax} versus $L_c/(2L_g + L_w)$ are shown in Fig. 1.30(b). The maximum coupling strength $g_{\max}$ is

$$g_{\max} = \frac{\omega_q}{2} \frac{L_g}{L_J + L_g} \frac{L_g}{2L_g + L_w - L_c}. \tag{1.181}$$

Introducing the coupler will change the qubit frequency. The frequency shift $\Delta\omega_q$ can be calculated as

$$\Delta\omega_q = \frac{1}{\sqrt{(L_J + L_g - M_{\text{eff}})C_q}} - \frac{1}{\sqrt{(L_J + L_g)C_q}} \simeq g. \tag{1.182}$$

The gmon can also be used to couple a transmon to a transmission line [141, 142]. The circuit is shown in Fig. 1.31. The inductive coupler only couples the series modes in the transmission line. For the transmission line with a short end, the effective RLC for its nth series mode can be found in Table 1.2. For the nth mode, its frequency $\omega_n = n\omega_{\text{FSR}}$, where

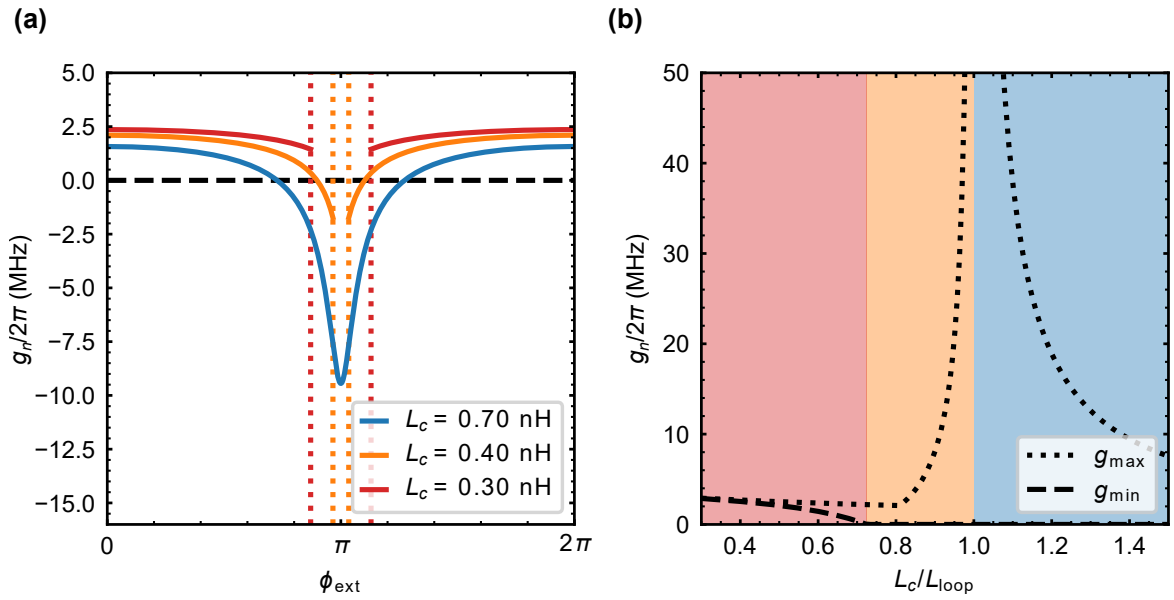

Figure 1.32: (a) Coupling strength g_n between the qubit and the transmission line mode changes as external phase ϕ_{ext} for different L_c. Dotted lines label the regime with multiple solutions of δ. (b) Maximum and minimum coupling strength $|g_n|$ for different L_c/L_{loop}, where L_{loop} is defined as $2L_g + L_w$. The different regimes are the same as Fig. 1.30. The related parameters are $\omega_q/2\pi = \omega_n/2\pi = 5.0$ GHz, $\omega_{\text{FSR}}/2\pi = 50$ MHz, $L_n = \pi Z_0/2\omega_{\text{FSR}} = 250$ nH, $L_g = 0.2$ nH, $L_w = 0.1$ nH, $L_J = 11$ nH, $C_q = 90$ fF.

$\omega_{\text{FSR}} = \pi v_p/l$ is the free spectrum range (FSR), and its effective inductance $L_n = n\pi Z_0/2\omega_n$, where Z_0 is the characteristic impedance of the transmission line. The coupling strength between the nth mode and qubit can directly be written down as

$$g_n = \frac{\sqrt{\omega_n \omega_q}}{2} \frac{M_{\text{eff}}}{\sqrt{(L_J + L_g)(L_n + L_g)}}. \tag{1.183}$$

The coupling strength g_n versus external flux ϕ_{ext} is shown in Fig. 1.32(a), where we assume $\omega_q = \omega_n$. The regime of $L_c < 2L_g + L_w$ is not plotted. We also show the maximum coupling strength $g_{\max}$ and minimum coupler strength $g_{\min}$ for different coupler junction inductance L_c in Fig. 1.32(b).

In the infinitely long line limit, $L_n \to \infty$, $g_n \to 0$, and $\omega_{\text{FSR}} \to 0$. The qubit is coupled to multiple modes, so the meaningful physical quantity is the decay rate κ into the long

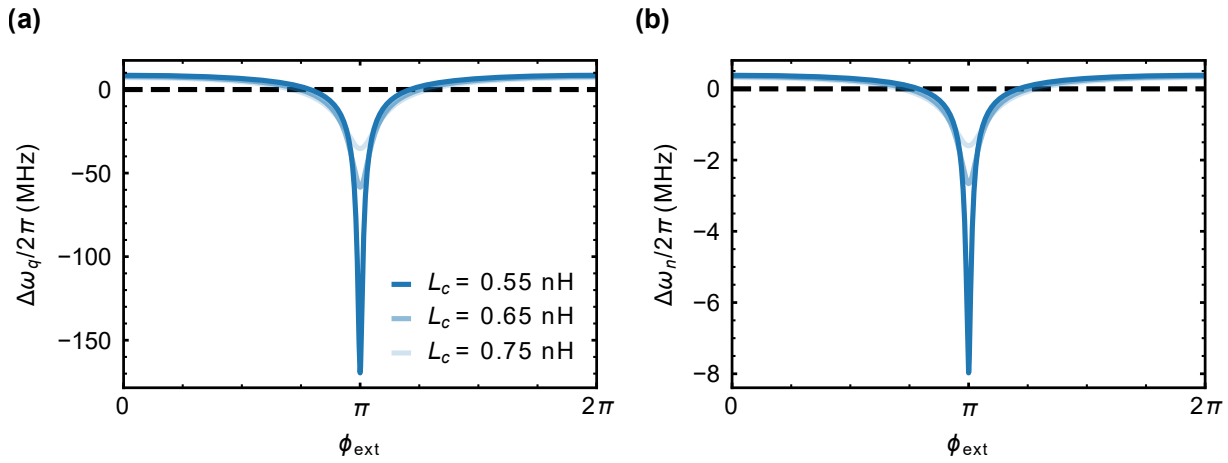

Figure 1.33: (a) Qubit and (b) transmission line mode frequency shift for different L_c. The related parameters are $\omega_q/2\pi = \omega_n/2\pi = 5.0$ GHz, $\omega_{\text{FSR}}/2\pi = 50$ MHz, $L_n = \pi Z_0/2\omega_{\text{FSR}} = 250$ nH, $L_g = 0.2$ nH, $L_w = 0.1$ nH, $L_J = 11$ nH, $C_q = 90$ fF.

transmission line, which can be determined by Fermi's golden rule,

$$\kappa = 2\pi g_n^2 \rho(\omega_q) = 2\pi \frac{g_n^2}{\omega_{\text{FSR}}} \simeq \frac{2\omega_q^2}{Z_0} \frac{M_{\text{eff}}^2}{L_J + L_g}, \tag{1.184}$$

where $\rho(\omega_q) = 1/\omega_{\text{FSR}}$ is the density of states at the qubit frequency ω_q. This expression is the same as the dissipation rate directly derived from Eq. 1.41, which is only related to the characteristic impedance of the transmission line Z_0 but not the length of the transmission line. As in the infinitely long line limit, the qubit cannot know what is happening on the other end.

The qubit frequency shift $\Delta\omega_q$ and the nth mode frequency shift $\Delta\omega_n$ can be calculated similar to Eq. 1.182,

$$\Delta\omega_q \simeq g_n \sqrt{\frac{\omega_q}{\omega_n}} \sqrt{\frac{L_n + L_g}{L_J + L_g}}, \tag{1.185}$$

$$\Delta\omega_n \simeq g_n \sqrt{\frac{\omega_n}{\omega_q}} \sqrt{\frac{L_J + L_g}{L_n + L_g}}. \tag{1.186}$$

The qubit frequency shift $\Delta\omega_q$ is much larger than the transmission line mode frequency

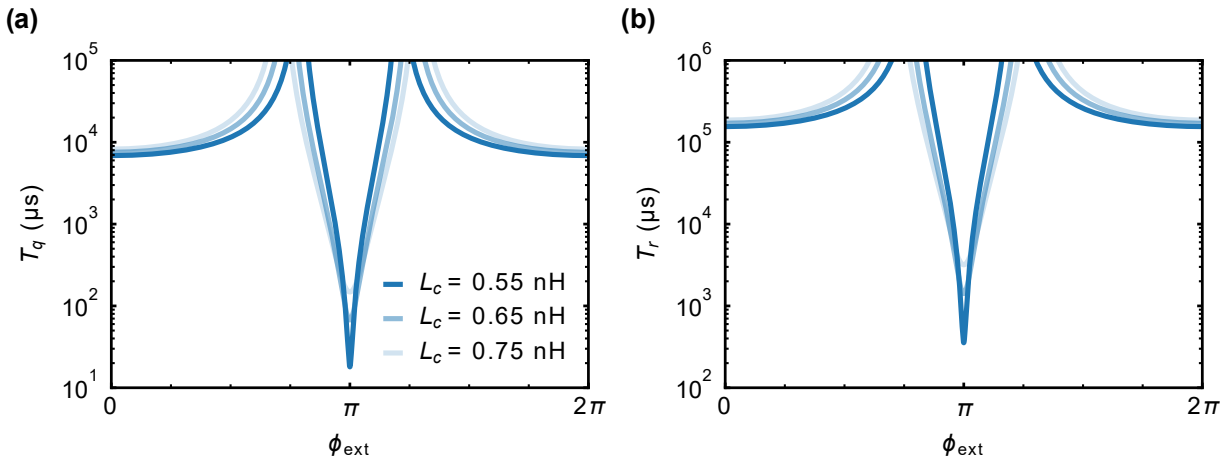

Figure 1.34: (a) Qubit lifetime T_q and (b) transmission line mode lifetime T_r limited by the coupler bias line changes as external flux ϕ_{ext} for different L_c. The related parameters are $\omega_q/2\pi = \omega_n/2\pi = 5.0$ GHz, $\omega_{\text{FSR}}/2\pi = 50$ MHz, $L_n = \pi Z_0/2\omega_{\text{FSR}} = 250$ nH, $L_g = 0.2$ nH, $L_w = 0.1$ nH, $L_J = 11$ nH, $C_q = 90$ fF, $M_g = 1.5$ pH, where M_g is the mutual inductance between the coupler bias line and the coupler loop.

shift $\Delta\omega_n$ because $L_n \gg L_J$ for long transmission lines (see Fig. 1.33). The qubit frequency shift $\Delta\omega_q$ can be compensated by an extra z-pulse when the coupler is turned on. There are crosstalks between the gmon bias line and the qubit SQUID, and also between the qubit z-bias line and the gmon loop in the experiment, which can be corrected by modifying the flux pulses we send.

To tune ϕ_{ext}, a bias line needs to be introduced, which will damp the qubit similar to the qubit z-bias line introduced in Section 1.4.2. The qubit lifetime T_q limit and the transmission line mode lifetime T_r limit are shown in Fig. 1.34, where $T_r \gg T_q$ because $L_n \gg L_J$. To overcome this limit, extra filtering circuits can be added to the coupler bias line [143]. When designing the filtering circuits, we need to be careful about the possible resonances that might be introduced.

In Chapters 2 and 3, we will use gmons to couple transmon qubits to transmission lines acting as quantum communication channels to build superconducting quantum networks.

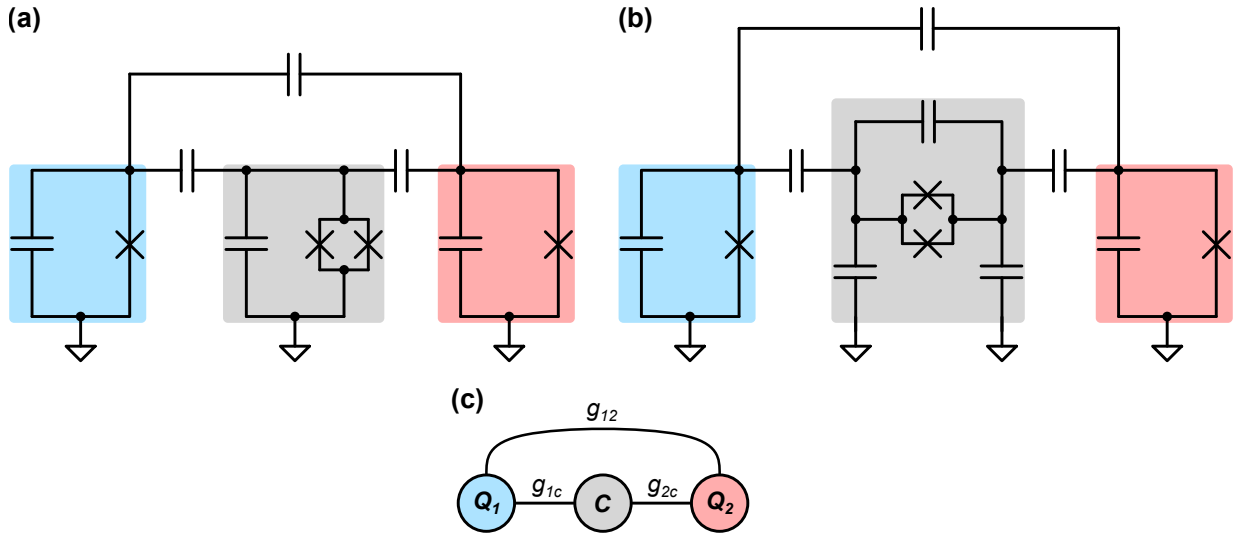

Figure 1.35: Circuits for capacitive couplers with a (a) grounded transmon and (b) floating transmon as the coupler to couple two transmon qubits, and (c) their coupled-mode representation.

1.5.2 Capacitive coupler

Inductive couplers can realize CZ gates with fidelity over 99% [137]. However, it is hard to couple multiple qubits to one qubit with inductive couplers (two at most [144, 145], otherwise the crosstalk will be too large). Capacitive coupling is more convenient as transmons can be designed to have large-size capacitors for coupling. The tunable element we have in hand is the junction, a tunable inductor. One way to realize such a capacitive coupler is to use a tunable transmon acting as a tunable resonator bus [146] which mediates the coupling between two transmon qubits. This scheme was first introduced in Refs. [147, 148] and experimentally demonstrated in Ref. [149].

The scheme for this kind of coupler is shown in Fig. 1.35. Here we assume all the transmon qubits are grounded [74] for simplicity. The circuit introduced in Ref. [148] is shown in Fig. 1.35(a), where the coupler is also a grounded transmon. An alternative circuit is to make the coupler floating [150, 151, 38] as is shown in Fig. 1.35(b). Both circuits can be quantized and we can get the total Hamiltonian H by modeling the transmons as Duffing

oscillators as in Eq. 1.122,

$$H/\hbar = \sum_{i=\{1,2,c\}} \omega_i a_i^\dagger a_i + \frac{\eta_i}{2} a_i^\dagger a_i^\dagger a_i a_i + \sum_{i=\{1,2\}} g_{ic}(a_i^\dagger a_c + a_c^\dagger a_i) + g_{12}(a_1^\dagger a_2 + a_2^\dagger a_1), \quad (1.187)$$

where ω_i is the frequency for the ith qubit or coupler, η_i is the corresponding anharmonicity, and g_{ij} is the coupling strength between the ith qubit/coupler and the jth qubit/coupler. RWA has been applied. When the detuning between and the ith qubit and the coupler Δ_{ic} is much larger than their coupling strength g_{ic}, i.e. $|\Delta_{ic}| \gg |g_{ic}|$, we can do Schrieffer-Wolff transformation (see Appendix C) to block-diagonalize the total Hamiltonian. If we ignore the nonlinear terms in H, the Schrieffer-Wolff transformation unitary U can be simply chosen as

$$U = \exp \sum_{i=1,2} \frac{g_{ic}}{\Delta_{ic}} (a_i^\dagger a_c - a_c^\dagger a_i), \quad (1.188)$$

with which we can get the effective coupling strength g_{eff} between the two dressed qubit modes,

$$g_{\text{eff}} = g_{12} + \frac{g_{1c} g_{2c}}{2} \Big(\frac{1}{\Delta_{1c}} + \frac{1}{\Delta_{2c}} \Big). \quad (1.189)$$

The first term is the direct coupling between two qubits and the second term comes from the virtual exchange of photons with the coupler mode [146]. For the circuit in Fig. 1.35(a), both qubits are coupled to the same pad of the coupler, the couplings g_{1c} and g_{2c} have the same sign, $g_{1c} g_{2c} > 0$. When we tune the coupler frequency above the qubit, i.e. $\Delta_{ic} < 0$, we can find a frequency to fully turn off the coupling. While for the circuit in Fig. 1.35(b), qubits are coupled to different pads of the coupler, which gives different signs for g_{1c} and g_{2c}, $g_{1c} g_{2c} < 0$. In this case, the coupler frequency needs to be set below the qubit frequency to turn off the coupling. More details on the quantization of the full circuits, higher-order corrections, and ZZ interactions can be found in Refs. [148, 149, 150, 151, 152].

This capacitive coupler can also be used to couple a transmon qubit to a transmission

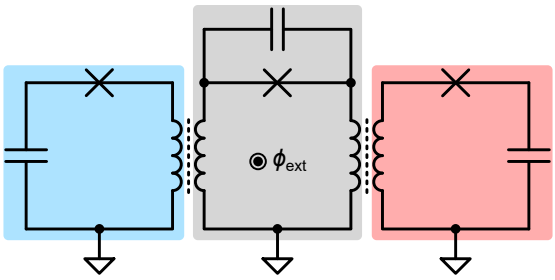

Figure 1.36: Circuit for gmon with coupler junction capacitance.

line, in which case, the coupler works as a transfer resonator between the qubit and the transmission line [32, 40, 41].

If we consider the self-capacitance of the coupler junction in the gmon circuit (see Fig. 1.36), the function of gmon can be understood similar to this capacitive coupler, i.e. the coupler mode mediates the coupling between two qubits [147]. The gmon coupler can be viewed as a capacitively-shunted rf-SQUID. When the coupler junction inductance is smaller than the loop linear inductance, the gmon coupler works similarly as a fluxonium qubit [153].

This kind of capacitive coupler has been widely used to demonstrate high-fidelity two-qubit gates [135, 154, 155, 156]. The coupler has also been used to couple multiple qubits to realize selective two-qubit gates [157] and multi-qubit gates [158]. Many of its variants have been reported [159, 160, 161, 162, 163, 164]. In Chapter 4, we will extend the circuit in Fig. 1.35(b) to realize tunable all-to-all connectivity between four transmon qubits.

1.6 Summary

In this chapter, we discussed the building blocks of superconducting quantum networks, including transmon qubits as quantum processing units, transmission lines as quantum communication channels, and tunable couplers for qubit-qubit and qubit-channel couplings. In the following chapters, we will integrate these elements to build quantum networks from two nodes to four nodes, following the fabrication process introduced in Appendix G and measuring them with the setup described in Appendix H.

CHAPTER 2
ENTANGLEMENT PURIFICATION IN A TWO-NODE NETWORK

2.1 Introduction

In Chapter 1, we give an introduction to the building blocks of superconducting quantum networks. Starting with this chapter, we are going to build the networks and present the experiments run on these setups.

In this chapter, we introduce a two-node network, where two quantum processors are connected by a 1-meter-long superconducting coaxial cable [35]. We demonstrate entanglement generation between two nodes and use the entanglement purification protocol to distill the entangled states to higher fidelities [165]. In addition, we use both dynamical decoupling and Rabi driving to protect the entangled states from local noise, increasing the effective qubit dephasing times.

2.2 Experimental setup

An overview of the experimental setup is shown in Fig. 2.1, with a schematic in Fig. 2.1(a) and a full circuit in Fig. 2.1(b). The system comprises two quantum network nodes A and B, where each node includes three capacitively-coupled transmon qubits Q_i^k ($i = 1, 2, 3$; $k = A, B$). Qubits $Q_3^{A,B}$ are not used in the following experiments. The central qubit Q_2^k in each node is directly coupled to a 1-meter-long niobium-titanium (NbTi) superconducting coaxial cable via a gmon coupler G^k. The cable is connected to the coupler by aluminum (Al) wirebonds. The packaged sample is shown in Fig. 2.2. More details can be found in Ref. [35]. The measurement setup can be found in Appendix H.

We first turn off the couplers and benchmark the qubits. The qubit parameters are listed

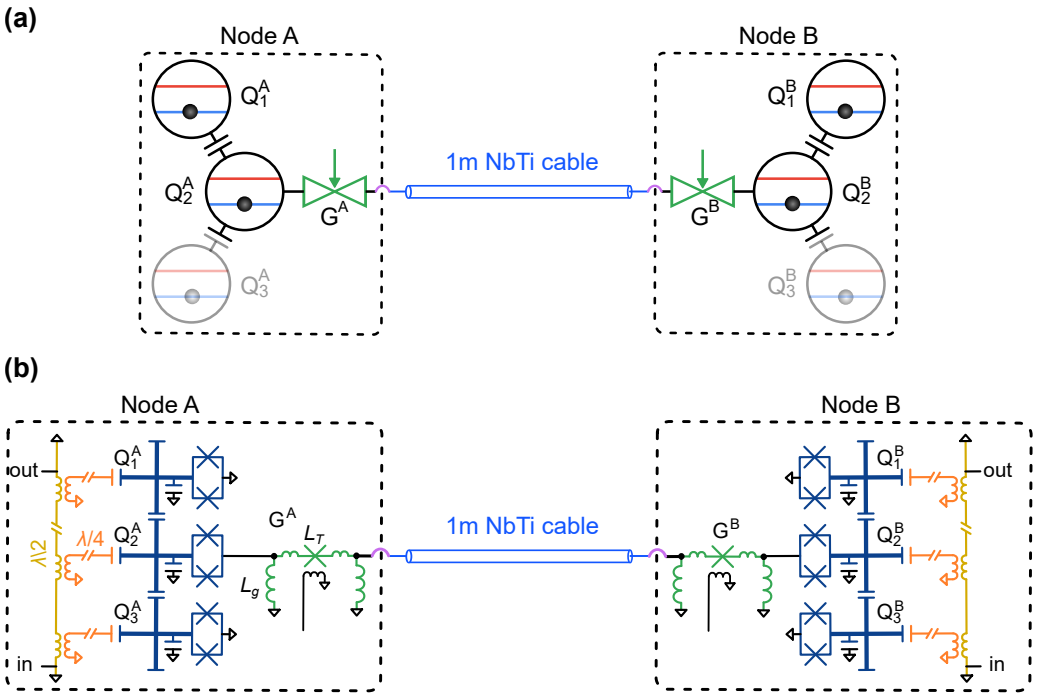

Figure 2.1: Overview of the two-node network: (a) schematic and (b) circuit. The network comprises two nodes A and B, each with three capacitively-coupled transmon qubits. The center qubit in each node is connected to a 1-meter-long superconducting NbTi coaxial cable through a tunable coupler. Each qubit is measured by a $\lambda/4$ readout resonator which is further coupled to a single-stage bandpass Purcell filter.

in Table 2.1. The qubits each have a relaxation time of $T_1 \approx 10$ μs and dephasing time $T_2 \approx 3$ μs.

We use randomized benchmarking (RB) to characterize the single qubit gate performance (see Section 1.4.6). Our single-qubit π gate duration is 30 ns and $\pi/2$ gate duration is 20 ns, for all rotation axes, with gate durations optimized to balance qubit lifetime with state leakage. To minimize the effect of the second excited state $|f\rangle$, we use a DRAG correction for all our single qubit gates [81]. We get an average single qubit RB gate fidelity of 99.8%.

We tune the frequency of our qubits to implement iSWAP and CZ gates as we discussed in Section 1.4.5. To swap an excitation between Q_1^k and Q_2^k in the same node, we bring Q_1^k and Q_2^k on resonance. At $\tau_{\text{iSWAP}} = \pi/2g_{12}^k \approx 15$ ns ($k = A, B$), we complete the $|eg\rangle \rightarrow i|ge\rangle$ process, which forms a iSWAP gate. To measure the efficiency of the iSWAP gate, we first

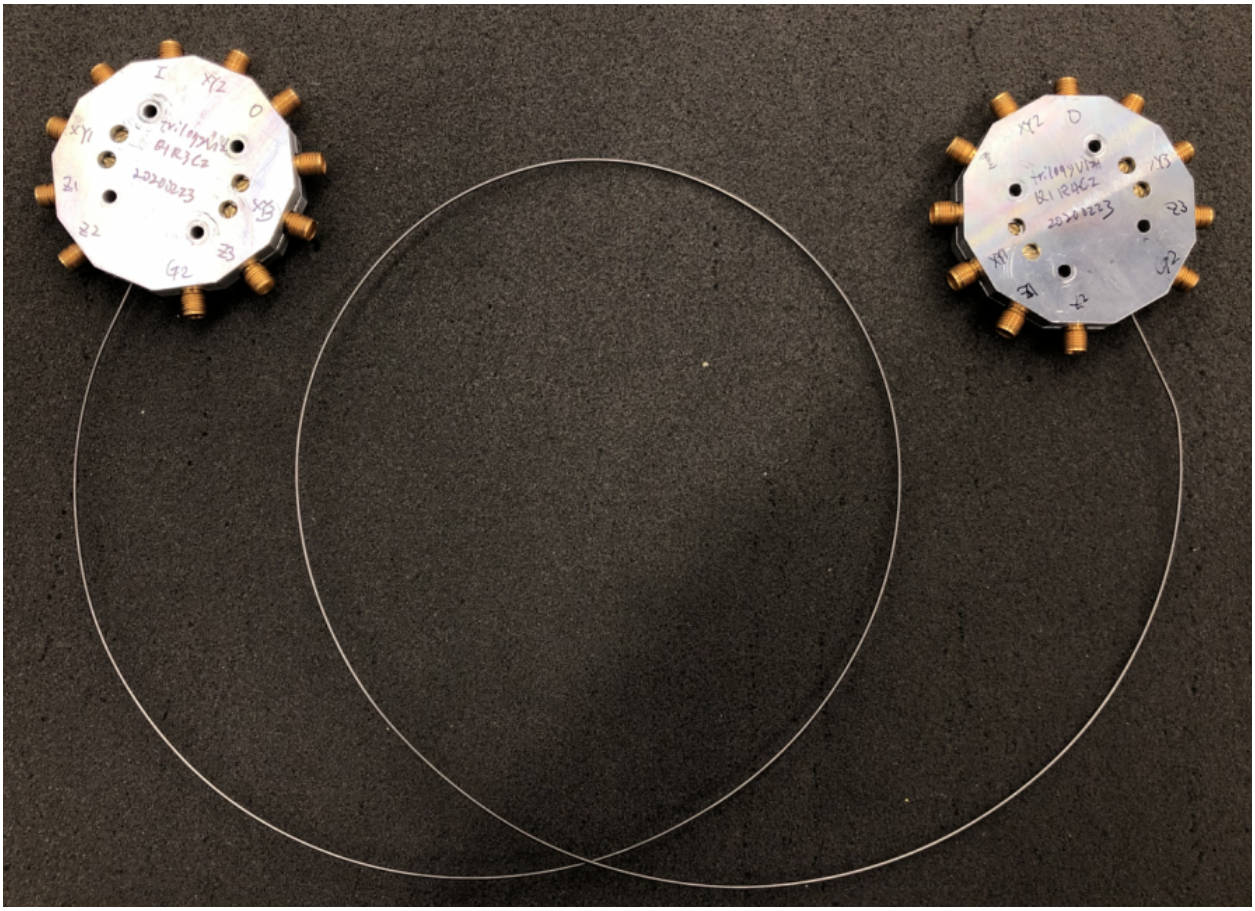

Figure 2.2: Photo of the two-node network, adapted from Ref. [35].

rotate Q_2^k to $|e\rangle$ and measure the excited state population P_e. Next, with Q_2^k in $|g\rangle$, we prepare Q_1^k in $|e\rangle$, then swap the excitation to Q_2^k, followed by a measurement of P_e for Q_2^k. Comparing the resulting P_e in the two experiments, we find a swap efficiency of $\sim 99\%$.

To implement a CZ gate between Q_1^k and Q_2^k, we bring $|ee\rangle$ and $|gf\rangle$ on resonance as we discussed in Section 1.4.5. When $|ee\rangle$ is on resonance with $|gf\rangle$, the two-qubit state will evolve as $|ee\rangle \rightarrow i|gf\rangle \rightarrow -|ee\rangle$, yielding a CZ gate in a time $\tau_{\mathrm{CZ}} \approx 21$ ns. To characterize the gate performance, we perform process tomography (see Section 1.4.6) to obtain the process χ matrix of the CZ gate. To overcome the issue of dynamical phase accumulated during the CZ gate, here we directly tune the phase of the tomography pulses to get the right CZ gate process χ matrix. We find process fidelities $\mathcal{F}_p$ for the CZ gate between Q_1^A–Q_2^A and

	Q_1^A	Q_2^A	Q_3^A	Q_1^B	Q_2^B	Q_3^B
$\omega_q/2\pi$	5.256 GHz	5.870 GHz	5.506 GHz	5.302 GHz	5.890 GHz	5.322 GHz
$\eta/2\pi$	−230 MHz	−150 MHz	−230 MHz	−230 MHz	−150 MHz	−230 MHz
T_1	8.9 μs	5.7 μs	6.3 μs	22.1 μs	9.2 μs	21.1 μs
T_ϕ	1.8 μs	3.1 μs	2.5 μs	2.2 μs	3.0 μs	1.8 μs
$\omega_r/2\pi$	6.605 GHz	6.550 GHz	6.503 GHz	6.506 GHz	6.556 GHz	6.608 GHz
τ_r	350 ns	450 ns	300 ns	400 ns	600 ns	350 ns
F_g	96.8%	97.4%	96.2%	98.8%	96.5%	98.3%
F_e	94.0%	92.7%	92.6%	93.6%	93.9%	93.9%

Table 2.1: Qubit parameters: the qubit operating frequency is ω_q; the qubit anharmonicity is η; the qubit lifetime and pure dephasing time at the operating point are T_1 and T_ϕ; the readout resonator frequency is ω_r; the readout pulse duration is τ_r; and the readout fidelities of $|g\rangle$ and $|e\rangle$ states are F_g and F_e.

Q_1^B–Q_2^B of $95.93\% \pm 0.64\%$ and $95.05\% \pm 0.68\%$, respectively. With two $\pi/2$ single qubit gates and a CZ gate, we can implement a CNOT gate.

The coaxial cable has a free spectral range $\omega_{\mathrm{FSR}}/2\pi = 105$ MHz, which is the frequency of its $\lambda/2$ resonance. We use the qubits to benchmark the communication channel. We first excite the qubit Q_2^A, then turn on the coupler G^A to coupling strength $g/2\pi = 4.3$ MHz while tuning the qubit into resonance with the 5.806 GHz communication mode ($L_n \sim 121$ nH); the other coupler is left off. The pulse sequence can be found in the inset of Fig. 2.3(a). The coupler junction is around $L_T \approx 0.62$ nH. The coupler has other linear inductance $2L_g = 0.4$ nH and $L_w = 0.1$ nH (see Eq. 1.175). We can observe vacuum Rabi oscillations between the qubit Q_2^A and the communication mode as is shown in Fig. 2.3(a). We also perform the same measurement on the qubit Q_2^B side with the results shown in Fig. 2.3(b). Numerical simulations show that the qubit T_1 and T_ϕ are shortened to around 2 μs and 1 μs respectively, likely due to losses associated with the wire-bond connection [35].

To characterize this mode, we first prepare Q_2^B in $|e\rangle$ and swap the excitation to the cable, leave the excitation in the cable mode for a time t, and then swap it back to Q_2^B to measure the remnant excitation, shown in Fig. 2.4. The swap duration used for this measurement is 30 ns. The measured T_{1r} is 477.3 ± 8.1 ns, corresponding to a quality factor $Q = 1.7 \times 10^4$.

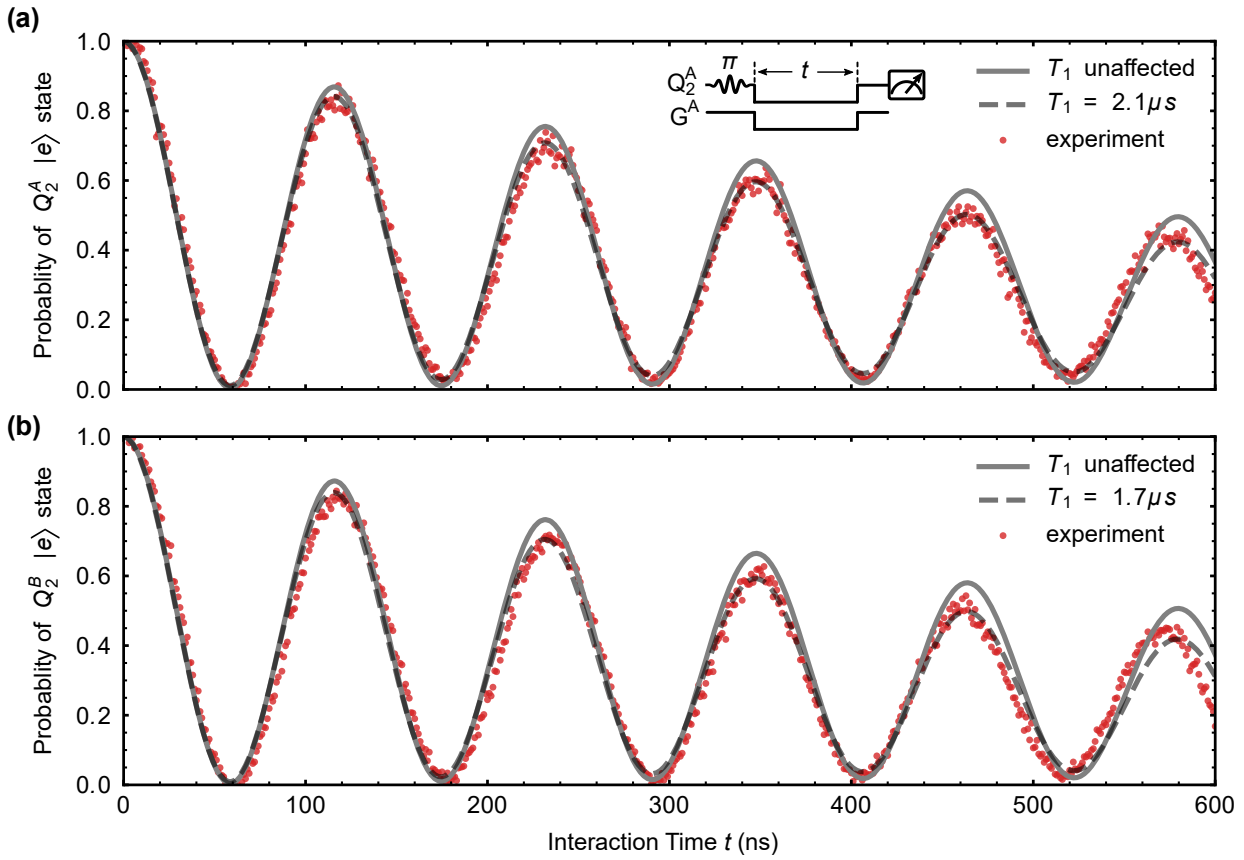

Figure 2.3: Vacuum Rabi oscillations between the 5.806 GHz communication mode and the qubit (a) Q_2^A and (b) Q_2^B. Red circles are experimental data, gray lines are numerical simulations with T_1 in Table 2.1. Grey dashed lines are numerical simulations with shortened T_1, which implies that T_1 is affected by the coupling strength between the qubit and cable.

The full Hamiltonian of our system in the rotating frame can be written using the following multi-qubit, multi-mode communication channel model:

$$\begin{aligned} H/\hbar = &\sum_{i=1,2,3}^{k=A,B} \Delta\omega_i^k a_i^{k\dagger}\sigma_i^k + \sum_{m=1}^{M}\left(m - \frac{M+1}{2}\right)\omega_{\mathrm{FSR}} b_m^\dagger b_m \\ &+ \sum_{j=1,3}^{k=A,B} g_{j,2}^k (a_2^k a_j^{k\dagger} + a_2^{k\dagger} a_j^k) \\ &+ \sum_{m=1}^{M} g_m^A (a_2^A b_m^\dagger + a_2^{A\dagger} b_m) + \sum_{m=1}^{M} (-1)^m g_m^B (a_2^B b_m^\dagger + a_2^{B\dagger} b_m), \end{aligned} \tag{2.1}$$

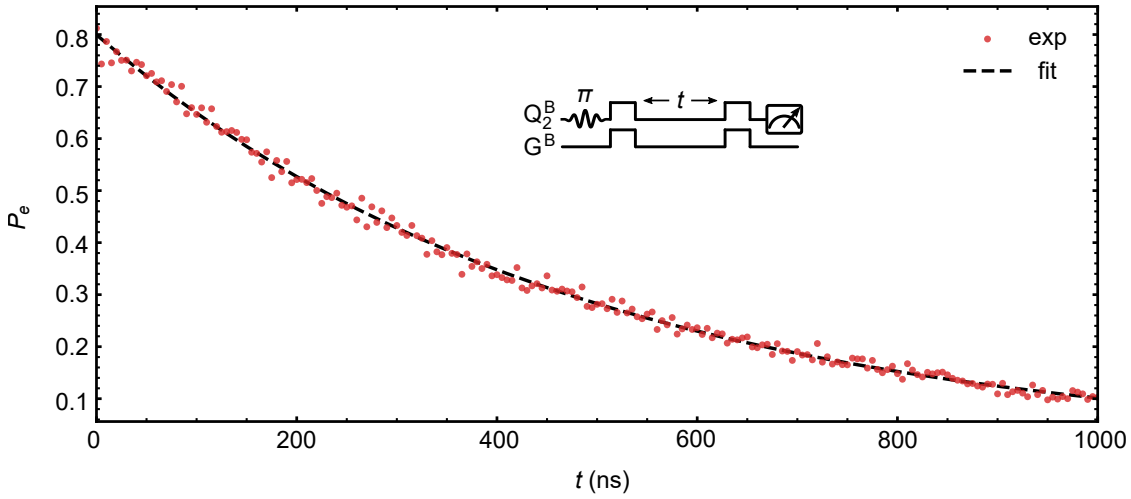

Figure 2.4: Lifetime measurement of the 5.806 GHz communication mode.

where a_i^k and b_m are the annihilation operators for qubit Q_i^k and the mth cable mode respectively, $\Delta\omega_i^k$ is the qubit frequency detuning to the rotating frame frequency, M is the number of standing modes considered in the simulation, ω_{FSR} is free spectral range of the cable modes, $g_{j,2}^k$ is the coupling strength between Q_j^k and Q_2^k, and g_m^k is the coupling strength between Q_2^k and the mth cable mode. The rotating frame frequency is set to the frequency of the communication mode. The sign of g_m^B alternates with the mode number m due to the parity dependence of the standing wave modes. We will use the above Hamiltonian and measured qubit and channel coherence times to simulate the system dynamics.

2.3 Entanglement generation

In Fig. 2.5, we display the deterministic generation of a Bell state distributed between nodes A and B. Using the tunable coupler, we swap a "half-photon" from Q_2^A to Q_2^B with the communication mode C as an intermediate bus. The pulse sequence is shown inset in Fig. 2.5(a), where we first apply a π pulse to bring Q_2^A from its ground state $|g\rangle$ to its first excited state $|e\rangle$, then turn on Q_2^A's coupler G^A to coupling strength $g^A/2\pi = 4.3$ MHz while tuning Q_2^A into resonance with the communication mode C. The swap time for a full

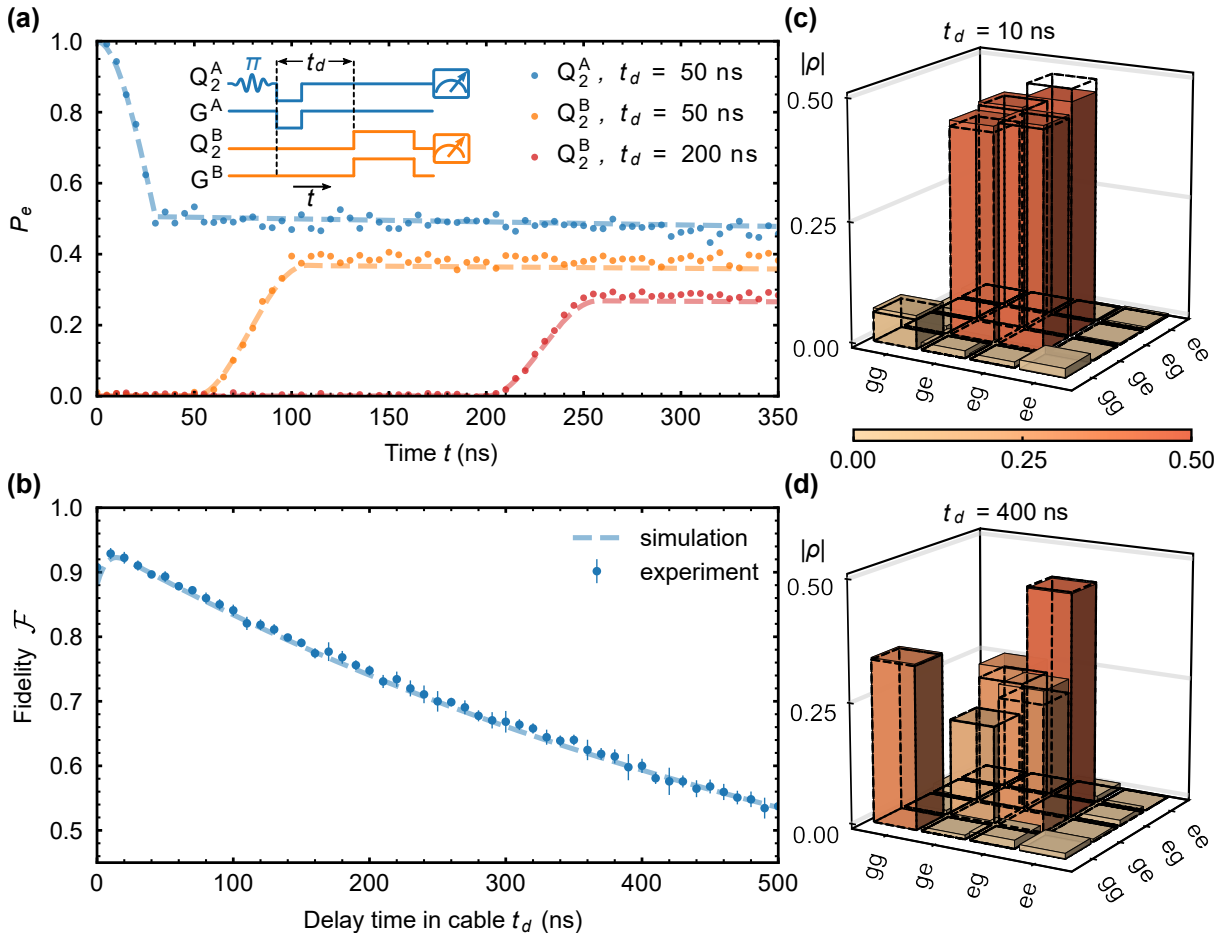

Figure 2.5: Deterministic Bell state generation. (a) Inset: Pulse sequence for Bell state generation, including the delay time t_d that the excitation resides in the communication mode C. Main plot shows $|e\rangle$ state population P_e in Q_2^A (blue), and in Q_2^B for different delay times in the cable $t_d = 50$ ns (orange) and $t_d = 200$ ns (red). (b) Bell state fidelity $\mathcal{F}$ as a function of delay time t_d. (c) Bell state tomography for $t_d = 10$ ns and (d) $t_d = 400$ ns. Blue dashed lines in (b) and (b), and dashed outline boxes in (c) and (d), are results from numerical simulations.

photon emission ($|e0g\rangle \rightarrow i|g1g\rangle$, representing states as $|Q_2^A C Q_2^B\rangle$) is $\sim$ 60 ns. Here we turn on the coupling for 30 ns, which swaps a half-excitation to the cable mode (ideally, $|e0g\rangle \rightarrow (|e0g\rangle + i|g1g\rangle)/\sqrt{2}$). We then turn off the coupler G^A and after a time delay t_d, set G^B's coupling strength to $g^B/2\pi = 4.3$ MHz while tuning Q_2^B into resonance with the communication mode. After a 60 ns full swap, this generates a Bell state between Q_2^A and Q_2^B, ideally $|\psi^-\rangle = (|eg\rangle - |ge\rangle)/\sqrt{2}$ (writing the two-qubit state as $|Q_2^A Q_2^B\rangle$). In Fig. 2.5(a)

we show the excited state probability for Q_2^B for two different delay times, $t_d = 50$ ns (orange) and 200 ns (red), along with Q_2^A (blue). These data clearly show the reduction in Q_2^B's excited state probability P_e with delay time t_d.

In Fig. 2.5(b), we display the effect of the delay time in the cable t_d on the Bell state fidelity $\mathcal{F}$, defined as $\mathcal{F} = \langle\psi^-|\rho|\psi^-\rangle$, displaying the two-qubit density matrix ρ measured using state tomography (see Section 1.4.6). Numerical simulations (dashed blue line) are in good agreement with the measurements. In Fig. 2.5(c-d) we show the measured density matrices for the time delays $t_d = 10$ ns and $t_d = 400$ ns. For the data in Fig. 2.5(c), the measured fidelity to the ideal Bell state is $\mathcal{F} = 92.89 \pm 0.85\%$, close to the numerical simulation result $\mathcal{F}^{\text{sim}} = 92.01\%$. The data indicate that the dominant infidelity is due to damping errors ($|1\rangle \rightarrow |0\rangle$) in the cable, which increase with delay time in the cable, with a much smaller contribution from phase errors in the qubits $(|g\rangle + |e\rangle)/\sqrt{2} \leftrightarrow (|g\rangle - |e\rangle)/\sqrt{2}$. Damping results in a larger $|\text{Tr}(\rho|gg\rangle\langle gg|)|$ component in the density matrix, while phase decoherence yields smaller off-diagonal terms in ρ. From the data at delay $t_d = 400$ ns, we estimate that $\sim 94\%$ percent of the infidelity is due to damping errors ($\sim 82\%$ from cable loss and $\sim 12\%$ from qubit decay) and $\sim 6\%$ percent is due to qubit dephasing.

2.4 Entanglement purification

Amplitude damping of the microwave photons limits the fidelity of the entangled pairs. Here we demonstrate the use of an entanglement purification protocol [166] to correct these errors. Entanglement purification via distillation has been demonstrated in linear optics [167, 168, 169, 170], as well as with trapped ions [171] and defects in diamond [172]. In superconducting qubits, mitigating the photon loss in a communication channel has been achieved using adiabatic methods [142] as well as through error-correctable qubits [173]. In contrast to adiabatic protocols which require remote synchronization [174, 142], purification protocols can achieve near unit-fidelity Bell states using only local operations. The purifica-

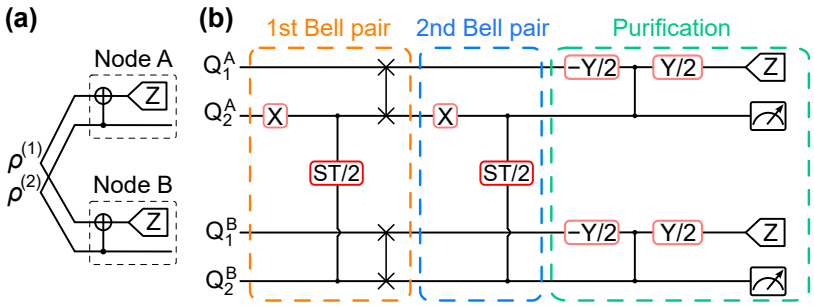

Figure 2.6: Entanglement purification. (a) Circuit schematic. (b) Experimental realization of the purification circuit in (a). The ST/2 process is a "half-photon" transfer process as in Fig. 2.5(a). We prepare the first Bell pair $|Q_2^A Q_2^B\rangle$ followed by swaps into $|Q_1^A Q_1^B\rangle$. We then generate the second Bell pair in $|Q_2^A Q_2^B\rangle$ and purify using these two pairs.

tion performance should be similar to protocols using error-correctable qubits, but with no additional requirements for intricate qubit encoding and quantum non-demolition measurements [175, 173]. Here we show that amplitude damping errors can be effectively corrected by a purification protocol including measurement and post-selection.

The purification circuit is shown in Fig. 2.6(a), where two impure Bell pairs $\rho^{(1)}$ and $\rho^{(2)}$ are created between the two nodes, which serve as the source ($\rho^{(1)}$) and target pairs ($\rho^{(2)}$). Parallel CNOT gates are performed between the qubits in each node, followed by Z measurements of the source pair $\rho^{(1)}$, using the measurement results to post-select from $\rho^{(2)}$. The result is a purified Bell pair ρ_f with a higher fidelity to the purification target state $|\psi^+\rangle = (|eg\rangle + |ge\rangle)/\sqrt{2}$ [166]. In the following, we will discuss how this purification circuit acts on different noise sources.

The four Bell states $|\psi^\pm\rangle$, $|\phi^\pm\rangle$ are

$$|\psi^\pm\rangle = \frac{1}{\sqrt{2}}(|eg\rangle \pm |eg\rangle), \tag{2.2}$$

$$|\phi^\pm\rangle = \frac{1}{\sqrt{2}}(|gg\rangle \pm |ee\rangle). \tag{2.3}$$

The ideal Bell state via cable-mediated entanglement is $|\psi^-\rangle$,

$$\rho_{\text{ideal}} = |\psi^-\rangle\langle\psi^-| = \frac{1}{2}\begin{bmatrix} 0 & 0 & 0 & 0 \\ 0 & 1 & -1 & 0 \\ 0 & -1 & 1 & 0 \\ 0 & 0 & 0 & 0 \end{bmatrix}. \tag{2.4}$$

For a bit-flip error channel with error probability p, the process is represented by the operators

$$E_0 = \sqrt{1-p}I, \tag{2.5}$$

$$E_1 = \sqrt{p}X. \tag{2.6}$$

If we assume only one qubit suffers from a bit-flip error, the final state will be

$$\rho = \mathcal{E}(\rho) = \sum_i I \otimes E_i \cdot \rho_{\text{ideal}} \cdot I \otimes E_i^\dagger = (1-\frac{p}{2})|\psi^-\rangle\langle\psi^-| + \frac{p}{2}|\phi^-\rangle\langle\phi^-|, \tag{2.7}$$

with a fidelity $\mathcal{F} = 1 - p/2$. After applying the bit-purification circuit shown in Fig. 2.6(a), the final state fidelity will be

$$\mathcal{F}' = \frac{\mathcal{F}^2}{\mathcal{F}^2 + (1-\mathcal{F})^2}, \tag{2.8}$$

with post-selection of $|gg\rangle$ or $|ee\rangle$.

For a phase-flip error channel, the process is represented by

$$E_0 = \sqrt{1-p}I, \tag{2.9}$$

$$E_1 = \sqrt{p}Z. \tag{2.10}$$

If we again assume only one qubit suffers from a phase-flip error, the final state will be

$$\rho = \mathcal{E}(\rho) = \sum_i I \otimes E_i \cdot \rho_{\text{ideal}} \cdot I \otimes E_i^\dagger = (1 - \frac{p}{2})|\psi^-\rangle\langle\psi^-| + \frac{p}{2}|\psi^+\rangle\langle\psi^+|, \tag{2.11}$$

with a final state fidelity $\mathcal{F} = 1 - p/2$, where $|\psi^+\rangle = (|eg\rangle + |ge\rangle)/\sqrt{2}$. The phase-purification circuit shown in Fig. 2.9(b) acts similarly to the bit-flip purification circuit.

Considering an amplitude-damping error channel, the channel representation is

$$E_0 = \begin{bmatrix} 1 & 0 \\ 0 & \sqrt{1-p} \end{bmatrix}, \tag{2.12}$$

$$E_1 = \begin{bmatrix} 0 & \sqrt{p} \\ 0 & 0 \end{bmatrix}. \tag{2.13}$$

Assuming only one qubit suffers an amplitude-damping error, the final state will be

$$\begin{aligned} \rho &= \sum_i I \otimes E_i \cdot \rho_{\text{ideal}} \cdot I \otimes E_i^\dagger \\ &= \frac{1+\sqrt{1-p}}{2}|\psi^-\rangle\langle\psi^-| + \frac{1-\sqrt{1-p}}{2}|\psi^+\rangle\langle\psi^+| + \frac{p}{2}(|gg\rangle\langle gg| - |ge\rangle\langle ge|) \\ &= \frac{1}{2}\begin{bmatrix} p & 0 & 0 & 0 \\ 0 & 1-p & -\sqrt{1-p} & 0 \\ 0 & -\sqrt{1-p} & 1 & 0 \\ 0 & 0 & 0 & 0 \end{bmatrix}, \end{aligned} \tag{2.14}$$

with fidelity

$$\mathcal{F} = \frac{2 - p + 2\sqrt{1-p}}{4} \sim 1 - \frac{p}{2}. \tag{2.15}$$

Applying the bit-purification circuit with post-selection of the $|gg\rangle$ state, the final state and

its fidelity will be

$$\rho' = \frac{1}{2(1-p+p^2)} \begin{bmatrix} p^2 & 0 & 0 & 0 \\ 0 & (1-p)^2 & 1-p & 0 \\ 0 & 1-p & 1 & 0 \\ 0 & 0 & 0 & 0 \end{bmatrix}, \tag{2.16}$$

$$\mathcal{F}' = \frac{(2-p)^2}{4(1-p+p^2)} \sim 1 - \frac{3p^2}{4}, \tag{2.17}$$

with a success rate $(1-p+p^2)/2$, and only part of damping errors are corrected. If we do the post-selection with the $|ee\rangle$ state, the final state and its fidelity will be

$$\rho' = |\psi^+\rangle\langle\psi^+|, \tag{2.18}$$

$$\mathcal{F}' = 1, \tag{2.19}$$

with a success rate of $(1-p)/2$ and all the damping errors are corrected.

If we consider both phase and amplitude-damping errors, the state before purification can be written as

$$\rho = (1-\epsilon_p)|\psi^-\rangle\langle\psi^-| + \epsilon_p|\psi^+\rangle\langle\psi^+| + \epsilon_d(|gg\rangle\langle gg| - |ge\rangle\langle ge|), \tag{2.20}$$

$$\mathcal{F} = 1 - \frac{\epsilon_d}{2} - \epsilon_p. \tag{2.21}$$

After applying the bit-purification circuit with post-selection of $|gg\rangle$, the final state will be

$$\rho' = \frac{1}{2(1-2\epsilon_d+4\epsilon_d^2)} \begin{bmatrix} 4\epsilon_d^2 & 0 & 0 & 0 \\ 0 & (1-2\epsilon_d)^2 & (1-2\epsilon_p)^2 & 0 \\ 0 & (1-2\epsilon_p)^2 & 1 & 0 \\ 0 & 0 & 0 & 0 \end{bmatrix}, \tag{2.22}$$

$$\mathcal{F}' = \frac{1-\epsilon_d-2\epsilon_p+\epsilon_d^2+2\epsilon_p^2}{1-2\epsilon_d+4\epsilon_d^2} \tag{2.23}$$

with a success rate $0.5-\epsilon_d+2\epsilon_d^2$ and non-zero ground state population $2\epsilon_d^2/(1-2\epsilon_d+4\epsilon_d^2)$. If we do the post-selection of $|ee\rangle$, the final state will be

$$\rho' = (1-\epsilon_p')|\psi^+\rangle\langle\psi^+| + \epsilon_p'|\psi^-\rangle\langle\psi^-|, \tag{2.24}$$

$$\epsilon_p' = \frac{2\epsilon_p-2\epsilon_p^2-\epsilon_d}{1-2\epsilon_d}, \tag{2.25}$$

$$\mathcal{F}' = 1-\epsilon_p' \cong 1+\epsilon_d-2\epsilon_p, \tag{2.26}$$

with a success rate $0.5-\epsilon_d$ and zero ground state population. Here we focus on the measurement result $|ee\rangle$, where the damping error is fully corrected and purification yields higher Bell state fidelities than the $|gg\rangle$ measurement result.

We implement the purification process as shown in Fig. 2.6(b). After generating the first Bell pair, shared between the two nodes in $|Q_2^A Q_2^B\rangle$, we apply two parallel iSWAP gates that transfer the state to $|Q_1^A Q_1^B\rangle$, with an efficiency over 99%. We then generate the second Bell pair in $|Q_2^A Q_2^B\rangle$ using the same sequence as for the first Bell pair. We indirectly vary the cable loss by changing the delay time t_d the half-photon resides in the cable. In the experiment, we find that the Bell state fidelity suffers if we leave the qubit frequency of Q_1^A fixed. This could be due to static ZZ interaction between Q_1^A and Q_2^A during the excitation pulse used for generating the second Bell state, as when generating the second Bell pair,

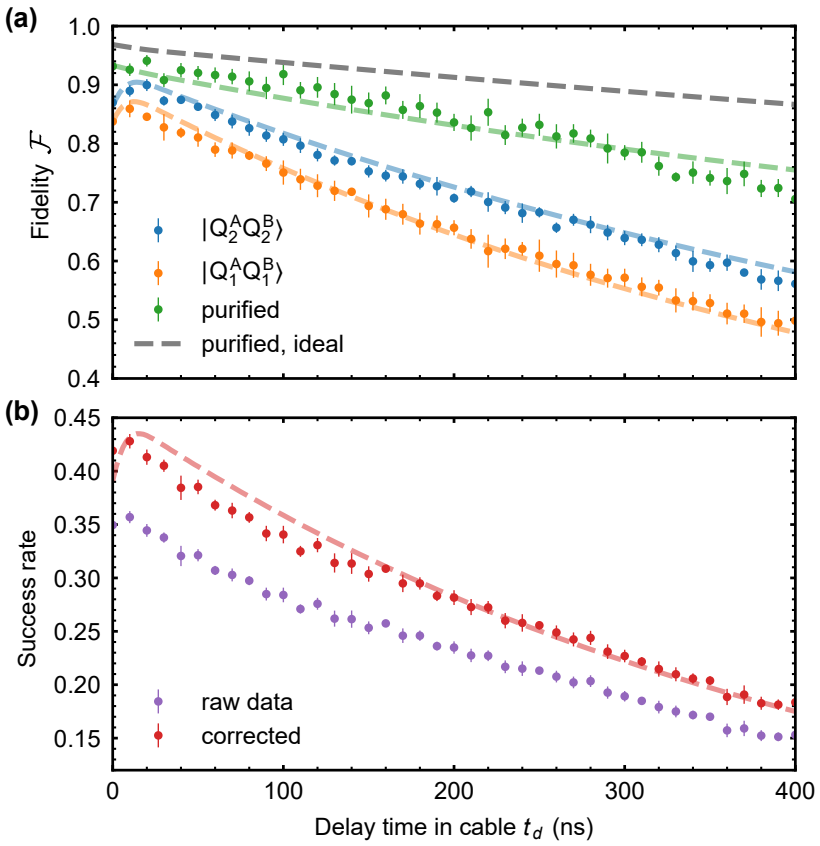

Figure 2.7: (a) Bell state fidelity $\mathcal{F}$ before purification for $|Q_2^AQ_2^B\rangle$ (blue) and $|Q_1^AQ_1^B\rangle$ (orange), and after purification for $|Q_2^AQ_2^B\rangle$ (green), each measured as a function of delay time t_d. The grey dashed line is for error-free purification between two identical impure Bell states. (b) Success rate for purification, which is the probability of measuring $|Q_1^AQ_1^B\rangle\rangle$ in $|ee\rangle$ with (red) and without (purple) readout correction (see Section 1.4.4).

both Q_1^A and Q_2^A have a population in their $|e\rangle$ states. We find that when we tune Q_1^A frequency from 5.25 GHz to $\sim$ 4.9 GHz, the fidelity of the second Bell state is closer to that of the initial state fidelity.

Pre-purification measurements of the two Bell states in $|Q_1^AQ_1^B\rangle$ and $|Q_2^AQ_2^B\rangle$, representing $\rho^{(1)}$ and $\rho^{(2)}$ respectively, are shown in Fig. 2.7(a). These indicate the fidelity of the second Bell pair in $|Q_2^AQ_2^B\rangle$ is a few percent lower than the Bell pair in Fig. 2.5(b), due to imperfections in the iSWAP gates and possible interference with the first Bell pair during the second Bell pair generation. The first Bell pair's fidelity also falls due to qubit decay during the second Bell pair generation. The purifying CNOT gate, with $|Q_2^AQ_2^B\rangle$ as the

control, is implemented using a CZ gate combined with two single-qubit $Y/2$ gates applied to $|Q_1^A Q_1^B\rangle$. Following the CNOT gates, we perform Z measurements of $Q_1^{A,B}$ and tomography measurements of $Q_2^{A,B}$. We post-select as purified states those with $|Q_1^A Q_1^B\rangle = |ee\rangle$; this purification process targets the ideal Bell state $|\psi^+\rangle$.

The fidelity of the purified state, representing ρ_{f}, is shown in Fig. 2.7(a) as a function of delay t_d. Larger t_d shows larger purification improvement, as there is more photon loss during cable transmission; the best fidelity of $94.09\% \pm 0.98\%$ is for the shortest delay $t_d = 20$ ns. The largest fractional improvement in fidelity, defined as the change in fidelity divided by the initial (pre-purification) fidelity, is 25%, achieved for the longest delay $t_d = 400$ ns. The success rate, given by the probability of measuring $|Q_1^A Q_1^B\rangle$ in $|ee\rangle$, is shown in Fig. 2.7(b), which falls for longer delay times, as expected: The main limitation is due to storage decay of the first Bell pair, whose lower fidelity limits both the success rate and the purified fidelity. The gray dashed line shows the expected purified Bell state fidelity for two identical Bell pairs matching $|Q_2^A Q_2^B\rangle$.

To better visualize the purification process, we present the full state tomography of the entanglement purification results when $t_d = 150$ ns in Fig. 2.8. When the measurement results for $|Q_1^A Q_1^B\rangle$ are not consistent, the final state of $|Q_2^A Q_2^B\rangle$ will be a mixed state (see Fig. 2.8(d-e)). When $|Q_1^A Q_1^B\rangle = |gg\rangle$, the final state of $|Q_2^A Q_2^B\rangle$ will have both damping and phase errors (see Fig. 2.8(c)). Only when $|Q_1^A Q_1^B\rangle = |ee\rangle$, then the damping error is corrected (see Fig. 2.8(f)), with a state fidelity $86.9 \pm 1.8\%$. The purified state has more than 10% fidelity improvement and damping errors are mostly corrected.

There are several other entanglement purification protocols [166, 176, 177] that can be implemented using this system. We performed numerical simulations to explore the expected results of each protocol shown in Fig. 2.9. The bit-purification circuit has the best outcomes. When using the phase error correction circuit, there is negligible improvement after purification, which is as expected, as the main errors are due to amplitude damping. In the

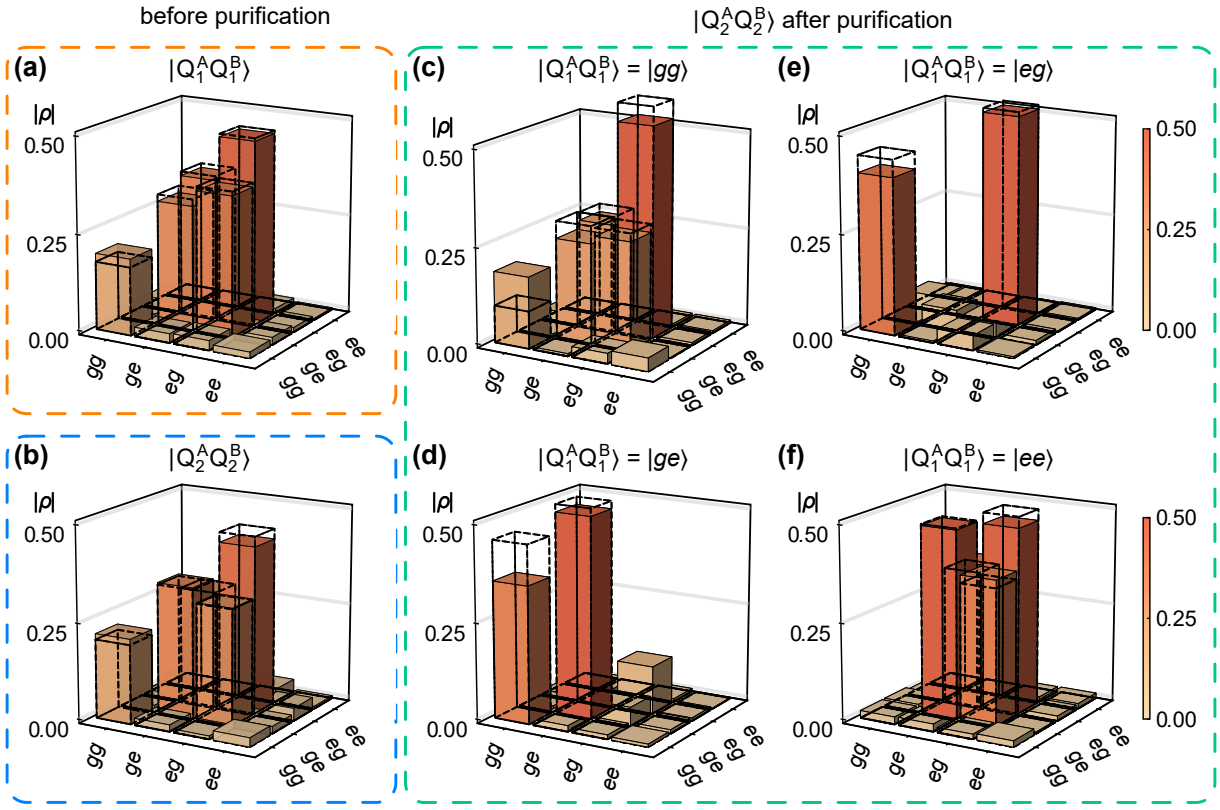

Figure 2.8: Full state tomography of entanglement purification results when $t_d = 150$ ns. (a-b) State tomography of (a) $|Q_1^AQ_1^B\rangle$ and (b) $|Q_2^AQ_2^B\rangle$ before purification. (c-f) State tomography of $|Q_2^AQ_2^B\rangle$ for different $|Q_1^AQ_1^B\rangle$ measurement results. Dashed lines are numerical simulation results.

simulations, double-selection purification introduced in Ref. [176] has similar performance to bit-purification when the cable delay t_d is small but becomes worse when t_d is large, resulting in larger (and therefore dominant) amplitude damping errors. Here we only perform purification that corrects damping errors, as this has the best simulated performance. More complex purification protocols [177] can be explored if we had a better quantum memory (e.g. larger T_1 in the storage qubits), or if we had multiple communication channels, avoiding the need to store the first Bell pair.

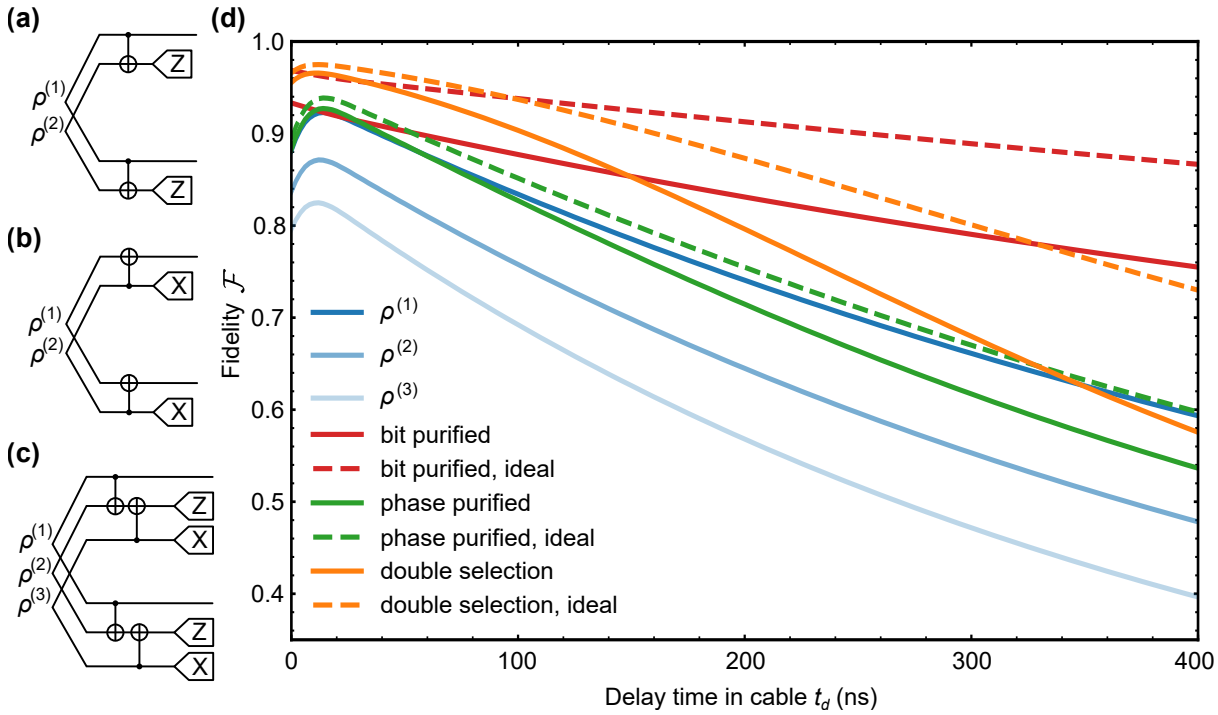

Figure 2.9: Results of numerical simulations to evaluate different entanglement purification protocols. (a-c) Different entanglement purification circuits used in numerical simulations: (a) bit-error purification circuit, (b) phase-error purification circuit, (c) double-selection purification circuit [176]. (d) Simulated purification results for the protocols in (a-c). Blue lines are states before purification including (lightest) and not including (darkest) state decay during state storage. Simulated results are for the bit-purification (red), phase-purification (green), and purification with double selection (orange). Dashed lines are purification results with ideal Bell pairs $\rho^{(0)}$, while solid lines include state decay during storage.

2.5 Entanglement protection

The purification protocol is mostly limited by decoherence in the qubits. The dephasing time $T_2 \sim 3$ μs of our qubits is significantly shorter than the energy relaxation time $T_1 \sim 10$ μs, indicative of extra dephasing channels, possibly due to flux noise, to which frequency-tunable transmons are particularly susceptible (see Section 1.4.2). Using either dynamical decoupling (DD), or a simpler Rabi drive (RD), we can protect the Bell pairs from the local noise that generates some of this decoherence. DD is a technique commonly used in spin systems [178, 179], where periodic pulse sequences average the effective environmental noise to near zero, yielding significantly extended qubit coherence times [180, 181, 182], as well

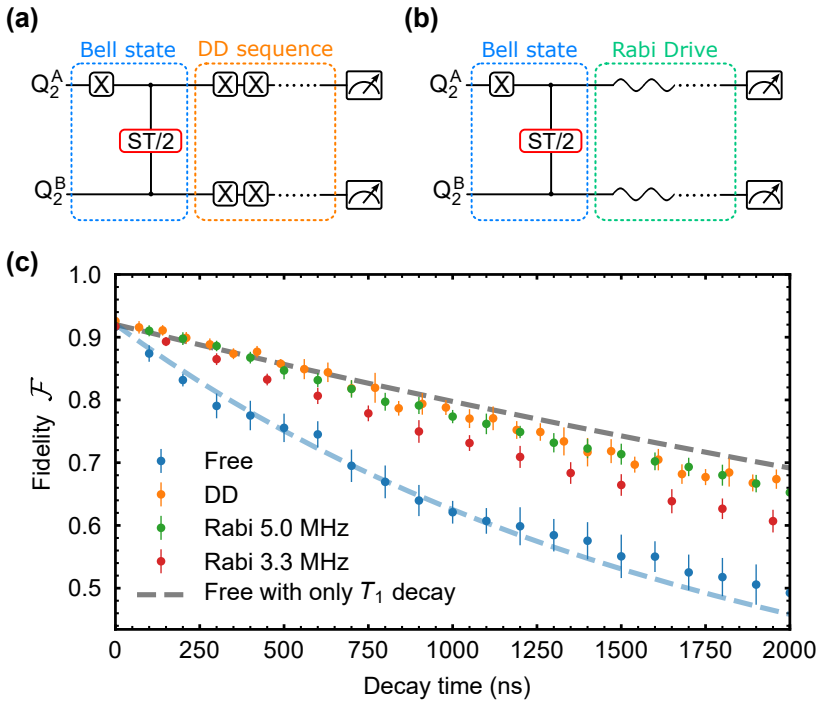

Figure 2.10: Entanglement protection using either dynamical decoupling (DD) or Rabi driving (RD). (a) Pulse sequence for DD and (b) RD. The ST/2 gate corresponds to the half-photon transfer process as shown in Fig. 2.5(b), with cable delay $t_d = 10$ ns. (c) Bell state fidelity as a function of time for free evolution (blue), DD (orange), and for Rabi drive strengths $\Omega/2\pi = 5$ MHz (green) and $\Omega/2\pi = 3.3$ MHz (red). Numerical simulations are for free evolution including amplitude and phase decay (blue dashed line) and for free evolution with only T_1 decay (grey dashed line).

as suppression of multi-qubit correlated noise [183, 184]. The quantum circuit for DD is shown in Fig. 2.10(a), where we apply a sequence of X gates to both qubits after generating a Bell state; the simpler RD is shown in Fig. 2.10(b). The DD X gate we use is a π-pulse with an additional DRAG correction [81]. The gate fidelity, as determined by randomized benchmarking [132], is 99.7%, with a gate duration of 30 ns. Following each X gate, we insert 5 ns of buffer time, so that each DD cycle, comprising two X gates, takes 70 ns. To evaluate the performance of the DD sequence, we perform state tomography after a varying number of DD cycles, with the results shown in Fig. 2.10(c). We see that DD significantly improves the Bell state fidelity, approaching the fidelity associated with pure T_1 dephasing

(gray dashed line). For a 1.4 μs evolution time, the state fidelity improves from $57.6 \pm 3.0\%$ to $71.7 \pm 2.3\%$.

We find that for a larger drive strength $\Omega/2\pi = 10.0$ MHz, the state fidelity decays much faster, which could be due to leakage to the higher excited states resulting in imperfect control of the qubit [165]. We also tried to combine RD/DD with entanglement purification to improve the performance of purification. However, we found in the experiment that to preserve the fidelity of the first Bell pair in $|Q_1^A Q_1^B\rangle$ during the generation of the second Bell pair, it is necessary to frequency-bias Q_1^A away from Q_2^A. This frequency bias requires applying a z pulse to Q_1^A. We found experimentally that the DD/RD signals did not improve the Bell state fidelities when combined with the z pulses. It could be due to spurious noise introduced by the z pulses, and/or imperfections in the pulse shapes. This meant we could not successfully combine DD/RD with purification.

2.6 Outlook

With this two-node superconducting quantum network, we demonstrate that purification protocols successfully correct amplitude-damping errors caused by the lossy communication channel, improving the state fidelity to $94.09 \pm 0.98\%$. There are also efforts to reduce the channel loss to directly generate entangled states with high fidelity [185]. The advantage of purification protocols is that their performance will only be limited by local gates and measurements, which are high-fidelity for superconducting qubits.

CHAPTER 3

QUANTUM SECRET SHARING IN A THREE-NODE NETWORK

3.1 Introduction

In Chapter 2, we use transmon qubits, gmon couplers, and coaxial cables to build a two-node superconducting quantum network. This scheme can be extended to three nodes, which can be used as a testbed for more quantum communication protocols.

Here we introduce a three-node network as is shown in Fig. 3.1. There are three nodes connected, forming a triangle structure. Each node contains two capacitively coupled transmon qubits. The transmon qubit is coupled to the communication channel through a gmon coupler. We use coplanar waveguide (CPW) lines as our communication channels instead of the coaxial cables used in the two-node network, which is a simpler first step towards a more difficult multi-chip experiment with coaxial cables.

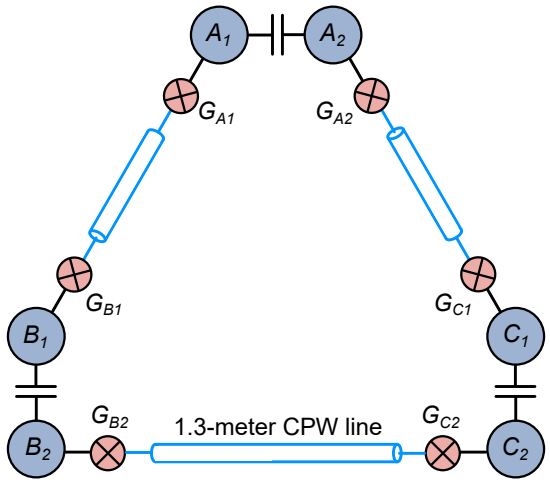

Figure 3.1: Overview of the three-node network. Three nodes form a triangle network, with two coupled qubits (dark blue) in each node. Each qubit is connected to its communication channel (light blue) through a tunable coupler (red).

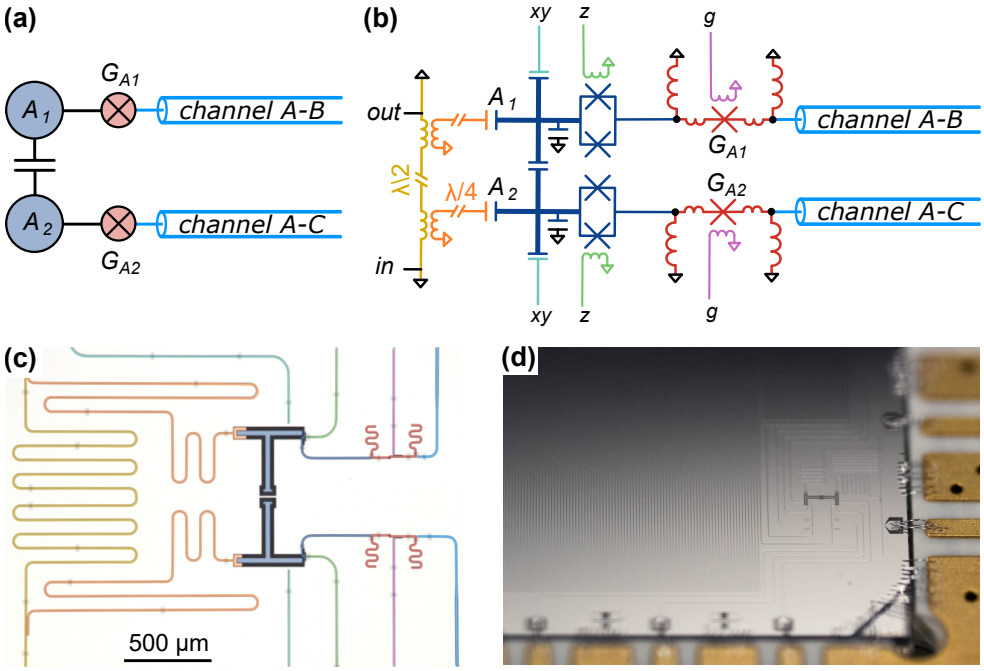

Figure 3.2: (a) Schematic, (b) circuit, (c) layout, and (d) photo of one node. Two capacitively coupled transmons (dark blue) are controlled individually by xy drive lines (cyan) and z flux lines (green). Each transmon is coupled to a communication channel (light blue) through a gmon coupler (red), with the coupling strength tuned by a g flux line (purple).

3.2 Experimental setup

A more detailed circuit and layout of each node are shown in Fig. 3.2. In Fig. 3.2(b), we present the circuit of each node, where two capacitively coupled transmons (dark blue) are controlled individually by xy drive lines (cyan) and z flux lines (green). Each transmon is coupled to a communication channel (light blue) through a gmon coupler (red), with the coupling strength tuned by a g flux line (purple).

In Fig. 3.2(c), we present the layout of one node, where we make the capacitors of the transmons to be a T shape instead of the commonly used X shape [74] to place the flux lines of two qubits and couplers further apart, aiming to minimize the flux crosstalk. Each qubit is dispersively coupled to a $\lambda/4$ resonator (orange) for measurement. There is a $\lambda/2$ single-stage bandpass Purcell filter (yellow) in each node to protect the qubits from the readout channel (see Section 1.4.4).

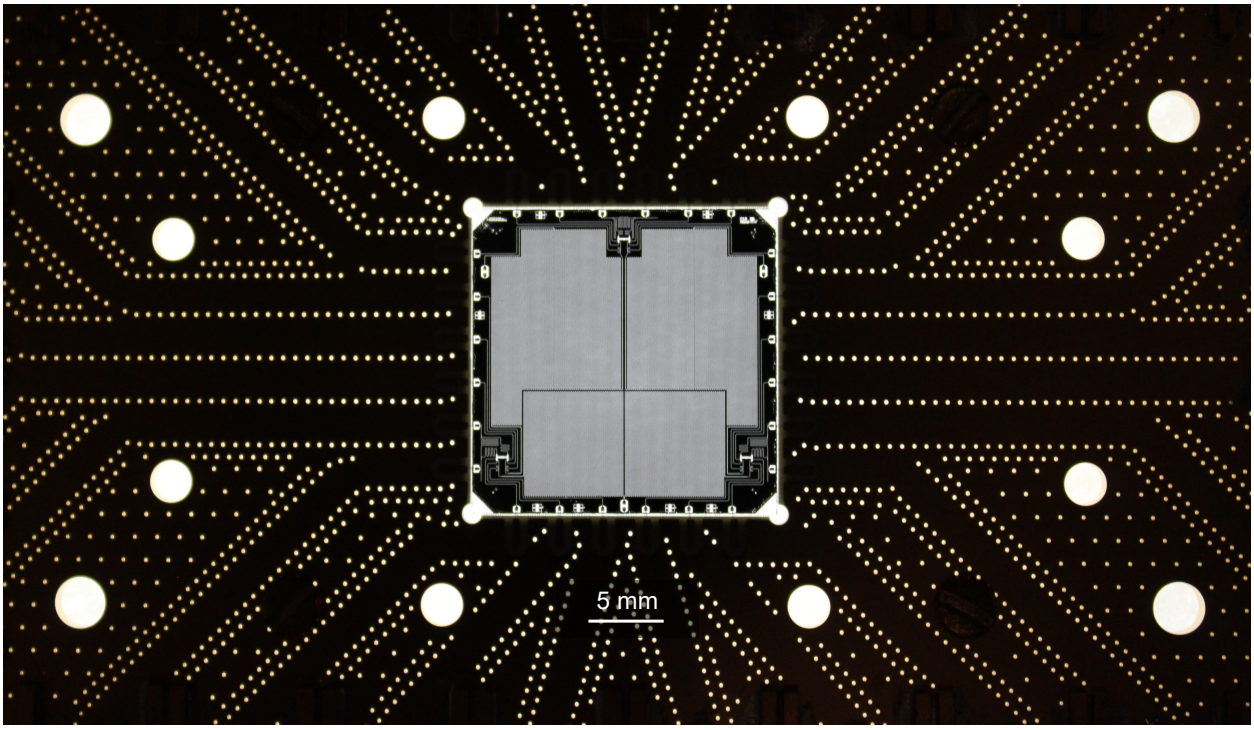

Figure 3.3: Photo of the three-node network. The 20 mm × 20 mm sample is wire-bonded to a PCB for measurement.

The photos of one node and the whole device are shown in Fig. 3.2(c) and Fig. 3.3 respectively. There is a 1.3-meter-long CPW line between two nodes (the meandered structure), which has a center conductor width of 8 μm and a gap to the ground of 4 μm, with a characteristic impedance of 50 Ω. The sample is fabricated on a 4-inch sapphire wafer and diced into a 20 mm × 20 mm die. A more detailed fabrication process of the qubits and long lines can be found in Appendix G. The sample is wire-bonded to a printed circuit board (PCB) with 24 SMA connectors and cooled in a dilution refrigerator for measurement. More details on the measurement setup can be found in Appendix H.

We first turn off the couplers and characterize the qubits. All the measured parameters are listed in Table 3.1. Each qubit has a relaxation time T_1 of around 10 μs and a pure dephasing time T_ϕ of around 800 ns. The relatively short T_ϕ is because the qubit operating frequencies are far below ($>$ 1 GHz) their maximum frequencies, which makes the qubits more sensitive to flux noise. The qubit A_1 has an unexpectedly shorter T_ϕ, which a noisy DC

	A_1	A_2	B_1	B_2	C_1	C_2
T_1	13 μs	7 μs	15 μs	12 μs	13 μs	10 μs
T_ϕ	170 ns	970 ns	700 ns	810 ns	600 ns	990 ns
$\omega_q/2\pi$	5.147 GHz	4.824 GHz	4.799 GHz	5.119 GHz	4.717 GHz	5.111 GHz
$\eta/2\pi$	-158 MHz	-167 MHz	-165 MHz	-166 MHz	-170 MHz	-171 MHz
$\omega_r/2\pi$	6.055 GHz	6.008 GHz	5.978 GHz	6.045 GHz	5.976 GHz	6.049 GHz
$\chi_{ge}/2\pi$	-2.1 MHz	-2.0 MHz	-4.2 MHz	-3.0 MHz	-3.6 MHz	-2.6 MHz
$\tau_r/2\pi$	820 ns	800 ns	720 ns	780 ns	560 ns	520 ns
F_g	98%	97%	99%	98%	99%	99%
F_e	93%	93%	95%	90%	94%	94%
$\mathcal{F}_{1Q}$	99.5%	99.4%	99.7%	99.6%	99.6%	99.6%
$g_{qq}/2\pi$	11.4 MHz		11.4 MHz		11.4 MHz	
$\zeta_{qq}/2\pi$	1.2 MHz		1.3 MHz		0.6 MHz	
$\mathcal{F}_{\mathrm{CZ}}$	N/A		95.5%		95.6%	

Table 3.1: Qubit parameters: the qubit operating frequency is ω_q; the qubit anharmonicity is η; the qubit lifetime and pure dephasing time at the operating point are T_1 and T_ϕ; the readout resonator frequency is ω_r; the readout resonator dispersive shift between qubit $|g\rangle$ and $|e\rangle$ states is χ_{ge}; the readout pulse duration is τ_r; the readout fidelities of $|g\rangle$ and $|e\rangle$ states are F_g and F_e; the average single-qubit gate fidelity measured by RB is $\mathcal{F}_{1Q}$; the qubit-qubit coupling strength and ZZ interaction strength are g_{qq} and ζ_{qq}; and the CZ gate fidelity measured by XEB is $\mathcal{F}_{\mathrm{CZ}}$.

source might cause as we observe a longer T_ϕ in a measurement before the data in Table 3.1 was taken. All the qubit anharmonicities are around -170 MHz. The small anharmonicity comes from the linear inductor in the gmon coupler (see Eq. 1.123). All the single qubit rotations are performed by 30 ns pulses with a cosine envelope and DRAG correction [81]. We benchmark all the single-qubit gates with randomized benchmarking (RB) and get an average gate fidelity of around 99.6% (see Section 1.4.6).

We detune the neighbor qubit away by around 300 MHz. We can realize iSWAP and CZ gates by biasing the frequency of one qubit (see Section 1.4.5). The coupling strength between two neighbor qubits g_{qq} is measured by the duration of the iSWAP gate between them, which gives an iSWAP gate duration of 22 ns and a CZ gate duration of 31 ns. The ZZ interaction strength ζ_{qq} is measured by probing the frequency shift of one qubit depending on the state of the other qubit, which is measured by a Ramsey-type experiment. We can

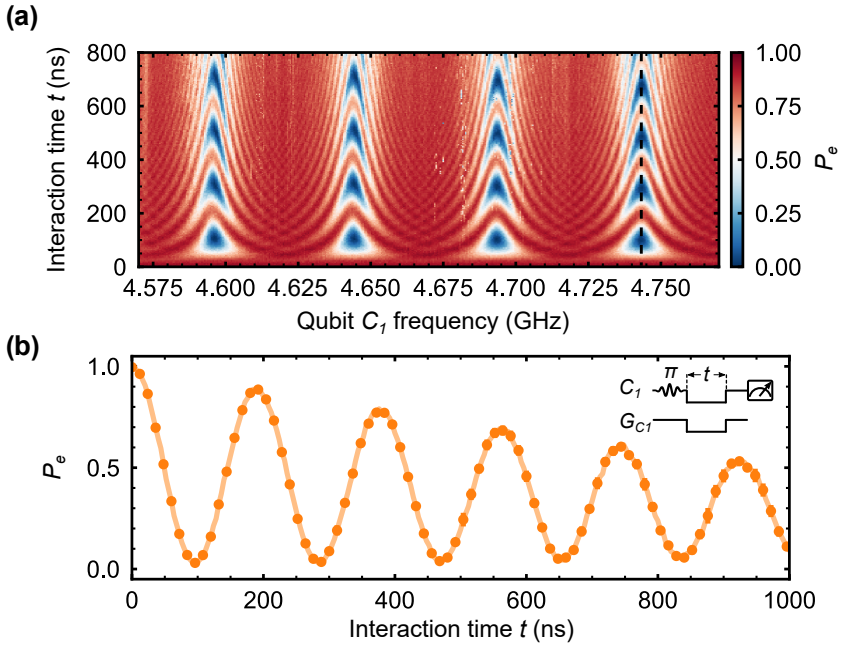

Figure 3.4: Vacuum Rabi oscillations between the qubit and communication modes: (a) sweeping the frequency of qubit C_1 and (b) interacting with the $\omega_c/2\pi = 4.743$ GHz communication mode (dashed line in (a)). The coupling strength between the qubit and the communication modes $g/2\pi$ is fixed to 2.5 MHz, corresponding to a swap duration of around 100 ns.

see that the measured ZZ interactions ζ_{qq} match well with Eq. 1.150. We benchmark the CZ gates by cross-entropy benchmarking (XEB) (see Section 1.4.6) and get an average gate fidelity of around 95.6%. We didn't benchmark the CZ gate between qubits A_1 and A_2 as it is not used in the following experiments due to the short T_ϕ of the qubit A_1. All the benchmarked qubit parameters are listed in Table 3.1.

We characterize the communication channels using the qubits. We first excite the qubit with π pulse and then turn on the coupler and sweep the qubit frequency simultaneously. The pulse sequence is shown in the inset of Fig. 3.4(b). In Fig. 3.4(a), we present the vacuum Rabi oscillations between the qubit and multiple communication modes, from which we can see that the 1.3-meter CPW line has a free spectrum range (FSR) $\omega_{\mathrm{FSR}}/2\pi$ of around 50 MHz. In Fig. 3.4(b), we plot the evolution of qubit excitation when interacting with the $\omega_c/2\pi = 4.743$ GHz mode (dashed line in Fig. 3.4(a)), which we will use as the communication mode.

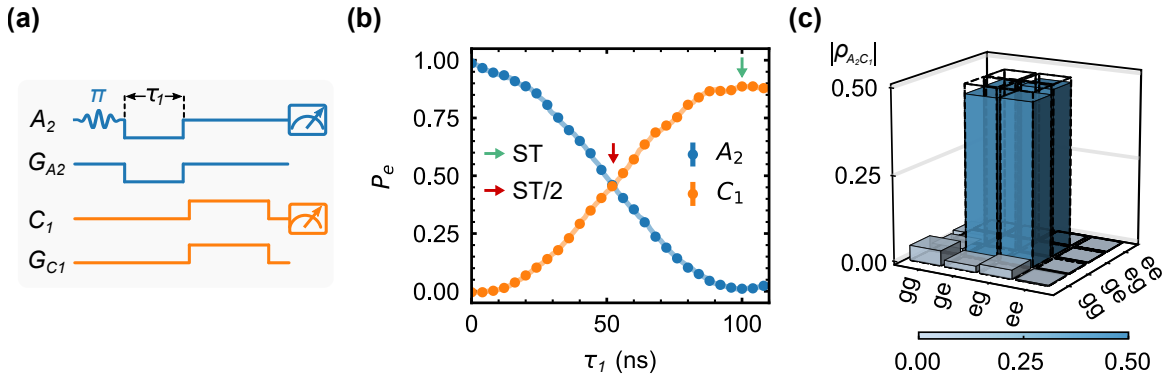

Figure 3.5: State transfer and entanglement generation between two nodes. (a) Pulse sequence. (b) Qubit $|e\rangle$ state populations P_e versus the duration of the first swap τ_1. ST stands for the state transfer process and ST/2 stands for the Bell state generation process. (c) The density matrix of the generated Bell state.

We use the same method in Fig. 2.4 to measure the lifetime T_1 of this communication mode, which gives us a T_1 of 1.2 μs. We also measure the dephasing time of the communication mode by preparing the qubit in the superposition state $(|g\rangle + |e\rangle)/\sqrt{2}$ using a $\pi/2$ pulse and swapping it to the communication mode and swapping it back, performing a Ramsey-like measurement. We get a dephasing time T_2 of 2.3 μs. All the measured results for three communication channels between three nodes are listed in Table 3.2. We can consistently get channel lifetimes T_1 of 1 μs, corresponding to quality factors of 3×10^4, lower than the long CPW lines used in Refs. [141, 186], which might be caused by the different geometry and fabrication process. The maximum coupling strength $g_{\max}$ between the qubit and the communication mode is around 10 MHz, corresponding to a coupler junction L_T of 0.7 nH (see Fig. 1.32). The maximum coupling strength $g_{\max}$ is smaller than the FSR ω_{FSR}, which means that before the photon is completely released to the communication channel, it will bounce back from the other end. Thus we cannot use the itinerant photon to realize state transfer [141, 187, 186].

We realize state transfer and entanglement generation between two nodes using the pulse sequence shown in Fig. 3.5(a). We first excite one qubit Q_1 to its $|e\rangle$ state, then turn on its coupler G_1 and bring the qubit on resonance with the communication mode for a duration

	$A_2 - C_1$	$C_2 - B_2$	$B_1 - A_1$
$\omega_c/2\pi$	4.743 GHz	5.135 GHz	4.905 GHz
T_1	1.2 μs	1.0 μs	1.0 μs
T_2	2.3 μs	2.0 μs	2.0 μs
η_t	$88.7 \pm 0.8\%$	$89.0 \pm 1.6\%$	$83.6 \pm 3.0\%$
$\mathcal{F}_{\text{Bell}}$	$95.1 \pm 0.8\%$	$95.3 \pm 1.0\%$	$86.2 \pm 0.5\%$

Table 3.2: Communication channels characterization: frequency $\omega_c/2\pi$, lifetime T_1, and dephasing time T_2. State transfer efficiency η_t and Bell state fidelity $\mathcal{F}_{\text{Bell}}$.

of τ_1. This will give us a state $\cos(g_1\tau_1)|e0\rangle + i\sin(g_1\tau_1)|g1\rangle$, where we write the quantum state as $|Q_1C\rangle$ and g_1 is the coupling strength between the qubit Q_1 and the communication mode. Then we turn on the coupler G_2 on the other side of the channel and bring the other qubit Q_2 on resonance with the communication mode for a duration of $\tau_2 = \pi/g_2$, which will swap states between the communication mode and the qubit Q_2, resulting in a state $\cos(g_1\tau_1)|eg\rangle - \sin(g_1\tau_1)|ge\rangle$, written in the form $|Q_1Q_2\rangle$. In Fig. 3.5(b), we plot the qubit $|e\rangle$ state populations versus the first swap duration τ_1. When $\tau_1 = \pi/2g_1$ (red arrow), we generate a Bell state $|\psi^-\rangle = (|eg\rangle - |ge\rangle)/\sqrt{2}$ similar to what we did in Chapter 2. We will label the Bell state generation process as ST/2. The generated Bell state between qubits A_2 and C_1 is plotted in Fig. 3.5(c), with a fidelity $\mathcal{F}_{\text{Bell}}$ of $95.1 \pm 0.8\%$. When $\tau_1 = \pi/g_1$ (green arrow), we realize the state transfer between two nodes, which we will label as ST. We get a state transfer efficiency η_t of $88.7 \pm 0.8\%$ between A_2 and C_1, defined as the transferred $|e\rangle$ state populations. To get high Bell state fidelity and state transfer efficiency, we set $g_1/2\pi$ to 2.5 MHz to minimize the leakage to other channel modes, and $g_2/2\pi$ to 3.1 MHz to maximize the swap speed.

We benchmark all three channels, with the lifetime T_1, dephasing time T_2, state transfer efficiency η_t and Bell state fidelity $\mathcal{F}_{\text{Bell}}$ listed in Table 3.2. The lower state transfer efficiency η_t and Bell state fidelity $\mathcal{F}_{\text{Bell}}$ between B_1 and A_1 comes from the short dephasing time of A_1 (see Table 3.1).

3.3 Entanglement swapping

We can explore more quantum communication protocols when extending to more quantum nodes. One example is entanglement swapping [188], with the scheme shown in Fig. 3.6(a). In entanglement swapping, we first prepare two Bell states in A_2C_1 and C_2B_2, and then do a Bell measurement on C_1C_2, which maps $|C_1C_2\rangle$ to one of the Bell states. The resulting state $|A_2B_2\rangle$ will also be a Bell state. Thus we can entangle qubits A_2 and B_2 without a direct communication channel.

Entanglement swapping can be viewed as a special case of quantum teleportation [189], where the state of C_1 is teleported to B_2 (or C_2 to A_2). Entanglement swapping helps build the quantum repeaters, which are key elements for long-distance quantum communication using fiber optics [190, 191]. Furthermore, entanglement-swapping experiments are also used to explore the bilocal correlations [192, 193, 194]. Recently, people showed the use of complex numbers in quantum theory is a requirement using the entanglement-swapping experiments [195, 196, 197].

In entanglement swapping, we need to perform a Bell measurement, which projects the two-qubit states to Bell states. For superconducting qubits, the dispersive readout measures the qubits along the z-axis. Thus we need to transform the Bell states to product states and then perform the readout, e.g. $|\psi^-\rangle \rightarrow |gg\rangle$. The circuit for entanglement swapping is shown in Fig. 3.6(b). To better visualize how the circuit works, we write down the states after each step. The Bell state we generate between two nodes is $|\psi^-\rangle = (|eg\rangle - |ge\rangle)/\sqrt{2}$. The initial state of two Bell states written in $|C_1C_2A_2B_2\rangle$ is

$$\frac{1}{2}(|ggee\rangle - |geeg\rangle - |egge\rangle + |eegg\rangle). \tag{3.1}$$

The $-Y/2$, $Y/2$ and CZ gates together form a CNOT gate with C_1 as the control qubit and

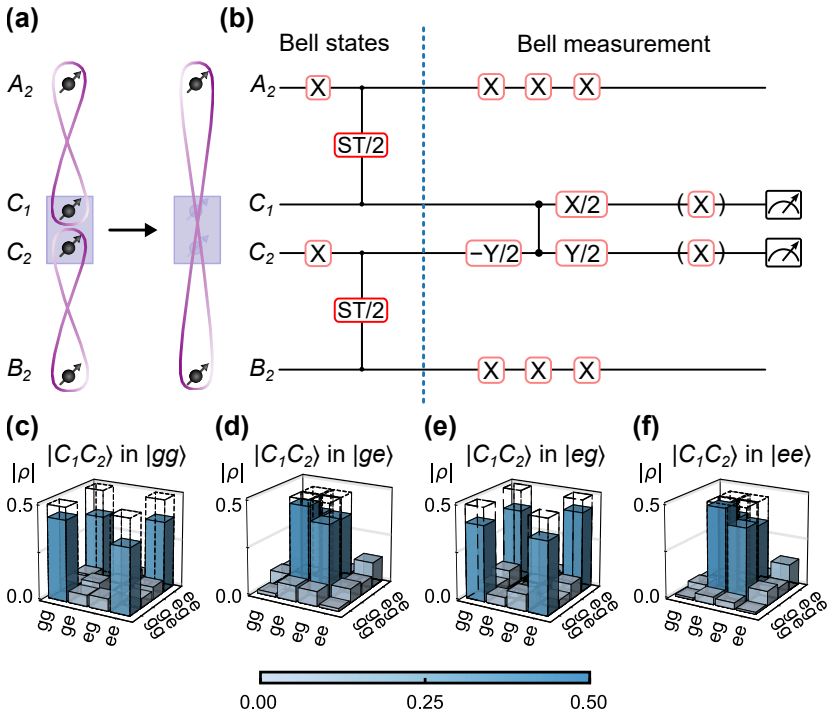

Figure 3.6: Entanglement swapping. (a) Schematic, (b) circuit realization, and (c-f) states of $|A_2B_2\rangle$ after the swapping depending on the measurement results on $|C_1C_2\rangle$. The entanglement on A_2C_1 and C_2B_2 is swapped to A_2B_2.

C_2 as the target qubit. After this CNOT gate, the state becomes

$$\frac{1}{2}(|ggee\rangle - |geeg\rangle - |eege\rangle + |eggg\rangle). \tag{3.2}$$

The $X/2$ gate transforms $|g\rangle$ to $(|g\rangle - i|e\rangle)/\sqrt{2}$ and $|e\rangle$ to $(-i|g\rangle + |e\rangle)/\sqrt{2}$, which gives us the state,

$$\begin{aligned}&\frac{1}{2\sqrt{2}}(|ggee\rangle - i|egee\rangle - |geeg\rangle + i|eeeg\rangle + i|gege\rangle - |eege\rangle - i|gggg\rangle + |eggg\rangle)\\ =&\frac{1}{2\sqrt{2}}\big(|gg\rangle(|ee\rangle - i|gg\rangle) - |ge\rangle(|eg\rangle - i|ge\rangle) + |eg\rangle(|gg\rangle - i|ee\rangle) - |ee\rangle(|ge\rangle - i|eg\rangle)\big).\end{aligned} \tag{3.3}$$

We also apply three dynamical decoupling (DD) X gates on A_2 and B_2 respectively to reduce the dephasing effects similar to what we did in Section 2.5. After these X gates, we get the

output states of $|A_2B_2\rangle = |\psi_{mn}\rangle$ when $|C_1C_2\rangle$ is measured in $|mn\rangle$,

$$|\psi_{gg}\rangle = \frac{1}{\sqrt{2}}(|gg\rangle - i|ee\rangle), \tag{3.4}$$

$$|\psi_{ge}\rangle = \frac{1}{\sqrt{2}}(|ge\rangle - i|eg\rangle), \tag{3.5}$$

$$|\psi_{eg}\rangle = \frac{1}{\sqrt{2}}(|gg\rangle + i|ee\rangle), \tag{3.6}$$

$$|\psi_{ee}\rangle = \frac{1}{\sqrt{2}}(|ge\rangle + i|eg\rangle), \tag{3.7}$$

which are all maximally entangled states with a phase difference from the Bell states. If we replace the $X/2$ gate with a $Y/2$ or a Hadamard H gate, all the output states will be Bell states. We perform the state tomography (see Section 1.4.6) of all four possible output states and get state fidelities of $77.9 \pm 1.6\%$, $81.5 \pm 1.5\%$, $80.2 \pm 1.2\%$, $81.8 \pm 1.3\%$, with the density matrices plotted in Fig. 3.6(c-g). To further reduce the measurement errors, we apply optional X gates on C_1 and C_2 to map $|C_1C_2\rangle$ to $|ee\rangle$ when doing the tomography of the target output states. The performance is limited by gate errors, measurement errors, and qubits A_2 and B_2 dephasing during local operations on qubits C_1 and C_2.

3.4 GHZ states generation

GHZ states [198] have many applications, e.g. quantum sensing [199, 7], quantum secret sharing (QSS) [200], etc. Here we generate GHZ states based on the Bell states between two nodes.

The circuit to generate GHZ states is shown in Fig. 3.7(a). We first generate a Bell state $|\psi^-\rangle = |ge\rangle - |eg\rangle$ between A_2 and C_1. By applying a CNOT gate between C_1 and C_2 and three DD X gates on A_2, we obtain a GHZ-3 state on $|A_2C_1C_2\rangle = (|ggg\rangle - |eee\rangle)/\sqrt{2}$, with a fidelity of $88.6 \pm 0.7\%$ and the density matrix plotted in Fig. 3.7(b). Then we transfer the C_2 state to B_1, which gives a GHZ-3 state on $|A_2C_1B_1\rangle = (|ggg\rangle + |eee\rangle)/\sqrt{2}$ across three

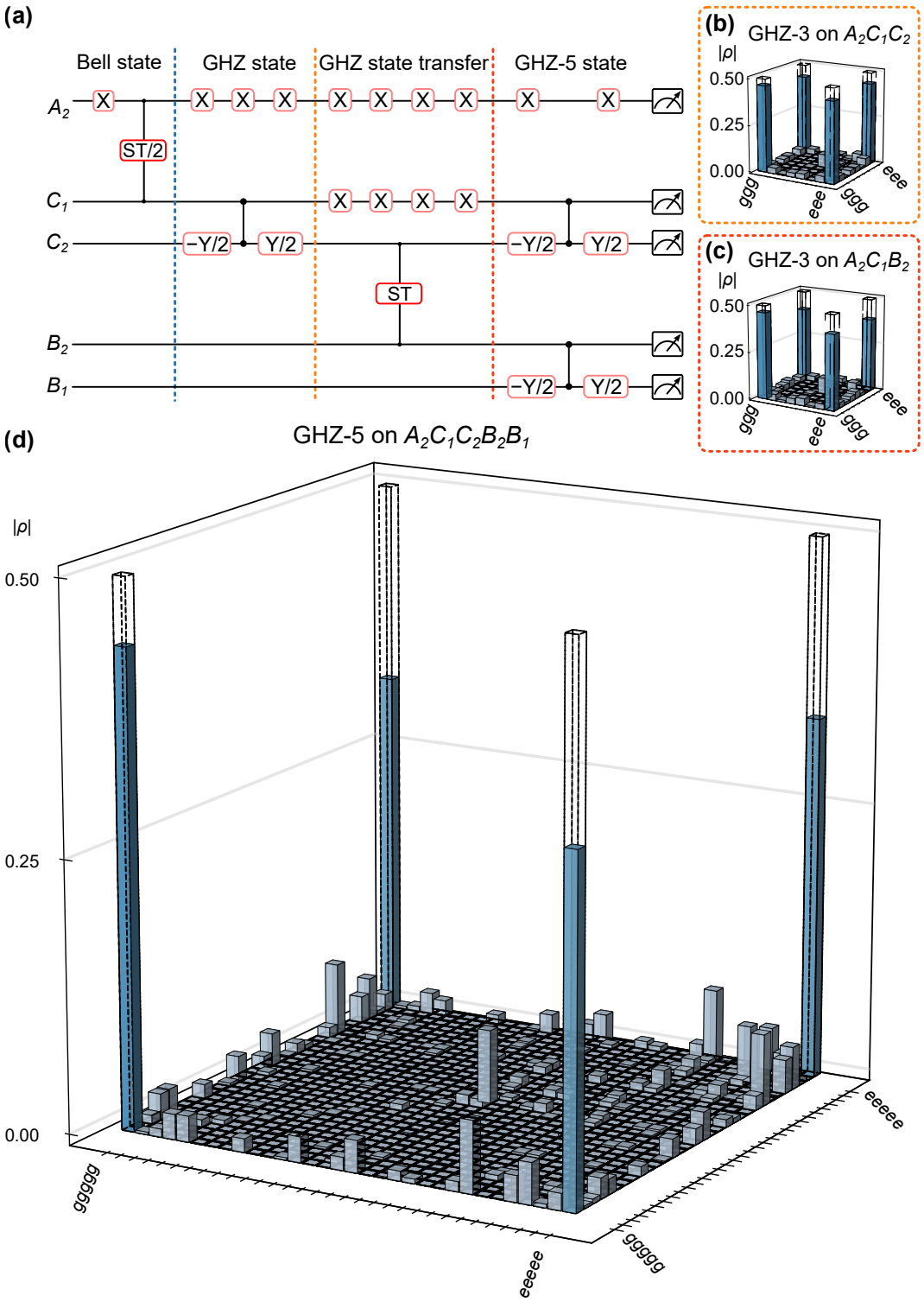

Figure 3.7: (a) Pulse sequence to generate GHZ states. The density matrix of the GHZ-3 states on qubits (b) $A_2C_1C_2$ with fidelity of $88.6 \pm 0.7\%$ and (c) $A_2C_1B_2$ with fidelity of $82.6 \pm 0.8\%$, and (d) the GHZ-5 state on qubits $A_2C_1C_2B_2B_1$ with fidelity of $70.3 \pm 1.1\%$.

nodes. There is a phase flip because the state transfer process is equivalent to two iSWAP gates. Similarly, we apply four DD X gates on A_2 and C_1 during the transfer process. We get a state fidelity of $82.6 \pm 0.8\%$ and the density matrix is plotted in Fig. 3.7(c). We observe a state fidelity improvement of around 5% compared with no DD gates. We can extend this GHZ-3 state to a GHZ-5 state by two parallel CNOT gates as is shown in Fig. 3.7(a). We did not involve the qubit A_1 because of its short dephasing time T_ϕ (see Table 3.1). The generated GHZ-5 state on $A_2C_1C_2B_2B_1$ is shown in Fig. 3.7(d), with fidelity of $70.3 \pm 1.1\%$ above the threshold of 50% for genuine multipartite entanglement [201].

3.5 Quantum secret sharing

Quantum secret sharing (QSS) is secret sharing using quantum states. Secret sharing refers to methods for distributing a secret, i.e. a bit string, among a group of n people [202, 203]. They can reconstruct the secret only when any group of $\geq k$ people combine their information. When there are fewer than k people, they cannot extract any information about the secret. This scheme is called the (k, n)-threshold scheme.

Quantum key distribution (QKD) ensures secure communication [1]. We can combine QKD with secret sharing for secure communication, which is however not elegant. We need to first establish mutual keys among different pairs of parties and then implement the classical secret-sharing procedure, which becomes more complicated when n is large. An alternative way is to use quantum states to split the information and ensure the security of the communication, which is QSS. There exist many different QSS protocols [200, 204, 205, 206, 207, 208, 209, 210, 211] and QSS has been demonstrated experimentally with optics [212, 213, 214, 215, 216] or locally connected superconducting qubits [217]. Here we introduce the QSS protocol using GHZ states in this three-node network [200].

Here we consider the simplest case, $k = n = 2$. Alice wants to share a secret (a bit) with Bob and Charlie. Only when Bob and Charlie combine their information, they can reveal

	Bob				
Charlie		$\|+x\rangle_B$	$\|-x\rangle_B$	$\|+y\rangle_B$	$\|-y\rangle_B$
	$\|+x\rangle_C$	$\|+x\rangle_A$	$\|-x\rangle_A$	$\|-y\rangle_A$	$\|+y\rangle_A$
	$\|-x\rangle_C$	$\|-x\rangle_A$	$\|+x\rangle_A$	$\|+y\rangle_A$	$\|-y\rangle_A$
	$\|+y\rangle_C$	$\|-y\rangle_A$	$\|+y\rangle_A$	$\|-x\rangle_A$	$\|+x\rangle_A$
	$\|-y\rangle_C$	$\|+y\rangle_A$	$\|-y\rangle_A$	$\|+x\rangle_A$	$\|-x\rangle_A$

Table 3.3: States of Alice depending on the measurement results of Bob and Charlie.

the secret Alice wants to share. Alice, Bob and Charlie first share a GHZ state $|\psi\rangle_{\text{GHZ}}$,

$$|\psi\rangle_{\text{GHZ}} = \frac{1}{\sqrt{2}}(|000\rangle + |111\rangle). \tag{3.8}$$

Then everyone randomly measures along the x or y axis and shares which axis they measure along via a classical, public channel. Bob and Charlie can decode what Alice measured half of the time. Repeating the above process many times, they can use a small fraction to detect whether eavesdropping exists by monitoring the success rate.

To better visualize the above process, we can rewrite the GHZ state,

$$|\psi\rangle_{\text{GHZ}} = \frac{1}{2}\big((|+x\rangle_A|+x\rangle_B+|-x\rangle_A|-x\rangle_B)|+x\rangle_C+(|+x\rangle_A|-x\rangle_B+|-x\rangle_A|+x\rangle_B)|-x\rangle_C\big), \tag{3.9}$$

where the subscript labels the qubit and $|\pm x\rangle$ are the eigenstates along the x axis

$$|+x\rangle = \frac{1}{\sqrt{2}}(|0\rangle + |1\rangle), \tag{3.10}$$

$$|-x\rangle = \frac{1}{\sqrt{2}}(|0\rangle - |1\rangle). \tag{3.11}$$

We can see that when everyone measures along the x axis, their measurement results are correlated. When the measurement results of Alice and Bob are consistent, the measurement result of Charlie will be $|+x\rangle$, while when the measurement results of Alice and Bob are inconsistent, the result of Charlie will be $|-x\rangle$. We list all the possible measurement results

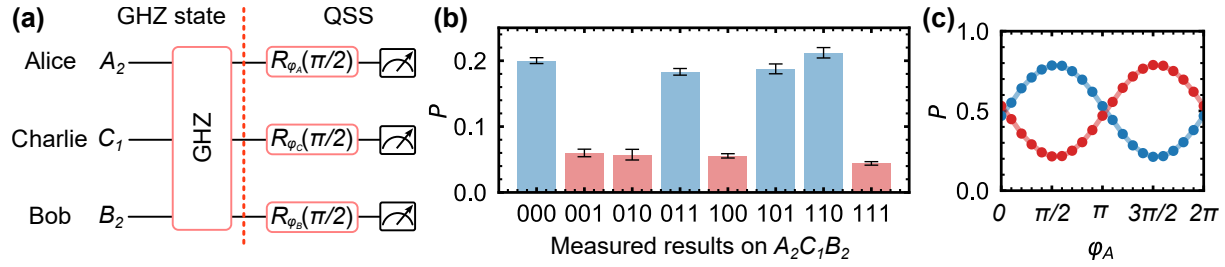

Figure 3.8: Quantum secret sharing (QSS). (a) Circuit for QSS. GHZ represents the GHZ state generation process on $A_2C_1B_2$ shown in Fig. 3.7(a). (b) Measured probabilities when all the qubits are measured along the x axis. The blue bars indicate that Bob and Charlie can successfully decode the secret. (c) Probabilities of measuring $A_2C_1B_2$ in 000, 011, 101, 110 (blue) and 001, 010, 100, 111 (red) versus φ_A.

in Table 3.3, where $|\pm y\rangle$ are the eigenstates along the y axis,

$$|+y\rangle = \frac{1}{\sqrt{2}}(|0\rangle + i|1\rangle), \tag{3.12}$$

$$|-y\rangle = \frac{1}{\sqrt{2}}(|0\rangle - i|1\rangle). \tag{3.13}$$

We can see that Bob or Charlie alone cannot extract any information about the bit Alice holds (1 for a + state and 0 for a − state). When Bob and Charlie combine their measurement results and everyone's measurement axis, they can reveal the bit Alice holds (Alice's measurement result) 50% of the time. Only when Bob and Charlie measure along the same axis and Alice measures along the x axis, or Bob and Charlie measure along the different axis and Alice measures along the y axis, Bob and Charlie can correctly decode the secret. Otherwise, Bob and Charlie cannot get any information about the secret even when combining their results. Because everyone randomly picks the measurement axis at the beginning, Bob and Charlie can decode what Alice measured half the time.

To demonstrate QSS, we use the circuit shown in Fig. 3.8(a). We first generate a GHZ-3 state on $A_2C_1B_2$, which is labeled Alice, Charlie, and Bob. The circuit to generate the GHZ-3 state is shown in Fig. 3.7(a) and the generated state is shown in Fig. 3.7(c). We will label $|g\rangle$ as $|0\rangle$, and $|e\rangle$ as $|1\rangle$. To realize measurement along the qubit x or y axis, we perform a

single-qubit $\pi/2$ rotation $R_\varphi(\pi/2)$ before the measurement along the qubit z axis, where φ is the angle to the x-axis on the xy plane of the Bloch sphere. When $\varphi = 0$, the measurement is along the y axis. When $\varphi = \pi/2$, the measurement is along the x axis. In Fig. 3.8(b), we plot the measured probabilities on $A_2C_1B_2$ along the x axis, i.e. $\varphi_A = \varphi_B = \varphi_C = \pi/2$. When the measurement results of Bob (B_2) and Charlie (C_1) are consistent/inconsistent, the bit Alice (A_2) holds should be 0/1, with these probabilities shown in blue bars in Fig. 3.8(b). These measured probabilities should all be 25% in the ideal case, while we get an average probability of $19.6 \pm 1.1\%$ because of imperfect state generation and readout errors. We can extract the QSS error rate of $21.5 \pm 1.1\%$, below the threshold of 25% described by a local theory [212]. Furthermore, we sweep φ_A and we can see the sum of probabilities of measuring 000, 011, 101, and 110 in $A_2C_1B_2$ changes proportional to $1 + \cos\varphi_A$ as is shown in Fig. 3.8(c). When $\varphi_A = 0$, we measure along Alice's y axis and we can see that the probability becomes 50%, which means Bob and Charlie cannot extract any information about the secret (50% means that it's just a random guess).

QSS promises a secure way to share secrets, which means that it can detect whether there is an eavesdropper. Suppose Eve wants to steal the information from Alice, Bob, and Charlie. Eve cannot directly copy the state from one party because of the no-cloning theorem [125]. However, she can still gain partial information using strategies like intercept-and-resend, entangle-and-measure, etc [217]. Here we give an example of an entangle-and-measure attack, where Eve tries to steal the secret by getting entangled with the other parties, and we are going to show that the QSS protocol can detect such an attack and Eve cannot gain more information about the secret than Bob and Charlie.

We use the circuit in Fig. 3.9(a) for the eavesdropper Eve (B_1) to perform the entangle-and-measure attack. We first perform a rotation $R_Y(\theta_E)$ along the y axis of Eve, which gives the state of Eve $|\psi\rangle_E = \cos(\theta_E/2)|0\rangle - \sin(\theta_E/2)|1\rangle$. Then a CZ gate between Eve and

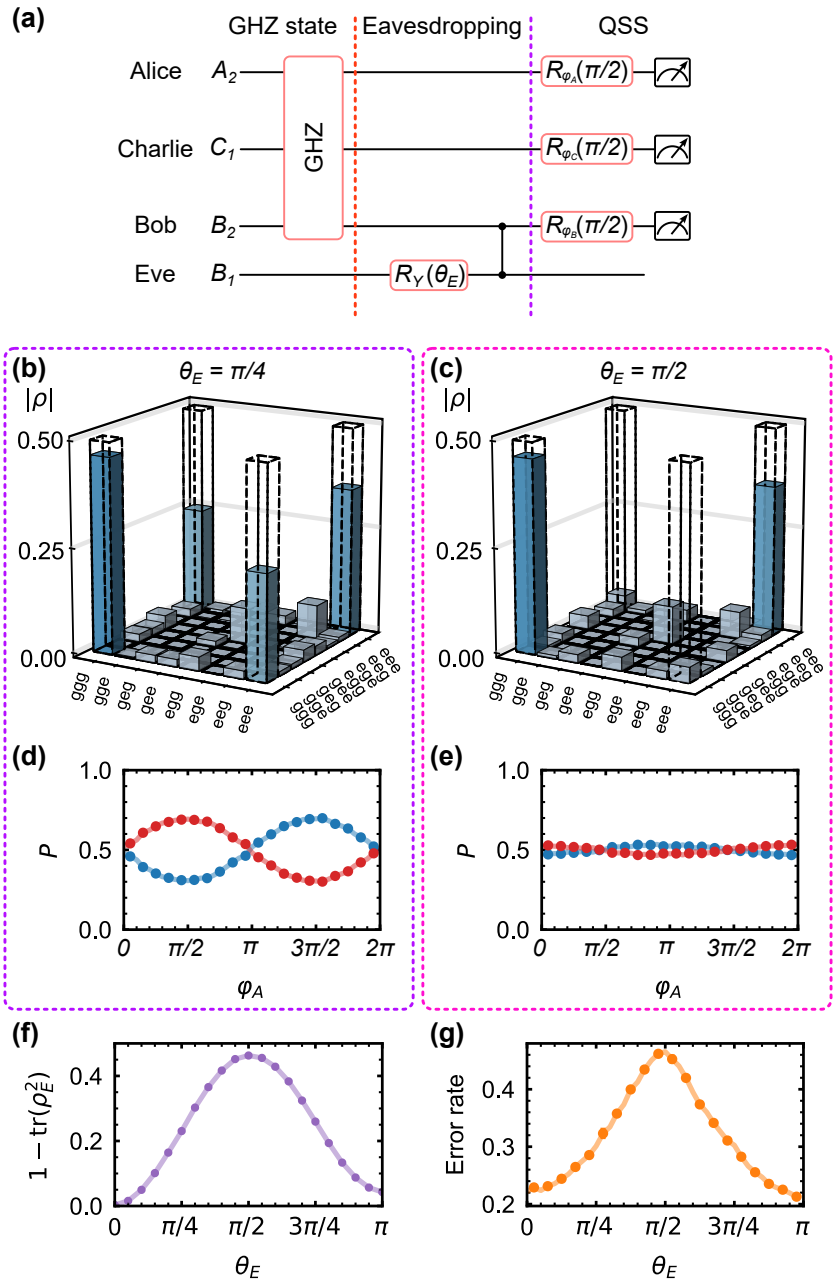

Figure 3.9: Detection of eavesdropping. (a) The circuit for the eavesdropper Eve (B_1) to perform the entangle-and-measure attack. (b-c) State tomography of $A_2C_1B_2$ when (b) $\theta_E = \pi/4$ and (e) $\theta_E = \pi/2$. (d-e) Probabilities of measuring $A_2C_1B_2$ in 000, 011, 101, 110 (blue) and 001, 010, 100, 111 (red) versus φ_A when (d) $\theta_E = \pi/4$ and (e) $\theta_E = \pi/2$. (f) Linear entropy of Eve (B_1) versus θ_E. (g) QSS error rate versus θ_E.

Bob entangles them together. The full state in $|A_2C_1B_2B_1\rangle = |\psi\rangle_{ACBE}$ becomes

$$|\psi\rangle_{ACBE} = \frac{1}{\sqrt{2}}\big(\cos\frac{\theta_E}{2}|0000\rangle + \cos\frac{\theta_E}{2}|1110\rangle - \sin\frac{\theta_E}{2}|0001\rangle + \sin\frac{\theta_E}{2}|1111\rangle\big). \quad (3.14)$$

When $\theta_E = 0$ or π, Eve is not entangled with Alice, Bob, and Charlie. When $0 < \theta_E < \pi$, Eve is entangled with the other three parties. Note that when $\theta_E = \pi/2$, the entangling operation acts as a part of a CNOT gate (see Fig. 3.7(a)). The state of $A_2C_1B_2$ becomes a mixed state, with the density matrix ρ_{ACB},

$$\rho_{ACB} = \frac{1}{2}(|000\rangle\langle 000| + |111\rangle\langle 111| + \cos\theta_E|111\rangle\langle 000| + \cos\theta_E|000\rangle\langle 111|). \quad (3.15)$$

Its fidelity to an ideal GHZ state ($|\psi\rangle_{\rm GHZ} = (|000\rangle \pm |111\rangle)/2$) becomes $(1 + |\cos\theta_E|)/\sqrt{2}$. In Fig. 3.9(b-c), we plot the density matrices of $A_2C_1B_2$ for $\theta_E = \pi/4$ and $\theta_E = \pi/2$. We can see that the off-diagonal terms of the density matrix drop compared with Fig. 3.7(c) and when $\theta_E = \pi/2$, the off-diagonal terms are close to zero as expected. We can also write down the density matrix of Eve ρ_E,

$$\rho_E = \frac{1 + \cos\theta_E}{2}|0\rangle\langle 0| + \frac{1 - \cos\theta_E}{2}|1\rangle\langle 1| \quad (3.16)$$

To show how entangled Eve is with the other three parties, we plot the linear entropy of Eve's state $1 - {\rm tr}(\rho_E^2)$ in Fig. 3.9(f). When Eve is not entangled with the other three parties ($\theta_E = 0$ or π), the state of Eve will be a pure state $1 - {\rm tr}(\rho_E^2) = 0$ in the ideal case.

After Eve gets entangled, the other three parties perform the QSS protocol as we described before. The QSS error rate becomes $(1 - |\cos\theta_E|)/4$. In Fig. 3.9(d-e), we plot the same quantities as in Fig. 3.8(c) for $\theta_E = \pi/4$ and $\pi/2$. We can see that visibility decreases as we increase θ_E from 0 to $\pi/2$. In Fig. 3.9(g), we plot the extracted QSS error rate versus θ_E. We can see that the more Eve gets entangled, i.e. the more information Eve can steal,

the more errors will be introduced. Thus by monitoring the error rate, Alice, Bob, and Charlie can detect whether there exists an eavesdropper.

The above argument is qualitative. We give a more quantitative analysis as follows. Here we first introduce Holevo's bound [218]. Considering a sender and receiver setup, where Alice prepares quantum states ρ_X where $X = 0,\ 1, \cdots, n$, with probability $p_0,\ p_1, \cdots, p_n$, and Bob measures the states using the positive operator-valued measure (POVM) $\{E_Y\}$ [125] with measurement outcomes $Y = 0,\ 1, \cdots, m$, the mutual information $H(X : Y)$ between the sent random variable X and the measured random variable Y is bounded by

$$H(X : Y) \leq S(\rho) - \sum_k p_k S(\rho_k), \tag{3.17}$$

where $S(\cdot)$ is the von Neumann entropy of a quantum state and ρ is the ensemble of the sent states $\rho = \sum p_k \rho_k$.

The above process described is a prepare-and-measure protocol. In terms of QSS, we perform an entanglement-based protocol to transfer the information, where Alice and Bob share an entangled state first and then perform POVM to transfer the information. The entanglement-based protocol can be understood using the prepare-and-measure protocol as follows. Alice performs POVM $\{E_{Ai}\}$ on her subsystem, which collapses the state of Bob to ρ_{Bi}. Then the state ρ_{Bi} is sent to Bob, with the probability p_i for Alice to obtain the specific outcome A_i. When the entangled state shared between Alice and Bob is a pure state $|\psi\rangle_{AB}$, the ensemble of the sent states ρ becomes

$$\begin{aligned} \rho &= \mathrm{tr}_A\big[(M_{Ai} \otimes I_B)|\psi\rangle\langle\psi|_{AB}(M_{Ai}^\dagger \otimes I_B)\big] \\ &= \sum_i \mathrm{tr}_A\big[|\psi\rangle\langle\psi|_{AB}(M_{Ai}^\dagger M_{Ai} \otimes I_B)\big] = \mathrm{tr}_A(|\psi\rangle\langle\psi|_{AB}) = \rho_B, \end{aligned} \tag{3.18}$$

where M_{Ai} is the measurement operator and $E_{Ai} = M_{Ai}^\dagger M_{Ai}$. The mutual information

between Alice and Bob $H(X:Y)$ is then bounded by

$$H(A:B) \leq S(\rho_B) - \sum_i p_i S(\rho_{Bi}). \tag{3.19}$$

In QSS, we want information about the secret obtained by Bob and Charlie more than Eve. Thus Bob and Charlie can in principle utilize the excess information to extract the shared secret. Here we consider the privacy bound $\mathcal{P}$, defined as

$$\mathcal{P} = \sup[H(A:BC) - H(A:E)], \tag{3.20}$$

where the supremum is taken over all possible strategies that Alice, Bob, and Charlie can use. According to Holevo-Schumacher-Westmoreland theorem [219, 220], the Holevo bound (Eq. 3.19) is achievable. Thus we have

$$\begin{aligned} \mathcal{P} &\geq H(A:BC) - \sup[H(A:E)] \\ &\geq S(\rho_{BC}) - \sum_i p_i S(\rho_{BCi}) - S(\rho_E) + \sum_i p_i S(\rho_{Ei}). \end{aligned} \tag{3.21}$$

If we assume all the errors come from the eavesdropping (i.e. Eve can get the most information) and Alice sends pure states to Bob, Charlie, and Eve every time (so that the Holevo bound can be achieved), we have $S(\rho_E) = S(\rho_{ABC})$ and $S(\rho_{Ei}) = S(\rho_{BCi})$. We get the lower bound of $\mathcal{P}$,

$$\mathcal{P} \geq S(\rho_{BC}) - S(\rho_{ABC}). \tag{3.22}$$

In the eavesdropping scheme introduced above, we have

$$\mathcal{P} \geq 1 + \frac{1-\cos\theta_E}{2}\log_2\frac{1-\cos\theta_E}{2} + \frac{1+\cos\theta_E}{2}\log_2\frac{1+\cos\theta_E}{2}, \tag{3.23}$$

which is always positive as shown in Fig. 3.10. Thus we prove that in the ideal case, Eve

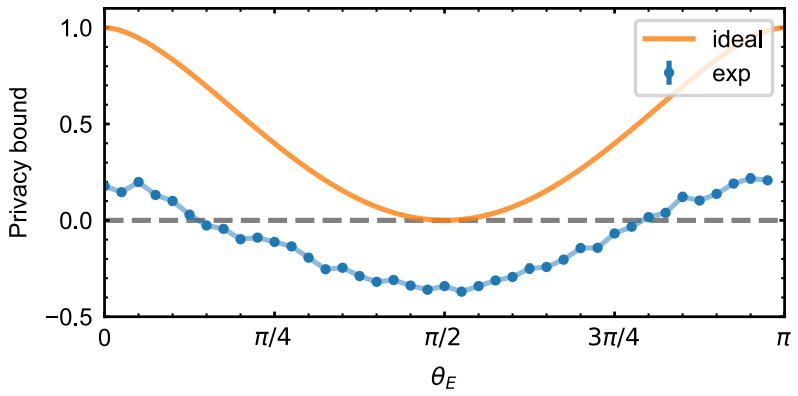

Figure 3.10: Lower bound of $\mathcal{P}$, directly calculated using $S(\rho_{BC}) - S(\rho_{ABC})$, versus θ_E. The density matrix ρ_{ABC} is determined by state tomography and $\rho_{BC} = \mathrm{tr}_A(\rho_{ABC})$.

cannot extract more information about the secret than Bob and Charlie with this entangle-and-measurement attack, which demonstrates the security of QSS. In experiments, we do the state tomography of ρ_{ABC} and calculate $S(\rho_{BC}) - S(\rho_{ABC})$, with the results shown in Fig. 3.10. We can see that the lower bounds are negative for some θ_E, mainly caused by the imperfect GHZ state generation. In reality, we can monitor the error rate to see whether eavesdropping exists and stop QSS if the error rate is above a certain threshold.

3.6 Outlook

With this three-node superconducting quantum network, we demonstrate entanglement swapping and quantum secret sharing with GHZ states. We show that QSS can detect the existence of eavesdropping. We only use up to five qubits and two communication channels for these experiments. We look forward to exploring more using the whole setup (six qubits and three communication channels), e.g. quantum network nonlocality [221, 222, 223], quantum Byzantine agreement [224], quantum voting [225, 226], etc.

CHAPTER 4

REALIZING ALL-TO-ALL CONNECTIVITY IN A FOUR-NODE NETWORK

4.1 Introduction

In previous chapters, we discussed the realization of superconducting quantum networks using transmons as quantum processing units, transmission lines as quantum communication channels, and gmons as tunable couplers connecting them. In this architecture, we need $N(N-1)/2$ communication channels to realize all-to-all connectivity between N quantum nodes. Furthermore, these channels have to be connected to different transmon qubits on each node [185]. In this chapter, we are going to introduce a "quantum router" to overcome these problems.

For Ethernet with many devices, we use an Ethernet switch to realize communication between arbitrary devices (see Fig. 4.1). We can build a similar device for transmons to realize signal routing between arbitrary qubit pairs [21]. This kind of central routing element has been implemented in different ways, e.g. a resonator bus [227], a shared coupler [228, 157], a multi-mode ring resonator [229], or multi-mode 3D microwave cavity with SNAIL couplers [230]. For the single-mode resonator coupling scheme [227], all transmons are coupled to one resonator with fixed coupling, where the couplings cannot be turned off. Frequency collisions will be an issue when scaling to a larger system for the other coupling schemes [229, 230, 157].

Figure 4.1: Photo of a TP-Link 24-port Ethernet switch.

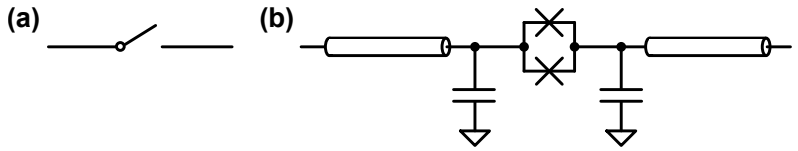

Figure 4.2: Circuit for a microwave switch.

Here we extend the capacitive coupler design introduced in Section 1.5.2 and combine this with a microwave switch concept [231, 232, 233] to realize a tunable multi-mode [58, 234] coupler connecting qubits, which overcomes the issues with existing protocols.

4.2 Circuit design

We first give an introduction to the way the microwave switch in Ref. [233] works. The schematic is shown in Fig. 4.2(a). A transmission line has a switch in the line. By turning on or off the switch, the signal will transmit or reflect. The switch itself contains a SQUID together with some capacitors (see Fig. 4.2(b)). The SQUID acts as a tunable inductor, $L_{\mathrm{SQUID}} = L_J/2|\cos(\phi_{\mathrm{ext}}/2)|$, with L_J the Josephson inductance of one junction. By tuning the effective inductance of the SQUID, we can change the effective impedance of the SQUID combined with capacitors. When ϕ_{ext} is set to $\pm\pi$, the SQUID acts like an open in the circuit, thus no signal can go through, representing a switch "off" state. When L_{SQUID} is set to a value that the impedance combined with those capacitors is matched with the transmission line, the signal can go through without any reflection, representing a switch "on" state.

Based on the microwave switch, we can simply extend it to multiple ports. In Fig. 4.3(a), we give an example with four ports, each with a switch in line, forming a router. By selectively choosing the pair of switches to turn on, we can route the signal as we want. Furthermore, to couple the router to the processing unit – transmon qubit, we choose capacitive coupling between them. Inductive coupling is also possible, while capacitive coupling is easier to design. Then we come up with the circuit shown in Fig. 4.3(b). Instead of placing the

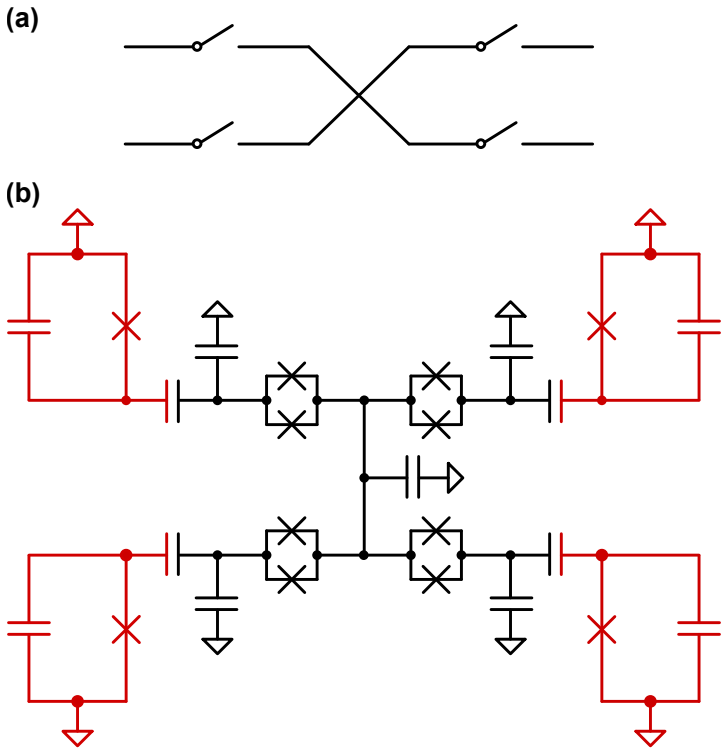

Figure 4.3: (a) Schematic of a microwave router with four ports and (b) its circuit with each port capacitively coupled to a transmon qubit.

quantum nodes meter away in previous chapters, here we focus on placing the processing units millimeters away and linking them with the flip-chip technique. Since the quantum channels – transmission lines are relatively short and open-ended, we can simply model them as some capacitors to ground.

In the following section, we will try to quantize the circuit and determine the circuit parameters.

4.3 Numerical simulation

To simplify the discussion, we start with a two-port router, with the circuit shown in Fig. 4.4. We also add the junction capacitance in the circuit. Note that this circuit can be treated as a two-SQUID version of the circuit in Fig. 1.35(b). Here we use a single junction to represent a tunable SQUID to simplify the notations.

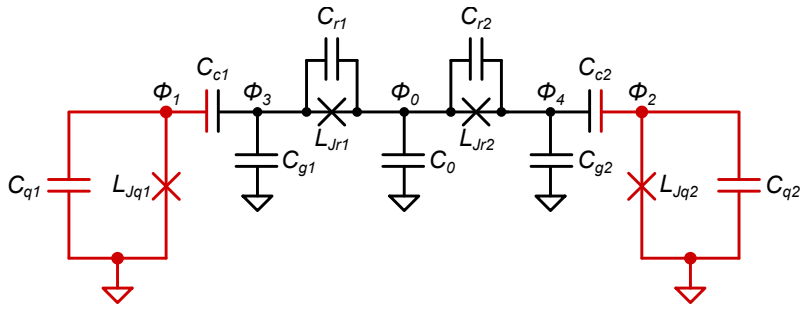

Figure 4.4: Circuit for a router with two ports.

Like what we did in Sections 1.2 and 1.4, we start from its Lagrangian $\mathcal{L}$,

$$\mathcal{L} = T - U. \tag{4.1}$$

The kinetic energy T is

$$\begin{aligned} T = \frac{1}{2}\Big(\frac{\Phi_0}{2\pi}\Big)^2 \big[&C_0\dot{\phi}_0^2 + C_{q1}\dot{\phi}_1^2 + C_{c1}(\dot{\phi}_3 - \dot{\phi}_1)^2 + C_{g1}\dot{\phi}_3^2 + C_{r1}(\dot{\phi}_0 - \dot{\phi}_3)^2 \\ &+ C_{q2}\dot{\phi}_2^2 + C_{c2}(\dot{\phi}_4 - \dot{\phi}_2)^2 + C_{g2}\dot{\phi}_4^2 + C_{r2}(\dot{\phi}_0 - \dot{\phi}_4)^2\big], \end{aligned} \tag{4.2}$$

where $\phi_k = 2\pi\Phi_k/\Phi_0$ is the Josephson phase. The potential energy U is

$$U = -E_{Jq1}\cos\phi_1 - E_{Jq2}\cos\phi_2 - E_{Jr1}\cos(\phi_3 - \phi_0) - E_{Jr2}\cos(\phi_4 - \phi_0), \tag{4.3}$$

where $E_{Jk} = \hbar^2/2e^2L_{Jk}$ is the Josephson energy. We can introduce the new flux variables as

$$\phi_0 = \phi_0, \tag{4.4}$$

$$\phi_{q1} = \phi_1, \tag{4.5}$$

$$\phi_{r1} = \phi_3 - \phi_0, \tag{4.6}$$

$$\phi_{q2} = \phi_2, \tag{4.7}$$

$$\phi_{r2} = \phi_4 - \phi_0. \tag{4.8}$$

The potential energy U becomes

$$U = -E_{Jq1}\cos\phi_{q1} - E_{Jq2}\cos\phi_{q2} - E_{Jr1}\cos\phi_{r1} - E_{Jr2}\cos\phi_{r2}. \tag{4.9}$$

In the basis of $\vec{\phi} = [\phi_0, \phi_{q1}, \phi_{r1}, \phi_{q2}, \phi_{r2}]^T$, the kinetic energy T can be rewritten as

$$T = \frac{1}{2}\Big(\frac{\Phi_0}{2\pi}\Big)^2 \dot{\vec{\phi}}^{\,T}\mathbf{C}\dot{\vec{\phi}}, \tag{4.10}$$

where the capacitance matrix $\mathbf{C}$ is,

$$\mathbf{C} = \begin{bmatrix} C_0 + C_{c1} + C_{g1} + C_{c2} + C_{g2} & -C_{c1} & C_{g1} + C_{c1} & -C_{c2} & C_{g2} + C_{c2} \\ -C_{c1} & C_{q1} + C_{c1} & -C_{c1} & 0 & 0 \\ C_{g1} + C_{c1} & -C_{c1} & C_{c1} + C_{g1} + C_{r1} & 0 & 0 \\ -C_{c2} & 0 & 0 & C_{q2} + C_{c2} & -C_{c2} \\ C_{g2} + C_{c2} & 0 & 0 & -C_{c2} & C_{c2} + C_{g2} + C_{r2} \end{bmatrix}. \tag{4.11}$$

From the Lagrangian $\mathcal{L}$, the conjugate coordinate to $\vec{\phi}$ can be written as

$$\vec{q} = \frac{\partial\mathcal{L}}{\partial\dot{\vec{\phi}}} = \frac{\partial T}{\partial\dot{\vec{\phi}}} = \Big(\frac{\Phi_0}{2\pi}\Big)^2\mathbf{C}\dot{\vec{\phi}}, \tag{4.12}$$

where $\vec{q} = [q_0, q_{q1}, q_{r1}, q_{q2}, q_{r2}]^T$. We can get the Hamiltonian H,

$$H = \vec{q}^{\,T}\dot{\vec{\phi}} - \mathcal{L} = \frac{1}{2}\Big(\frac{2\pi}{\Phi_0}\Big)\vec{q}^{\,T}\mathbf{C}^{-1}\vec{q} + U. \tag{4.13}$$

We can throw away the terms associated with q_0 and ϕ_0 because $\dot{q}_0 = 0$. The charge q_0 gives a uniform charge on the qubits' and couplers' pads. By defining $n = q/\hbar$ and calculating

$\mathbf{C}^{-1}$, we can get the Hamiltonian H written in ϕ and n,

$$\begin{aligned} H &= 4E_{Cq1}n_{q1}^2 + 4E_{Cq2}n_{q2}^2 + 4E_{Cr1}n_{r1}^2 + 4E_{Cr2}n_{r2}^2 \\ &+ 4E_{Cq1,q2}n_{q1}n_{q2} + 4E_{Cr1,r2}n_{r1}n_{r2} + 4E_{Cq1,r2}n_{q1}n_{r2} + 4E_{Cq2,r1}n_{q2}n_{r1} \\ &+ 4E_{Cq1,r1}n_{q1}n_{r1} + 4E_{Cq2,r2}n_{q2}n_{r2} \\ &- E_{Jq1}\cos\phi_{q1} - E_{Jq2}\cos\phi_{q2} - E_{Jr1}\cos\phi_{r1} - E_{Jr2}\cos\phi_{r2}, \end{aligned} \tag{4.14}$$

where $E_{C,kl} = e^2[\mathbf{C}^{-1}]_{kl}$ and $E_{C,k} = e^2[\mathbf{C}^{-1}]_{kk}/2$ with $\{k,l\} \in \{q_1, q_2, r_1, r_2\}$. Note that $E_{C,ij}$ can be negative. With the canonical quantization, we have the commutation relation between ϕ_k and n_k,

$$[\phi_k, n_k] = i. \tag{4.15}$$

The creation and annihilation operators can be defined as

$$a_k = \frac{1}{\sqrt{2}}\left(\left(\frac{E_{Jk}}{8E_{Ck}}\right)^{\frac{1}{4}}\phi_k + i\left(\frac{8E_{Ck}}{E_{Jk}}\right)^{\frac{1}{4}}n_k\right), \tag{4.16}$$

$$a_k^\dagger = \frac{1}{\sqrt{2}}\left(\left(\frac{E_{Jk}}{8E_{Ck}}\right)^{\frac{1}{4}}\phi_k - i\left(\frac{8E_{Ck}}{8E_{Jk}}\right)^{\frac{1}{4}}n_k\right). \tag{4.17}$$

In the transmon limit ($E_{Jk} \gg E_{Ck}$, which doesn't hold when L_{Jk} is very large), we can expand the cosine terms in the Hamiltonian, which gives us the Hamiltonian of coupled Duffing oscillators,

$$\begin{aligned} H/\hbar = &\sum_k^{q_1,q_2,r_1,r_2}\left(\omega_k a_k^\dagger a_k + \frac{\eta_k}{2}a_k^\dagger a_k^\dagger a_k a_k\right) - \sum_{k,l}^{1,2} g_{qkrl}(a_{qk}^\dagger - a_{qk})(a_{rl}^\dagger - a_{rl}) \\ &- g_{q1q2}(a_{q1}^\dagger - a_{q1})(a_{q2}^\dagger - a_{q2}) - g_{r1r2}(a_{r1}^\dagger - a_{r1})(a_{r2}^\dagger - a_{r2}), \end{aligned} \tag{4.18}$$

where we have

$$\omega_k = \sqrt{8E_{Jk}E_{Ck}}/\hbar - E_{Ck}/\hbar, \tag{4.19}$$

$$\eta_k = -E_{Ck}/\hbar, \tag{4.20}$$

$$g_{kl} = \frac{E_{Ck,l}}{\sqrt{2}\hbar}\left(\frac{E_{Jk}}{E_{Ck}}\frac{E_{Jl}}{E_{Cl}}\right)^{\frac{1}{4}}. \tag{4.21}$$

The coupling strength g_{kl} satisfy,

$$g_{q1q2},\ g_{q1r1},\ g_{q2r2},\ g_{r1r2} > 0, \tag{4.22}$$

$$g_{q1r2},\ g_{q2r1} < 0, \tag{4.23}$$

$$|g_{q1r2}|,\ |g_{q2r1}|,\ g_{q1r1},\ g_{q2r2},\ g_{r1r2} \gg g_{q1q2}. \tag{4.24}$$

To extract the effective qubit-qubit coupling strength, we can use the Schrieffer-Wolff transformation (see Appendix C) to decouple the router modes from the qubit modes, i.e. eliminate terms like $g_{qkrl}(a_{qk} - a_{qk}^\dagger)(a_{rl} - a_{rl}^\dagger)$ in the Hamiltonian. We can write the total Hamiltonian H as

$$H = H_q + H_r + H_{qq} + H_{rr} + H_{qr}. \tag{4.25}$$

We want to find a unitary transformation $U = e^S$ where S is anti-Hermitian so that the transformed Hamiltonian H' will be

$$H' = e^S H e^{-S} = H'_q + H'_r + H'_{qq} + H'_{rr}. \tag{4.26}$$

We need S to satisfy

$$H_{qr} + [S, H_q + H_r + H_{qq} + H_{rr}] = 0. \tag{4.27}$$

Here we assume S has the form

$$S = \sum_{m,n}^{1,2} x_{mn}(a^\dagger_{qm}a_{rn} - a_{qm}a^\dagger_{rn}) + y_{mn}(a^\dagger_{qm}a^\dagger_{rn} - a_{qm}a_{rn}). \tag{4.28}$$

To determine the coefficients x_{mn} and y_{mn}, we calculate all the commutators,

$$[a^\dagger_{qm}a_{rn} - a_{qm}a^\dagger_{rn}, a^\dagger_{qm}a_{qm}] = -a^\dagger_{qm}a_{rn} - a_{qm}a^\dagger_{rn}, \tag{4.29}$$

$$[a^\dagger_{qm}a_{rn} - a_{qm}a^\dagger_{rn}, a^\dagger_{rn}a_{rn}] = a^\dagger_{qm}a_{rn} + a_{qm}a^\dagger_{rn}, \tag{4.30}$$

$$[a^\dagger_{qm}a_{rn} - a_{qm}a^\dagger_{rn}, a^\dagger_{qm}a^\dagger_{qm}a_{qm}a_{qm}] = -2a^\dagger_{qm}a^\dagger_{qm}a_{qm}a_{rn} - 2a^\dagger_{qm}a_{qm}a_{qm}a^\dagger_{rn}, \tag{4.31}$$

$$[a^\dagger_{qm}a_{rn} - a_{qm}a^\dagger_{rn}, a^\dagger_{rn}a^\dagger_{rn}a_{rn}a_{rn}] = 2a^\dagger_{qm}a^\dagger_{rn}a_{rn}a_{rn} + 2a_{qm}a^\dagger_{rn}a^\dagger_{rn}a_{rn}, \tag{4.32}$$

$$\begin{aligned}&[a^\dagger_{qm}a_{rn} - a_{qm}a^\dagger_{rn}, a^\dagger_{qk}a_{ql} + a_{qk}a^\dagger_{ql} - a^\dagger_{qk}a^\dagger_{ql} - a_{qk}a_{ql}]\\ &= \delta_{mk}(-a^\dagger_{ql}a_{rn} - a_{ql}a^\dagger_{rn} + a^\dagger_{ql}a^\dagger_{rn} + a_{ql}a_{rn})\\ &\qquad + \delta_{ml}(-a^\dagger_{qk}a_{rn} - a_{qk}a^\dagger_{rn} + a^\dagger_{qk}a^\dagger_{rn} + a_{qk}a_{rn}),\end{aligned} \tag{4.33}$$

$$\begin{aligned}&[a^\dagger_{qm}a_{rn} - a_{qm}a^\dagger_{rn}, a^\dagger_{rk}a_{rl} + a_{rk}a^\dagger_{rk} - a^\dagger_{rk}a^\dagger_{rl} - a_{rk}a_{rl}]\\ &= \delta_{nk}(a^\dagger_{qm}a_{rl} + a_{qm}a^\dagger_{rl} - a^\dagger_{qm}a^\dagger_{rl} - a_{qm}a_{rl})\\ &\qquad + \delta_{nl}(a^\dagger_{qm}a_{rk} + a_{qm}a^\dagger_{rk} - a^\dagger_{qm}a^\dagger_{rk} - a_{qm}a_{rk}),\end{aligned} \tag{4.34}$$

$$\begin{aligned}&[a^\dagger_{qm}a_{rn} - a_{qm}a^\dagger_{rn}, a^\dagger_{qk}a_{rl} + a_{qk}a^\dagger_{rl} - a^\dagger_{qk}a^\dagger_{rl} - a_{qk}a_{rl}]\\ &= \delta_{nl}(a^\dagger_{qm}a_{qk} + a_{qm}a^\dagger_{qk} - a^\dagger_{qm}a^\dagger_{qk} - a_{qm}a_{qk})\\ &\qquad - \delta_{mk}(a^\dagger_{rn}a_{rl} + a_{rn}a^\dagger_{rl} - a^\dagger_{rn}a^\dagger_{rl} - a_{rn}a_{rl}),\end{aligned} \tag{4.35}$$

$$[a^\dagger_{qm}a^\dagger_{rn} - a_{qm}a_{rn}, a^\dagger_{qm}a_{qm}] = -a^\dagger_{qm}a^\dagger_{rn} - a_{qm}a_{rn}, \tag{4.36}$$

$$[a^\dagger_{qm}a^\dagger_{rn} - a_{qm}a_{rn}, a^\dagger_{rn}a_{rn}] = -a^\dagger_{qm}a^\dagger_{rn} - a_{qm}a_{rn}, \tag{4.37}$$

$$[a^\dagger_{qm}a^\dagger_{rn} - a_{qm}a_{rn}, a^\dagger_{qm}a^\dagger_{qm}a_{qm}a_{qm}] = -2a^\dagger_{qm}a^\dagger_{qm}a_{qm}a_{rn} - 2a^\dagger_{qm}a_{qm}a_{qm}a^\dagger_{rn}, \tag{4.38}$$

$$[a^\dagger_{qm}a^\dagger_{rn} - a_{qm}a_{rn}, a^\dagger_{rn}a^\dagger_{rn}a_{rn}a_{rn}] = -2a^\dagger_{qm}a^\dagger_{rn}a^\dagger_{rn}a_{rn} - 2a_{qm}a^\dagger_{rn}a_{rn}a_{rn}, \tag{4.39}$$

$$
\begin{aligned}
&[a^\dagger_{qm}a^\dagger_{rn} - a_{qm}a_{rn}, a^\dagger_{qk}a_{ql} + a_{qk}a^\dagger_{qk} - a^\dagger_{qk}a^\dagger_{ql} - a_{qk}a_{ql}] \\
&= \delta_{mk}(a^\dagger_{ql}a_{rn} + a_{ql}a^\dagger_{rn} - a^\dagger_{ql}a^\dagger_{rn} - a_{ql}a_{rn}) \\
&\qquad + \delta_{ml}(a^\dagger_{qk}a_{rn} + a_{qk}a^\dagger_{rn} - a^\dagger_{qk}a^\dagger_{rn} - a_{qk}a_{rn}), \qquad (4.40) \\
&[a^\dagger_{qm}a^\dagger_{rn} - a_{qm}a_{rn}, a^\dagger_{rk}a_{rl} + a_{rk}a^\dagger_{rk} - a^\dagger_{rk}a^\dagger_{rl} - a_{rk}a_{rl}] \\
&= \delta_{nk}(a^\dagger_{qm}a_{rl} + a_{qm}a^\dagger_{rl} - a^\dagger_{qm}a^\dagger_{rl} - a_{qm}a_{rl}) \\
&\qquad + \delta_{nl}(a^\dagger_{qm}a_{rk} + a_{qm}a^\dagger_{rk} - a^\dagger_{qm}a^\dagger_{rk} - a_{qm}a_{rk}), \qquad (4.41) \\
&[a^\dagger_{qm}a^\dagger_{rn} - a_{qm}a_{rn}, a^\dagger_{qk}a_{rl} + a_{qk}a^\dagger_{rl} - a^\dagger_{qk}a^\dagger_{rl} - a_{qk}a_{rl}] \\
&= \delta_{nl}(a^\dagger_{qm}a_{qk} + a_{qm}a^\dagger_{qk} + a^\dagger_{qm}a^\dagger_{qk} - a_{qm}a_{qk}) \\
&\qquad + \delta_{mk}(a^\dagger_{rn}a_{rl} + a_{rn}a^\dagger_{rl} + a^\dagger_{rn}a^\dagger_{rl} - a_{rn}a_{rl}). \qquad (4.42)
\end{aligned}
$$

To satisfy Eq. 4.3, the coefficients x_{mn} and y_{mn} need to satisfy

$$
\begin{bmatrix}
0 & 0 & -g_{r1r2} & g_{q1q2} & -\Sigma_{q1r1} & 0 & -g_{r1r2} & -g_{q1q2} \\
0 & 0 & g_{q1q2} & -g_{r1r2} & 0 & -\Sigma_{q2r2} & -g_{q1q2} & -g_{r1r2} \\
-g_{r1r2} & g_{q1q2} & 0 & 0 & -g_{r1r2} & -g_{q1q2} & -\Sigma_{q1r2} & 0 \\
g_{q1q2} & -g_{r1r2} & 0 & 0 & -g_{q1q2} & -g_{r1r2} & 0 & -\Sigma_{q2r1} \\
-\Delta_{q1r1} & 0 & g_{r1r2} & -g_{q1q2} & 0 & 0 & g_{r1r2} & g_{q1q2} \\
0 & -\Delta_{q2r2} & -g_{q1q2} & g_{r1r2} & 0 & 0 & g_{q1q2} & g_{r1r2} \\
g_{r1r2} & -g_{q1q2} & -\Delta_{q1r2} & 0 & g_{r1r2} & g_{q1q2} & 0 & 0 \\
-g_{q1q2} & g_{r1r2} & 0 & -\Delta_{q2r1} & g_{q1q2} & g_{r1r2} & 0 & 0
\end{bmatrix}
\begin{bmatrix} x_{11} \\ x_{22} \\ x_{12} \\ x_{21} \\ y_{11} \\ y_{22} \\ y_{12} \\ y_{21} \end{bmatrix}
=
\begin{bmatrix} g_{q1r1} \\ g_{q2r2} \\ g_{q1r2} \\ g_{q2r1} \\ -g_{q1r1} \\ -g_{q2r2} \\ -g_{q1r2} \\ -g_{q2r1} \end{bmatrix},
\qquad (4.43)
$$

where

$$
\Sigma_{qmrn} = \omega_{qm} + \omega_{rn}, \qquad (4.44)
$$

$$
\Delta_{qmrn} = \omega_{qm} - \omega_{rn}. \qquad (4.45)
$$

Here, we ignore the terms related to anharmonicity for simplicity. When $g_{q1q2},\ g_{r1r2} \ll |\Delta_{qmrn}|$, the coefficients x_{mn} and y_{mn} become

$$x_{mn} = \frac{g_{qmrn}}{\Delta_{qmrn}}, \tag{4.46}$$

$$y_{mn} = -\frac{g_{qmrn}}{\Sigma_{qmrn}}, \tag{4.47}$$

which have the same form as in Ref. [148]. However, $g_{r1r2} \sim |\Delta_{qmrn}|$ in our case. Thus, we can only solve Eq. 4.43 numerically. The effective coupling strength g_{eff} between two qubits is

$$g_{\text{eff}} = g_{q1q2} + \frac{1}{2}\big((x_{11}+y_{11})g_{q2r1} + (x_{22}+y_{22})g_{q1r2} + (x_{12}+y_{12})g_{q2r2} + (x_{21}+y_{21})g_{q1r1}\big). \tag{4.48}$$

The frequencies of the dressed qubit states are

$$\widetilde{\omega}_{q1} = \omega_{q1} + (x_{11} + y_{11})g_{q1r1} + (x_{12} + y_{12})g_{q1r2}, \tag{4.49}$$

$$\widetilde{\omega}_{q2} = \omega_{q2} + (x_{21} + y_{21})g_{q2r1} + (x_{22} + y_{22})g_{q2r2}. \tag{4.50}$$

The ZZ coupling ζ between two qubits can also be calculated by the perturbation theory [149]. However, the analytical formula will be very complicated because more modes are involved in our circuit.

The interaction strength g_{eff} can also be calculated using the impedance analysis as we discussed in Section 1.2.4 by treating the junctions as linear inductors. We can calculate the input impedance $Z_{\text{in}}(\omega)$ from one point to the ground. The zeros and poles of $\text{Im}[Z_{\text{in}}(\omega)]$ give the resonances in the circuit. If we bring the two qubits on resonance, the effective coupling strength g_{eff} is given by the splitting of the bare qubit frequencies,

$$g_{\text{eff}} = \frac{1}{2}(\omega_1 - \omega_2), \tag{4.51}$$

where ω_1 and ω_2 are the two closest frequencies to the bare qubit frequencies. This method requires the circuit to be symmetric, i.e. the two qubits have the same bare frequency. Otherwise, we need to scan one qubit frequency to get the energy splitting $2|g_{\text{eff}}|$, which is time-consuming. This linear impedance analysis doesn't consider the junction non-linearity, which cannot be used to calculate the ZZ-interaction strength ζ.

Refs. [235, 236] present a way to calculate the coupling strength g_{eff} and ZZ interaction strength ζ from the impedance of the coupler while considering the weak non-linearity of the transmons. Their results are summarized in Appendix F. With their results, we can efficiently calculate the coupling strength g_{eff} and ZZ interaction strength ζ from the impedance of the circuit. Note that this method requires that all the modes work in the transmon limit and $|\omega_{q1} - \omega_{q2}| \gg |g_{\text{eff}}|$ when calculating the ZZ interaction strength ζ. We will call it Z-method.

Furthermore, we can directly quantize the circuit numerically using Python packages like scQubit [237, 238] and SQcircuit [239]. Similar to what we did in the impedance analysis, we calculate all the eigenenergies of the system. When the two qubits are on resonance, the effective coupling strength is given by the splitting of the qubit frequencies as we discussed. Similar to the linear impedance analysis, if the two qubits have different bare frequencies, i.e. the circuit is not symmetric, we need to scan one qubit frequency to get the energy splitting $2|g_{\text{eff}}|$, which is very time-consuming. The ZZ interaction strength ζ is given by

$$\zeta = \widetilde{\omega}_{|ee\rangle} - \widetilde{\omega}_{|ge\rangle} - \widetilde{\omega}_{|eg\rangle}, \tag{4.52}$$

where $\widetilde{\omega}_{|ij\rangle}$ is the energy of the dressed qubit state $|ij\rangle$. Although direct diagonalization can give us the exact values, the calculation times grow exponentially with the number of modes in the system and are much slower than the other methods we mentioned above. We first apply the other methods to determine the system parameters and then verify the results by direct diagonalization.

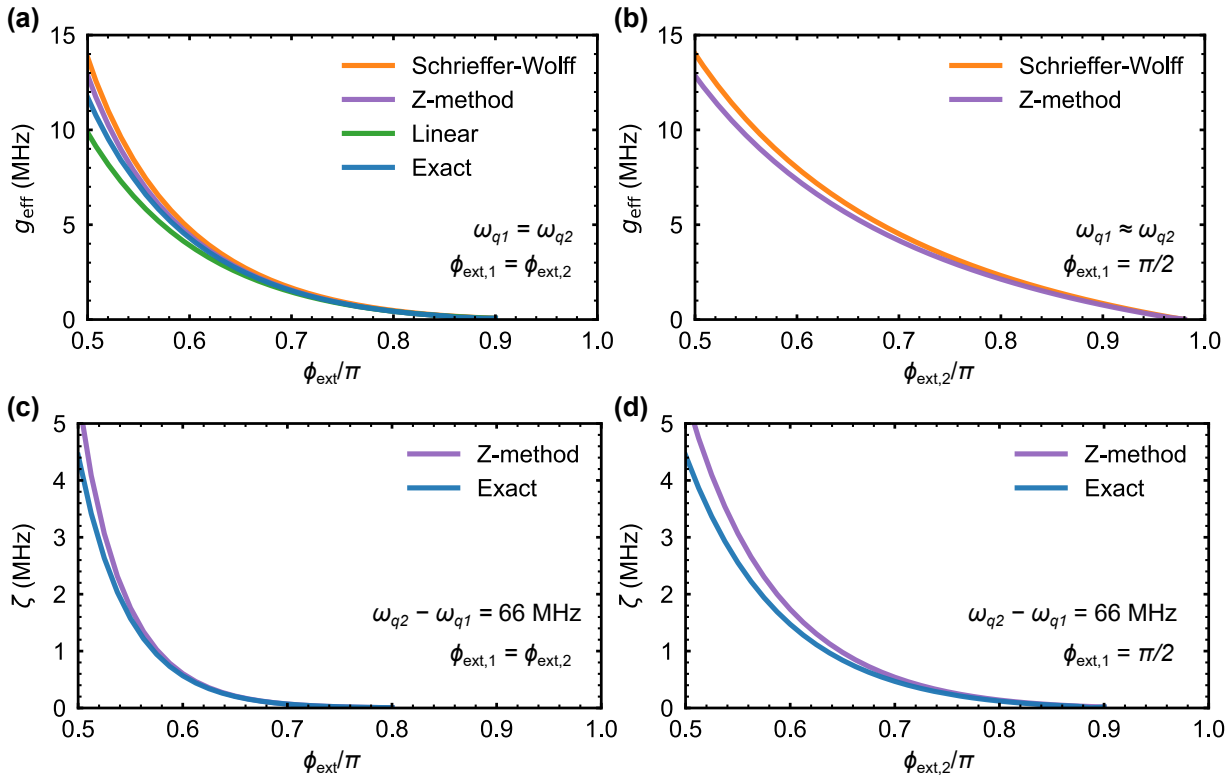

Figure 4.5: Qubit-qubit couplings with a two-port router. (a) Qubit-qubit effective coupling strength $g_{\rm eff}$ and (c) ZZ interaction strength ζ by tuning the two external fluxes $\phi_{\rm ext,1}$ and $\phi_{\rm ext,2}$ simultaneously, $\phi_{\rm ext,1} = \phi_{\rm ext,2} = \phi_{\rm ext}$. (b) Qubit-qubit effective coupling strength $g_{\rm eff}$ and (d) ZZ interaction strength ζ by fixing one switch on, $\phi_{\rm ext,1} = \pi/2$ and tuning the other external flux $\phi_{\rm ext,2}$. Different colors label different calculation methods. The related circuit parameters are listed in the main text.

We compare different approaches as shown in Fig. 4.5. We tune the router junction L_{Jrk} by tuning the external flux $\phi_{{\rm ext},k}$ through the SQUID loop, $L_{Jrk} = L_{Jr}/\cos(\phi_{{\rm ext},k}/2)$. In Fig. 4.5(a), we tune $\phi_{\rm ext,1}$ and $\phi_{\rm ext,2}$ simultaneously and make the circuit symmetric. All methods mentioned above can be used to calculate the effective coupling strength $g_{\rm eff}$. The related parameters are $C_q = 100$ fF, $C_c = 20$ fF, $C_r = 7.5$ fF, $C_g = 420$ fF, $C_0 = 780$ fF, $L_{Jr} = 4$ nH and $L_{Jq} = 8$ nH, which give the qubit frequencies $\omega_{q1}/2\pi = \omega_{q2}/2\pi = 4.988$ GHz and qubit anharmonicities $\eta_{q1}/2\pi = \eta_{q2}/2\pi = -172$ MHz. From Fig. 4.5(a), we can see that the couplings calculated by the perturbation theory (Schrieffer-Wolff transformation) and Z-method agree well with the exact values obtained by diagonalization using SQcircuit.

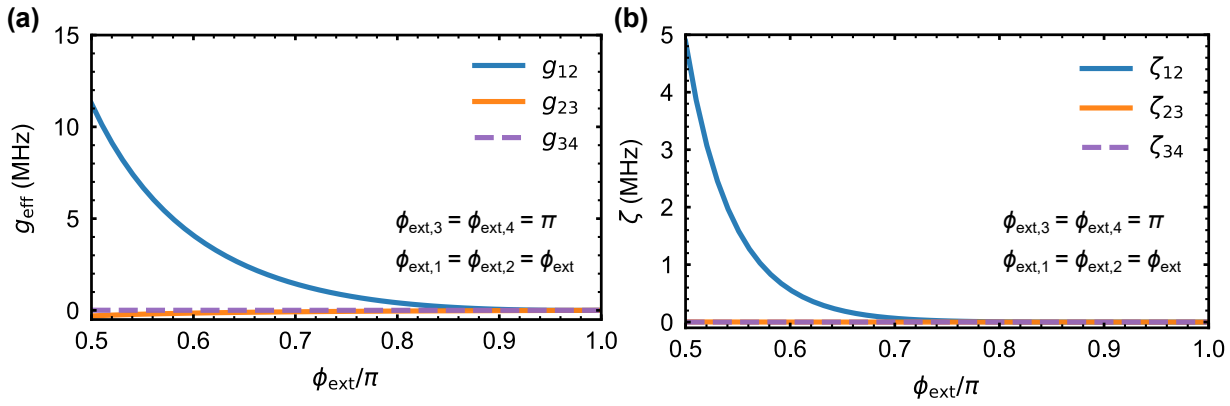

Figure 4.6: Qubit-qubit couplings with a four-port router. (a) The effective coupling strength g_{ij} and ZZ interaction strength ζ_{ij} between the ith and jth qubits by turning off the switches connected to qubits Q_3 and Q_4, $\phi_{\text{ext},3} = \phi_{\text{ext},4} = \pi$, and the turn on the switches connected to qubits Q_1 and Q_2 simultaneously, $\phi_{\text{ext},1} = \phi_{\text{ext},2} = \phi_{\text{ext}}$. All the values are calculated using the Z-method and the related circuit parameters are listed in the main text.

To demonstrate that we can turn off the coupling by tuning one switch, we fix $\phi_{\text{ext},1} = \pi/2$ (switch on) and tune $\phi_{\text{ext},2}$. Because $\phi_{\text{ext},1}$ and $\phi_{\text{ext},2}$ are different, ω_{q1} and ω_{q2} are slightly detuned. To extract the effective coupling from diagonalization and linear impedance analysis, we need to sweep one qubit frequency, which is very time-consuming. Here we present the results calculated by the Schrieffer-Wolff transformation and Z-method shown in Fig. 4.5(b). We can see that tuning $\phi_{\text{ext},2}$ close to π can turn off the coupling. The residual couplings (< 15 kHz) come from the small coupler junction capacitance. The coupler junction capacitance can be reduced by using larger L_{Jr} (smaller junction area). However, larger L_{Jr} requires a larger ϕ_{ext} tuning range to get the target coupling strength.

We use the Z-method and diagonalization to calculate the ZZ interaction strength ζ. To calculate ζ using the Z-method, we tune the second qubit frequency $\omega_{q2}/2\pi$ to 5.054 GHz by setting $L_{Jq2} = 7.8$ nH. In Fig. 4.5(c-d), we show that when we turn off the coupling, the ZZ interaction ζ also goes to zero. Note that if we bring two qubits on resonance, the calculated ζ by diagonalization is very close to the values when the two qubits are detuned.

The two-port circuit can be extended to a four-port circuit as is shown in Fig. 4.3. Here we use the same circuit parameters as in the two-node circuit. We detune the four qubits

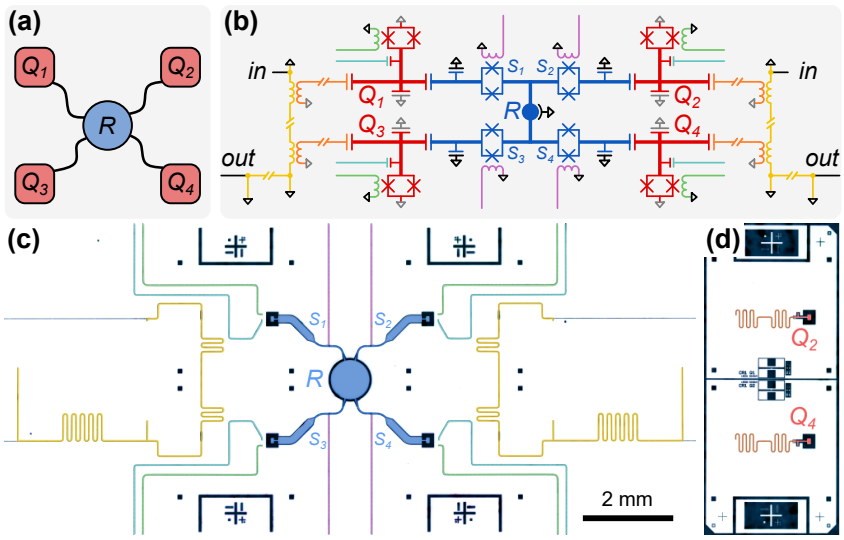

Figure 4.7: (a) Schematic of the device: four qubits Q_i (red) are coupled to a router R (blue); (b) Circuit diagram: four transmons (red) are capacitively coupled to the router (blue). Each transmon is controlled by a flux line (green) and a drive line (cyan), and dispersively readout by a $\lambda/4$ resonator (orange). Each two of the readout resonators are coupled to a two-stage bandpass Purcell filter (yellow) (see Section 1.4.4). There are four flux lines (purple) to tune the flux across the SQUID loops in the router. (c) Layout for the motherboard with the router and all control wires. (d) Layout for the daughterboard with two qubits and their readout resonators.

by changing their junction inductance $L_{Jq1} = L_{Jq3} = 8$ nH and $L_{Jq2} = L_{Jq4} = 7.8$ nH, which give the qubit frequencies $\omega_{q1}/2\pi = \omega_{q3}/2\pi = 4.988$ GHz and $\omega_{q2}/2\pi = \omega_{q4}/2\pi = 5.054$ GHz. Here to demonstrate that we can selectively turn on the coupling between the qubit pair, we turn off the switches connected to qubits Q_3 and Q_4 and turn on the switches connected to qubits Q_1 and Q_2. The effective coupling strength g_{ij} and ZZ interaction strength ζ_{ij} between the ith and jth qubits calculated by the Z-method are shown in Fig. 4.6. We can see that when the coupling between Q_1 and Q_2 is on, the other qubits remain uncoupled. This demonstrates the scalability of our approach.

4.4 Experimental realization

With the numerical simulation, we can determine the target parameters. The full circuit of the device is shown in Fig. 4.7(b), where we omit the junction capacitors and include all the

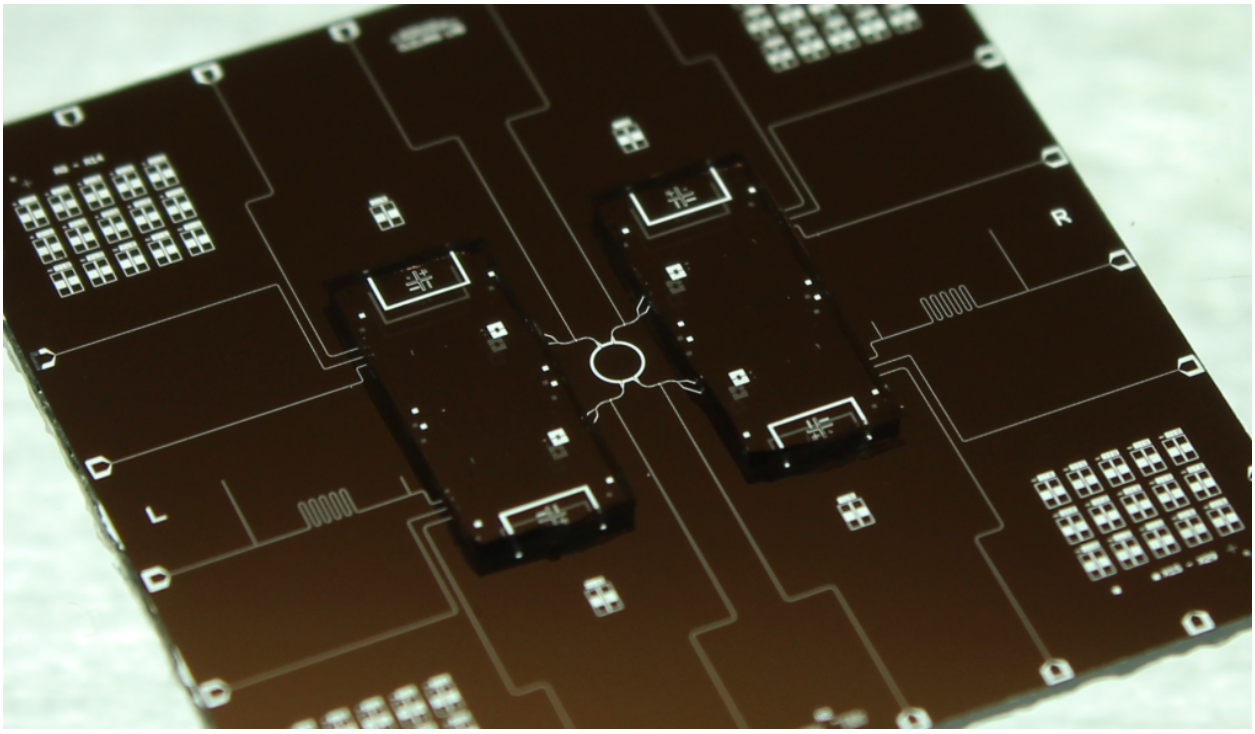

Figure 4.8: Photo of the assembled device, with two daughterboards sitting on one motherboard. The motherboard is 20 mm × 20 mm and the daughterboards are 3 mm × 7 mm. This device was fabricated by Xuntao Wu.

control lines. To determine the actual device layout, we use Sonnet to simulate the layout. Examples using Sonnet for circuit simulation can be found in Ref. [77]. We make the qubits and their readout resonators on a separate chip to demonstrate the modularity of our design, with the layouts shown in Fig. 4.7(c) and (d). There are two qubits on one daughterboard. Two daughterboards are flip-chip [240, 122] bonded on the motherboard which contains the router and all the control lines. Note that the daughterboards are non-galvanically connected to the motherboard. Thus their grounds are not connected. We use different colors to mark their grounds in Fig. 4.7(b) (grey and black).

We follow the process in Appendix G to fabricate the sample. The size of the motherboard is 20 mm×20 mm, which is the same as the three-node sample introduced in Chapter 3. Each daughterboard is 3 mm × 7 mm. The assembled device is shown in Fig. 4.8. The device is wire-bonded to the sample box and cooled down in a dilution refrigerator for measurement.

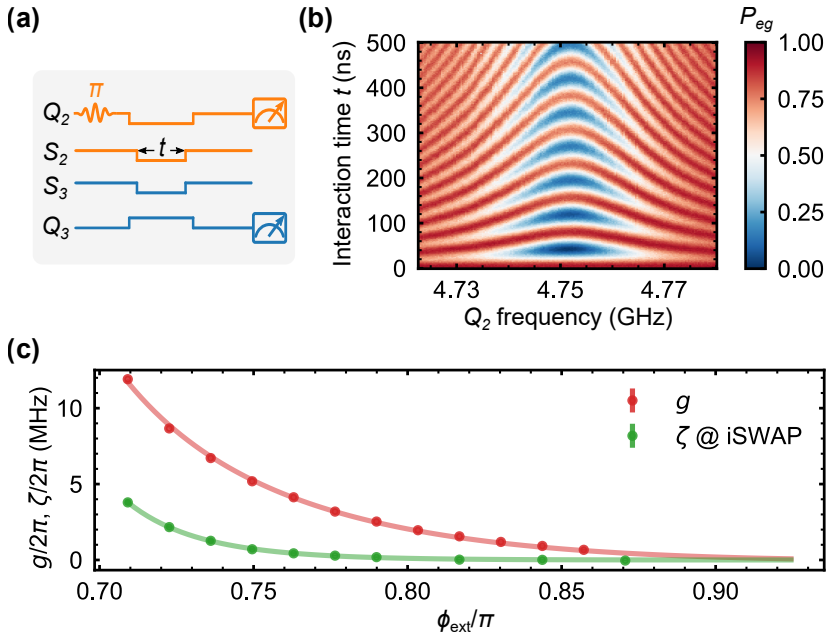

Figure 4.9: Router characterization. (a) The pulse sequence of Rabi swaps between Q_2 and Q_3, with switch pulses shorter than qubit flux pulses. (b) By sweeping the qubit Q_2 frequency, we generate a chevron pattern. (c) Effective coupling strength g, and parasitic ZZ interaction strength ζ between Q_2 and Q_3, as a function of switch external fluxes ϕ_{ext}, from on (left) to off (right).

The measurement setup can be found in Appendix H. We operate all the qubits at the frequencies $\omega_q/2\pi$ around 4.6 GHz. All the qubits have anharmonicities $\eta/2\pi \sim -170$ MHz, relaxation times $T_1 \sim 30$ μs and pure dephasing times $T_\phi \sim 800$ ns.

We use the pulse sequence in Fig. 4.9(a) to calibrate the router. During the qubit idling times, we bias all the switches to the "off" status. We excite one qubit Q_i to its $|e\rangle$ by an X gate. Then we turn on the switches S_i and S_j which are connected to Q_i and Q_j and biasing the frequencies of Q_i and Q_j. When sweeping the frequency of one qubit Q_i, we can generate a chevron pattern as is shown in Fig. 4.9(b), from which we can determine the qubit-qubit coupling strength g. By scanning the external fluxes ϕ_{ext} across across S_i and S_j ($\phi_{\text{ext}} = \phi_{\text{ext},i} = \phi_{\text{ext},j}$), we can get how the coupling strength g changes as ϕ_{ext} as is shown in Fig. 4.9(c). To extract the ZZ interaction strength ζ, we perform a cross-Ramsey-type experiment [156]. We first prepare the qubits in $(|eg\rangle + |gg\rangle)/\sqrt{2}$ or $(|ee\rangle + |ge\rangle)/\sqrt{2}$

states. By measuring the phase accumulation on the state $|ee\rangle$ after an iSWAP gate, we can determine the ZZ interaction strength ζ. The measured ζ versus ϕ_{ext} is shown in Fig. 4.9(c). The measured results match well with the numerical simulations (solid lines).

As we discussed in Section 1.4.5, bringing $|ee\rangle$ on resonance with $|gf\rangle$ with a duration of $\tau_{\text{CZ}} = \pi/\sqrt{2}g$, we can realize a CZ gate between two qubits. We use cross-entropy benchmarking (XEB) (see Section 1.4.6) to benchmark the CZ gates between all six qubit pairs. We can get an average gate fidelity $\mathcal{F}_{\text{CZ}}$ of $96.00 \pm 0.10\%$ with a duration of around 40 ns, and best fidelity of $97.14 \pm 0.04\%$, mainly limited by dephasing of the qubits. If we assume the qubit relaxation times T_1 are 100 μs and no extra dephasing, the simulated gate fidelity $\mathcal{F}_{\text{CZ}}$ can be as high as 99.5%, above the surface code threshold [13]. By simultaneously applying single qubits on the uncoupled qubits during the two-qubit gate benchmarking sequence, we find that the gate fidelities (both single-qubit and two-qubit gates) are not affected, indicating negligible interference when the switches are turned off.

4.5 Outlook

With this router design, we present a hardware-efficient way to link multiple quantum processors for future fault-tolerant distributed quantum computing architectures [22]. Current performance is mainly limited by the qubit coherence times and pulse distortions, which can be further improved by the fabrication process [241, 242] and pulse shaping [243, 244]. When the quantum processors are placed further apart, this design can also realize the routing of itinerant microwave photons [141, 187, 186]. In addition, when more than two switches are turned on simultaneously, we can directly synthesize multi-qubit entangling gates [245, 158, 246]. With enhanced connectivity, we can also perform error correction codes with higher thresholds and lower overhead [247, 248] or investigate quantum many-body dynamics that rely on high connectivity.

APPENDIX A

QUANTUM LINEAR RESPONSE THEORY

Here we consider a system with Hamiltonian H applied with some external field $H_{\text{ext}} = f(t)B$, where B is an operator in the system. The total Hamiltonian is $H_{\text{tot}} = H + H_{\text{ext}}$. We want to study the system's response to the external field. For an operator A in the system, we have

$$\delta\langle A(t)\rangle = -i\int_{-\infty}^{t} \mathrm{d}t' \langle [A(t), B(t')]\rangle f(t'), \tag{A.1}$$

where $\delta\langle A(t)\rangle$ is the difference of $\langle A(t)\rangle$ with and without the external field and we keep terms to first order in $f(t)$. The above equation can be written as

$$\delta\langle A(t)\rangle = \int_{-\infty}^{\infty} \mathrm{d}t' G^R_{AB}(t-t') f(t'), \tag{A.2}$$

where the Green's function $G^R_{AB}(t-t')$ is given by

$$G^R_{AB}(t-t') = -i\theta(t-t')\langle [A(t), B(t')]\rangle. \tag{A.3}$$

Here $\theta(t)$ is the Heaviside step function. The retarded Green's function thus gives the system's response to an external field. The density of states $\rho_A(\omega)$ is given by the imaginary part of the Fourier transform of $G^R_{AA}(t)$,

$$G^R_{AA}(\omega) = \int_{-\infty}^{+\infty} \mathrm{d}t\, e^{i\omega t} G^R_{AA}(t) = -i\int_{0}^{+\infty} \mathrm{d}t\, e^{i\omega t}\langle [A(t), A(0)]\rangle, \tag{A.4}$$

$$\rho_A(\omega) = -\frac{1}{\pi}\mathrm{Im}[G^R_{AA}(\omega)]. \tag{A.5}$$

APPENDIX B

QUANTUM INPUT-OUTPUT THEORY

Here we consider a system interacting with a bosonic heat bath [49, 50], in the form

$$H = H_{\rm sys} + H_B + H_{\rm int}, \tag{B.1}$$

$$H_B = \hbar \int_{-\infty}^{\infty} {\rm d}\omega \ \omega b^\dagger(\omega) b(\omega), \tag{B.2}$$

$$H_{\rm int} = i\hbar \int_{-\infty}^{\infty} {\rm d}\omega \ g(\omega)[b^\dagger(\omega)c - c^\dagger b(\omega)], \tag{B.3}$$

where $b(\omega)$ are boson annihilation operators for the bath and c is one of several possible system operators. We want to study the system dynamics Solving the Heisenberg equations of motion for $b(\omega)$ and an arbitrary system operator a, we have

$$\dot{b}(\omega) = -i\omega b(\omega) + g(\omega)c, \tag{B.4}$$

$$\dot{a} = -\frac{i}{\hbar}[a, H_{\rm sys}] + \int {\rm d}\omega \ g(\omega) \left(b^\dagger(\omega)[a,c] - [a,c^\dagger]b(\omega) \right), \tag{B.5}$$

and we can solve the dynamics of b to obtain

$$\begin{aligned} b(\omega) &= e^{-i\omega(t-t_0)} b_0(\omega) + g(\omega) \int_{t_0}^{t} {\rm d}t' \ e^{-i\omega(t-t')} c(t') \\ &= e^{-i\omega(t-t_1)} b_1(\omega) - g(\omega) \int_{t}^{t_1} {\rm d}t' \ e^{-i\omega(t-t')} c(t'), \end{aligned} \tag{B.6}$$

where $b_0(\omega)$ is the value of $b(\omega)$ at $t = t_0$ and $b_1(\omega)$ is the value of $b(\omega)$ at $t = t_1$. Finally, we can get the dynamics for a,

$$\begin{aligned} \dot{a} = &-\frac{i}{\hbar}[a, H_{\rm sys}] \\ &+ \int {\rm d}\omega \ g(\omega) \left(e^{i\omega(t-t_0)} b_0^\dagger(\omega)[a,c] - [a,c^\dagger] e^{-i\omega(t-t_0)} b_0(\omega) \right) \\ &+ \int {\rm d}\omega \ g^2(\omega) \int_{t_0}^{t} {\rm d}t' \ \left(e^{i\omega(t-t')} c^\dagger(t')[a,c] - [a,c^\dagger] e^{-i\omega(t-t')} c(t') \right). \end{aligned} \tag{B.7}$$

Here we use the First Markov Approximation,

$$g(\omega) = \sqrt{\frac{\kappa}{2\pi}}, \tag{B.8}$$

and define the in and out fields as

$$b_{\text{in}}(t) = \frac{1}{\sqrt{2\pi}} \int \mathrm{d}\omega \; e^{-i\omega(t-t_0)} b_0(\omega), \tag{B.9}$$

$$b_{\text{out}}(t) = \frac{1}{\sqrt{2\pi}} \int \mathrm{d}\omega \; e^{-i\omega(t-t_1)} b_1(\omega). \tag{B.10}$$

Combining these equations, we get the quantum Langevin equation,

$$\dot{a} = -\frac{i}{\hbar}[a, H_{\text{sys}}] + \left[\frac{\kappa}{2}c^\dagger + \sqrt{\kappa} b_{\text{in}}^\dagger(t)\right][a, c] - [a, c^\dagger]\left[\frac{\kappa}{2}c + \sqrt{\kappa} b_{\text{in}}(t)\right], \tag{B.11}$$

$$\dot{a} = -\frac{i}{\hbar}[a, H_{\text{sys}}] - \left[\frac{\kappa}{2}c^\dagger - \sqrt{\kappa} b_{\text{out}}^\dagger(t)\right][a, c] + [a, c^\dagger]\left[\frac{\kappa}{2}c - \sqrt{\kappa} b_{\text{out}}(t)\right], \tag{B.12}$$

where b_{in} and b_{out} have the relation

$$b_{\text{out}}(t) = \sqrt{\kappa} c(t) + b_{\text{in}}(t), \tag{B.13}$$

which is called the input-output relation.

APPENDIX C

SCHRIEFFER-WOLFF TRANSFORMATION

Here we consider a Hamiltonian,

$$H = H_0 + \epsilon V. \tag{C.1}$$

We want to find a unitary transformation $U = e^S$, where S is anti-Hermitian such that the transformed Hamiltonian $H' = e^S H e^{-S}$ is block diagonal up to any desired order of ϵ. We set the S as a power serious of ϵ,

$$S = \epsilon S_1 + \epsilon^2 S_2 + \epsilon^3 S_3 + \mathcal{O}(\epsilon^4). \tag{C.2}$$

Using the Baker-Hausdorff formula, we have

$$\begin{aligned}
H' &= e^S H e^{-S} \\
&= H + [S, H] + \frac{1}{2!}[S, [S, H]] + \cdots \\
&= H_0 + \epsilon V + [S, H_0] + \epsilon[S, V] + \frac{1}{2!}[S, [S, H_0]] + \frac{\epsilon}{2!}[S, [S, V]] + \cdots \\
&= H_0 + \epsilon\big(V + [S_1, H_0\big) + \epsilon^2\big([S_2, H_0] + [S_1, V] + \frac{1}{2!}[S_1, [S_1, H_0]]\big) \\
&\quad + \epsilon^3\big([S_3, H_0] + \frac{1}{2!}[S_1, [S_2, H_0]] + \frac{1}{2!}[S_2, [S_1, H_0]] + \frac{1}{2!}[S_1, [S_1, V]] \\
&\quad + \frac{1}{3!}[S_1, [S_1, [S_1, H_0]]]\big) + \mathcal{O}(\epsilon^4).
\end{aligned} \tag{C.3}$$

When we choose appropriate S_1 so that $V + [S_1, H_0] = 0$ and $S_2 = 0$, we have

$$H' = H_0 + \frac{\epsilon^2}{2}[S_1, V] + \mathcal{O}(\epsilon^3). \tag{C.4}$$

APPENDIX D

COUPLED TRANSMISSION LINES

Here we discuss the coupled transmission lines. The effective circuit for two coupled transmission lines is shown in Fig. D.1. Similar to a single transmission line, we can write down telegrapher equations to describe their dynamics,

$$\frac{\partial v_1(z,t)}{\partial z} = -L_l \frac{\partial i_1(z,t)}{\partial t} - L_m \frac{\partial i_2(z,t)}{\partial t}, \tag{D.1}$$

$$\frac{\partial v_2(z,t)}{\partial z} = -L_l \frac{\partial i_2(z,t)}{\partial t} - L_m \frac{\partial i_1(z,t)}{\partial t}, \tag{D.2}$$

$$\frac{\partial i_1(z,t)}{\partial z} = -C_l \frac{\partial v_1(z,t)}{\partial t} + C_m \frac{\partial v_2(z,t)}{\partial t}, \tag{D.3}$$

$$\frac{\partial i_2(z,t)}{\partial z} = -C_l \frac{\partial v_2(z,t)}{\partial t} + C_m \frac{\partial v_1(z,t)}{\partial t}, \tag{D.4}$$

where $v_k(z,t)$ and $i_k(z,t)$ are the voltage and current the kth transmission line position z and time t, L_l is the distributed inductance, L_m is the distributed mutual inductance, C_l is the capacitance per length, C_m is the coupled capacitance per length. We already assume the two transmission lines are identical and there is no loss in the system. The above equations can be rearranged to

$$\frac{\partial v_+(z,t)}{\partial z} = -(L_l + L_m) \frac{\partial i_+(z,t)}{\partial t}, \tag{D.5}$$

$$\frac{\partial v_-(z,t)}{\partial z} = -(L_l - L_m) \frac{\partial i_-(z,t)}{\partial t}, \tag{D.6}$$

$$\frac{\partial i_+(z,t)}{\partial z} = -(C_l - C_m) \frac{\partial v_+(z,t)}{\partial t}, \tag{D.7}$$

$$\frac{\partial i_-(z,t)}{\partial z} = -(C_l + C_m) \frac{\partial v_-(z,t)}{\partial t}, \tag{D.8}$$

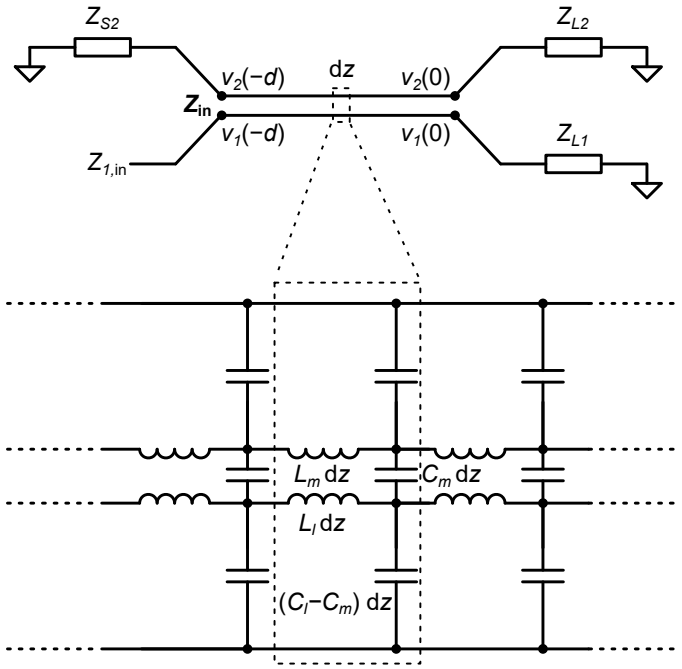

Figure D.1: Lumped-element equivalent circuit for coupled transmission lines with source and load impedances.

where $v_\pm = v_1 \pm v_2$ and $i_\pm = i_1 \pm i_2$. We can get the phase velocities v_p and phase constants β of the two modes,

$$v_{p+} = \frac{1}{\sqrt{(L_l + L_m)(C_l - C_m)}}, \tag{D.9}$$

$$v_{p-} = \frac{1}{\sqrt{(L_l - L_m)(C_l + C_m)}}, \tag{D.10}$$

$$\beta_+ = \omega / v_{p+} = \omega\sqrt{(L_l + L_m)(C_l - C_m)}, \tag{D.11}$$

$$\beta_- = \omega / v_{p-} = \omega\sqrt{(L_l - L_m)(C_l + C_m)}. \tag{D.12}$$

When the two transmission lines are in a homogeneous medium, we have $v_{p+} = v_{p-} = 1/\sqrt{\mu\epsilon}$ and $\beta_+ = \beta_- = \beta$, where μ and ϵ are the permeability and permittivity of the medium. Here we assume a homogeneous medium to simplify the discussion and we can get

$$\frac{L_m}{C_m} = \frac{L_l}{C_l} = Z_0^2, \tag{D.13}$$

where Z_0 is the characteristic impedance of two uncoupled transmission lines. The effective characteristic impedance of the two modes are

$$Z_+ = \sqrt{\frac{L_l + L_m}{C_l - C_m}}, \tag{D.14}$$

$$Z_- = \sqrt{\frac{L_l - L_m}{C_l + C_m}}. \tag{D.15}$$

We have

$$Z_+ Z_- = Z_0^2. \tag{D.16}$$

Similar to the single transmission line, we can get the input impedance matrix $\mathbf{Z}_{\text{in}}$ at position $z = -d$ [249],

$$\mathbf{Z}_{\text{in}}(-d) = \left(\mathbf{I} + \mathbf{\Gamma} e^{-2j\beta d}\right)\left(\mathbf{I} - \mathbf{\Gamma} e^{-2j\beta d}\right)^{-1} \mathbf{Z}_C, \tag{D.17}$$

where $\mathbf{I}$ is the 2×2 identity matrix, $\mathbf{Z}_C$ is the characteristic impedance of the coupled lines,

$$\mathbf{Z}_C = \frac{1}{2}\begin{bmatrix} Z_+ + Z_- & Z_+ - Z_- \\ Z_+ - Z_- & Z_+ + Z_- \end{bmatrix}, \tag{D.18}$$

and $\mathbf{\Gamma}$ is the reflection coefficient at the load,

$$\mathbf{\Gamma} = (\mathbf{Z}_L - \mathbf{Z}_C)(\mathbf{Z}_L + \mathbf{Z}_C)^{-1}, \tag{D.19}$$

with $\mathbf{Z}_L$,

$$\mathbf{Z}_L = \begin{bmatrix} Z_{L1} & 0 \\ 0 & Z_{L2} \end{bmatrix}. \tag{D.20}$$

If the lines are in an inhomogeneous medium, we have $\beta_+ \neq \beta_-$, and Eq. D.17 needs to be modified [249]. When the second input port is terminated with a source impedance Z_{S2}, we

have

$$Z_{11}i_1 + Z_{12}i_2 = v_1, \tag{D.21}$$

$$Z_{21}i_1 + Z_{22}i_2 + Z_{S2}i_2 = 0, \tag{D.22}$$

where we write $\mathbf{Z}_{\text{in}}$ as

$$\mathbf{Z}_{\text{in}} = \begin{bmatrix} Z_{11} & Z_{12} \\ Z_{21} & Z_{22} \end{bmatrix}. \tag{D.23}$$

We can get the input impedance from the first port, $Z_{1,\text{in}}$,

$$Z_{1,\text{in}} = \frac{v_1}{i_1} = Z_{11} - \frac{Z_{12}Z_{21}}{Z_{22} + Z_{S2}}. \tag{D.24}$$

Note that we always have $Z_{12} = Z_{21}$ for passive circuits.

We can verify that when the two lines are uncoupled, i.e. $L_m = C_m = 0$, Eqs. D.17 and D.24 become Eq. 1.87.

When $Z_{L1} = Z_{L2} = Z_0$, we have

$$\mathbf{\Gamma} = \frac{1}{2Z_0 + Z_+ + Z_-} \begin{bmatrix} 0 & -(Z_+ - Z_-) \\ -(Z_+ - Z_-) & 0 \end{bmatrix}. \tag{D.25}$$

The input impedance matrix $\mathbf{Z}_{\text{in}}$ becomes,

$$\mathbf{Z}_{\text{in}} = \frac{1}{2} \begin{bmatrix} \frac{1+\alpha}{1-\alpha}Z_+ + \frac{1-\alpha}{1+\alpha}Z_- & \frac{1+\alpha}{1-\alpha}Z_+ - \frac{1-\alpha}{1+\alpha}Z_- \\ \frac{1+\alpha}{1-\alpha}Z_+ - \frac{1-\alpha}{1+\alpha}Z_- & \frac{1+\alpha}{1-\alpha}Z_+ + \frac{1-\alpha}{1+\alpha}Z_- \end{bmatrix}, \tag{D.26}$$

where the coefficient α satisfies,

$$\alpha = -\frac{(Z_+ - Z_-)}{2Z_0 + Z_+ + Z_-} e^{-2j\beta d}. \tag{D.27}$$

When $Z_{S2} = Z_0$, we have

$$Z_{1,\text{in}} = Z_0, \tag{D.28}$$

which forms a directional coupler [45]. The coupling coefficient C of the directional coupler is $C = (Z_+ - Z_-)/(Z_+ + Z_-)$.

When the two lines are weakly coupled, i.e. $\delta = L_m/L_l = C_m/C_l \ll 1$, we have

$$Z_\pm = Z_0 \pm \delta Z_0 + \frac{1}{2}\delta^2 Z_0. \tag{D.29}$$

The characteristic impedance $\mathbf{Z}_C$ of the coupled lines is

$$\mathbf{Z}_C = Z_0 \begin{bmatrix} 1+\frac{1}{2}\delta^2 & \delta \\ \delta & 1+\frac{1}{2}\delta^2 \end{bmatrix}. \tag{D.30}$$

The reflection coefficient $\mathbf{\Gamma}$ becomes

$$\mathbf{\Gamma} = \begin{bmatrix} \frac{Z_{L1}-Z_0}{Z_{L1}+Z_0} - \frac{Z_0 Z_{L1}(Z_{L2}-Z_0)}{(Z_{L1}+Z_0)^2(Z_{L2}+Z_0)}\delta^2 & -\frac{2Z_0 Z_{L1}}{(Z_{L1}+Z_0)(Z_{L2}+Z_0)}\delta \\ -\frac{2Z_0 Z_{L2}}{(Z_{L1}+Z_0)(Z_{L2}+Z_0)}\delta & \frac{Z_{L2}-Z_0}{Z_{L2}+Z_0} - \frac{Z_0 Z_{L2}(Z_{L1}-Z_0)}{(Z_{L2}+Z_0)^2(Z_{L1}+Z_0)}\delta^2 \end{bmatrix}, \tag{D.31}$$

from which we can calculate the input impedance matrix $\mathbf{Z}_{\text{in}}$ and the input impedance of the first port $Z_{1,\text{in}}$.

When $Z_{L1} = 0$, the input impedance of the first port $Z_{1,\text{in}}$ becomes

$$Z_{1,\text{in}} = \frac{\delta^2(\beta d)^2 Z_0^2}{Z_{L2} + Z_{S2}}, \tag{D.32}$$

where we assume the coupling length $\beta d \ll 1$. If we let $M = L_m d$, the above result can be rewritten as

$$Z_{1,\text{in}} = \frac{\omega^2 M^2}{Z_{L2} + Z_{S2}}, \tag{D.33}$$

which is the same as Eq. 1.39.

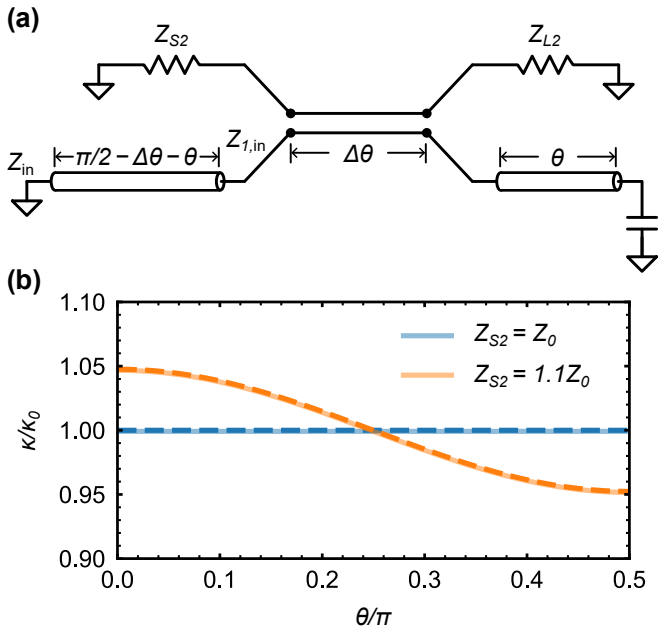

Figure D.2: (a) Circuit for a $\lambda/4$ resonator coupled to a transmission line. (b) Dissipation rate κ of the $\lambda/4$ resonator versus the coupling position θ for $Z_{L2} = Z_{S2} = Z_0$ (blue) and $Z_{L2} = Z_0$ and $Z_{S2} = 1.1Z_0$ (orange). The solid lines are calculated using Eq. D.34 and Table 1.1 while the dashed lines are calculated using Eq. D.35. We assume $\delta = 0.2$, $\Delta\theta = 0.05$ and $\kappa_0 = 2\omega_0(\delta\Delta\theta)^2/\pi$ in the calculation.

Using the above results, we can calculate the dissipation rate κ of a hanger resonator. The circuit is shown in Fig. D.2(a). Here we consider a $\lambda/4$ resonator coupled to a transmission line at position θ. We have $Z_{S2} = Z_{L2} = Z_0$ and $Z_{L1} = Z_0/j\tan\theta$. The input impedance Z_{in} from the short end of the $\lambda/4$ resonator is

$$Z_{\text{in}} = Z_0 \frac{Z_{1,\text{in}} + jZ_0\tan(\pi/2 - \Delta\theta - \theta)}{Z_0 + jZ_{1,\text{in}}\tan(\pi/2 - \Delta\theta - \theta)}, \tag{D.34}$$

from which we can calculate the dissipation rate κ and coupling quality factor Q_c of the $\lambda/4$ resonator using Table 1.1. Here we choose to calculate Z_{in} from the short end because the resonance acts like a series resonance seen from the short end, which is more convenient to calculate the dissipation rate from the impedance Z_{in} (see Table 1.1). We find that when the coupling length is short, i.e. $\Delta\theta = \beta d \ll 1$, the dissipation rate κ can be approximately written as the sum of the dissipation rate κ_i from the inductive coupling (Eq. 1.90) and

κ_c from capacitive coupling (Eq. 1.91) as shown in Fig. D.2(b). If we let $M = L_m d$ and $C_\kappa = C_m d$, the dissipation rate κ can be written as

$$\begin{aligned}\kappa = \kappa_i + \kappa_c &= \frac{4\omega_0^3 M^2}{\pi Z_0 (Z_{S2} + Z_{L2})} \sin^2\theta + \frac{4\omega_0^3 C_\kappa^2 Z_0 Z_{L2} Z_{S2}}{\pi (Z_{S2} + Z_{L2})} \cos^2\theta \\ &= \frac{4\omega_0 (\delta\Delta\theta)^2}{\pi} \Big(\frac{Z_0}{Z_{S2} + Z_{L2}} \sin^2\theta + \frac{Z_{L2} Z_{S2}}{Z_0 (Z_{S2} + Z_{L2})} \cos^2\theta \Big),\end{aligned} \tag{D.35}$$

where ω_0 is the frequency of the $\lambda/4$ resonator. Note that we have a different definition of θ from Fig. 1.10. When $Z_{L2} = Z_{S2} = Z_0$, the dissipation rate is

$$\kappa = \frac{2\omega_0 (\delta\Delta\theta)^2}{\pi}, \tag{D.36}$$

which is independent of the coupling position θ. When $Z_{L2} \neq Z_{S2}$ (e.g. there is some impedance mismatch in the wiring), the dissipation rate will depend on the coupling point (see Fig. D.2(b)). From the numerical calculation, we also find that when the coupling length $\Delta\theta = \beta d$ is not close to zero, the dissipation rate κ is smaller than the approximate expression in Eq. D.35 and is still independent of the coupling point when $Z_{L2} = Z_{S2} = Z_0$.

We can also analyze the coupling between two transmission line resonators. The circuit is shown in Fig. D.3(a). Here we consider coupled $\lambda/2$ and $\lambda/4$ resonators. The source and load impedances become $Z_{L1} = -jZ_0 \cot\theta_1$, $Z_{L2} = jZ_0 \tan\theta_2$, and $Z_{S2} = jZ_0 \tan(\pi - \Delta\theta - \theta_2)$, from which we can calculate the input impedance Z_{in} from the short end. We bring the two resonators on resonance, and the coupling strength g is determined by

$$g = \frac{\omega_2 - \omega_1}{2}, \tag{D.37}$$

where ω_1 and ω_2 are the two zeroes in $\text{Im}[Z_{\text{in}}(\omega)]$. There is another pole between ω_1 and ω_2 at ω_0, which is the bare frequency of the two resonators. The numerical results are shown in Fig. D.3(b). We find that when the coupling length is short, i.e. $\Delta\theta = \beta d \ll 1$, the coupling

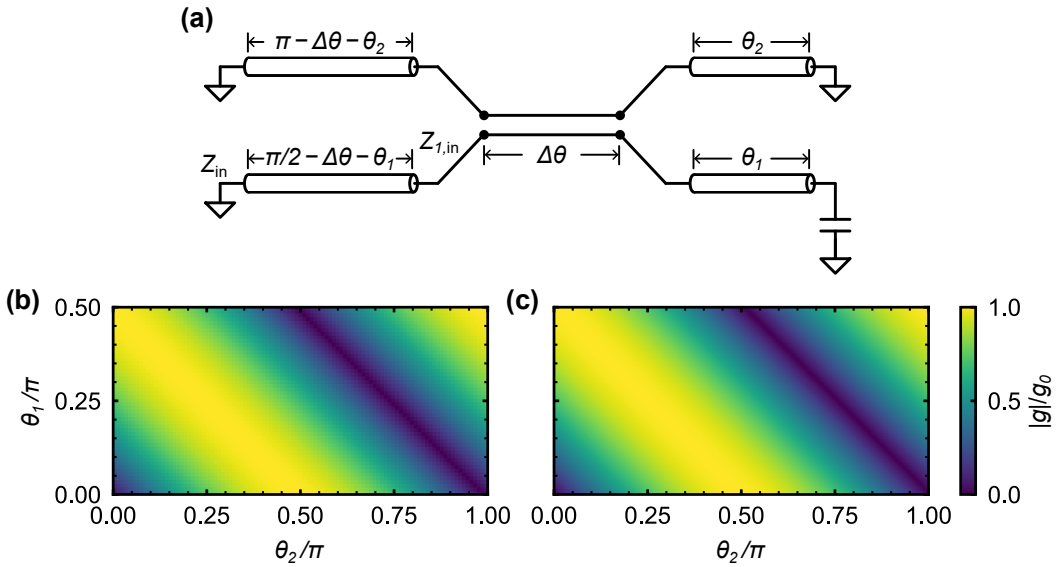

Figure D.3: (a) Circuit for coupled $\lambda/4$ (bottom) and $\lambda/2$ (top) resonators. (b) Coupling strength $|g|$ versus coupling position θ_1 and θ_2 calculated using Eq. D.37 and (c) Eq. D.38. We assume $\delta = 0.2$, $\Delta\theta = 0.05$ and $g_0 = \sqrt{2}\omega_0\delta\Delta\theta/\pi$ in the calculation.

strength g can be approximately written as the sum of the coupling g_i from the inductive coupling (Eq. 1.92) and g_c from the capacitive coupling (Eq. 1.93). If we let $M = L_m d$ and $C_c = C_m d$, the coupling strength g can be written as

$$\begin{aligned} g = g_i + g_c &= \frac{\sqrt{2}}{\pi}\frac{M}{Z_0}\omega_0^2 \sin\theta_1 \cos\theta_2 + \frac{\sqrt{2}}{\pi} C_c Z_0 \omega_0^2 \cos\theta_1 \sin\theta_2 \\ &= \frac{\sqrt{2}}{\pi}\omega_0 \delta\Delta\theta \sin(\theta_1 + \theta_2). \end{aligned} \tag{D.38}$$

Note that the definition of θ_1 here differs from Fig. 1.11. We need to be careful about the signs of the couplings g_i and g_c. The results calculated using Eq. D.38 are shown in Fig. D.3(c) and we can see good agreement with the numerical results in Fig. D.3(b). When $\theta_1 + \theta_2 = \pi$, we have $g_i = -g_c$ and $g = 0$. When $\theta_1 = \theta_2$, we have $g_i = g_c$ and the non-RWA terms in the coupling become zero (see Section 1.2.2). Analysis of couplings based on S-parameters can be found in Ref. [250].

APPENDIX E

CLASSICAL FILTER SYNTHESIS

Here we introduce the synthesis of classical filters [45]. The design flow of a bandpass filter is shown in Fig. E.1. We start with a low-pass filter prototype, convert it to a bandpass design, and finally convert it to a practical implementation. A low-pass filter prototype is shown in Fig. E.1(a), where we start with normalized values and set the target 3 dB cutoff frequency $\omega_c = 1$ rad/s. The coefficients $\{g_k\}$ are the numbers of the circuit elements in units of Ω and we set $g_0 = 1$. Different choices of $\{g_k\}$ give different frequency responses. For different responses (Butterworth, Chebyshev, linear phase, etc.). The coefficients $\{g_k\}$ can be calculated using the insertion loss technique and Cauer synthesis [100]. The reflected power at the input port of the network is given by

$$|\Gamma(\omega)|^2 = 1 - \frac{1}{P_L(\omega)} = \frac{P_L(\omega) - 1}{P_L(\omega)}, \tag{E.1}$$

where $P_L(\omega)$ is the power loss function. For a Butterworth (maximally flat) response, the power loss function $P_L(\omega)$ has the form,

$$P_L(\omega) = A(1 + \omega^{2N}), \tag{E.2}$$

where the parameter A controls the impedance match and N is the order of the filter. When $A = 1$, there is no reflection at $\omega = 0$. We will set $A \geq 1$ here. For $A < 0$, the filter acts as an amplifier [100]. Labeling $s = j\omega$, and inserting the Butterworth response, we have

$$|\Gamma(s)|^2 = \frac{\frac{A-1}{A} + (-1)^N s^{2N}}{1 + (-1)^N s^{2N}} = \Gamma(s)\Gamma(-s). \tag{E.3}$$

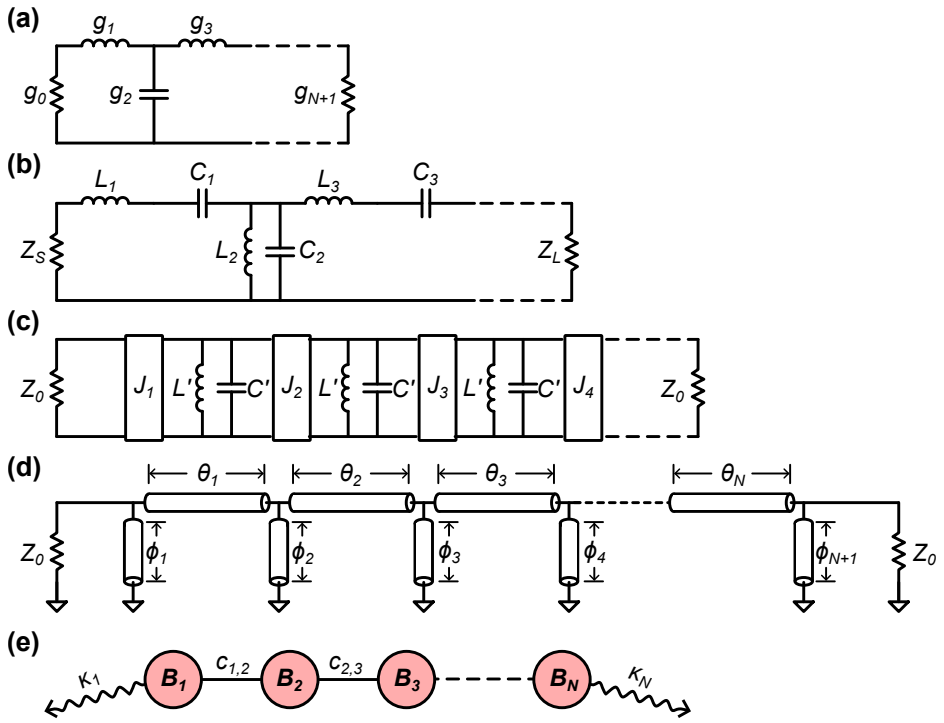

Figure E.1: Design flow of bandpass filters. (a) Low-pass prototype, using capacitors and inductors. (b) Bandform transformation from lowpass to bandpass. (c) Bandpass filter with admittance inverters J_n, using only parallel LC resonators. (d) Implementation using sections of transmission lines. (e) Coupled-mode picture for an Nth order filter, with dissipation rate κ_j for the jth resonator B_j and coupling strength $c_{j,j+1}$ between resonators B_j and B_{j+1}.

Here we choose a positive sign for $\Gamma(s)$ and we can get

$$\Gamma(s) = \frac{R(s)}{D(s)} = \frac{\Pi_{k=1}^{N}(s - z_k)}{\Pi_{k=1}^{N}(s - p_k)}, \tag{E.4}$$

where s_k are complex roots of $R(s)$ and p_k are complex roots of $D(s)$, where we choose them from the left half-plane of the complex plane. We can get the input impedance of the network $Z(s)$ from $\Gamma(s)$,

$$Z(s) = \frac{1 + \Gamma(s)}{1 - \Gamma(s)} = \frac{D(s) + R(s)}{D(s) - R(s)}. \tag{E.5}$$

Insertion loss	Order N	g_0g_1	g_1g_2	g_2g_3	g_3g_4	g_4g_5	g_5g_6	g_6g_7
0 dB	1	2.000	2.000					
	2	1.414	2.000	1.414				
	3	1.000	2.000	2.000	1.000			
	4	0.765	1.414	3.414	1.414	0.765		
	5	0.618	1.000	3.236	3.236	1.000	0.618	
	6	0.518	0.732	2.732	3.732	2.732	0.732	0.518
10 dB	1	38.97	1.026					
	2	54.40	1.026	0.716				
	3	57.45	2.035	0.678	0.504			
	4	58.50	2.445	1.730	0.420	0.385		
	5	58.97	2.645	2.366	1.249	0.279	0.311	
	6	59.22	2.755	2.755	1.882	0.919	0.198	0.260
20 dB	1	399.0	1.003					
	2	563.6	1.003	0.708				
	3	597.5	2.003	0.668	0.500			
	4	607.6	2.417	1.709	0.415	0.383		
	5	615.2	2.621	2.344	1.237	0.277	0.309	
	6	618.3	2.734	2.734	1.868	0.911	0.196	0.259
30 dB	1	3999	1.000					
	2	5655	1.000	0.707				
	3	5997	2.000	0.667	0.500			
	4	6120	2.415	1.707	0.414	0.383		
	5	6178	2.618	2.342	1.236	0.276	0.309	
	6	6209	2.732	2.732	1.866	0.911	0.196	0.259

Table E.1: g coefficients for maximally flat low-pass filter prototypes, with $g_0 = 1$.

From Cauer synthesis, we can write $Z(s)$ using $\{g_k\}$,

$$Z(s) = g_1 s + \frac{1}{g_2 s + \frac{1}{g_3 s + \cdots}}. \tag{E.6}$$

Note there is no s after g_{N+1}. We can determine all $\{g_k\}$ by the above two equations. Some calculated $\{g_k\}$ are listed in Table E.1.

With the low-pass prototype, we can transform it into a bandpass filter. Assuming the bandpass filter has a passband between ω_1 and ω_2, we can define its center frequency ω_0 and

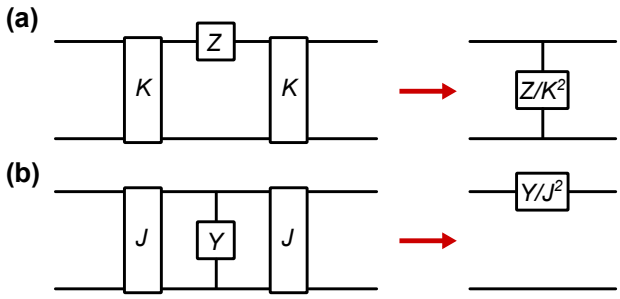

Figure E.2: Functionality of (a) impedance and (b) admittance inverters.

bandwidth ratio Δ as

$$\omega_0 = \sqrt{\omega_1 \omega_2}, \tag{E.7}$$

$$\Delta = \frac{\omega_2 - \omega_1}{\omega_0}. \tag{E.8}$$

Then we can transform the low-pass filter prototype by replacing the inductors with series LC resonators and capacitors with parallel LC resonators as is shown in Fig. E.1(b), with the values,

$$L_{2k+1} = \frac{\Delta Z_0}{\omega_0 g_{2k+1}}, \tag{E.9}$$

$$C_{2k+1} = \frac{g_{2k+1}}{\Delta \omega_0 Z_0}, \tag{E.10}$$

$$L_{2k+2} = \frac{g_{2k+2} Z_0}{\Delta \omega_0}, \tag{E.11}$$

$$C_{2k+2} = \frac{\Delta}{\omega_0 g_{2k+1} Z_0}, \tag{E.12}$$

where we assume the input and output circuits have the same characteristic impedance $Z_S = Z_L = Z_0$.

However, the circuit in Fig. E.1(b) is not easy to implement. We can further transform the circuit to a circuit with only parallel or series LC resonators (see Fig. E.1(c)) using admittance or impedance inverters. The impedance/admittance inverters can convert the

series impedance to parallel admittance or vice versa. An ideal impedance inverter K (or admittance inverter J with $J = 1/K$) have the $ABCD$ matrix,

$$\begin{bmatrix} A & B \\ C & D \end{bmatrix} = \begin{bmatrix} 0 & jK \\ j/K & 0 \end{bmatrix} = \begin{bmatrix} 0 & j/J \\ jJ & 0 \end{bmatrix}. \tag{E.13}$$

When a series impedance Z is sandwiched by two impedance inverters K (see Fig. E.2(a)), the total $ABCD$ matrix for this circuit becomes

$$\begin{bmatrix} A & B \\ C & D \end{bmatrix} = \begin{bmatrix} 0 & jK \\ j/K & 0 \end{bmatrix} \begin{bmatrix} 1 & Z \\ 0 & 1 \end{bmatrix} \begin{bmatrix} 0 & jK \\ j/K & 0 \end{bmatrix} = e^{i\pi} \begin{bmatrix} 1 & 0 \\ Z/K^2 & 1 \end{bmatrix}, \tag{E.14}$$

which is the $ABCD$ matrix of a parallel circuit with admittance Z/K^2. When a parallel admittance Y is sandwiched by two admittance inverters J (see Fig. E.2(b)), the total $ABCD$ matrix becomes

$$\begin{bmatrix} A & B \\ C & D \end{bmatrix} = \begin{bmatrix} 0 & j/J \\ jJ & 0 \end{bmatrix} \begin{bmatrix} 1 & 0 \\ Y & 1 \end{bmatrix} \begin{bmatrix} 0 & j/J \\ jJ & 0 \end{bmatrix} = e^{i\pi} \begin{bmatrix} 1 & Y/J^2 \\ 0 & 1 \end{bmatrix}, \tag{E.15}$$

which is the $ABCD$ matrix of a series circuit with impedance Y/J^2. In Fig. E.3, we give examples of the impedance and admittance inverters. Comparing Fig. E.3(a) and Fig. 1.27, we can see that the impedance inverters are just couplers for inductive coupling. Comparing Fig. E.3(b) and Fig. 1.2(a), we can see that the admittance inverters are couplers for capacitive coupling, which compensate the frequency shifts by the negative capacitors. More examples of inverters can be found in Ref. [45]. In practice, the inverters only work for a certain bandwidth. Bandpass filters designed by inverters can have a bandwidth ratio Δ up to around 10%.

In Fig. E.1(c), we present a circuit using only admittance inverters and parallel LC

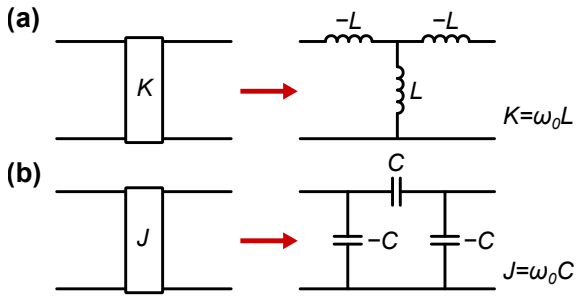

Figure E.3: Examples of (a) impedance and (b) admittance inverters.

resonators. When the inductors and capacitors in Fig. E.1(c) have the same values,

$$L' = \frac{2Z_0}{\pi\omega_0}, \tag{E.16}$$

$$C' = \frac{\pi}{2Z_0\omega_0}, \tag{E.17}$$

the admittance inverters need to satisfy

$$Z_0 J_n = \sqrt{\frac{\pi\Delta}{2g_{n-1}g_n}} \quad \text{for } n = 1, N+1, \tag{E.18}$$

$$Z_0 J_n = \frac{\pi\Delta}{2\sqrt{g_{n-1}g_n}} \quad \text{for } n = 2, \cdots, N. \tag{E.19}$$

If we use the circuit in Fig. E.3(b) as the admittance inverters, the circuit in Fig. E.1(c) can be treated as capacitively coupled parallel LC resonators. Note that the negative capacitors in the admittance inverter can be absorbed into its neighbor parallel LC resonators.

In practice, we can use transmission lines instead of lumped elements to make the resonators. Here we present a circuit using only sections of transmission lines in Fig. E.1(d). The grounded transmission lines act as impedance inverters, which is a variant of the circuit in Fig. E.3(a). The whole circuit in Fig. E.1(d) can be treated as inductively coupled $\lambda/2$

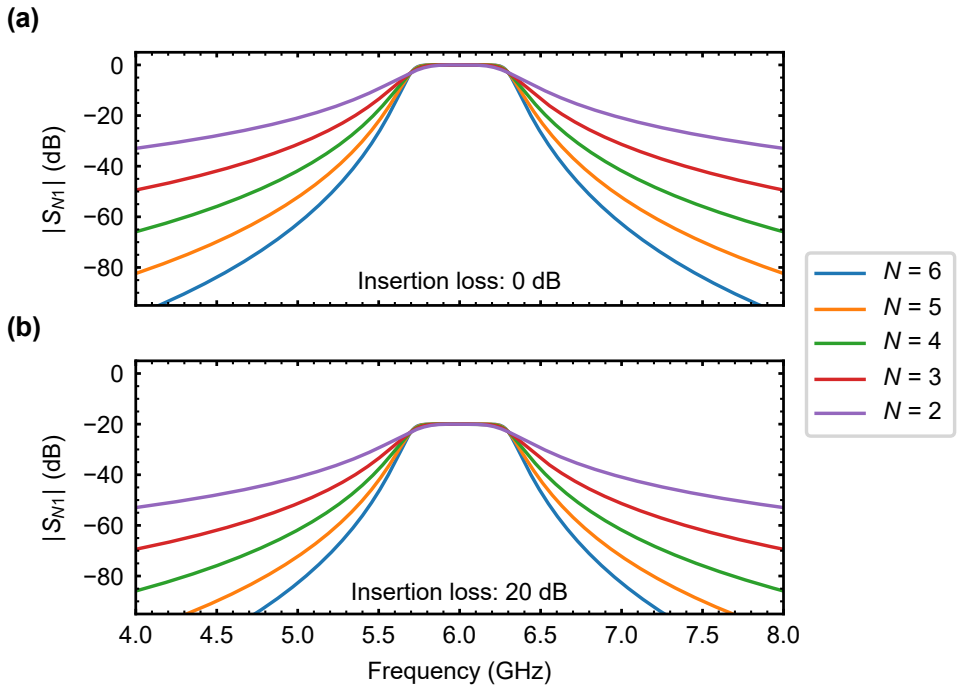

Figure E.4: Transmission coefficients $|S_{N1}|$ for different orders N with insertion loss (a) 0 dB and (b) 20 dB. All the filters have the same center frequency $\omega_0/2\pi = 6$ GHz and bandwidth $\Delta\omega_0/2\pi = 600$ MHz.

resonators. The length of each line needs to satisfy

$$\phi_n = \arctan\left(\frac{Z_0/K_n}{1-(Z_0/K_n)^2}\right), \tag{E.20}$$

$$\theta_n = \pi - \arctan(Z_0/K_n) - \arctan(Z_0/K_{n+1}), \tag{E.21}$$

where ϕ_n and θ_n represent $\beta\ell$ with β the phase constant at frequency ω_0, and $K_n = 1/J_n$ in Eqs. E.18 and E.19. We set the impedance of all the transmission lines to be Z_0, which is the same as the source and load circuit impedance.

With the impedance/admittance inverters, the bandpass filters can be treated as coupled series/parallel resonators as is shown in Fig. E.1(e) [251, 100]. The dispassion rates of the

first and last resonators and the coupling strength between resonators are given by

$$\kappa_1 = \frac{\Delta\omega_0}{g_0 g_1}, \tag{E.22}$$

$$\kappa_N = \frac{\Delta\omega_0}{g_N g_{N+1}}, \tag{E.23}$$

$$c_{k,k+1} = \frac{\Delta\omega_0}{2\sqrt{g_k g_{k+1}}}. \tag{E.24}$$

From Table E.1, we can see that for large insertion loss, $\kappa_1 \ll \kappa_N$. In the infinite insertion loss limit, we get a singly terminated filter. With this coupled-mode view, we can directly calculate the transmission coefficients S_{N1} from Eq. 1.61. Note that the case of $N = 1$ has been discussed in Section 1.2.5. The transmission coefficients S_{N1} for different filters with different orders N and insertion loss are shown in Fig. E.4. We achieve flat $|S_{N1}|$ in the passband as expected. From the coupled-mode view, the filter bandwidth can be broad as long as the RWA holds. If we use coupled transmission line resonators to balance out the non-RWA terms (see Appendix D), we can achieve a broader bandwidth.

In Fig. E.5, we give an example of a four-stage 20 dB insertion loss filter for qubit readout. The layout is shown in Fig. E.5(a), where four readout resonators are coupled to the first stage of the filter. The photo of the whole device is shown in Fig. E.5(b). To couple more readout resonators to the first stage, we can use an $n\lambda/2$ resonator as the first stage. To further reduce the footprint of the filter, we can use lumped-element resonators for other stages.

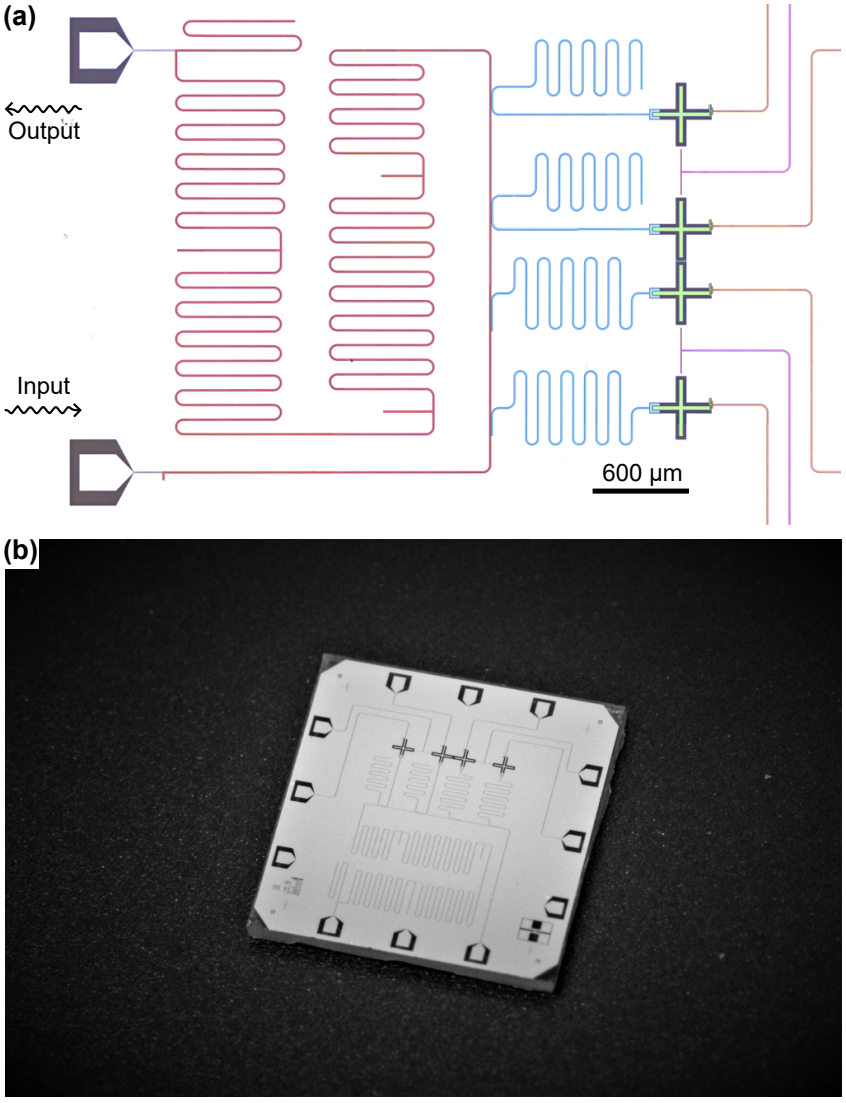

Figure E.5: (a) Layout of a four-stage bandpass filter for qubit readout: four transmon qubits (green) are capacitively coupled to $\lambda/4$ readout resonators (blue), which are coupled to the first stage of the filter (red). The xy drive lines and z flux lines are marked in magenta and orange respectively. (b) Photo of the whole device, with a size of 6 mm $\times$ 6 mm. This device was fabricated by Yash Joshi.

APPENDIX F

IMPEDANCE RESPONSE FORMULAS FOR COUPLINGS

Exact calculation of qubit-qubit coupling strength g_{eff} and ZZ interaction strength ζ requires full-diagonalization of the circuit Hamiltonian, which becomes very computationally demanding when many modes/junctions are involved. Refs. [235, 236] present a way to calculate the coupling strength g_{eff} and ZZ interaction strength ζ directly from the impedance of the coupler while considering the weak non-linearity of the transmons. Their results are summarized as follows.

Here we consider two transmons coupled by a two-port linear network as is shown in Fig. F.1, where the capacitors of the transmons are absorbed in the network. The qubits' frequencies ω_k and anharmonicities η_k are given by the capacitance matrix $\mathbf{C}$ as we discussed before (see e.g. Eqs. 4.19 and 4.20). More accurate formulas for ω_k and η_k are

$$\omega_k = \omega_{Jk} - \frac{E_{Ck}/\hbar}{1 - E_{Ck}/\hbar\omega_{Jk}}, \tag{F.1}$$

$$\eta_k = -\frac{\alpha_{kk}^2 E_{Ck}/\hbar}{1 - 2\alpha_{kk}^2 E_{Ck}/\hbar\omega_k}, \tag{F.2}$$

where $\omega_{Jk} = 1/\sqrt{L_{Jk}C_k} = \sqrt{8E_{Jk}E_{Ck}}$ with $C_k = e^2/2E_{Ck}$ obtained from the capacitance matrix $\mathbf{C}$ and α_{kk} is the correction coefficient given by

$$\alpha_{kk} = \frac{1}{2} - \frac{3}{4}\sqrt{\frac{C_k}{L_k}}\text{Im}[Z_{kk}(\omega_k)] - \frac{1}{4}\sqrt{\frac{C_k}{L_k}}\omega_k \text{Im}\Big[\frac{\mathrm{d}Z_{kk}(\omega)}{\mathrm{d}\omega}\Big|_{\omega=\omega_k}\Big], \tag{F.3}$$

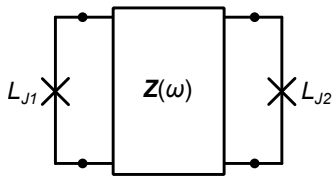

Figure F.1: Circuit for two transmons coupled by a two-port linear network.

where $L_k = 1/\omega_k^2 C_k = L_{Jk}/(1-2E_{Ck}/\hbar\omega_k)$ is the effective inductance of the qubit and Z_{kk} is the diagonal term of the impedance matrix $\mathbf{Z}(\omega)$. The coefficient $\alpha_{kk} \cong 1$ in the transmon regime. The coupling strength g_{eff} is given by the impedance matrix $\mathbf{Z}(\omega)$,

$$g_{\text{eff}} = -\frac{1}{4}\sqrt{\frac{\omega_1\omega_2}{L_1 L_2}}\text{Im}\Big[\frac{Z_{12}(\omega_1)}{\omega_1} + \frac{Z_{12}(\omega_2)}{\omega_2}\Big], \tag{F.4}$$

where Z_{12} is the off-diagonal term of the impedance matrix $\mathbf{Z}(\omega)$. When there are junctions in $\mathbf{Z}(\omega)$ and they work in the transmon limit $E_J \gg E_C$, we can linearize them similar to what we did to transmon qubits, i.e. replacing L_J with $L = 1/\omega^2 C = L_J/(1-2E_C/\hbar\omega)$, where ω is the frequency of the corresponding mode (see Eq. F.1). Readers can verify that the coupling strength of fixed (Eqs. 1.20 and 1.24) and tunable couplings (Eqs. 1.177 and 1.189) can be directly calculated from this formula.

When $|g_{\text{eff}}| \ll |\omega_1 - \omega_2|$, the ZZ interaction ζ can be written as

$$\zeta = \zeta_K + \zeta_J, \tag{F.5}$$

where ζ_K is the direct ZZ coupling and ζ_J is the ZZ coupling from the exchange coupling. The direct ZZ coupling ζ_K is given by

$$\zeta_K = 2\eta_1\big(\frac{\omega_1}{\omega_2}\big)\alpha_{12}^2 + 2\eta_2\big(\frac{\omega_2}{\omega_1}\big)\alpha_{21}^2, \tag{F.6}$$

where α_{kl} are given by

$$\alpha_{kl} = \sqrt{\frac{C_k}{L_l}}\frac{1}{2(\omega_k^2 - \omega_l^2)}\text{Im}[(\omega_k^2 - 2\omega_l^2)Z_{12}(\omega_l) + \omega_k\omega_l Z_{12}(\omega_k)]. \tag{F.7}$$

The coupling ζ_J is similar to Eq. 1.150 but with some corrections on the interaction strength

between the higher excited states, which is given by

$$\zeta_J = 2\frac{J_1^2(\eta_2 - \Delta) + J_2^2(\eta_1 + \Delta)}{(\Delta + \eta_1)(\Delta - \eta_2)}, \tag{F.8}$$

where $\Delta = \omega_1 - \omega_2$ and J_k is the effective coupling strength between the higher excited states, i.e. J_1 is the coupling strength between the $|fg\rangle$ and $|ee\rangle$ states, and J_2 is the coupling strength between the $|gf\rangle$ and $|ee\rangle$ states. When $J_1 = J_2 = g_{\text{eff}}$, we come back to Eq. 1.150. The couplings J_k are given by

$$J_1 = -\frac{1}{4}\sqrt{\frac{\omega_1\omega_2}{L_1L_2}}\text{Im}\Big[\beta_{11}\frac{Z_{12}(\omega_1)}{\omega_1} + \beta_{12}\frac{Z_{12}(\omega_2)}{\omega_2}\Big], \tag{F.9}$$

$$J_2 = -\frac{1}{4}\sqrt{\frac{\omega_1\omega_2}{L_1L_2}}\text{Im}\Big[\beta_{21}\frac{Z_{12}(\omega_1)}{\omega_1} + \beta_{22}\frac{Z_{12}(\omega_2)}{\omega_2}\Big], \tag{F.10}$$

where the correction factors β_{11}, β_{12}, β_{21} and β_{22} are

$$\beta_{11} = 1 + 2\frac{\omega_1\eta_1}{\omega_1^2 - \omega_2^2}, \tag{F.11}$$

$$\beta_{12} = 1 - 2\frac{\omega_1\eta_1}{\omega_1^2 - \omega_2^2} + 4\frac{\eta_1}{\omega_1}, \tag{F.12}$$

$$\beta_{21} = 1 - 2\frac{\omega_2\eta_2}{\omega_2^2 - \omega_1^2} + 4\frac{\eta_2}{\omega_2}, \tag{F.13}$$

$$\beta_{11} = 1 + 2\frac{\omega_2\eta_2}{\omega_2^2 - \omega_1^2}. \tag{F.14}$$

The above discussion can be extended to multiple transmon qubits, where the two-port impedance matrix $\mathbf{Z}(\omega)$ becomes an N-port impedance matrix.

APPENDIX G

FABRICATION

The fabrication of our superconducting quantum processors is done in the Pritzker Nanofabrication Facility at the University of Chicago. The recipes for transmon qubits were developed and improved by Hung-Shen Chang, Youpeng Zhong, Ming-Han Chou, and Joel Grebel. Readers can refer to their theses [252, 77, 143, 253] for more details. The non-galvanic flip-chip technique was developed by Kevin Satzinger and Chris Conner [240, 122].

G.1 Fabrication of superconducting qubits in 3 days

Here we will only give a rough timeline for the fabrication of a superconducting quantum processor as the process keeps being improved. The below process can consistently achieve qubit T_1 over 10 μs. For a hardworking graduate student, finishing the below process in three days is not hard.

- Day 1
  - 8:00 am, get into the cleanroom, pick a 4-inch sapphire wafer, solvent clean it, and bake it.
  - 9:00 am, Al layer deposition.
  - 9:30 am, photolithography for the base layer.
  - 10:30 am, Cl etch the base layer and clean the photoresist.
  - 11:00 am, photolithography for the Au marker.
  - 11:30 am, Ti/Au layer deposition.
  - 12:00 pm, leave the wafer in 80C NMP for liftoff and go out for lunch.
  - 4:00 pm, clean the wafer and do the photolithography for the SiO_2 layer.

  - 4:30 pm, leave the wafer in the SiO_2 deposition tool for overnight pump down.
  - 5:00 pm, go home.

- Day 2
  - 8:00 am, get into the cleanroom and deposit SiO_2.
  - 9:30 am, leave the wafer in 80C NMP for liftoff and go out for a cup of coffee.
  - 1:30 pm, clean the wafer and dice it into quarters.
  - 2:30 pm, e-beam lithography for the junction layer.
  - 3:30 pm, leave the wafer in the junction deposition tool for overnight pumpdown.
  - 4:00 pm, go home.

- Day 3
  - 8:00 am, get into the cleanroom and deposit junction layers.
  - 9:40 am, leave the wafer in 80C NMP for liftoff and go out for a cup of coffee.
  - 2:00 pm, clean the wafer and do the photolithography for the Al bandage layer.
  - 2:30 pm, pump down the bandage layer deposition tool.
  - 5:00 pm, Al bandage layer deposition.
  - 5:30 pm, leave the wafer in 80C NMP for liftoff and get out for dinner.
  - 8:30 pm, vent the vapor HF tool and dice the quarter wafer into chips.
  - 9:00 pm, etch out SiO_2 with vapor HF.
  - 10:00 pm, go home.

- Day 4
  - 8:00 am, do the flip-chip assembly if needed.

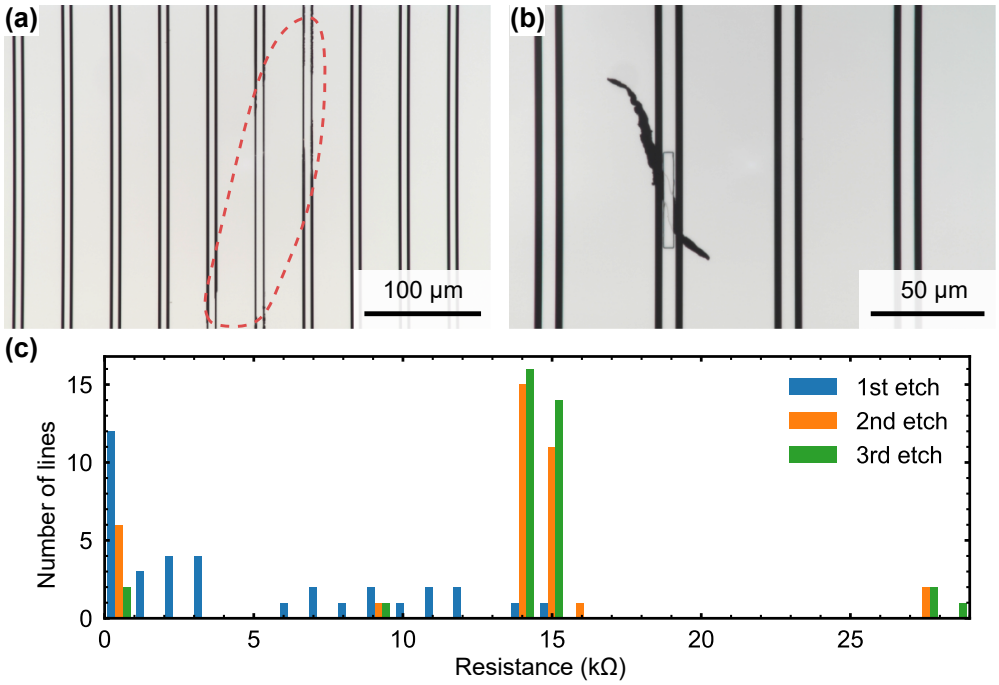

Figure G.1: (a) Short indicated by the red dashed line fixed by a second etch. (b) Open fixed by a bandage layer. (c) Measured resistance of 36 1.3-meter-long lines on a 4-inch wafer after the first, second, and third etch.

- 10:00 am, wire bond the sample.
- 12:00 pm, go out for lunch.
- 1:00 pm, prepare to cool down the sample and pray it will work as expected.

G.2 Fabrication of 1.3-meter-long CPW lines

In Chapter 3, we discussed a three-node sample where a 1.3-meter-long line transmission line links every two nodes. The total length of the transmission lines is around 4 meters on one chip and 50 meters on a 4-inch wafer. Making all of these transmission lines perfect is challenging. To detect whether the long lines are defective, we put a test pad in the center of the long line for resistance measurement. The long lines are shorted to ground on the two ends which are connected to gmon couplers.

If the measured resistance from the test pad to the ground is below the expected value,

the line is shorted to the ground somewhere, which is caused by the imperfect etch of the base layer, e.g. some dust falls on the photoresist before the etch. These can be fixed by a second etch as is shown in Fig. G.1(a), where we shrink the CPW line gap from 4 μm to 2 μm to avoid potential misalignment by the photolithography. In Fig. G.1(c), we present the measured resistances of 36 1.3-meter-long lines on a 4-inch wafer after the first, second, and third etch. We can see that most of the short can be fixed with a second etch.

If the measured resistance from the test pad to the ground is above the expected value, the line is broken somewhere which is caused by the imperfect base layer deposition, e.g. some dust falls on the wafer before the metal deposition. We do a bandage layer deposition to fix these breakpoints as is shown in Fig. G.1(b). The modified process for the base layer is described as follows.

- Pick a 4-inch sapphire wafer, solvent-clean it, and bake it.
- Al layer deposition.
- Photolithography for the base layer. The long lines have 8 μm width and 4 μm gap.
- Cl etch the base layer and clean the photoresist.
- Photolithography for the long lines with 2 μm gaps.
- Cl etch the long lines and clean the photoresist (see Fig. G.1(a)).
- Measure the resistance of all the long lines and locate the breakpoints of the long lines.
- Photolithography for the breakpoints of the long lines.
- Al bandage layer deposition and liftoff to fix these breakpoints (see Fig. G.1(b)).
- Measure the resistance of all the long lines to detect if there are other defects and fix them following the above process if necessary.

- Photolithography for the links between the test pads and the center of the long lines.
- Cl etch the test pads and clean the photoresist.

The above process can be extended to all the control lines, especially for multi-qubit samples.

APPENDIX H

MEASUREMENT SETUP

H.1 Sample packaging

After the sample is fabricated, it is a die of size 6 mm × 15 mm (two-node sample in Chapter 2) or 20 mm × 20 mm (three-node sample in Chapter 3 and four-node sample in Chapter 4). To measure the sample, we need to wire bond it to a printed circuit board (PCB) with aluminum wires. The PCB has no solder mask for better thermalization. The commonly used SMA connectors are soldered on the PCB for signals in and out. Here we use the non-magnetic connectors to minimize the effects of residual magnetic fields. We added vias connecting the grounds of different layers in the PCB to reduce the crosstalk between neighbor signal traces [254]. We have designed the PCBs with 12 and 24 connectors, with examples shown in Fig. H.1. Smaller connectors like SMP, SMPM, or PkZ connectors can be used for denser wiring. The sample sits in an aluminum cavity, which is superconducting and offers better shielding than copper. To reduce the qubit loss from the packaging mode, we minimize the size of the cavity to bring the cavity frequency higher. For the packaging for 20 mm × 20 mm samples, the cavity resonance frequency is around 7.5 GHz. We place all the qubit and readout resonator frequencies below 6 GHz. The loss from the packaging cavity can be further minimized by the flip-chip technique, which also acts as a shield for the qubits. Note that the substrate of the sample itself also has resonances. Like normal vias on PCBs, through-silicon vias [60] can be used to reduce such an effect. Aluminum is a poor conductor of heat because it is superconducting. For better thermalization of the sample, we mount the PCB on a gold-plated oxygen-free high thermal conductivity (OFHC) copper stand in the new design as is shown in Fig. H.1(e).

We place the aluminum package in a magnetic shield to further reduce the effects of

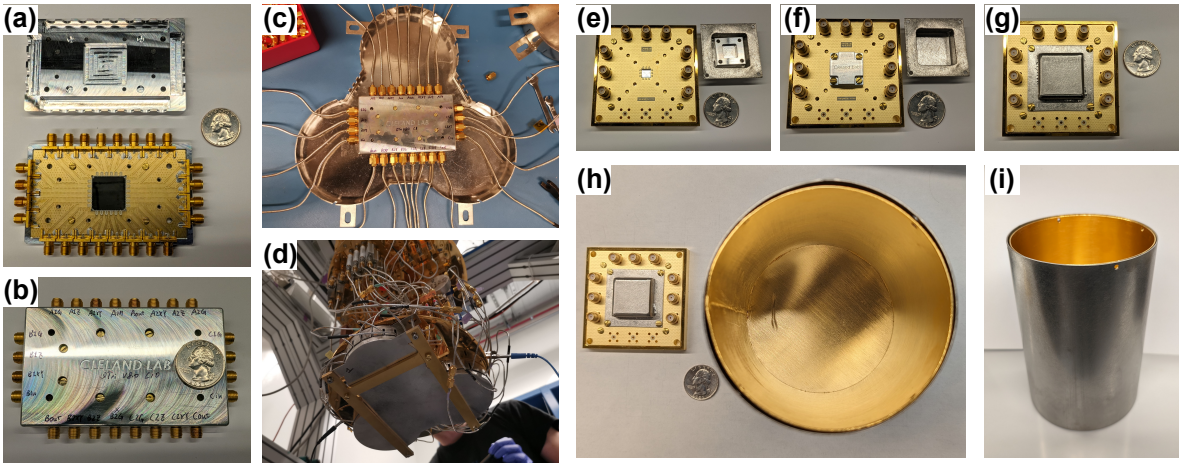

Figure H.1: (a-d) Sample packaging for 20 mm × 20 mm chip with 24 SMA connectors. The sample is wire bonded to the PCB which is mounted on an aluminum box. The aluminum box is placed in a mu-metal shield and mounted to the fridge. (e-i) Sample packaging for 6 mm × 6 mm chip with 12 SMA connectors. The PCB is mounted on a gold-plated copper stand. The whole package will be placed in the cylinders with the inner one to be painted with a black coating and the outer one to be a mu-metal shield.

fluctuations of external magnetic fields. The magnetic shields fabricated by amuneal[1] are made of mu-metal and hydrogen annealed for better permeabilities in low temperatures. Some magnetic shields are shown in Fig. H.1(c) and (i).

The energy gap of aluminum is 3.4×10^{-4} eV, corresponding to a frequency of 88 GHz. Infrared photons (300 GHz to 430 THz) can break the Cooper pairs and generate quasiparticles, limiting the qubit lifetimes. Absorbing materials can be painted on the shield for better protection. One example is a black coating made of silica powder, fine carbon powder, and 1 mm silicon carbide grains in stycast epoxy [255, 256, 257]. In our new packaging design, a separate gold-plated copper cylinder is inside the mu-metal shield for black coating as shown in Fig. H.1(i).

1. `https://www.amuneal.com`

H.2 Control line filtering

The packaged sample is mounted at the mixing chamber stage of the dilution refrigerator, which can cool down to below 10 mK. We use a Bluefors[2] LD-400 dilution refrigerator in our experiment. Before the control pulses arrive at the sample, filters need to be added at different stages to suppress unwanted signals [258]. An example wiring diagram is shown in Fig. H.2(a). Different input/output lines have different configurations.

For output lines that collect the readout signals, we use superconducting (NbTi) cables between the mixing chamber and the cryogenic low noise amplifier at the 4 K stage to reduce the cable insertion loss. To reduce the thermal noise coming down from the hot stages, three 20 dB cryo isolators are connected inline at the mixing chamber. To save space under the mixing chamber, the cryo isolators can be mounted above the mixing chamber as shown in Fig. H.2(b).

For qubit xy lines and read-in lines, we add 20 dB attenuation at the 4 K stage and more than 30 dB attenuation at the mixing chamber to reduce the thermal noise coming from the upper stages. The attenuator combination can be optimized by placing more attenuators at the still stage to reduce the heat load of the mixing chamber as shown in Fig. H.2(b). To better suppress unwanted signals at higher frequencies, commercial low-pass filters are added. For signals over tens of GHz (e.g. infrared photons), the commercial low-pass filters become transparent. Similar to the black coating mentioned above, filters filled with absorbing materials are added inline. Commonly used commercial absorbers are from Laird Eccosorb CR series[3] [259, 260, 261, 127]. The Eccosorb filters also provide better thermalization of the signal lines compared with the coaxial cables which rely on the Teflon dielectric.

For qubit and coupler flux lines, we use a DC line (< 1 MHz) combined with a fast-flux

2. https://bluefors.com

3. https://www.laird.com/products/absorbers/structural-absorbers/castable-liquid-absorber/eccosorb-cr

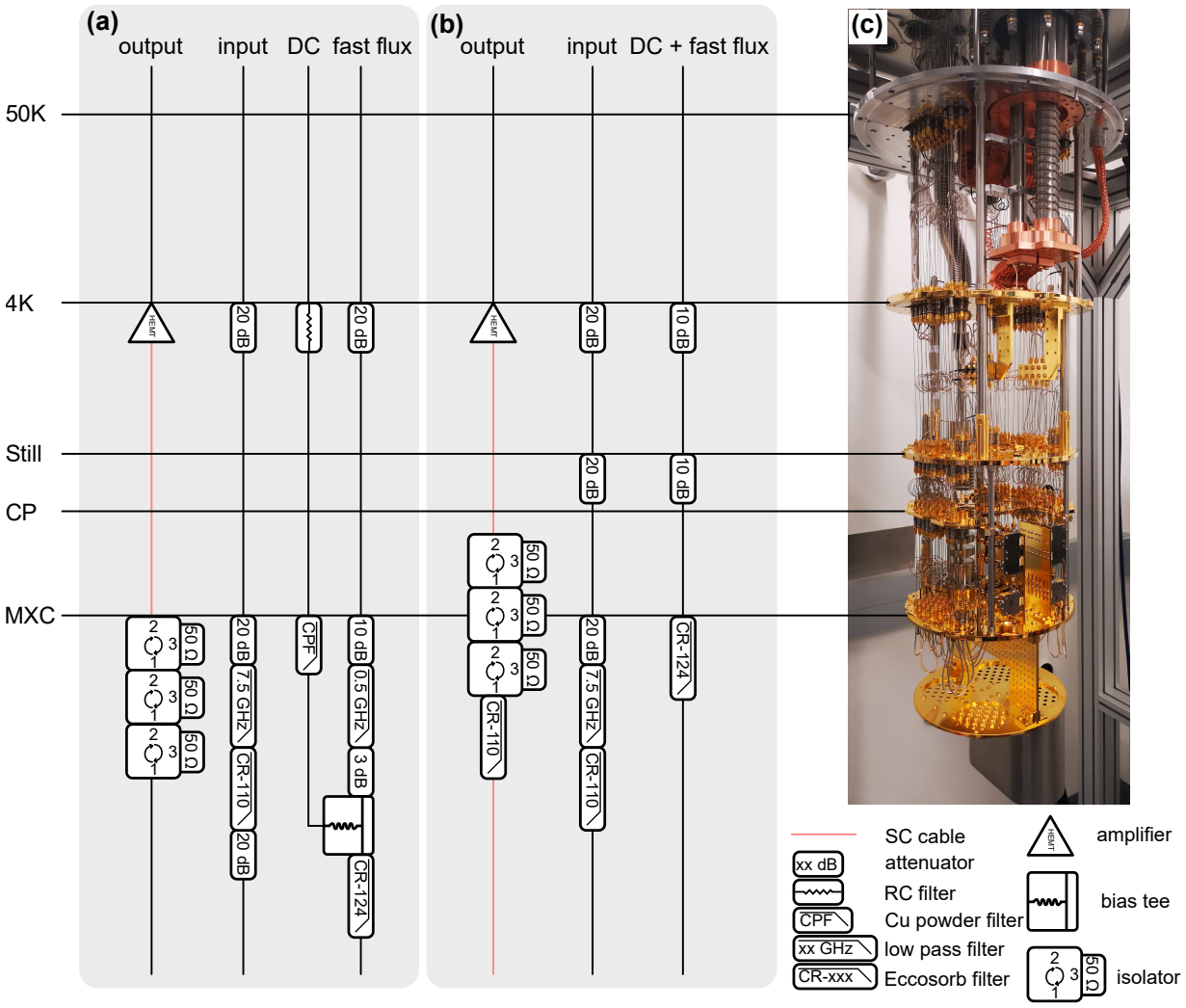

Figure H.2: (a) Wiring diagram for samples measured in previous chapters. (b) Optimized wiring diagram. There are 0 dB attenuators at each stage, which are not plotted. (c) Photo of the inner side of a wired Bluefors LD-400 dilution refrigerator.

line (< 500 MHz) using a bias tee. There is an RC filter with 1.5 kΩ resistance at the 4 K stage and a copper powder filter on the DC line before the bias tee. The copper powder filters were first introduced in Ref. [262] and are commonly used to filter out higher frequency signals [263, 264, 265, 266, 267, 268]. For the fast-flux lines, we add 20 dB attenuators at the 4 K stage and 10 dB more attenuators at the mixing chamber. There is a 500 MHz/1 GHz commercial low-pass filter before the bias tee. After the bias tee, we add a customized Eccosorb filter with a NbTi center trace. The superconducting center trace helps block the

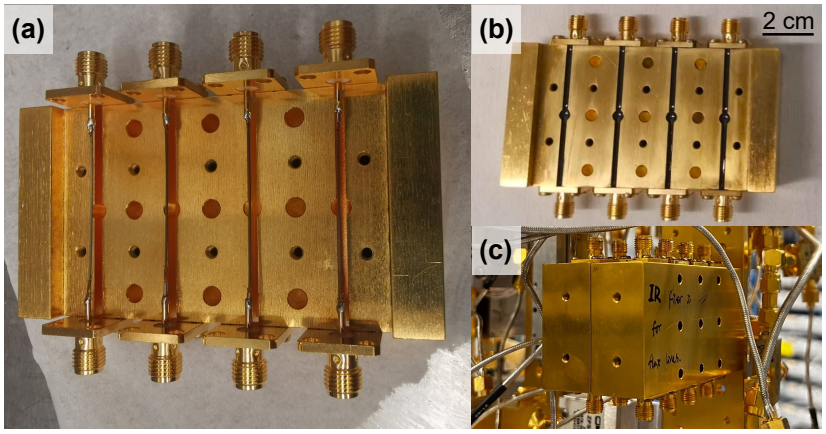

Figure H.3: Eccosorb filters. (a) NbTi wires are soldered to the SMA connectors. (b) Filters are filled with CR-124. (c) Filters are packaged and mounted on the dilution refrigerator.

heat generated before it. The NbTi wires come with a copper jacket, which is removed by leaving it in 40°C copper etchant CE-200 for 40 minutes. The copper at two ends is kept for soldering the wire to the connectors. The filters are shown in Fig. H.3. Here we choose Eccosorb CR-124 as the absorbing material, which gives a 3 dB cutoff frequency of 200 MHz. This flux line configuration can be simplified to using only one fast-flux line as shown in Fig. H.2(b).

With all these attenuators, filters, and isolators, we need to be careful with the impedance mismatch, which will also limit the gate fidelity [269] or affect the readout resonator dissipation rate κ_r [270].

H.3 Control electronics

We need to generate the pulses of different frequencies to control the qubits. The block diagrams for the pulse generation are shown in Fig. H.4.

For DC and fast flux control (0 to 300 MHz), pulses can be directly generated from a 1 Gsps speed digital-analog converter (DAC). We add a differential amplifier after the DAC to reduce the common mode noise and a Gaussian low pass filter to filter out the clock signal and get a smooth pulse shape [77].

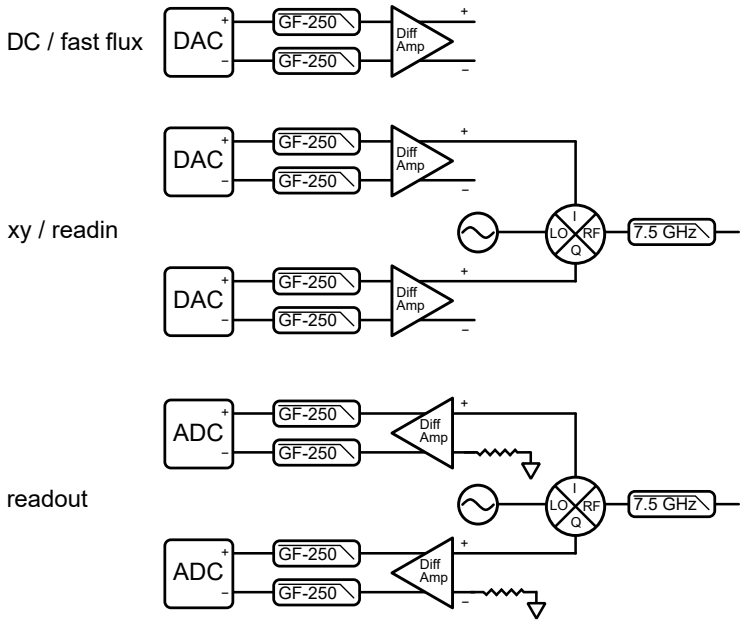

Figure H.4: Block diagrams for pulse generation. GF-250 represents a Gaussian filter with a 3 dB cutoff frequency of 250 MHz.

For qubit xy control, we need pulses of frequency around 5 GHz. One way to generate these pulses is to do mixing using a local oscillator (LO) and a mixer. The LO generates continuous waves at frequency f_{LO} and the DAC generates signal at frequency f_{IR}, the signal after the mixer has two sidebands with frequencies $f_{\mathrm{RF}} = f_{\mathrm{LO}} \pm f_{\mathrm{IR}}$. With proper filtering, we can keep only one sideband. Another way to remove the unwanted sideband is to use the in-phase quadrature (IQ) mixer, which contains two mixers and one sideband is removed by destructive interference. In practice, f_{IR} can be up to 300 MHz for a 1 Gsps speed DAC. For qubits' detuning within 600 MHz, we can use one LO for all qubits. IQ mixers are imperfect in reality, thus we need to correct the LO and sideband leakage [77, 271]. Using DACs with higher sampling rates, we can directly generate high-frequency signals without mixers [272].

The readout resonator drive (readin) is similar to the qubit xy control. Because of the large qubit-resonator detuning, we need a separate LO. The readout signals are down-converted by an IQ mixer and collected by an analog-digital converter (ADC), from which we can tell the qubit state. The mixers for readin and readout share the same LO.

BIBLIOGRAPHY

[1] Charles H. Bennett and Gilles Brassard. Quantum cryptography: Public key distribution and coin tossing. In *Proceedings of the IEEE International Conference on Computers, Systems and Signal Processing*, pages 175–179, Bangalore, December 1984.

[2] David Deutschand Richard Jozsa. Rapid solution of problems by quantum computation. *Proceedings of the Royal Society of London. Series A: Mathematical and Physical Sciences*, 439(1907):553–558, December 1992.

[3] P.W. Shor. Algorithms for quantum computation: discrete logarithms and factoring. In *Proceedings 35th Annual Symposium on Foundations of Computer Science*, SFCS-94, pages 124–134. IEEE Comput. Soc. Press, November 1994.

[4] A. Yu. Kitaev. Quantum measurements and the Abelian Stabilizer Problem. *arXiv preprint*, quant-ph/9511026, November 1995.

[5] Lov K. Grover. A fast quantum mechanical algorithm for database search. In *Proceedings of the twenty-eighth annual ACM symposium on Theory of computing - STOC '96*, STOC '96. ACM Press, 1996.

[6] Seth Lloyd. Universal quantum simulators. *Science*, 273(5278):1073–1078, August 1996.

[7] C. L. Degen, F. Reinhard, and P. Cappellaro. Quantum sensing. *Reviews of Modern Physics*, 89(3):035002, July 2017.

[8] Peter W. Shor. Scheme for reducing decoherence in quantum computer memory. *Physical Review A*, 52(4):R2493–R2496, October 1995.

[9] Yulin Wu, Wan-Su Bao, Sirui Cao, Fusheng Chen, Ming-Cheng Chen, Xiawei Chen, Tung-Hsun Chung, Hui Deng, Yajie Du, Daojin Fan, Ming Gong, Cheng Guo, Chu

Guo, Shaojun Guo, Lianchen Han, Linyin Hong, He-Liang Huang, Yong-Heng Huo, Liping Li, Na Li, Shaowei Li, Yuan Li, Futian Liang, Chun Lin, Jin Lin, Haoran Qian, Dan Qiao, Hao Rong, Hong Su, Lihua Sun, Liangyuan Wang, Shiyu Wang, Dachao Wu, Yu Xu, Kai Yan, Weifeng Yang, Yang Yang, Yangsen Ye, Jianghan Yin, Chong Ying, Jiale Yu, Chen Zha, Cha Zhang, Haibin Zhang, Kaili Zhang, Yiming Zhang, Han Zhao, Youwei Zhao, Liang Zhou, Qingling Zhu, Chao-Yang Lu, Cheng-Zhi Peng, Xiaobo Zhu, and Jian-Wei Pan. Strong quantum computational advantage using a superconducting quantum processor. *Physical Review Letters*, 127(18):180501, October 2021.

[10] Sebastian Krinner, Nathan Lacroix, Ants Remm, Agustin Di Paolo, Elie Genois, Catherine Leroux, Christoph Hellings, Stefania Lazar, Francois Swiadek, Johannes Herrmann, Graham J. Norris, Christian Kraglund Andersen, Markus Müller, Alexandre Blais, Christopher Eichler, and Andreas Wallraff. Realizing repeated quantum error correction in a distance-three surface code. *Nature*, 605(7911):669–674, May 2022.

[11] Rajeev Acharya, Igor Aleiner, Richard Allen, Trond I. Andersen, Markus Ansmann, Frank Arute, Kunal Arya, Abraham Asfaw, Juan Atalaya, Ryan Babbush, Dave Bacon, Joseph C. Bardin, Joao Basso, Andreas Bengtsson, Sergio Boixo, Gina Bortoli, Alexandre Bourassa, Jenna Bovaird, Leon Brill, Michael Broughton, Bob B. Buckley, David A. Buell, Tim Burger, Brian Burkett, Nicholas Bushnell, Yu Chen, Zijun Chen, Ben Chiaro, Josh Cogan, Roberto Collins, Paul Conner, William Courtney, Alexander L. Crook, Ben Curtin, Dripto M. Debroy, Alexander Del Toro Barba, Sean Demura, Andrew Dunsworth, Daniel Eppens, Catherine Erickson, Lara Faoro, Edward Farhi, Reza Fatemi, Leslie Flores Burgos, Ebrahim Forati, Austin G. Fowler, Brooks Foxen, William Giang, Craig Gidney, Dar Gilboa, Marissa Giustina, Alejandro Grajales Dau, Jonathan A. Gross, Steve Habegger, Michael C. Hamilton, Matthew P. Harrigan, Sean D. Harrington, Oscar Higgott, Jeremy Hilton, Markus Hoffmann, Sabrina Hong, Trent Huang, Ashley Huff, William J. Huggins, Lev B. Ioffe, Sergei V.

Isakov, Justin Iveland, Evan Jeffrey, Zhang Jiang, Cody Jones, Pavol Juhas, Dvir Kafri, Kostyantyn Kechedzhi, Julian Kelly, Tanuj Khattar, Mostafa Khezri, Mária Kieferová, Seon Kim, Alexei Kitaev, Paul V. Klimov, Andrey R. Klots, Alexander N. Korotkov, Fedor Kostritsa, John Mark Kreikebaum, David Landhuis, Pavel Laptev, Kim-Ming Lau, Lily Laws, Joonho Lee, Kenny Lee, Brian J. Lester, Alexander Lill, Wayne Liu, Aditya Locharla, Erik Lucero, Fionn D. Malone, Jeffrey Marshall, Orion Martin, Jarrod R. McClean, Trevor McCourt, Matt McEwen, Anthony Megrant, Bernardo Meurer Costa, Xiao Mi, Kevin C. Miao, Masoud Mohseni, Shirin Montazeri, Alexis Morvan, Emily Mount, Wojciech Mruczkiewicz, Ofer Naaman, Matthew Neeley, Charles Neill, Ani Nersisyan, Hartmut Neven, Michael Newman, Jiun How Ng, Anthony Nguyen, Murray Nguyen, Murphy Yuezhen Niu, Thomas E. O'Brien, Alex Opremcak, John Platt, Andre Petukhov, Rebecca Potter, Leonid P. Pryadko, Chris Quintana, Pedram Roushan, Nicholas C. Rubin, Negar Saei, Daniel Sank, Kannan Sankaragomathi, Kevin J. Satzinger, Henry F. Schurkus, Christopher Schuster, Michael J. Shearn, Aaron Shorter, Vladimir Shvarts, Jindra Skruzny, Vadim Smelyanskiy, W. Clarke Smith, George Sterling, Doug Strain, Marco Szalay, Alfredo Torres, Guifre Vidal, Benjamin Villalonga, Catherine Vollgraff Heidweiller, Theodore White, Cheng Xing, Z. Jamie Yao, Ping Yeh, Juhwan Yoo, Grayson Young, Adam Zalcman, Yaxing Zhang, and Ningfeng Zhu. Suppressing quantum errors by scaling a surface code logical qubit. *Nature*, 614(7949):676–681, February 2023.

[12] Youngseok Kim, Andrew Eddins, Sajant Anand, Ken Xuan Wei, Ewout van den Berg, Sami Rosenblatt, Hasan Nayfeh, Yantao Wu, Michael Zaletel, Kristan Temme, and Abhinav Kandala. Evidence for the utility of quantum computing before fault tolerance. *Nature*, 618(7965):500–505, June 2023.

[13] Austin G. Fowler, Matteo Mariantoni, John M. Martinis, and Andrew N. Cleland. Surface codes: Towards practical large-scale quantum computation. *Physical Review*

A, 86(3):032324, September 2012.

[14] Michael E. Beverland, Prakash Murali, Matthias Troyer, Krysta M. Svore, Torsten Hoefler, Vadym Kliuchnikov, Guang Hao Low, Mathias Soeken, Aarthi Sundaram, and Alexander Vaschillo. Assessing requirements to scale to practical quantum advantage. *arXiv preprint*, 2211.07629, November 2022.

[15] Jared B. Hertzberg, Eric J. Zhang, Sami Rosenblatt, Easwar Magesan, John A. Smolin, Jeng-Bang Yau, Vivekananda P. Adiga, Martin Sandberg, Markus Brink, Jerry M. Chow, and Jason S. Orcutt. Laser-annealing Josephson junctions for yielding scaled-up superconducting quantum processors. *npj Quantum Information*, 7(1):129, August 2021.

[16] Antti P. Vepsäläinen, Amir H. Karamlou, John L. Orrell, Akshunna S. Dogra, Ben Loer, Francisca Vasconcelos, David K. Kim, Alexander J. Melville, Bethany M. Niedzielski, Jonilyn L. Yoder, Simon Gustavsson, Joseph A. Formaggio, Brent A. VanDevender, and William D. Oliver. Impact of ionizing radiation on superconducting qubit coherence. *Nature*, 584(7822):551–556, August 2020.

[17] Matt McEwen, Lara Faoro, Kunal Arya, Andrew Dunsworth, Trent Huang, Seon Kim, Brian Burkett, Austin Fowler, Frank Arute, Joseph C. Bardin, Andreas Bengtsson, Alexander Bilmes, Bob B. Buckley, Nicholas Bushnell, Zijun Chen, Roberto Collins, Sean Demura, Alan R. Derk, Catherine Erickson, Marissa Giustina, Sean D. Harrington, Sabrina Hong, Evan Jeffrey, Julian Kelly, Paul V. Klimov, Fedor Kostritsa, Pavel Laptev, Aditya Locharla, Xiao Mi, Kevin C. Miao, Shirin Montazeri, Josh Mutus, Ofer Naaman, Matthew Neeley, Charles Neill, Alex Opremcak, Chris Quintana, Nicholas Redd, Pedram Roushan, Daniel Sank, Kevin J. Satzinger, Vladimir Shvarts, Theodore White, Z. Jamie Yao, Ping Yeh, Juhwan Yoo, Yu Chen, Vadim Smelyanskiy, John M. Martinis, Hartmut Neven, Anthony Megrant, Lev Ioffe, and Rami Barends. Resolving

catastrophic error bursts from cosmic rays in large arrays of superconducting qubits. *Nature Physics*, 18(1):107–111, December 2021.

[18] Xue-Gang Li, Jun-Hua Wang, Yao-Yao Jiang, Guang-Ming Xue, Xiao-Xia Cai, Jun Zhou, Ming Gong, Zhao-Feng Liu, Shuang-Yu Zheng, Deng-Ke Ma, Mo Chen, Wei-Jie Sun, Shuang Yang, Fei Yan, Yi-Rong Jin, Xue-Feng Ding, and Hai-Feng Yu. Direct evidence for cosmic-ray-induced correlated errors in superconducting qubit array. *arXiv preprint*, 2402.04245, February 2024.

[19] Patrick M. Harrington, Mingyu Li, Max Hays, Wouter Van De Pontseele, Daniel Mayer, H. Douglas Pinckney, Felipe Contipelli, Michael Gingras, Bethany M. Niedzielski, Hannah Stickler, Jonilyn L. Yoder, Mollie E. Schwartz, Jeffrey A. Grover, Kyle Serniak, William D. Oliver, and Joseph A. Formaggio. Synchronous detection of cosmic rays and correlated errors in superconducting qubit arrays. *arXiv preprint*, 2402.03208, February 2024.

[20] Kaitlin N. Smith, Gokul Subramanian Ravi, Jonathan M. Baker, and Frederic T. Chong. Scaling superconducting quantum computers with chiplet architectures. In *2022 55th IEEE/ACM International Symposium on Microarchitecture (MICRO)*. IEEE, October 2022.

[21] Sergey Bravyi, Oliver Dial, Jay M. Gambetta, Darío Gil, and Zaira Nazario. The future of quantum computing with superconducting qubits. *Journal of Applied Physics*, 132(16):160902, October 2022.

[22] Qian Xu, Alireza Seif, Haoxiong Yan, Nam Mannucci, Bernard Ousmane Sane, Rodney Van Meter, Andrew N. Cleland, and Liang Jiang. Distributed quantum error correction for chip-level catastrophic errors. *Physical Review Letters*, 129(24):240502, December 2022.

[23] Daniel Gottesman and Isaac L. Chuang. Demonstrating the viability of universal quantum computation using teleportation and single-qubit operations. *Nature*, 402(6760):390–393, November 1999.

[24] Liang Jiang, Jacob M. Taylor, Anders S. Sørensen, and Mikhail D. Lukin. Distributed quantum computation based on small quantum registers. *Physical Review A*, 76(6):062323, December 2007.

[25] C. Monroe, R. Raussendorf, A. Ruthven, K. R. Brown, P. Maunz, L.-M. Duan, and J. Kim. Large-scale modular quantum-computer architecture with atomic memory and photonic interconnects. *Physical Review A*, 89(2):022317, February 2014.

[26] Kevin S. Chou, Jacob Z. Blumoff, Christopher S. Wang, Philip C. Reinhold, Christopher J. Axline, Yvonne Y. Gao, L. Frunzio, M. H. Devoret, Liang Jiang, and R. J. Schoelkopf. Deterministic teleportation of a quantum gate between two logical qubits. *Nature*, 561(7723):368–373, September 2018.

[27] David Barral, F. Javier Cardama, Guillermo Díaz, Daniel Faílde, Iago F. Llovo, Mariamo Mussa Juane, Jorge Vázquez-Pérez, Juan Villasuso, César Piñeiro, Natalia Costas, Juan C. Pichel, Tomás F. Pena, and Andrés Gómez. Review of distributed quantum computing. From single QPU to high performance quantum computing. *arXiv preprint*, 2404.01265, April 2024.

[28] H. J. Kimble. The quantum internet. *Nature*, 453(7198):1023–1030, June 2008.

[29] M. Pompili, S. L. N. Hermans, S. Baier, H. K. C. Beukers, P. C. Humphreys, R. N. Schouten, R. F. L. Vermeulen, M. J. Tiggelman, L. dos Santos Martins, B. Dirkse, S. Wehner, and R. Hanson. Realization of a multinode quantum network of remote solid-state qubits. *Science*, 372(6539):259–264, April 2021.

[30] Jian-Long Liu, Xi-Yu Luo, Yong Yu, Chao-Yang Wang, Bin Wang, Yi Hu, Jun Li, Ming-Yang Zheng, Bo Yao, Zi Yan, Da Teng, Jin-Wei Jiang, Xiao-Bing Liu, Xiu-Ping Xie, Jun Zhang, Qing-He Mao, Xiao Jiang, Qiang Zhang, Xiao-Hui Bao, and Jian-Wei Pan. Creation of memory–memory entanglement in a metropolitan quantum network. *Nature*, 629(8012):579–585, May 2024.

[31] Zheshen Zhang and Quntao Zhuang. Distributed quantum sensing. *Quantum Science and Technology*, 6(4):043001, July 2021.

[32] P. Kurpiers, P. Magnard, T. Walter, B. Royer, M. Pechal, J. Heinsoo, Y. Salathé, A. Akin, S. Storz, J.-C. Besse, S. Gasparinetti, A. Blais, and A. Wallraff. Deterministic quantum state transfer and remote entanglement using microwave photons. *Nature*, 558(7709):264–267, June 2018.

[33] P. Campagne-Ibarcq, E. Zalys-Geller, A. Narla, S. Shankar, P. Reinhold, L. Burkhart, C. Axline, W. Pfaff, L. Frunzio, R. J. Schoelkopf, and M. H. Devoret. Deterministic remote entanglement of superconducting circuits through microwave two-photon transitions. *Physical Review Letters*, 120(20):200501, May 2018.

[34] N. Leung, Y. Lu, S. Chakram, R. K. Naik, N. Earnest, R. Ma, K. Jacobs, A. N. Cleland, and D. I. Schuster. Deterministic bidirectional communication and remote entanglement generation between superconducting qubits. *npj Quantum Information*, 5(1):18, February 2019.

[35] Youpeng Zhong, Hung-Shen Chang, Audrey Bienfait, Étienne Dumur, Ming-Han Chou, Christopher R. Conner, Joel Grebel, Rhys G. Povey, Haoxiong Yan, David I. Schuster, and Andrew N. Cleland. Deterministic multi-qubit entanglement in a quantum network. *Nature*, 590(7847):571–575, February 2021.

[36] Christopher J. Axline, Luke D. Burkhart, Wolfgang Pfaff, Mengzhen Zhang, Kevin Chou, Philippe Campagne-Ibarcq, Philip Reinhold, Luigi Frunzio, S. M. Girvin, Liang Jiang, M. H. Devoret, and R. J. Schoelkopf. On-demand quantum state transfer and entanglement between remote microwave cavity memories. *Nature Physics*, 14(7):705–710, April 2018.

[37] Alysson Gold, J. P. Paquette, Anna Stockklauser, Matthew J. Reagor, M. Sohaib Alam, Andrew Bestwick, Nicolas Didier, Ani Nersisyan, Feyza Oruc, Armin Razavi, Ben Scharmann, Eyob A. Sete, Biswajit Sur, Davide Venturelli, Cody James Winkleblack, Filip Wudarski, Mike Harburn, and Chad Rigetti. Entanglement across separate silicon dies in a modular superconducting qubit device. *npj Quantum Information*, 7(1):142, September 2021.

[38] Mark Field, Angela Q. Chen, Ben Scharmann, Eyob A. Sete, Feyza Oruc, Kim Vu, Valentin Kosenko, Joshua Y. Mutus, Stefano Poletto, and Andrew Bestwick. Modular superconducting-qubit architecture with a multichip tunable coupler. *Physical Review Applied*, 21(5):054063, May 2024.

[39] Mohammad Mirhosseini, Alp Sipahigil, Mahmoud Kalaee, and Oskar Painter. Superconducting qubit to optical photon transduction. *Nature*, 588(7839):599–603, December 2020.

[40] P. Magnard, S. Storz, P. Kurpiers, J. Schär, F. Marxer, J. Lütolf, T. Walter, J.-C. Besse, M. Gabureac, K. Reuer, A. Akin, B. Royer, A. Blais, and A. Wallraff. Microwave quantum link between superconducting circuits housed in spatially separated cryogenic systems. *Physical Review Letters*, 125(26):260502, December 2020.

[41] Simon Storz, Josua Schär, Anatoly Kulikov, Paul Magnard, Philipp Kurpiers, Janis Lütolf, Theo Walter, Adrian Copetudo, Kevin Reuer, Abdulkadir Akin, Jean-Claude

Besse, Mihai Gabureac, Graham J. Norris, Andrés Rosario, Ferran Martin, José Martinez, Waldimar Amaya, Morgan W. Mitchell, Carlos Abellan, Jean-Daniel Bancal, Nicolas Sangouard, Baptiste Royer, Alexandre Blais, and Andreas Wallraff. Loophole-free Bell inequality violation with superconducting circuits. *Nature*, 617(7960):265–270, May 2023.

[42] M. Renger, S. Gandorfer, W. Yam, F. Fesquet, M. Handschuh, K. E. Honasoge, F. Kronowetter, Y. Nojiri, M. Partanen, M. Pfeiffer, H. van der Vliet, A. J. Matthews, J. Govenius, R. N. Jabdaraghi, M. Prunnila, A. Marx, F. Deppe, R. Gross, and K. G. Fedorov. Cryogenic microwave link for quantum local area networks. *arXiv preprint*, 2308.12398, August 2023.

[43] Uri Vool and Michel Devoret. Introduction to quantum electromagnetic circuits. *International Journal of Circuit Theory and Applications*, 45(7):897–934, June 2017.

[44] Daniel T. Sank, Sergei V. Isakov, and Mostafa Khezri. Balanced coupling in superconducting circuits. In *APS March Meeting*, March 2024.

[45] David M. Pozar. *Microwave Engineering*. John Wiley & Sons, Inc, November 2011.

[46] A. A. Clerk, M. H. Devoret, S. M. Girvin, Florian Marquardt, and R. J. Schoelkopf. Introduction to quantum noise, measurement, and amplification. *Reviews of Modern Physics*, 82(2):1155–1208, April 2010.

[47] E. M. Purcell. *Spontaneous Emission Probabilities at Radio Frequencies*, pages 839–839. Springer US, 1995.

[48] Evan Jeffrey, Daniel Sank, J. Y. Mutus, T. C. White, J. Kelly, R. Barends, Y. Chen, Z. Chen, B. Chiaro, A. Dunsworth, A. Megrant, P. J. J. O'Malley, C. Neill, P. Roushan, A. Vainsencher, J. Wenner, A. N. Cleland, and John M. Martinis. Fast accurate state

measurement with superconducting qubits. *Physical Review Letters*, 112(19):190504, May 2014.

[49] C. W. Gardiner and M. J. Collett. Input and output in damped quantum systems: Quantum stochastic differential equations and the master equation. *Physical Review A*, 31(6):3761–3774, June 1985.

[50] Crispin Gardiner and Peter Zoller. *Quantum Noise: A Handbook of Markovian and Non-Markovian Quantum Stochastic Methods with Applications to Quantum Optics*. Springer Berlin, Heidelberg, August 2004.

[51] Mark Srednicki. *Quantum Field Theory*. Cambridge University Press, January 2007.

[52] Mohammad Mirhosseini, Eunjong Kim, Vinicius S. Ferreira, Mahmoud Kalaee, Alp Sipahigil, Andrew J. Keller, and Oskar Painter. Superconducting metamaterials for waveguide quantum electrodynamics. *Nature Communications*, 9(1):3706, September 2018.

[53] H. Wang, A.P. Zhuravel, S. Indrajeet, B.G. Taketani, M.D. Hutchings, Y. Hao, F. Rouxinol, F.K. Wilhelm, M.D. LaHaye, A.V. Ustinov, and B.L.T. Plourde. Mode structure in superconducting metamaterial transmission-line resonators. *Physical Review Applied*, 11(5):054062, May 2019.

[54] S. Indrajeet, H. Wang, M.D. Hutchings, B.G. Taketani, Frank K. Wilhelm, M.D. LaHaye, and B.L.T. Plourde. Coupling a superconducting qubit to a left-handed metamaterial resonator. *Physical Review Applied*, 14(6):064033, December 2020.

[55] Vinicius S. Ferreira, Jash Banker, Alp Sipahigil, Matthew H. Matheny, Andrew J. Keller, Eunjong Kim, Mohammad Mirhosseini, and Oskar Painter. Collapse and revival of an artificial atom coupled to a structured photonic reservoir. *Physical Review X*, 11(4):041043, December 2021.

[56] Eunjong Kim, Xueyue Zhang, Vinicius S. Ferreira, Jash Banker, Joseph K. Iverson, Alp Sipahigil, Miguel Bello, Alejandro González-Tudela, Mohammad Mirhosseini, and Oskar Painter. Quantum electrodynamics in a topological waveguide. *Physical Review X*, 11(1):011015, January 2021.

[57] Marco Scigliuzzo, Giuseppe Calajò, Francesco Ciccarello, Daniel Perez Lozano, Andreas Bengtsson, Pasquale Scarlino, Andreas Wallraff, Darrick Chang, Per Delsing, and Simone Gasparinetti. Controlling atom-photon bound states in an array of Josephson-junction resonators. *Physical Review X*, 12(3):031036, September 2022.

[58] Xueyue Zhang, Eunjong Kim, Daniel K. Mark, Soonwon Choi, and Oskar Painter. A superconducting quantum simulator based on a photonic-bandgap metamaterial. *Science*, 379(6629):278–283, January 2023.

[59] Charles Kittel. *Introduction to Solid State Physics*. John Wiley & Sons, Inc, November 2004.

[60] T. M. Hazard, W. Woods, D. Rosenberg, R. Das, C. F. Hirjibehedin, D. K. Kim, J. M. Knecht, J. Mallek, A. Melville, B. M. Niedzielski, K. Serniak, K. M. Sliwa, D. R. W. Yost, J. L. Yoder, W. D. Oliver, and M. E. Schwartz. Characterization of superconducting through-silicon vias as capacitive elements in quantum circuits. *Applied Physics Letters*, 123(15):154004, October 2023.

[61] M. Göppl, A. Fragner, M. Baur, R. Bianchetti, S. Filipp, J. M. Fink, P. J. Leek, G. Puebla, L. Steffen, and A. Wallraff. Coplanar waveguide resonators for circuit quantum electrodynamics. *Journal of Applied Physics*, 104(11):113904, December 2008.

[62] Jiansong Gao. *The Physics of Superconducting Microwave Resonators*. PhD thesis, California Institute of Technology, May 2008.

[63] M. S. Khalil, M. J. A. Stoutimore, F. C. Wellstood, and K. D. Osborn. An analysis method for asymmetric resonator transmission applied to superconducting devices. *Journal of Applied Physics*, 111(5):054510, March 2012.

[64] Qi-Ming Chen, Meike Pfeiffer, Matti Partanen, Florian Fesquet, Kedar E. Honasoge, Fabian Kronowetter, Yuki Nojiri, Michael Renger, Kirill G. Fedorov, Achim Marx, Frank Deppe, and Rudolf Gross. Scattering coefficients of superconducting microwave resonators. I. Transfer matrix approach. *Physical Review B*, 106(21):214505, December 2022.

[65] Kevin Lalumière, Barry C. Sanders, A. F. van Loo, A. Fedorov, A. Wallraff, and A. Blais. Input-output theory for waveguide QED with an ensemble of inhomogeneous atoms. *Physical Review A*, 88(4):043806, October 2013.

[66] Qi-Ming Chen, Matti Partanen, Florian Fesquet, Kedar E. Honasoge, Fabian Kronowetter, Yuki Nojiri, Michael Renger, Kirill G. Fedorov, Achim Marx, Frank Deppe, and Rudolf Gross. Scattering coefficients of superconducting microwave resonators. II. System-bath approach. *Physical Review B*, 106(21):214506, December 2022.

[67] A. Megrant, C. Neill, R. Barends, B. Chiaro, Yu Chen, L. Feigl, J. Kelly, Erik Lucero, Matteo Mariantoni, P. J. J. O'Malley, D. Sank, A. Vainsencher, J. Wenner, T. C. White, Y. Yin, J. Zhao, C. J. Palmstrøm, John M. Martinis, and A. N. Cleland. Planar superconducting resonators with internal quality factors above one million. *Applied Physics Letters*, 100(11):113510, March 2012.

[68] S. Probst, F. B. Song, P. A. Bushev, A. V. Ustinov, and M. Weides. Efficient and robust analysis of complex scattering data under noise in microwave resonators. *Review of Scientific Instruments*, 86(2):024706, February 2015.

[69] Anton Frisk Kockum, Per Delsing, and Göran Johansson. Designing frequency-dependent relaxation rates and Lamb shifts for a giant artificial atom. *Physical Review A*, 90(1):013837, July 2014.

[70] Bharath Kannan, Max J. Ruckriegel, Daniel L. Campbell, Anton Frisk Kockum, Jochen Braumüller, David K. Kim, Morten Kjaergaard, Philip Krantz, Alexander Melville, Bethany M. Niedzielski, Antti Vepsäläinen, Roni Winik, Jonilyn L. Yoder, Franco Nori, Terry P. Orlando, Simon Gustavsson, and William D. Oliver. Waveguide quantum electrodynamics with superconducting artificial giant atoms. *Nature*, 583(7818):775–779, July 2020.

[71] Nicolas Gheeraert, Shingo Kono, and Yasunobu Nakamura. Programmable directional emitter and receiver of itinerant microwave photons in a waveguide. *Physical Review A*, 102(5):053720, November 2020.

[72] Bharath Kannan, Aziza Almanakly, Youngkyu Sung, Agustin Di Paolo, David A. Rower, Jochen Braumüller, Alexander Melville, Bethany M. Niedzielski, Amir Karamlou, Kyle Serniak, Antti Vepsäläinen, Mollie E. Schwartz, Jonilyn L. Yoder, Roni Winik, Joel I-Jan Wang, Terry P. Orlando, Simon Gustavsson, Jeffrey A. Grover, and William D. Oliver. On-demand directional microwave photon emission using waveguide quantum electrodynamics. *Nature Physics*, 19(3):394–400, January 2023.

[73] Jens Koch, Terri M. Yu, Jay Gambetta, A. A. Houck, D. I. Schuster, J. Majer, Alexandre Blais, M. H. Devoret, S. M. Girvin, and R. J. Schoelkopf. Charge-insensitive qubit design derived from the Cooper pair box. *Physical Review A*, 76(4):042319, October 2007.

[74] R. Barends, J. Kelly, A. Megrant, D. Sank, E. Jeffrey, Y. Chen, Y. Yin, B. Chiaro, J. Mutus, C. Neill, P. O'Malley, P. Roushan, J. Wenner, T. C. White, A. N. Cle-

land, and John M. Martinis. Coherent Josephson qubit suitable for scalable quantum integrated circuits. *Physical Review Letters*, 111(8):080502, August 2013.

[75] B. D. Josephson. The discovery of tunnelling supercurrents. *Reviews of Modern Physics*, 46(2):251–254, April 1974.

[76] Dennis Willsch, Dennis Rieger, Patrick Winkel, Madita Willsch, Christian Dickel, Jonas Krause, Yoichi Ando, Raphaël Lescanne, Zaki Leghtas, Nicholas T. Bronn, Pratiti Deb, Olivia Lanes, Zlatko K. Minev, Benedikt Dennig, Simon Geisert, Simon Günzler, Sören Ihssen, Patrick Paluch, Thomas Reisinger, Roudy Hanna, Jin Hee Bae, Peter Schüffelgen, Detlev Grützmacher, Luiza Buimaga-Iarinca, Cristian Morari, Wolfgang Wernsdorfer, David P. DiVincenzo, Kristel Michielsen, Gianluigi Catelani, and Ioan M. Pop. Observation of Josephson harmonics in tunnel junctions. *Nature Physics*, February 2024.

[77] Youpeng Zhong. *Violating Bell's Inequality with Remotely-Connected Superconducting Qubits*. PhD thesis, University of Chicago, March 2019.

[78] Simon E. Nigg, Hanhee Paik, Brian Vlastakis, Gerhard Kirchmair, S. Shankar, Luigi Frunzio, M. H. Devoret, R. J. Schoelkopf, and S. M. Girvin. Black-box superconducting circuit quantization. *Physical Review Letters*, 108(24):240502, January 2012.

[79] Xianjing Zhou, Gerwin Koolstra, Xufeng Zhang, Ge Yang, Xu Han, Brennan Dizdar, Xinhao Li, Ralu Divan, Wei Guo, Kater W. Murch, David I. Schuster, and Dafei Jin. Single electrons on solid neon as a solid-state qubit platform. *Nature*, 605(7908):46–50, May 2022.

[80] Ziqian Li, Tanay Roy, David Rodríguez Pérez, Kan-Heng Lee, Eliot Kapit, and David I. Schuster. Autonomous error correction of a single logical qubit using two transmons. *Nature Communications*, 15(1):1681, February 2024.

[81] F. Motzoi, J. M. Gambetta, P. Rebentrost, and F. K. Wilhelm. Simple pulses for elimination of leakage in weakly nonlinear qubits. *Physical Review Letters*, 103(11):110501, September 2009.

[82] T. Figueiredo Roque, Aashish A. Clerk, and Hugo Ribeiro. Engineering fast high-fidelity quantum operations with constrained interactions. *npj Quantum Information*, 7(1):28, February 2021.

[83] Zhiyuan Li, Pei Liu, Peng Zhao, Zhenyu Mi, Huikai Xu, Xuehui Liang, Tang Su, Weijie Sun, Guangming Xue, Jing-Ning Zhang, Weiyang Liu, Yirong Jin, and Haifeng Yu. Error per single-qubit gate below 10^{-4} in a superconducting qubit. *npj Quantum Information*, 9(1):111, November 2023.

[84] Mingkang Xia, Chao Zhou, Chenxu Liu, Param Patel, Xi Cao, Pinlei Lu, Boris Mesits, Maria Mucci, David Gorski, David Pekker, and Michael Hatridge. Fast superconducting qubit control with sub-harmonic drives. *arXiv preprint*, 2306.10162, June 2023.

[85] Aashish Sah, Suman Kundu, Heikki Suominen, Qiming Chen, and Mikko Möttönen. Decay-protected superconducting qubit with fast control enabled by integrated on-chip filters. *arXiv preprint*, 2402.08906, February 2024.

[86] S. Kono, K. Koshino, D. Lachance-Quirion, A. F. van Loo, Y. Tabuchi, A. Noguchi, and Y. Nakamura. Breaking the trade-off between fast control and long lifetime of a superconducting qubit. *Nature Communications*, 11(1):3683, July 2020.

[87] A. Wallraff, D. I. Schuster, A. Blais, L. Frunzio, J. Majer, M. H. Devoret, S. M. Girvin, and R. J. Schoelkopf. Approaching unit visibility for control of a superconducting qubit with dispersive readout. *Physical Review Letters*, 95(6):060501, August 2005.

[88] Daniel Thomas Sank. *Fast, Accurate State Measurement in Superconducting Qubits*. PhD thesis, University of California, Santa Barbara, September 2014.

[89] Zhiling Wang, Zenghui Bao, Yukai Wu, Yan Li, Cheng Ma, Tianqi Cai, Yipu Song, Hongyi Zhang, and Luming Duan. Improved superconducting qubit state readout by path interference. *Chinese Physics Letters*, 38(11):110303, December 2021.

[90] Alec Yen, Yufeng Ye, Kaidong Peng, Jennifer Wang, Gregory Cunningham, Michael Gingras, Bethany M. Niedzielski, Hannah Stickler, Kyle Serniak, Mollie E. Schwartz, and Kevin P. O'Brien. All-pass readout for robust and scalable quantum measurement. *arXiv preprint*, 2403.01375, March 2024.

[91] Alec Yen, Yufeng Ye, Kaidong Peng, Jennifer Wang, Gregory Cunningham, Michael Gingras, Bethany M. Niedzielski, Hannah Stickler, Kyle Serniak, Mollie E. Schwartz, and Kevin P. O'Brien. Interferometric Purcell suppression of spontaneous emission in a superconducting qubit. *arXiv preprint*, 2405.10107, May 2024.

[92] Manuel H. Muñoz-Arias, Cristóbal Lledó, and Alexandre Blais. Qubit readout enabled by qubit cloaking. *Physical Review Applied*, 20(5):054013, November 2023.

[93] Daniel Sank, Zijun Chen, Mostafa Khezri, J. Kelly, R. Barends, B. Campbell, Y. Chen, B. Chiaro, A. Dunsworth, A. Fowler, E. Jeffrey, E. Lucero, A. Megrant, J. Mutus, M. Neeley, C. Neill, P. J. J. O'Malley, C. Quintana, P. Roushan, A. Vainsencher, T. White, J. Wenner, Alexander N. Korotkov, and John M. Martinis. Measurement-induced state transitions in a superconducting qubit: Beyond the rotating wave approximation. *Physical Review Letters*, 117(19):190503, November 2016.

[94] Ross Shillito, Alexandru Petrescu, Joachim Cohen, Jackson Beall, Markus Hauru, Martin Ganahl, Adam G.M. Lewis, Guifre Vidal, and Alexandre Blais. Dynamics of transmon ionization. *Physical Review Applied*, 18(3):034031, September 2022.

[95] Mostafa Khezri, Alex Opremcak, Zijun Chen, Kevin C. Miao, Matt McEwen, Andreas Bengtsson, Theodore White, Ofer Naaman, Daniel Sank, Alexander N. Korotkov,

Yu Chen, and Vadim Smelyanskiy. Measurement-induced state transitions in a superconducting qubit: Within the rotating-wave approximation. *Physical Review Applied*, 20(5):054008, November 2023.

[96] Marie Frédérique Dumas, Benjamin Groleau-Paré, Alexander McDonald, Manuel H. Muñoz-Arias, Cristóbal Lledó, Benjamin D'Anjou, and Alexandre Blais. Unified picture of measurement-induced ionization in the transmon. *arXiv preprint*, 2402.06615, February 2024.

[97] Jose Aumentado. Superconducting parametric amplifiers: The state of the art in Josephson parametric amplifiers. *IEEE Microwave Magazine*, 21(8):45–59, August 2020.

[98] Tanay Roy, Suman Kundu, Madhavi Chand, A. M. Vadiraj, A. Ranadive, N. Nehra, Meghan P. Patankar, J. Aumentado, A. A. Clerk, and R. Vijay. Broadband parametric amplification with impedance engineering: Beyond the gain-bandwidth product. *Applied Physics Letters*, 107(26):262601, December 2015.

[99] J. Grebel, A. Bienfait, É. Dumur, H.-S. Chang, M.-H. Chou, C. R. Conner, G. A. Peairs, R. G. Povey, Y. P. Zhong, and A. N. Cleland. Flux-pumped impedance-engineered broadband Josephson parametric amplifier. *Applied Physics Letters*, 118(14):142601, April 2021.

[100] Ofer Naaman and José Aumentado. Synthesis of parametrically coupled networks. *PRX Quantum*, 3(2):020201, May 2022.

[101] Ryan Kaufman, Theodore White, Mark I. Dykman, Andrea Iorio, George Sterling, Sabrina Hong, Alex Opremcak, Andreas Bengtsson, Lara Faoro, Joseph C. Bardin, Tim Burger, Robert Gasca, and Ofer Naaman. Josephson parametric amplifier with

Chebyshev gain profile and high saturation. *Physical Review Applied*, 20(5):054058, November 2023.

[102] C. Macklin, K. O'Brien, D. Hover, M. E. Schwartz, V. Bolkhovsky, X. Zhang, W. D. Oliver, and I. Siddiqi. A near-quantum-limited Josephson traveling-wave parametric amplifier. *Science*, 350(6258):307–310, September 2015.

[103] M. D. Reed, B. R. Johnson, A. A. Houck, L. DiCarlo, J. M. Chow, D. I. Schuster, L. Frunzio, and R. J. Schoelkopf. Fast reset and suppressing spontaneous emission of a superconducting qubit. *Applied Physics Letters*, 96(20):203110, May 2010.

[104] Alexandre Blais, Arne L. Grimsmo, S. M. Girvin, and Andreas Wallraff. Circuit quantum electrodynamics. *Reviews of Modern Physics*, 93(2):025005, May 2021.

[105] Nicholas T. Bronn, Yanbing Liu, Jared B. Hertzberg, Antonio D. Córcoles, Andrew A. Houck, Jay M. Gambetta, and Jerry M. Chow. Broadband filters for abatement of spontaneous emission in circuit quantum electrodynamics. *Applied Physics Letters*, 107(17):172601, October 2015.

[106] B. M. Smitham, Christie S Chiu, Jeronimo G Martinez, and Andrew A. Houck. Novel wideband Purcell filters for circuit QED. In *APS March Meeting*, volume 68, page 3, March 2023.

[107] Yibiao Zhou, Xiao Cai, Yuzhen Zheng, Boyi Zhou, Yu Wang, Kanglin Xiong, and Jiagui Feng. High-suppression-ratio and wide bandwidth four-stage Purcell filter for multiplexed superconducting qubit readout. *Journal of Applied Physics*, 135(2):024402, January 2024.

[108] Eyob A. Sete, John M. Martinis, and Alexander N. Korotkov. Quantum theory of a bandpass Purcell filter for qubit readout. *Physical Review A*, 92(1):012325, July 2015.

[109] Liangyu Chen, Hang-Xi Li, Yong Lu, Christopher W. Warren, Christian J. Križan, Sandoko Kosen, Marcus Rommel, Shahnawaz Ahmed, Amr Osman, Janka Biznárová, Anita Fadavi Roudsari, Benjamin Lienhard, Marco Caputo, Kestutis Grigoras, Leif Grönberg, Joonas Govenius, Anton Frisk Kockum, Per Delsing, Jonas Bylander, and Giovanna Tancredi. Transmon qubit readout fidelity at the threshold for quantum error correction without a quantum-limited amplifier. *npj Quantum Information*, 9(1):26, March 2023.

[110] Johannes Heinsoo, Christian Kraglund Andersen, Ants Remm, Sebastian Krinner, Theodore Walter, Yves Salathé, Simone Gasparinetti, Jean-Claude Besse, Anton Potočnik, Andreas Wallraff, and Christopher Eichler. Rapid high-fidelity multiplexed readout of superconducting qubits. *Physical Review Applied*, 10(3):034040, September 2018.

[111] François Swiadek, Ross Shillito, Paul Magnard, Ants Remm, Christoph Hellings, Nathan Lacroix, Quentin Ficheux, Dante Colao Zanuz, Graham J. Norris, Alexandre Blais, Sebastian Krinner, and Andreas Wallraff. Enhancing dispersive readout of superconducting qubits through dynamic control of the dispersive shift: Experiment and theory. *arXiv preprint*, 2307.07765, July 2023.

[112] Hamid Reza Mohebbi, Olaf Benningshof, Ivar Taminiau, Guo-Xing Miao, and David Cory. Superconducting coplanar interdigital filter with robust packaging. *IEEE Transactions on Applied Superconductivity*, 25(3):1500604, 2014.

[113] Agnetta Y. Cleland, Marek Pechal, Pieter-Jan C. Stas, Christopher J. Sarabalis, E. Alex Wollack, and Amir H. Safavi-Naeini. Mechanical Purcell filters for microwave quantum machines. *Applied Physics Letters*, 115(26):263504, December 2019.

[114] Seong Hyeon Park, Gahyun Choi, Gyunghun Kim, Jaehyeong Jo, Bumsung Lee, Geonyoung Kim, Kibog Park, Yong-Ho Lee, and Seungyong Hahn. Characterization of

broadband Purcell filters with compact footprint for fast multiplexed superconducting qubit readout. *Applied Physics Letters*, 124(4):044003, January 2024.

[115] Haoxiong Yan, Xuntao Wu, Andrew Lingenfelter, Yash J. Joshi, Gustav Andersson, Christopher R. Conner, Ming-Han Chou, Joel Grebel, Jacob M. Miller, Rhys G. Povey, Hong Qiao, Aashish A. Clerk, and Andrew N. Cleland. Broadband bandpass Purcell filter for circuit quantum electrodynamics. *Applied Physics Letters*, 123(13):134001, September 2023.

[116] Haoxiong Yan, Xuntao Wu, Andrew Lingenfelter, Yash Joshi, Gustav Andersson, Christopher R. Conner, Ming-Han Chou, Joel Grebel, Jacob M. Miller, Rhys G. Povey, Hong Qiao, Aashish A. Clerk, and Andrew N. Cleland. Broadband Purcell filter design for superconducting qubits. In *APS March Meeting*, March 2024.

[117] Y. Sunada, S. Kono, J. Ilves, S. Tamate, T. Sugiyama, Y. Tabuchi, and Y. Nakamura. Fast readout and reset of a superconducting qubit coupled to a resonator with an intrinsic Purcell filter. *Physical Review Applied*, 17(4):044016, April 2022.

[118] Yoshiki Sunada, Kenshi Yuki, Zhiling Wang, Takeaki Miyamura, Jesper Ilves, Kohei Matsuura, Peter A. Spring, Shuhei Tamate, Shingo Kono, and Yasunobu Nakamura. Photon-noise-tolerant dispersive readout of a superconducting qubit using a nonlinear Purcell filter. *PRX Quantum*, 5(1):010307, January 2024.

[119] Cristóbal Lledó, Rémy Dassonneville, Adrien Moulinas, Joachim Cohen, Ross Shillito, Audrey Bienfait, Benjamin Huard, and Alexandre Blais. Cloaking a qubit in a cavity. *Nature Communications*, 14(1):6313, October 2023.

[120] Nicolas Didier, Jérôme Bourassa, and Alexandre Blais. Fast quantum nondemolition readout by parametric modulation of longitudinal qubit-oscillator interaction. *Physical Review Letters*, 115(20):203601, November 2015.

[121] R. Barends, J. Kelly, A. Megrant, A. Veitia, D. Sank, E. Jeffrey, T. C. White, J. Mutus, A. G. Fowler, B. Campbell, Y. Chen, Z. Chen, B. Chiaro, A. Dunsworth, C. Neill, P. O'Malley, P. Roushan, A. Vainsencher, J. Wenner, A. N. Korotkov, A. N. Cleland, and John M. Martinis. Superconducting quantum circuits at the surface code threshold for fault tolerance. *Nature*, 508(7497):500–503, April 2014.

[122] C. R. Conner, A. Bienfait, H.-S. Chang, M.-H. Chou, É. Dumur, J. Grebel, G. A. Peairs, R. G. Povey, H. Yan, Y. P. Zhong, and A. N. Cleland. Superconducting qubits in a flip-chip architecture. *Applied Physics Letters*, 118(23):232602, June 2021.

[123] Trevor McCourt, Charles Neill, Kenny Lee, Chris Quintana, Yu Chen, Julian Kelly, Jeffrey Marshall, V. N. Smelyanskiy, M. I. Dykman, Alexander Korotkov, Isaac L. Chuang, and A. G. Petukhov. Learning noise via dynamical decoupling of entangled qubits. *Physical Review A*, 107(5):052610, May 2023.

[124] A. Kandala, K. X. Wei, S. Srinivasan, E. Magesan, S. Carnevale, G. A. Keefe, D. Klaus, O. Dial, and D. C. McKay. Demonstration of a high-fidelity CNOT gate for fixed-frequency transmons with engineered zz suppression. *Physical Review Letters*, 127(13):130501, September 2021.

[125] Michael A. Nielsen and Isaac L. Chuang. *Quantum Computation and Quantum Information*. Cambridge University Press, 2010.

[126] Line Hjortshøj Pedersen, Niels Martin Møller, and Klaus Mølmer. Fidelity of quantum operations. *Physics Letters A*, 367(1–2):47–51, July 2007.

[127] Tahereh Abad, Jorge Fernández-Pendás, Anton Frisk Kockum, and Göran Johansson. Universal fidelity reduction of quantum operations from weak dissipation. *Physical Review Letters*, 129(15):150504, October 2022.

[128] Tahereh Abad, Yoni Schattner, Anton Frisk Kockum, and Göran Johansson. Impact of decoherence on the fidelity of quantum gates leaving the computational subspace. *arXiv preprint*, 2302.13885, February 2023.

[129] Richard Jozsa. Fidelity for mixed quantum states. *Journal of Modern Optics*, 41(12):2315–2323, December 1994.

[130] Michał Horodecki, Paweł Horodecki, and Ryszard Horodecki. General teleportation channel, singlet fraction, and quasidistillation. *Physical Review A*, 60(3):1888–1898, September 1999.

[131] Joseph Emerson, Robert Alicki, and Karol Życzkowski. Scalable noise estimation with random unitary operators. *Journal of Optics B: Quantum and Semiclassical Optics*, 7(10):S347–S352, September 2005.

[132] E. Knill, D. Leibfried, R. Reichle, J. Britton, R. B. Blakestad, J. D. Jost, C. Langer, R. Ozeri, S. Seidelin, and D. J. Wineland. Randomized benchmarking of quantum gates. *Physical Review A*, 77(1):012307, January 2008.

[133] J. M. Chow, J. M. Gambetta, L. Tornberg, Jens Koch, Lev S. Bishop, A. A. Houck, B. R. Johnson, L. Frunzio, S. M. Girvin, and R. J. Schoelkopf. Randomized benchmarking and process tomography for gate errors in a solid-state qubit. *Physical Review Letters*, 102(9):090502, March 2009.

[134] Sergio Boixo, Sergei V. Isakov, Vadim N. Smelyanskiy, Ryan Babbush, Nan Ding, Zhang Jiang, Michael J. Bremner, John M. Martinis, and Hartmut Neven. Characterizing quantum supremacy in near-term devices. *Nature Physics*, 14(6):595–600, April 2018.

[135] Frank Arute, Kunal Arya, Ryan Babbush, Dave Bacon, Joseph C. Bardin, Rami Barends, Rupak Biswas, Sergio Boixo, Fernando G. S. L. Brandao, David A. Buell,

Brian Burkett, Yu Chen, Zijun Chen, Ben Chiaro, Roberto Collins, William Courtney, Andrew Dunsworth, Edward Farhi, Brooks Foxen, Austin Fowler, Craig Gidney, Marissa Giustina, Rob Graff, Keith Guerin, Steve Habegger, Matthew P. Harrigan, Michael J. Hartmann, Alan Ho, Markus Hoffmann, Trent Huang, Travis S. Humble, Sergei V. Isakov, Evan Jeffrey, Zhang Jiang, Dvir Kafri, Kostyantyn Kechedzhi, Julian Kelly, Paul V. Klimov, Sergey Knysh, Alexander Korotkov, Fedor Kostritsa, David Landhuis, Mike Lindmark, Erik Lucero, Dmitry Lyakh, Salvatore Mandrà, Jarrod R. McClean, Matthew McEwen, Anthony Megrant, Xiao Mi, Kristel Michielsen, Masoud Mohseni, Josh Mutus, Ofer Naaman, Matthew Neeley, Charles Neill, Murphy Yuezhen Niu, Eric Ostby, Andre Petukhov, John C. Platt, Chris Quintana, Eleanor G. Rieffel, Pedram Roushan, Nicholas C. Rubin, Daniel Sank, Kevin J. Satzinger, Vadim Smelyanskiy, Kevin J. Sung, Matthew D. Trevithick, Amit Vainsencher, Benjamin Villalonga, Theodore White, Z. Jamie Yao, Ping Yeh, Adam Zalcman, Hartmut Neven, and John M. Martinis. Quantum supremacy using a programmable superconducting processor. *Nature*, 574(7779):505–510, October 2019.

[136] T. Brown, E. Doucet, D. Ristè, G. Ribeill, K. Cicak, J. Aumentado, R. Simmonds, L. Govia, A. Kamal, and L. Ranzani. Trade off-free entanglement stabilization in a superconducting qutrit-qubit system. *Nature Communications*, 13(1):3994, July 2022.

[137] Yu Chen, C. Neill, P. Roushan, N. Leung, M. Fang, R. Barends, J. Kelly, B. Campbell, Z. Chen, B. Chiaro, A. Dunsworth, E. Jeffrey, A. Megrant, J. Y. Mutus, P. J. J. O'Malley, C. M. Quintana, D. Sank, A. Vainsencher, J. Wenner, T. C. White, Michael R. Geller, A. N. Cleland, and John M. Martinis. Qubit architecture with high coherence and fast tunable coupling. *Physical Review Letters*, 113(22):220502, November 2014.

[138] Michael R. Geller, Emmanuel Donate, Yu Chen, Michael T. Fang, Nelson Leung,

Charles Neill, Pedram Roushan, and John M. Martinis. Tunable coupler for superconducting Xmon qubits: Perturbative nonlinear model. *Physical Review A*, 92(1):012320, July 2015.

[139] Martin Rymarz and David P. DiVincenzo. Consistent quantization of nearly singular superconducting circuits. *Physical Review X*, 13(2):021017, May 2023.

[140] A. Miano, V.R. Joshi, G. Liu, W. Dai, P.D. Parakh, L. Frunzio, and M.H. Devoret. Hamiltonian extrema of an arbitrary flux-biased Josephson circuit. *PRX Quantum*, 4(3):030324, August 2023.

[141] Y. P. Zhong, H.-S. Chang, K. J. Satzinger, M.-H. Chou, A. Bienfait, C. R. Conner, É. Dumur, J. Grebel, G. A. Peairs, R. G. Povey, D. I. Schuster, and A. N. Cleland. Violating Bell's inequality with remotely connected superconducting qubits. *Nature Physics*, 15(8):741–744, April 2019.

[142] H.-S. Chang, Y. P. Zhong, A. Bienfait, M.-H. Chou, C. R. Conner, É. Dumur, J. Grebel, G. A. Peairs, R. G. Povey, K. J. Satzinger, and A. N. Cleland. Remote entanglement via adiabatic passage using a tunably dissipative quantum communication system. *Physical Review Letters*, 124(24):240502, June 2020.

[143] Ming-Han Chou. *Quantum Measurements of Microwave-Frequency Acoustic Resonators with Superconducting Circuits*. PhD thesis, University of Chicago, March 2023.

[144] C. Neill, P. Roushan, M. Fang, Y. Chen, M. Kolodrubetz, Z. Chen, A. Megrant, R. Barends, B. Campbell, B. Chiaro, A. Dunsworth, E. Jeffrey, J. Kelly, J. Mutus, P. J. J. O'Malley, C. Quintana, D. Sank, A. Vainsencher, J. Wenner, T. C. White, A. Polkovnikov, and J. M. Martinis. Ergodic dynamics and thermalization in an isolated quantum system. *Nature Physics*, 12(11):1037–1041, July 2016.

[145] C. Neill, P. Roushan, K. Kechedzhi, S. Boixo, S. V. Isakov, V. Smelyanskiy, A. Megrant, B. Chiaro, A. Dunsworth, K. Arya, R. Barends, B. Burkett, Y. Chen, Z. Chen, A. Fowler, B. Foxen, M. Giustina, R. Graff, E. Jeffrey, T. Huang, J. Kelly, P. Klimov, E. Lucero, J. Mutus, M. Neeley, C. Quintana, D. Sank, A. Vainsencher, J. Wenner, T. C. White, H. Neven, and J. M. Martinis. A blueprint for demonstrating quantum supremacy with superconducting qubits. *Science*, 360(6385):195–199, April 2018.

[146] J. Majer, J. M. Chow, J. M. Gambetta, Jens Koch, B. R. Johnson, J. A. Schreier, L. Frunzio, D. I. Schuster, A. A. Houck, A. Wallraff, A. Blais, M. H. Devoret, S. M. Girvin, and R. J. Schoelkopf. Coupling superconducting qubits via a cavity bus. *Nature*, 449(7161):443–447, September 2007.

[147] Charles James Neill. *A path towards quantum supremacy with superconducting qubits*. PhD thesis, University of California, Santa Barbara, December 2017.

[148] Fei Yan, Philip Krantz, Youngkyu Sung, Morten Kjaergaard, Daniel L. Campbell, Terry P. Orlando, Simon Gustavsson, and William D. Oliver. Tunable coupling scheme for implementing high-fidelity two-qubit gates. *Physical Review Applied*, 10(5):054062, November 2018.

[149] X. Li, T. Cai, H. Yan, Z. Wang, X. Pan, Y. Ma, W. Cai, J. Han, Z. Hua, X. Han, Y. Wu, H. Zhang, H. Wang, Yipu Song, Luming Duan, and Luyan Sun. Tunable coupler for realizing a controlled-phase gate with dynamically decoupled regime in a superconducting circuit. *Physical Review Applied*, 14(2):024070, August 2020.

[150] J. Stehlik, D. M. Zajac, D. L. Underwood, T. Phung, J. Blair, S. Carnevale, D. Klaus, G. A. Keefe, A. Carniol, M. Kumph, Matthias Steffen, and O. E. Dial. Tunable coupling architecture for fixed-frequency transmon superconducting qubits. *Physical Review Letters*, 127(8):080505, August 2021.

[151] Eyob A. Sete, Angela Q. Chen, Riccardo Manenti, Shobhan Kulshreshtha, and Stefano Poletto. Floating tunable coupler for scalable quantum computing architectures. *Physical Review Applied*, 15(6):064063, June 2021.

[152] Ji Chu and Fei Yan. Coupler-assisted controlled-phase gate with enhanced adiabaticity. *Physical Review Applied*, 16(5):054020, November 2021.

[153] Vladimir E. Manucharyan, Jens Koch, Leonid I. Glazman, and Michel H. Devoret. Fluxonium: Single Cooper-pair circuit free of charge offsets. *Science*, 326(5949):113–116, October 2009.

[154] Yuan Xu, Ji Chu, Jiahao Yuan, Jiawei Qiu, Yuxuan Zhou, Libo Zhang, Xinsheng Tan, Yang Yu, Song Liu, Jian Li, Fei Yan, and Dapeng Yu. High-fidelity, high-scalability two-qubit gate scheme for superconducting qubits. *Physical Review Letters*, 125(24):240503, December 2020.

[155] Michele C. Collodo, Johannes Herrmann, Nathan Lacroix, Christian Kraglund Andersen, Ants Remm, Stefania Lazar, Jean-Claude Besse, Theo Walter, Andreas Wallraff, and Christopher Eichler. Implementation of conditional phase gates based on tunable *ZZ* interactions. *Physical Review Letters*, 125(24):240502, December 2020.

[156] Youngkyu Sung, Leon Ding, Jochen Braumüller, Antti Vepsäläinen, Bharath Kannan, Morten Kjaergaard, Ami Greene, Gabriel O. Samach, Chris McNally, David Kim, Alexander Melville, Bethany M. Niedzielski, Mollie E. Schwartz, Jonilyn L. Yoder, Terry P. Orlando, Simon Gustavsson, and William D. Oliver. Realization of high-fidelity CZ and *ZZ*-free iswap gates with a tunable coupler. *Physical Review X*, 11(2):021058, June 2021.

[157] G. B. P. Huber, F. A. Roy, L. Koch, I. Tsitsilin, J. Schirk, N. J. Glaser, N. Bruckmoser, C. Schweizer, J. Romeiro, G. Krylov, M. Singh, F. X. Haslbeck, M. Knudsen, A. Marx,

F. Pfeiffer, C. Schneider, F. Wallner, D. Bunch, L. Richard, L. Södergren, K. Liegener, M. Werninghaus, and S. Filipp. Parametric multi-element coupling architecture for coherent and dissipative control of superconducting qubits. *arXiv preprint*, 2403.02203, March 2024.

[158] Niklas J. Glaser, Federico Roy, and Stefan Filipp. Controlled-controlled-phase gates for superconducting qubits mediated by a shared tunable coupler. *Physical Review Applied*, 19(4):044001, April 2023.

[159] Hayato Goto. Double-transmon coupler: Fast two-qubit gate with no residual coupling for highly detuned superconducting qubits. *Physical Review Applied*, 18(3):034038, September 2022.

[160] Peng Zhao, Yingshan Zhang, Guangming Xue, Yirong Jin, and Haifeng Yu. Tunable coupling of widely separated superconducting qubits: A possible application toward a modular quantum device. *Applied Physics Letters*, 121(3):032601, July 2022.

[161] Daniel L. Campbell, Archana Kamal, Leonardo Ranzani, Michael Senatore, and Matthew D. LaHaye. Modular tunable coupler for superconducting circuits. *Physical Review Applied*, 19(6):064043, June 2023.

[162] Gui-Han Liang, Xiao-Hui Song, Cheng-Lin Deng, Xu-Yang Gu, Yu Yan, Zheng-Yang Mei, Si-Lu Zhao, Yi-Zhou Bu, Yong-Xi Xiao, Yi-Han Yu, Ming-Chuan Wang, Tong Liu, Yun-Hao Shi, He Zhang, Xiang Li, Li Li, Jing-Zhe Wang, Ye Tian, Shi-Ping Zhao, Kai Xu, Heng Fan, Zhong-Cheng Xiang, and Dong-Ning Zheng. Tunable-coupling architectures with capacitively connecting pads for large-scale superconducting multiqubit processors. *Physical Review Applied*, 20(4):044028, October 2023.

[163] Rui Li, Kentaro Kubo, Yinghao Ho, Zhiguang Yan, Yasunobu Nakamura, and Hayato Goto. Realization of high-fidelity CZ gate based on a double-transmon coupler. *arXiv preprint*, 2402.18926, February 2024.

[164] Elena Yu. Egorova, Alena S. Kazmina, Ilya A. Simakov, Ilya N. Moskalenko, Nikolay N. Abramov, Daria A. Kalacheva, Viktor B. Lubsanov, Alexey N. Bolgar, Nataliya Maleeva, and Ilya S. Besedin. High-performance superconducting two-qubit gate using a three-mode tunable coupler. *arXiv preprint*, 2405.10886, May 2024.

[165] Haoxiong Yan, Youpeng Zhong, Hung-Shen Chang, Audrey Bienfait, Ming-Han Chou, Christopher R. Conner, Étienne Dumur, Joel Grebel, Rhys G. Povey, and Andrew N. Cleland. Entanglement purification and protection in a superconducting quantum network. *Physical Review Letters*, 128(8):080504, February 2022.

[166] Charles H. Bennett, Gilles Brassard, Sandu Popescu, Benjamin Schumacher, John A. Smolin, and William K. Wootters. Purification of noisy entanglement and faithful teleportation via noisy channels. *Physical Review Letters*, 76(5):722–725, January 1996.

[167] Jian-Wei Pan, Christoph Simon, Časlav Brukner, and Anton Zeilinger. Entanglement purification for quantum communication. *Nature*, 410(6832):1067–1070, April 2001.

[168] Jian-Wei Pan, Sara Gasparoni, Rupert Ursin, Gregor Weihs, and Anton Zeilinger. Experimental entanglement purification of arbitrary unknown states. *Nature*, 423(6938):417–422, May 2003.

[169] Xiao-Min Hu, Cen-Xiao Huang, Yu-Bo Sheng, Lan Zhou, Bi-Heng Liu, Yu Guo, Chao Zhang, Wen-Bo Xing, Yun-Feng Huang, Chuan-Feng Li, and Guang-Can Guo. Long-distance entanglement purification for quantum communication. *Physical Review Letters*, 126(1):010503, January 2021.

[170] Sebastian Ecker, Philipp Sohr, Lukas Bulla, Marcus Huber, Martin Bohmann, and Rupert Ursin. Experimental single-copy entanglement distillation. *Physical Review Letters*, 127(4):040506, July 2021.

[171] R. Reichle, D. Leibfried, E. Knill, J. Britton, R. B. Blakestad, J. D. Jost, C. Langer, R. Ozeri, S. Seidelin, and D. J. Wineland. Experimental purification of two-atom entanglement. *Nature*, 443(7113):838–841, October 2006.

[172] N. Kalb, A. A. Reiserer, P. C. Humphreys, J. J. W. Bakermans, S. J. Kamerling, N. H. Nickerson, S. C. Benjamin, D. J. Twitchen, M. Markham, and R. Hanson. Entanglement distillation between solid-state quantum network nodes. *Science*, 356(6341):928–932, June 2017.

[173] Luke D. Burkhart, James D. Teoh, Yaxing Zhang, Christopher J. Axline, Luigi Frunzio, M.H. Devoret, Liang Jiang, S.M. Girvin, and R.J. Schoelkopf. Error-detected state transfer and entanglement in a superconducting quantum network. *PRX Quantum*, 2(3):030321, August 2021.

[174] Nikolay V. Vitanov, Andon A. Rangelov, Bruce W. Shore, and Klaas Bergmann. Stimulated Raman adiabatic passage in physics, chemistry, and beyond. *Reviews of Modern Physics*, 89(1):015006, March 2017.

[175] W Dür and H J Briegel. Entanglement purification and quantum error correction. *Reports on Progress in Physics*, 70(8):1381–1424, July 2007.

[176] Keisuke Fujii and Katsuji Yamamoto. Entanglement purification with double selection. *Physical Review A*, 80(4):042308, October 2009.

[177] Stefan Krastanov, Victor V. Albert, and Liang Jiang. Optimized entanglement purification. *Quantum*, 3:123, February 2019.

[178] H. Y. Carr and E. M. Purcell. Effects of diffusion on free precession in nuclear magnetic resonance experiments. *Physical Review*, 94(3):630–638, May 1954.

[179] S. Meiboom and D. Gill. Modified spin-echo method for measuring nuclear relaxation times. *Review of Scientific Instruments*, 29(8):688–691, August 1958.

[180] Jonas Bylander, Simon Gustavsson, Fei Yan, Fumiki Yoshihara, Khalil Harrabi, George Fitch, David G. Cory, Yasunobu Nakamura, Jaw-Shen Tsai, and William D. Oliver. Noise spectroscopy through dynamical decoupling with a superconducting flux qubit. *Nature Physics*, 7(7):565–570, May 2011.

[181] Bibek Pokharel, Namit Anand, Benjamin Fortman, and Daniel A. Lidar. Demonstration of fidelity improvement using dynamical decoupling with superconducting qubits. *Physical Review Letters*, 121(22):220502, November 2018.

[182] Zijun Chen, Kevin J. Satzinger, Juan Atalaya, Alexander N. Korotkov, Andrew Dunsworth, Daniel Sank, Chris Quintana, Matt McEwen, Rami Barends, Paul V. Klimov, Sabrina Hong, Cody Jones, Andre Petukhov, Dvir Kafri, Sean Demura, Brian Burkett, Craig Gidney, Austin G. Fowler, Alexandru Paler, Harald Putterman, Igor Aleiner, Frank Arute, Kunal Arya, Ryan Babbush, Joseph C. Bardin, Andreas Bengtsson, Alexandre Bourassa, Michael Broughton, Bob B. Buckley, David A. Buell, Nicholas Bushnell, Benjamin Chiaro, Roberto Collins, William Courtney, Alan R. Derk, Daniel Eppens, Catherine Erickson, Edward Farhi, Brooks Foxen, Marissa Giustina, Ami Greene, Jonathan A. Gross, Matthew P. Harrigan, Sean D. Harrington, Jeremy Hilton, Alan Ho, Trent Huang, William J. Huggins, L. B. Ioffe, Sergei V. Isakov, Evan Jeffrey, Zhang Jiang, Kostyantyn Kechedzhi, Seon Kim, Alexei Kitaev, Fedor Kostritsa, David Landhuis, Pavel Laptev, Erik Lucero, Orion Martin, Jarrod R. McClean, Trevor McCourt, Xiao Mi, Kevin C. Miao, Masoud Mohseni, Shirin Montazeri, Wojciech Mruczkiewicz, Josh Mutus, Ofer Naaman, Matthew Neeley, Charles Neill,

Michael Newman, Murphy Yuezhen Niu, Thomas E. O'Brien, Alex Opremcak, Eric Ostby, Bálint Pató, Nicholas Redd, Pedram Roushan, Nicholas C. Rubin, Vladimir Shvarts, Doug Strain, Marco Szalay, Matthew D. Trevithick, Benjamin Villalonga, Theodore White, Z. Jamie Yao, Ping Yeh, Juhwan Yoo, Adam Zalcman, Hartmut Neven, Sergio Boixo, Vadim Smelyanskiy, Yu Chen, Anthony Megrant, and Julian Kelly. Exponential suppression of bit or phase errors with cyclic error correction. *Nature*, 595(7867):383–387, July 2021.

[183] Jiawei Qiu, Yuxuan Zhou, Chang-Kang Hu, Jiahao Yuan, Libo Zhang, Ji Chu, Wenhui Huang, Weiyang Liu, Kai Luo, Zhongchu Ni, Xianchuang Pan, Zhixuan Yang, Yimeng Zhang, Yuanzhen Chen, Xiu-Hao Deng, Ling Hu, Jian Li, Jingjing Niu, Yuan Xu, Tongxing Yan, Youpeng Zhong, Song Liu, Fei Yan, and Dapeng Yu. Suppressing coherent two-qubit errors via dynamical decoupling. *Physical Review Applied*, 16(5):054047, November 2021.

[184] Siyuan Niu, Aida Todri-Sanial, and Nicholas T. Bronn. Multi-qubit dynamical decoupling for enhanced crosstalk suppression. *arXiv preprint*, 2403.05391, March 2024.

[185] Jingjing Niu, Libo Zhang, Yang Liu, Jiawei Qiu, Wenhui Huang, Jiaxiang Huang, Hao Jia, Jiawei Liu, Ziyu Tao, Weiwei Wei, Yuxuan Zhou, Wanjing Zou, Yuanzhen Chen, Xiaowei Deng, Xiuhao Deng, Changkang Hu, Ling Hu, Jian Li, Dian Tan, Yuan Xu, Fei Yan, Tongxing Yan, Song Liu, Youpeng Zhong, Andrew N. Cleland, and Dapeng Yu. Low-loss interconnects for modular superconducting quantum processors. *Nature Electronics*, 6(3):235–241, February 2023.

[186] Joel Grebel, Haoxiong Yan, Ming-Han Chou, Gustav Andersson, Christopher R. Conner, Yash J. Joshi, Jacob M. Miller, Rhys G. Povey, Hong Qiao, Xuntao Wu, and Andrew N. Cleland. Bidirectional multiphoton communication between remote superconducting nodes. *Physical Review Letters*, 132(4):047001, January 2024.

[187] Jiawei Qiu, Yang Liu, Jingjing Niu, Ling Hu, Yukai Wu, Libo Zhang, Wenhui Huang, Yuanzhen Chen, Jian Li, Song Liu, Youpeng Zhong, Luming Duan, and Dapeng Yu. Deterministic quantum teleportation between distant superconducting chips. *arXiv preprint*, 2302.08756, February 2023.

[188] M. Żukowski, A. Zeilinger, M. A. Horne, and A. K. Ekert. "Event-ready-detectors" Bell experiment via entanglement swapping. *Physical Review Letters*, 71(26):4287–4290, December 1993.

[189] Charles H. Bennett, Gilles Brassard, Claude Crépeau, Richard Jozsa, Asher Peres, and William K. Wootters. Teleporting an unknown quantum state via dual classical and Einstein-Podolsky-Rosen channels. *Physical Review Letters*, 70(13):1895–1899, March 1993.

[190] H.-J. Briegel, W. Dür, J. I. Cirac, and P. Zoller. Quantum repeaters: The role of imperfect local operations in quantum communication. *Physical Review Letters*, 81(26):5932–5935, December 1998.

[191] Nicolas Sangouard, Christoph Simon, Hugues de Riedmatten, and Nicolas Gisin. Quantum repeaters based on atomic ensembles and linear optics. *Reviews of Modern Physics*, 83(1):33–80, March 2011.

[192] C. Branciard, N. Gisin, and S. Pironio. Characterizing the nonlocal correlations created via entanglement swapping. *Physical Review Letters*, 104(17):170401, April 2010.

[193] Cyril Branciard, Denis Rosset, Nicolas Gisin, and Stefano Pironio. Bilocal versus nonbilocal correlations in entanglement-swapping experiments. *Physical Review A*, 85(3):032119, March 2012.

[194] Nicolas Brunner, Daniel Cavalcanti, Stefano Pironio, Valerio Scarani, and Stephanie Wehner. Bell nonlocality. *Reviews of Modern Physics*, 86(2):419–478, April 2014.

[195] Marc-Olivier Renou, David Trillo, Mirjam Weilenmann, Thinh P. Le, Armin Tavakoli, Nicolas Gisin, Antonio Acín, and Miguel Navascués. Quantum theory based on real numbers can be experimentally falsified. *Nature*, 600(7890):625–629, December 2021.

[196] Zheng-Da Li, Ya-Li Mao, Mirjam Weilenmann, Armin Tavakoli, Hu Chen, Lixin Feng, Sheng-Jun Yang, Marc-Olivier Renou, David Trillo, Thinh P. Le, Nicolas Gisin, Antonio Acín, Miguel Navascués, Zizhu Wang, and Jingyun Fan. Testing real quantum theory in an optical quantum network. *Physical Review Letters*, 128(4):040402, January 2022.

[197] Ming-Cheng Chen, Can Wang, Feng-Ming Liu, Jian-Wen Wang, Chong Ying, Zhong-Xia Shang, Yulin Wu, M. Gong, H. Deng, F.-T. Liang, Qiang Zhang, Cheng-Zhi Peng, Xiaobo Zhu, Adán Cabello, Chao-Yang Lu, and Jian-Wei Pan. Ruling out real-valued standard formalism of quantum theory. *Physical Review Letters*, 128(4):040403, January 2022.

[198] Daniel M. Greenberger, Michael A. Horne, and Anton Zeilinger. *Going Beyond Bell's Theorem*, pages 69–72. Springer Netherlands, 1989.

[199] D. Leibfried, M. D. Barrett, T. Schaetz, J. Britton, J. Chiaverini, W. M. Itano, J. D. Jost, C. Langer, and D. J. Wineland. Toward Heisenberg-limited spectroscopy with multiparticle entangled states. *Science*, 304(5676):1476–1478, June 2004.

[200] Mark Hillery, Vladimír Bužek, and André Berthiaume. Quantum secret sharing. *Physical Review A*, 59(3):1829–1834, March 1999.

[201] Otfried Gühne and Michael Seevinck. Separability criteria for genuine multiparticle entanglement. *New Journal of Physics*, 12(5):053002, May 2010.

[202] Adi Shamir. How to share a secret. *Communications of the ACM*, 22(11):612–613, November 1979.

[203] G. R. Blakley. Safeguarding cryptographic keys. In *1979 International Workshop on Managing Requirements Knowledge (MARK)*. IEEE, June 1979.

[204] Richard Cleve, Daniel Gottesman, and Hoi-Kwong Lo. How to share a quantum secret. *Physical Review Letters*, 83(3):648–651, July 1999.

[205] Daniel Gottesman. Theory of quantum secret sharing. *Physical Review A*, 61(4):042311, March 2000.

[206] Anders Karlsson, Masato Koashi, and Nobuyuki Imoto. Quantum entanglement for secret sharing and secret splitting. *Physical Review A*, 59(1):162–168, January 1999.

[207] Guo-Ping Guo and Guang-Can Guo. Quantum secret sharing without entanglement. *Physics Letters A*, 310(4):247–251, April 2003.

[208] Li Xiao, Gui Lu Long, Fu-Guo Deng, and Jian-Wei Pan. Efficient multiparty quantum-secret-sharing schemes. *Physical Review A*, 69(5):052307, May 2004.

[209] Zhan-jun Zhang and Zhong-xiao Man. Multiparty quantum secret sharing of classical messages based on entanglement swapping. *Physical Review A*, 72(2):022303, August 2005.

[210] Zhan-jun Zhang, Yong Li, and Zhong-xiao Man. Multiparty quantum secret sharing. *Physical Review A*, 71(4):044301, April 2005.

[211] Damian Markham and Barry C. Sanders. Graph states for quantum secret sharing. *Physical Review A*, 78(4):042309, October 2008.

[212] W. Tittel, H. Zbinden, and N. Gisin. Experimental demonstration of quantum secret sharing. *Physical Review A*, 63(4):042301, March 2001.

[213] Yu-Ao Chen, An-Ning Zhang, Zhi Zhao, Xiao-Qi Zhou, Chao-Yang Lu, Cheng-Zhi Peng, Tao Yang, and Jian-Wei Pan. Experimental quantum secret sharing and third-man quantum cryptography. *Physical Review Letters*, 95(20):200502, November 2005.

[214] S. Gaertner, C. Kurtsiefer, M. Bourennane, and H. Weinfurter. Experimental demonstration of four-party quantum secret sharing. *Physical Review Letters*, 98(2):020503, January 2007.

[215] Jan Bogdanski, Nima Rafiei, and Mohamed Bourennane. Experimental quantum secret sharing using telecommunication fiber. *Physical Review A*, 78(6):062307, December 2008.

[216] B. A. Bell, D. Markham, D. A. Herrera-Martí, A. Marin, W. J. Wadsworth, J. G. Rarity, and M. S. Tame. Experimental demonstration of graph-state quantum secret sharing. *Nature Communications*, 5(1):5480, November 2014.

[217] Nirupam Basak, Nayana Das, Goutam Paul, Kaushik Nandi, and Nixon Patel. Quantum secret sharing protocol using GHZ state: implementation on ibm qiskit. *Quantum Information Processing*, 22(11):393, October 2023.

[218] A. S. Holevo. Bounds for the quantity of information transmitted by a quantum communication channel. *Problemy Peredachi Informatsii*, 9(3):3–11, 1973.

[219] A. S. Holevo. The capacity of the quantum channel with general signal states. *IEEE Transactions on Information Theory*, 44(1):269–273, 1998.

[220] Benjamin Schumacher and Michael D. Westmoreland. Sending classical information via noisy quantum channels. *Physical Review A*, 56(1):131–138, July 1997.

[221] Marc-Olivier Renou, Elisa Bäumer, Sadra Boreiri, Nicolas Brunner, Nicolas Gisin, and Salman Beigi. Genuine quantum nonlocality in the triangle network. *Physical Review Letters*, 123(14):140401, September 2019.

[222] Armin Tavakoli, Alejandro Pozas-Kerstjens, Ming-Xing Luo, and Marc-Olivier Renou. Bell nonlocality in networks. *Reports on Progress in Physics*, 85(5):056001, March 2022.

[223] Ning-Ning Wang, Chao Zhang, Huan Cao, Kai Xu, Bi-Heng Liu, Yun-Feng Huang, Chuan-Feng Li, Guang-Can Guo, Nicolas Gisin, Tamás Kriváchy, and Marc-Olivier Renou. Experimental genuine quantum nonlocality in the triangle network. *arXiv preprint*, 2401.15428, January 2024.

[224] Leslie Lamport, Robert Shostak, and Marshall Pease. The Byzantine generals problem. *ACM Transactions on Programming Languages and Systems*, 4(3):382–401, July 1982.

[225] Mark Hillery, Mário Ziman, Vladimír Bužek, and Martina Bieliková. Towards quantum-based privacy and voting. *Physics Letters A*, 349(1–4):75–81, January 2006.

[226] Peng Xue and Xin Zhang. A simple quantum voting scheme with multi-qubit entanglement. *Scientific Reports*, 7(1), August 2017.

[227] Chao Song, Kai Xu, Hekang Li, Yu-Ran Zhang, Xu Zhang, Wuxin Liu, Qiujiang Guo, Zhen Wang, Wenhui Ren, Jie Hao, Hui Feng, Heng Fan, Dongning Zheng, Da-Wei Wang, H. Wang, and Shi-Yao Zhu. Generation of multicomponent atomic Schrödinger cat states of up to 20 qubits. *Science*, 365(6453):574–577, August 2019.

[228] Tim Menke, William P. Banner, Thomas R. Bergamaschi, Agustin Di Paolo, Antti Vepsäläinen, Steven J. Weber, Roni Winik, Alexander Melville, Bethany M. Niedzielski, Danna Rosenberg, Kyle Serniak, Mollie E. Schwartz, Jonilyn L. Yoder, Alán Aspuru-Guzik, Simon Gustavsson, Jeffrey A. Grover, Cyrus F. Hirjibehedin, Andrew J. Kerman, and William D. Oliver. Demonstration of tunable three-body interactions between superconducting qubits. *Physical Review Letters*, 129(22):220501, November 2022.

[229] Sumeru Hazra, Anirban Bhattacharjee, Madhavi Chand, Kishor V. Salunkhe, Sriram Gopalakrishnan, Meghan P. Patankar, and R. Vijay. Ring-resonator-based coupling architecture for enhanced connectivity in a superconducting multiqubit network. *Physical Review Applied*, 16(2):024018, August 2021.

[230] Chao Zhou, Pinlei Lu, Matthieu Praquin, Tzu-Chiao Chien, Ryan Kaufman, Xi Cao, Mingkang Xia, Roger S. K. Mong, Wolfgang Pfaff, David Pekker, and Michael Hatridge. Realizing all-to-all couplings among detachable quantum modules using a microwave quantum state router. *npj Quantum Information*, 9(1):54, June 2023.

[231] M. Pechal, J.-C. Besse, M. Mondal, M. Oppliger, S. Gasparinetti, and A. Wallraff. Superconducting switch for fast on-chip routing of quantum microwave fields. *Physical Review Applied*, 6(2):024009, August 2016.

[232] O. Naaman, M. O. Abutaleb, C. Kirby, and M. Rennie. On-chip Josephson junction microwave switch. *Applied Physics Letters*, 108(11):112601, March 2016.

[233] H.-S. Chang, K. J. Satzinger, Y. P. Zhong, A. Bienfait, M.-H. Chou, C. R. Conner, É. Dumur, J. Grebel, G. A. Peairs, R. G. Povey, and A. N. Cleland. A fast and large bandwidth superconducting variable coupler. *Applied Physics Letters*, 117(24):244001, December 2020.

[234] David C. McKay, Ravi Naik, Philip Reinhold, Lev S. Bishop, and David I. Schuster. High-contrast qubit interactions using multimode cavity QED. *Physical Review Letters*, 114(8):080501, February 2015.

[235] Firat Solgun, David P. DiVincenzo, and Jay M. Gambetta. Simple impedance response formulas for the dispersive interaction rates in the effective Hamiltonians of low anharmonicity superconducting qubits. *IEEE Transactions on Microwave Theory and Techniques*, 67(3):928–948, March 2019.

[236] Firat Solgun and Srikanth Srinivasan. Direct calculation of ZZ interaction rates in multimode circuit quantum electrodynamics. *Physical Review Applied*, 18(4):044025, October 2022.

[237] Peter Groszkowski and Jens Koch. Scqubits: a Python package for superconducting qubits. *Quantum*, 5:583, November 2021.

[238] Sai Pavan Chitta, Tianpu Zhao, Ziwen Huang, Ian Mondragon-Shem, and Jens Koch. Computer-aided quantization and numerical analysis of superconducting circuits. *New Journal of Physics*, 24(10):103020, October 2022.

[239] Taha Rajabzadeh, Zhaoyou Wang, Nathan Lee, Takuma Makihara, Yudan Guo, and Amir H. Safavi-Naeini. Analysis of arbitrary superconducting quantum circuits accompanied by a Python package: SQcircuit. *Quantum*, 7:1118, September 2023.

[240] K. J. Satzinger, C. R. Conner, A. Bienfait, H.-S. Chang, Ming-Han Chou, A. Y. Cleland, É. Dumur, J. Grebel, G. A. Peairs, R. G. Povey, S. J. Whiteley, Y. P. Zhong, D. D. Awschalom, D. I. Schuster, and A. N. Cleland. Simple non-galvanic flip-chip integration method for hybrid quantum systems. *Applied Physics Letters*, 114(17):173501, April 2019.

[241] Alexander P. M. Place, Lila V. H. Rodgers, Pranav Mundada, Basil M. Smitham, Mattias Fitzpatrick, Zhaoqi Leng, Anjali Premkumar, Jacob Bryon, Andrei Vrajitoarea, Sara Sussman, Guangming Cheng, Trisha Madhavan, Harshvardhan K. Babla, Xuan Hoang Le, Youqi Gang, Berthold Jäck, András Gyenis, Nan Yao, Robert J. Cava, Nathalie P. de Leon, and Andrew A. Houck. New material platform for superconducting transmon qubits with coherence times exceeding 0.3 milliseconds. *Nature Communications*, 12(1):1779, March 2021.

[242] Chenlu Wang, Xuegang Li, Huikai Xu, Zhiyuan Li, Junhua Wang, Zhen Yang, Zhenyu Mi, Xuehui Liang, Tang Su, Chuhong Yang, Guangyue Wang, Wenyan Wang, Yongchao Li, Mo Chen, Chengyao Li, Kehuan Linghu, Jiaxiu Han, Yingshan Zhang, Yulong Feng, Yu Song, Teng Ma, Jingning Zhang, Ruixia Wang, Peng Zhao, Weiyang Liu, Guangming Xue, Yirong Jin, and Haifeng Yu. Towards practical quantum computers: transmon qubit with a lifetime approaching 0.5 milliseconds. *npj Quantum Information*, 8(1):3, January 2022.

[243] Yuval Baum, Mirko Amico, Sean Howell, Michael Hush, Maggie Liuzzi, Pranav Mundada, Thomas Merkh, Andre R.R. Carvalho, and Michael J. Biercuk. Experimental deep reinforcement learning for error-robust gate-set design on a superconducting quantum computer. *PRX Quantum*, 2(4):040324, November 2021.

[244] V. V. Sivak, A. Eickbusch, H. Liu, B. Royer, I. Tsioutsios, and M. H. Devoret. Model-free quantum control with reinforcement learning. *Physical Review X*, 12(1):011059, March 2022.

[245] Marie Lu, Jean-Loup Ville, Joachim Cohen, Alexandru Petrescu, Sydney Schreppler, Larry Chen, Christian Jünger, Chiara Pelletti, Alexei Marchenkov, Archan Banerjee, William P. Livingston, John Mark Kreikebaum, David I. Santiago, Alexandre Blais, and Irfan Siddiqi. Multipartite entanglement in Rabi-driven superconducting qubits. *PRX Quantum*, 3(4):040322, November 2022.

[246] Sainan Huai, Kunliang Bu, Xiu Gu, Zhenxing Zhang, Shuoming An, Xiaopei Yang, Yuan Li, Tianqi Cai, and Yicong Zheng. Fast joint parity measurement via collective interactions induced by stimulated emission. *Nature Communications*, 15(1):3045, April 2024.

[247] Sergey Bravyi, Andrew W. Cross, Jay M. Gambetta, Dmitri Maslov, Patrick Rall, and Theodore J. Yoder. High-threshold and low-overhead fault-tolerant quantum memory. *Nature*, 627(8005):778–782, March 2024.

[248] Qian Xu, J. Pablo Bonilla Ataides, Christopher A. Pattison, Nithin Raveendran, Dolev Bluvstein, Jonathan Wurtz, Bane Vasić, Mikhail D. Lukin, Liang Jiang, and Hengyun Zhou. Constant-overhead fault-tolerant quantum computation with reconfigurable atom arrays. *Nature Physics*, April 2024.

[249] Clayton R. Paul. *Analysis of Multiconductor Transmission Lines*. John Wiley & Sons, Inc, October 2007.

[250] Ebrahim Forati, Brandon W. Langley, and Ani Nersisyan. On the electromagnetic couplings in superconducting qubit circuits. *arXiv preprint*, 2405.11426, May 2024.

[251] G. Matthaei, L. Young, and E. M. T. Jones. *Microwave Filters, Impedance-Matching Networks, and Coupling Structures*. Artech House, June 1908.

[252] Hung-Shen Chang. *Remote Entanglement via Adiabatic Passage Using a Tunably Dissipative Quantum Communication System*. PhD thesis, University of Chicago, March 2021.

[253] Joel Grebel. *Bidirectional Multi-Photon Communication between Remote Superconducting Resonators*. PhD thesis, University of Chicago, June 2023.

[254] Sihao Huang, Benjamin Lienhard, Greg Calusine, Antti Vepsäläinen, Jochen Braumüller, David K. Kim, Alexander J. Melville, Bethany M. Niedzielski, Jonilyn L. Yoder, Bharath Kannan, Terry P. Orlando, Simon Gustavsson, and William D. Oliver. Microwave package design for superconducting quantum processors. *PRX Quantum*, 2(2):020306, April 2021.

[255] T.O. Klaassen, J.H. Blok, J.N. Hovenier, G. Jakob, D. Rosenthal, and K.J. Wildeman. Absorbing coatings and diffuse reflectors for the Herschel platform sub-millimeter spectrometers HIFI and PACS. In *Proceedings, IEEE Tenth International Conference on Terahertz Electronics*, THZ-02, pages 32–35. IEEE, 2002.

[256] J. J. A. Baselmans, S. J. C. Yates, Betty Young, Blas Cabrera, and Aaron Miller. Long quasiparticle lifetime in Aluminum Microwave Kinetic Inductance Detectors using coaxial stray light filters. In *AIP Conference Proceedings*, volume 1185, pages 160–163. AIP, 2009.

[257] R. Barends, J. Wenner, M. Lenander, Y. Chen, R. C. Bialczak, J. Kelly, E. Lucero, P. O'Malley, M. Mariantoni, D. Sank, H. Wang, T. C. White, Y. Yin, J. Zhao, A. N. Cleland, John M. Martinis, and J. J. A. Baselmans. Minimizing quasiparticle generation from stray infrared light in superconducting quantum circuits. *Applied Physics Letters*, 99(11):113507, September 2011.

[258] S. Krinner, S. Storz, P. Kurpiers, P. Magnard, J. Heinsoo, R. Keller, J. Lütolf, C. Eichler, and A. Wallraff. Engineering cryogenic setups for 100-qubit scale superconducting circuit systems. *EPJ Quantum Technology*, 6(1):2, May 2019.

[259] D F Santavicca and D E Prober. Impedance-matched low-pass stripline filters. *Measurement Science and Technology*, 19(8):087001, June 2008.

[260] Michael Fang. Development of hardware for scaling up superconducting qubits and simulation of quantum chaos. Bachelor's thesis, University of California, Santa Barbara, June 2015.

[261] Graham J. Norris. Improving infrared-blocking microwave filters. Semester report, ETH Zurich, October 2017.

[262] John M. Martinis, Michel H. Devoret, and John Clarke. Experimental tests for the quantum behavior of a macroscopic degree of freedom: The phase difference across a Josephson junction. *Physical Review B*, 35(10):4682–4698, April 1987.

[263] A. Fukushima, A. Sato, A. Iwasa, Y. Nakamura, T. Komatsuzaki, and Y. Sakamoto. Attenuation of microwave filters for single-electron tunneling experiments. *IEEE Transactions on Instrumentation and Measurement*, 46(2):289–293, April 1997.

[264] K. Bladh, D. Gunnarsson, E. Hürfeld, S. Devi, C. Kristoffersson, B. Smålander, S. Pehrson, T. Claeson, P. Delsing, and M. Taslakov. Comparison of cryogenic filters for use in single electronics experiments. *Review of Scientific Instruments*, 74(3):1323–1327, March 2003.

[265] F. P. Milliken, J. R Rozen, G. A. Keefe, and R. H. Koch. 50 Ω characteristic impedance low-pass metal powder filters. *Review of Scientific Instruments*, 78(2):024701, February 2007.

[266] A. Lukashenko and A. V. Ustinov. Improved powder filters for qubit measurements. *Review of Scientific Instruments*, 79(1):014701, January 2008.

[267] Filipp Mueller, Raymond N. Schouten, Matthias Brauns, Tian Gang, Wee Han Lim, Nai Shyan Lai, Andrew S. Dzurak, Wilfred G. van der Wiel, and Floris A. Zwanenburg. Printed circuit board metal powder filters for low electron temperatures. *Review of Scientific Instruments*, 84(4):044706, April 2013.

[268] Christian P. Scheller, Sarah Heizmann, Kristine Bedner, Dominic Giss, Matthias Meschke, Dominik M. Zumbühl, Jeramy D. Zimmerman, and Arthur C. Gossard. Silver-epoxy microwave filters and thermalizers for millikelvin experiments. *Applied Physics Letters*, 104(21):211106, May 2014.

[269] Slawomir Simbierowicz, Volodymyr Y. Monarkha, Suren Singh, Nizar Messaoudi, Philip Krantz, and Russell E. Lake. Microwave calibration of qubit drive line components at millikelvin temperatures. *Applied Physics Letters*, 120(5):054004, January 2022.

[270] Daniel Sank, Alex Opremcak, Andreas Bengtsson, Mostafa Khezri, Zijun Chen, Ofer Naaman, and Alexander Korotkov. System characterization of dispersive readout in superconducting qubits. *arXiv preprint*, 2402.00413, February 2024.

[271] Johannes Herrmann, Christoph Hellings, Stefania Lazar, Fabian Pfäffli, Florian Haupt, Tobias Thiele, Dante Colao Zanuz, Graham J. Norris, Flavio Heer, Christopher Eichler, and Andreas Wallraff. Frequency up-conversion schemes for controlling superconducting qubits. *arXiv preprint*, 2210.02513, October 2022.

[272] Leandro Stefanazzi, Kenneth Treptow, Neal Wilcer, Chris Stoughton, Collin Bradford, Sho Uemura, Silvia Zorzetti, Salvatore Montella, Gustavo Cancelo, Sara Sussman, Andrew Houck, Shefali Saxena, Horacio Arnaldi, Ankur Agrawal, Helin Zhang, Chunyang Ding, and David I. Schuster. The QICK (Quantum Instrumentation Control Kit): Readout and control for qubits and detectors. *Review of Scientific Instruments*, 93(4), April 2022.